The Role of Relativistic Effects in Future Cosmic Surveys

Sobral Blanco, Daniel

How to cite

SOBRAL BLANCO, Daniel. The Role of Relativistic Effects in Future Cosmic Surveys. 2024. doi: 10.13097/archive-ouverte/unige:178894

This publication URL: https://archive-ouverte.unige.ch//unige:178894
Publication DOI: 10.13097/archive-ouverte/unige:178894

UNIVERSITÉ DE GENÈVE
Section de Physique
Department de Physique Théorique

FACULTÉ DES SCIENCES
C. Bonvin (Supervisor)

The Role of Relativistic Effects in Future Cosmic Surveys

THÈSE

présentée à la Faculté des sciences de l'Université de Genève
pour obtenir le grade de
Docteur ès sciences, mention physique

par
Daniel Sobral Blanco
de
Ponferrada (Spain)

Thése N° 5832

GENÈVE
Atelier de reproduction de la Section de Physique
2024

UNIVERSITÉ
DE GENÈVE
FACULTÉ DES SCIENCES

DOCTORAT ÈS SCIENCES, MENTION PHYSIQUE

Thèse de Monsieur Daniel SOBRAL BLANCO

intitulée :

«The Role of Relativistic Effects in Future Cosmic Surveys»

La Faculté des sciences, sur le préavis de

Madame C. BONVIN, professeure associée et directrice de thèse
Département de physique théorique

Monsieur J. CARRON, professeur assistant
Département de physique théorique

Monsieur I. TUTUSAUS LLEIXA, docteur
Institut de Recherche en Astrophysique et Planétologie (IRAP), Université de Toulouse, Toulouse, France

Monsieur R. MAARTENS, professeur
Department of Physics and Astronomy, University of Western Cape, Cape Town, South Africa

autorise l'impression de la présente thèse, sans exprimer d'opinion sur les propositions qui y sont énoncées.

Genève, le 12 juillet 2024

Thèse - 5832 -

Le Décanat

N.B. - La thèse doit porter la déclaration précédente et remplir les conditions énumérées dans les "Informations relatives aux thèses de doctorat à l'Université de Genève".

Confía en el tiempo, que suele dar dulces salidas a muchas amargas dificultades.

— Miguel de Cervantes Saavedra.

Dedicado a la memoria de Enrique Sobral Correa.

1954 – 2024

DEO GRATIAS

> *I... a universe of atoms, an atom in the Universe.*
>
> — Richard P. Feynman.

ACKNOWLEDGMENTS

The content of this Thesis would not have been possible without the help, guidance and patience of my supervisor, Prof. Camille Bonvin. You been an unvaluable mentor and a trully example to follow. Many thanks for trusting me as a Ph. D. student and for all the time invested in our discussions. I wish to extend my gratitude to my other external collaborators, Dr. I. Tutusaus, Dr. M. Mancarella, Prof. C. Clarkson and Prof. R. Maartens, whose help has been crucial for the development the projects hereby contained.

I would like also to thank the Jury Members of my defence, Dr. I. Tutusaus, Dr. J. Carron and Prof. R. Maartens, for the time invested in reading and evaluating my work. It is trully an honor to know that you have enjoyed reading such a long piece of work.

Many thanks also to all the people in the wonderful group that Prof. Bonvin has created through the years: Sveva (Svevita), Francesco (Paquito), Nastassia, Martin, Enea, Lawrence, Maria and some others that are no longer part of the group. I had an unbelievable and unforgetable time among you. We did some awesome physics and also had plenty of fun together. My gratitude needs also to be extended to many other members of the DPT: Viraj (Virajito), Giulia, Goran, Niccolo, Francesco (Iacovelli), Ahmad... You are all part of a group of great people and great physicists.

Away from the Academic relations, I have to express my gratitude to my parents. I could only find continuous and unconditonal support from their side since I took the decission that I wanted to pursue a Ph. D. in Physics. I deeply thank them for understanding me, despite the faces they made when I attempted to explain what I was doing.

There is also the friendship side of life, a cruciall pillar which provides additional support even at a distance. Many thanks to my lifelong friends in El Bierzo, a place where I will always be eager to return. Many thanks as well to my old friends from the BSc years, the 'Club Axial', together with whom I started this journey through science and shared the first steps towards the right path. I am really proud of how well we have done since then, even after chosing different paths. Many thanks as well to my more 'virtual' friends forming the 'Conçilio Rulante'. It is great to find such a fun, high-energy and lively group of people. You are all great and I am convinced we are going to make it.

Last, but not least, I cannot go forward without expressing my gratitude to the love of my life, my sweet Marianela. You light up my life. A few lines here will not do justice on how well you make me feel and the self-confidence that having you in my life has earned me. I thank you and I kindly ask for a small apology for the difficult times when we were apart. Thanks for the thousands of hours on the phone, thanks for your always kind words, thanks for your support, thanks for listening me practice for my defence, thanks for making our little home more cozy and beautiful. Thanks for being you.

RÉSUMÉ

Le Cosmos, « *la dernière frontière* ». On l'imagine souvent comme une vaste tapisserie tissée de fils tendus par les interactions gravitationnelles. Nous savons avec certitude que la *structure à grande échelle* observée n'est pas simplement une scène statique, mais un portrait dynamique façonné par divers phénomènes. Les *distortions dans l'espace des redshifts*, par exemple, fournissent des preuves des vitesses particulières des galaxies, révélant des motifs anisotropes dans leur regroupement. Cette anisotropie n'est pas aléatoire ; elle est une conséquence directe de ces vitesses particulières, une vaste et complexe danse de galaxies se déplaçant sous l'influence de la gravité. Tout aussi remarquable est l'effet de *lentillage gravitationnel*. Les structures massives comme les amas de galaxies peuvent déformer cette tapisserie, agissant comme une loupe cosmique qui courbe les chemins de la lumière provenant de galaxies lointaines. Cela induit des distorsions dans les positions apparentes et les formes de ces objets lumineux en arrière-plan, offrant aux astronomes un outil puissant pour cartographier la distribution de la matière et la géométrie de l'Univers. De toute évidence, ces deux phénomènes sont des sondes cruciales pour tester le lien entre la matière et la géométrie, ou, comme nous les scientifiques l'appelons, la théorie de la Relativité Générale. En fait, les relevés cosmiques ont déjà mesuré ces effets et fourni des contraintes de haute précision sur les paramètres pertinents.

Il est intéressant de noter que des effets supplémentaires sont prédits pour y contribuer. La communauté les appelle *effets relativistes*. Dans cette thèse, nous nous concentrons sur eux, avec une attention particulière sur le *redshift gravitationnel*. Il se produit lorsque les photons sortent des puits de potentiel gravitationnel, perdant de l'énergie dans le processus, ce qui se traduit par un décalage supplémentaire vers le rouge. Ce phénomène, qui a été mesuré dans des contextes astrophysiques, est souvent négligé dans les études cosmologiques. Cependant, nous montrons qu'il sera définitivement une partie cruciale des analyses des futurs relevés cosmiques. Nous démontrons que cet effet sert de sonde directe de la géométrie de l'espace-temps et qu'il sera décisif pour lever les dégénérescences parmi les paramètres régissant la modélisation de la structure à grande échelle à des époques tardives, comme mesuré par la prochaine génération de relevés galactiques de Stage IV. En somme, nous proposons jusqu'à trois applications et implications possibles pour les mesures de ce phénomène à l'échelle cosmologique.

La Partie i de cette thèse sert d'introduction au sujet. Tout d'abord, nous fournissons une introduction non exhaustive à la modélisation de la structure à grande échelle à des époques tardives. En particulier, nous résumons le calcul des *comptages de galaxies* au premier ordre en théorie des perturbations, en tenant compte des effets systématiques connus sous le nom de biais d'*évolution* et de *magnification*, qui modulent l'amplitude des effets relativistes. Nous définissons également la *cisaillement gravitationnel* comme l'observable pertinente de la lentille faible prise en compte dans nos travaux de recherche. Deuxièmement, nous développons la machinerie statistique nécessaire pour les études ultérieures. Pour le cas spectroscopique, nous commençons par les *spectres de puissance* de l'espace des décalages vers le rouge dans le domaine de Fourier. Ensuite, nous calculons les multipôles de la fonction de corrélation du regroupement des galaxies à deux points

pour le cas plus général de deux populations de traceurs, ce qui est crucial pour mesurer le *redshift gravitationnel* et d'autres corrections relativistes. Plus précisément, nous montrons que ces effets génèrent des *multipôles impairs* dans la fonction de corrélation. Complémentairement à ces résultats, nous calculons la matrice de covariance associée aux multipôles, pour laquelle nous fournissons également une recette généralisée pour le cas de multiples populations de traceurs. En outre, nous résumons le calcul des *spectres de puissance harmoniques*, qui sont généralement la cible des analyses des relevés photométriques. Enfin, nous décrivons les techniques d'inférence utilisées dans les parties suivantes.

Dans la Partie ii, nous introduisons un nouveau test de gravité indépendant du modèle ciblant le stress anisotrope, c'est-à-dire le rapport entre les deux potentiels métriques. Nous démontrons qu'une mesure du *redshift gravitationnel* est un proxy pour une mesure indépendante du potentiel de distorsion temporelle. Ainsi, nous construisons l'estimateur correspondant basé sur les multipôles de la fonction de corrélation à deux points, qui isole la contribution des distorsions temporelles. Ensuite, en combinaison avec des mesures de la *lentillage gravitationnel*, nous montrons qu'il est possible de construire un estimateur pour mesurer le stress anisotrope qui est exempt de toute hypothèse sur la théorie sous-jacente de la gravité, à part le fait que les photons suivent des géodésiques nulles. Nous appuyons nos résultats avec des prévisions de Fisher à partir desquelles nous déduisons les contraintes sur les estimateurs attendus pour les relevés de Stage IV, tels que la Phase 2 du Square Kilometer Array et le Legacy Survey of Space and Time de l'Observatoire Vera Rubin.

Dans la Partie iii, nous proposons une deuxième application pour la mesure du *redshift gravitationnel*. Dans ce cas, nous démontrons que les effets relativistes sont cruciaux pour contraindre davantage l'espace des paramètres des modèles de gravité modifiée. En particulier, nous adoptons le cadre de la Théorie Effective de l'Énergie Noire, permettant des interactions supplémentaires dans le *secteur sombre*. Nous calculons l'expression explicite du *redshift gravitationnel* en fonction des paramètres de la théorie effective. Nous développons un code capable de calculer les observables du regroupement des galaxies pour toute théorie dans ce cadre, et produisons des analyses Monte Carlo Markov Chain pour évaluer l'impact de l'inclusion des effets relativistes. En résumé, nous démontrons que le *redshift gravitationnel* est crucial pour lever les dégénérescences entre les paramètres.

Enfin, une possible troisième application des effets relativistes dans la structure à grande échelle est présentée dans la Partie iv. En faisant l'hypothèse que la Relativité Générale soit la bonne théorie de la gravité, nous exploitons le fait que, contrairement aux perturbations de densité et aux *distortions dans l'espace des redshifts*, les effets relativistes sont directement sensibles à certains paramètres de relevé et de population nommés les biais de *magnification* et d'*évolution*. Il est intéressant de noter que contraindre ces quantités est crucial pour augmenter la précision dans la mesure des déviations par rapport à la Gaussianité. Par conséquent, nous étudions la possibilité d'inférer des contraintes sur ces effets systématiques importants à partir de l'analyse du regroupement des galaxies seulement. Encore une fois, des prévisions de Fisher sont produites pour évaluer l'impact des multipôles impairs de la fonction de corrélation à deux points sur les connaissances préalables hypothétiques concernant les biais. De plus, nous étudions comment cet impact est affecté par la manière choisie de diviser la population en multiples traceurs.

SUMMARY

The Cosmos, *'the final frontier'*. People often imagine it as a great tapestry woven with the threads stretched by gravitational interactions. We know for certain that the observed *large-scale structure* is not merely a static display but a dynamic portrait shaped by various phenomena. The so-called *redshift-space distortions*, for instance, provide evidence for the peculiar velocities of galaxies, which in turn reveal anisotropic patterns in the clustering of galaxies. This anisotropy is not random; it is a direct consequence of these peculiar velocities, a vast and intricate dance of galaxies moving under the influence of gravity. Equally remarkable is the *gravitational lensing* effect. Massive structures like galaxy clusters can warp the tapestry, acting as a cosmic magnifying glass which bends the paths of light from distant galaxies. This induces distortions in the apparent positions and shapes of these background luminous objects, providing astronomers with a powerful tool to map the distribution of matter and the geometry of the Universe. Evidently, these two phenomena are crucial probes to test the link between matter and geometry, or, as we the scientists like to name it, the theory of General Relativity. In fact, cosmic surveys have already been able to measure these effects and provide high precision constraints on the relevant parameters.

Interestingly enough, additional effects are predicted to contribute. The community refer to them as *relativistic effects*. In this Thesis, we focus on them, with special emphasis on the *gravitational redshift*. It occurs when the photons climb out of gravitational potential wells, loosing energy in the process, which translates into an additional redshift. This phenomenon, which has been measured in astrophysical contexts, is often overlooked in cosmological studies. However, we show that it will definitely be a crucial part of future cosmic surveys analyses. We demonstrate that this effect serves as a direct probe of the geometry of the space time and that it will be decisive in breaking degeneracies among the parameters governing the modeling of the large-scale structure at late times, as measured by the upcoming generation of Stage IV galaxy surveys. All in all, we propose up to three possible applications and implications for measurements of this phenomenon on cosmological scales.

Part i of this Thesis is intended to serve as a gentle introduction to the topic. First, we provide with a non-exhaustive introduction to the modeling of the large-scale structure at late times. In particular, we summarize the computation of the *galaxy number counts* at linear order in perturbation theory, taking into account the systematic effects known as *evolution* and *magnification* biases, which modulate the amplitude of the relativistic effects. We also define the *lensing convergence* to be the relevant weak-lensing observable taken into account in our works. Secondly, we develop the statistical machinery that will be needed in the subsequent studies. For the spectroscopic case, we start by the redshift-space *power spectra* in the Fourier realm. Then, we compute the 2-point galaxy clustering correlation function multipoles for the more general case of two populations of tracers, which turns out to be crucial to measure the gravitational redshift and other relativistic corrections. More precisely, we show that these effects generate *odd multipoles* in the correlation function. Complementary to these results is the computation of the covariance matrix associated to the multipoles, for which we similarly provide

a generalized recipe for the case of multiple populations of tracers. In addition, we summarize the computation of the *harmonic power spectra* which are typically the target of photometric surveys analyses. Finally, we describe the inference techniques that are used in the posterior Parts.

In Part ii, we introduce a new model-independent test of gravity targeting the anisotropic stress, i.e. the ratio between the two metric potentials. We demonstrate that a measurement of the gravitational redshift is a proxy for an independent measurement of the time distortions potential. Thus, we construct the correspondent estimator based on the multipoles of the 2-pt correlation function, which isolates the time distortions contribution. Then, in combination with measurements of the lensing convergence, we show that it is possible to construct an estimator to measure the anisotropic stress which is free of any assumption about the underlying theory of gravity, apart from the fact that photons follow null geodesics. We support our findings with Fisher forecasts from which we infer the constraints on the estimators expected for Stage IV surveys, such as the Phase 2 of the Square Kilometer Array and the Legacy Survey of Space and Time of the Vera Rubin's Observatory.

In Part iii, we propose a second application for the measurement of the gravitational redshift. In this case, we demonstrate that the relativistic effects are crucial to further constrain the parameter space of modified gravity models. In particular, we adopt the Effective Theory of Dark Energy framework, allowing for additional interactions in the *dark sector*. We compute the explicit expression for the gravitational redshift as a function of the effective theory parameters. We develop a code which is able to compute the galaxy clustering observables for any theory within this framework, and produce Monte Carlo Markov Chain analyses to assess the impact of including the relativistic effects into the game. In a nutshell, we demonstrate the gravitational redshift to be crucial in breaking degeneracies between the parameters.

Finally, a possible third application of the relativistic effects in the large-scale structure is presented in Part iv. Assuming General Relativity is the true theory of gravity, we exploit the fact that, in contrast with the density perturbations and the Redshift-space distortions, the relativistic effects are directly sensitive to some survey and population parameters named the *magnification* and *evolution biases*. Interestingly, constraining these quantities is crucial to increase the precision in measuring deviations from Gaussianity. Therefore, we study the possibility to infer constraints on these important systematic effects from galaxy clustering analysis alone. Yet again, Fisher forecasts are produced assessing the impact of the odd multipoles of the 2-pt correlation function on hypothetical prior knowledge about the biases. In addition, we study how this impact is affected by the manner chosen to split the population into multiple tracers.

PUBLICATIONS

The following works have been considered as part of this thesis:

1. **D. Sobral Blanco** and C. Bonvin; *Measuring anisotropic stress with relativistic effects*. In: Phys. Rev. D 104, 063516 – 8 Sept. 2021 or arXiv:2102.05086 [astro-ph.CO].
2. **D. Sobral Blanco** and C. Bonvin; *Measuring the distortion of time with relativistic effects in large-scale structure*. In: M.N.R.A.S. Volume 519, Issue 1, February 2023 or arXiv:2205.02567 [astro-ph.CO].
3. I. Tutusaus, **D. Sobral Blanco**, C. Bonvin; *Combining gravitational lensing and gravitational redshift to measure the anisotropic stress with future galaxy surveys*. In: Phys. Rev. D 107, 083526 – 24 Apr. 2023 or arXiv:2209.08987 [astro-ph.CO].
4. S. Castello, M. Mancarella, N. Grimm, **D. Sobral Blanco**, I. Tutusaus, C. Bonvin; *Gravitational Redshift Constraints on the Effective Theory of Interacting Dark Energy*. In: JCAP, Vol. 2024, 2 May 2024 or arXiv:2311.14425 [astro-ph.CO].
5. **D. Sobral Blanco**, C. Bonvin, C. Clarkson, R Maartens; *Using relativistic effects in large-scale structure to constrain astrophysical properties of galaxy populations*. In: arXiv:2406.19908 [astro-ph.CO].

JURY MEMBERS

- Prof. Camille Bonvin
  Département de Physique Théorique & Center for Astroparticle Physics, Université de Genève, 24 Quai E. Ansermet, CH-1211 Genève 4, Switzerland.
- Prof. Julien Carron
  Département de Physique Théorique & Center for Astroparticle Physics, Université de Genève, 24 Quai E. Ansermet, CH-1211 Genève 4, Switzerland.
- Prof. Isaac Tutusaus Lleixa
  Institut de Recherche en Astrophysique et Planétologie (IRAP), Université de Toulouse, CNRS, UPS, CNES, 14 Av. Edouard Belin, 31400, Toulouse, France.
- Prof. Roy Maartens
  Department of Physics & Astronomy, University of Western Cape, Cape Town 7535, South Africa.

I would like to thank them all for having accepted to be part of the jury for my thesis defense.

CONTENTS

i Introduction

ii Measuring the Anisotropic Stress with Relativistic Effects

III Gravitational Redshift Constraints on the Effective Theory of Interacting Dark Energy

IV Constraints on magnification and evolution biases from the odd multipoles v Summary of Conclusions and Outlook

vi Appendix

LIST OF FIGURES

LIST OF TABLES

NOTATIONS

List of symbols and abbreviations used in the thesis

Symbols	
c	speed of light. We work in units of $c = 1$.
a	scale factor.
H	Hubble parameter (H_0 denotes Hubble parameter today).
$\mathcal{H}$	comoving Hubble parameter $\mathcal{H} = aH$.
h	reduced Hubble parameter $h = H_0/100$ km/s/Mpc.
τ ,τ_0	cosmic time (today).
t, t_0	conformal time (today), $t = \int \frac{d\tau}{a}$.
$\dot{f}$	derivative with respect to t, $\dot{f} = \frac{df}{dt}$.
f'	derivative with respect to $\ln a$, $f' = \frac{df}{d\ln a}$.
z	redshift.
$\mathbf{n}$	line-of-sight direction.
$\mathbf{d}$	relative position of two objects $\mathbf{d} = \mathbf{x}_1 - \mathbf{x}_2$.
d	comoving separation between two objects, $d = \lvert\mathbf{x}_1 - \mathbf{x}_2\rvert$.
$\mathbf{x}$	position in comoving coordinates, $\mathbf{x} = r\,\mathbf{n}$.
r	comoving distance to a given point, $r = t_0 - t$.
$\mathbf{k}$	wave vector of Fourier modes, $\mathbf{k} = k\,\hat{\mathbf{k}}$.
Φ, Ψ	Bardeen potentials: spatial and time distortions.
ρ, n_{g}	comoving galaxy number density.
δ_{g}	galaxy density perturbations.
δ, δ_{m}	density/matter density contrast in comoving gauge.
D_g, D_s	density variable in the constant curvature/Newtonian gauges.
Δ	observable galaxy number counts.
$\mathbf{V}(\mathbf{x})$	Gauge invariant velocity potential.
$\mathbf{v}(\mathbf{x})$	velocity perturbation in longitudinal gauge.
$v(x)$	velocity potential $\mathbf{v} = -\nabla v$.
$V(k)$	defined as $v(k) = k^{-1}V(k)$.
$D_1(z)$	matter growth function.
$f(z)$	velocity growth rate.
$P_{\mathrm{in}}(k)$	power spectrum of primordial fluctuations.
$P_{\delta\delta}(k)$	density perturbations power spectrum.
$P^{lin}_{\delta\delta}(k)$	linear density power spectrum.

$\xi(\theta, z_1, z_2)$	two-point correlation function.
$C_\ell(z_1, z_2)$	unequal-time angular power spectra.
b	galaxy bias.
s	magnification bias.
$f^{\rm evol}$	evolution bias.
κ, $\kappa_{\rm g}$, $\kappa_{\rm v}$	full convergence, lensing convergence, Doppler lensing.
γ_1 and γ_2; γ	shear components; complex shear.
$\mathcal{P}_\ell$(x)	Legendre polynomials.
$Y_{\ell m}(\vartheta, \varphi)$	Spherical harmonics.
$J_n(x)$	Bessel functions.
$j_\ell(x)$	Spherical Bessel functions.
δ_{ij}, δ^D	Kronecker and Dirac delta functions.
Abbreviations	
(Λ)CDM	(Cosmological constant) Cold dark matter.
ADM	Arnowitt-Deser-Misner formalism.
BAO	Baryon Acoustic Oscillations.
CMB	Cosmic Microwave Background.
DE	Dark Energy.
DES	Dark Energy Survey.
DESI	Dark Energy Spectroscopic Instrument.
EFT	Effective Field Theory.
FLRW	Friedmann-Lemaître-Robertson-Walker.
GR	General relativit.
IA	Intrinsic Alignments.
IDE	Interacting Dark Energy.
LSS	Large-scale structure.
PNG	Primordial Non-Gaussianities.
RSD	redshift-space distortions.
SKA	Square Kilometer Array.
SSDS	Sloan Digital Sky Survey.

Part I

INTRODUCTION

1

THE LATE-TIMES LARGE-SCALE STRUCTURE

‘And God said, Let there be light: and there was light’ (*Genesis, 1:3*). This is the common starting point of the Myth of Creation for the Abrahamic religions. According to this Tradition, the history of the Universe, Earth and mankind began with the propagation of light and, in a certain sense it also does for science. The *study of the Heavens* is as old as Civilization itself, and seeks to answer one of the deepest questions for human beings: Why are we here? However, the assumptions and techniques applied in the seek of answers have significantly varied throughout History. Until very recently with the discovery of the existence of the gravitational waves, the only source of information about the Heavens was the light emitted by distant objects. Therefore, this endeavor is mostly an attempt to understand the Universe through the study of light propagation and the physical effects affecting it.

Our current understanding of Cosmology, which is the branch of modern science devoted to the study of the Heavens, i.e. the origin, evolution of structures and the ultimate fate of the Universe, relies on the *cosmological principle*: our location in the Universe should not be statistically distinguishable from the position of any other observer. No particular directions should be preferred either. These two hypotheses, together with the observational evidence indicating *isotropy* on large scales, lead to the conclusion that the Universe should be *homogeneous*. However, this assumption falters as soon as we take a look at our cosmic neighbourhood. We see an intricate structure in which planets and stars join together to form galaxies, the galaxies evolve into groups forming clusters, which are distributed along filaments and clumps in between which there exist large void regions (see fig. 1.1), in a manner that is very unlikely to have arisen from randomness. We call this large-scale structure (LSS) as the *Cosmic Web*. However, we still believe in isotropy and homogeneity at sufficiently large scales. This leads to the Big Bang paradigm in which we attempt to explain the Universe using the Einstein’s theory of General Relativity (GR), whose equations can be solved exactly for an expanding, homogeneous and isotropic background. [1] This geometry was first investigated by Friedmann in the early 1920s, and later applied to describe the universe by Lemaître (1927), Robertson and Walker (1936). This solution to the Einstein’s equation receives the name of the Friedmann-Lemaître-Robertson-Walker (FLRW) model, and is the foundation of the *Concordance Model* of Cosmology. Other common name within the community, possibly more descriptive, is that of ΛCDM model. We say that the Universe where (and when) we live is undergoing an accelerating expansion thanks to a mysterious force called *Dark Energy* (DE), described by a Cosmological Constant Λ, and

---

[1] We preferred to avoid including here all the details about the basic equations of Cosmology. As of today, we are fortunate to have at our disposal an extensive literature on the subject written by much more experienced scientists. In fact, the author himself has learned from e.g. [1, 2].

is full of *Cold Dark Matter* (CDM). The only way to shed light over so much darkness is to develop techniques that allow us to confront the model against observations, in a hope to unveil the latent mysteries. A crucial mystery that seems to be solvable only through cosmic observations is e.g. how to describe the dark energy component, which represents $\sim 70\%$ of the present day's Universe energy budget. Is it that it actually exists and has a constant, ever present energy density or are we missing something? Does it come from a departure from General Relativity at large scales instead, better described by an alternative theory?

Interestingly, the Big Bang paradigm is reinforced by the landmark evidence for the existence of an ubiquitous microwave radiation originated when the Universe became transparent and photons started to travel free throughout the spacetime. This relic from the Early Universe is known as the *Cosmic Microwave Background* (CMB) and was accidentally discovered in 1965 by A. Penzias & R. Wilson, who measured a homogeneous black-body spectrum at a temperature of $\sim 3\,\mathrm{K}$, implying the definitive success of the Big Bang paradigm. However, later on, in 1992 the COBE satellite mission discovered anisotropies in the CMB meaning that the early Universe was not completely homogeneous, but that small perturbations were present in the cosmic plasma. These fluctuations are quantified by deviations from the background temperature of order 10^{-5}.

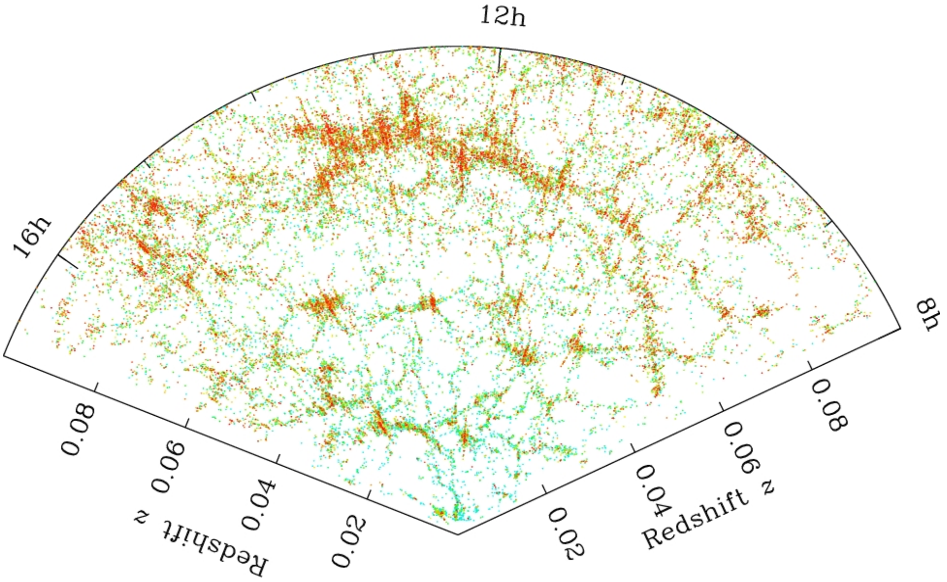

Figure 1.1: A map of the Cosmic Web in a thin sector of the sky, from the Sloan Digital Sky Survey (SDSS-II). Our planet is at the vertex of the wedge, and it spans about 1.3 billion light years to the past. The dots are galaxies arrayed in clumps, filaments and sheets. Blank spaces are the *cosmic voids*. The color of the points is related to the age of the main stars at each galaxy: red points have mostly old stars, while blue dots show galaxies with younger populations. Interestingly, the number and size of voids agree with theoretical models in which they evolve under gravitational collapse starting from a nearly-smooth distribution of dark matter. Borrowed from M. Blanton and the SDSS SDSS Press Release Images.

The fact that the deviations from homogeneity and isotropy in the CMB are small is of the highest relevance. They do not imply the need to go beyond the Big Bang paradigm, but rather can be accommodated through a natural extension, by assuming the early Universe fluctuations to be the seeds that became into the current large-scale structures (LSS) via gravitational instability. More precisely, we assume that the initial fluctuations required to trigger the process of gravitational instability arise from tiny quantum fluctuations that have been enhanced during an inflationary period before the photons decoupled from the early plasma. In other words, the modern paradigm of Cosmology is that the Cosmic Web emerged from gravitational collapse of small perturbations generated in the early Universe and can be consistently described by perturbations around the smooth, homogeneous and isotropic background, as long as we avoid regimes that cannot be described by small perturbations. Starting from this hypothesis, we can think of Cosmology as the branch of science attempting to describe the large-scale physics of the Universe through General Relativity and statistics. Importantly, a careful definition of the physical quantities is of utmost importance to develop consistent tests of gravity that can be used to confront the theory with the observations of the Cosmic Web.

In this Chapter we provide the theoretical ingredients for the study of the late-times LSS in the linear regime. For that purpose, we will adopt the modern approach of the gauge invariant perturbation theory. We first summarize the basic elements for studies in a perturbed Friedmann Universe in sec. 1.1. Consecutively, we introduce the fully relativistic and gauge-invariant expressions for the *galaxy number counts fluctuations* in sec. 1.2 and the *lensing convergence* in sec. 1.3. Finally, in sec. 1.4 we discuss the inclusion of important tracer-dependent effects such as the *magnification* and *evolution* bias and provide the final expression for the galaxy number counts, useful for spectroscopic galaxy surveys.

1.1 THE PERTURBED FRIEDMANN UNIVERSE

The small deviations from the homogeneous and isotropic background are the seeds of fluctuations in the geometry and in the matter distribution. At late times, this scenario is that of a perturbed Friedmann Universe endowed with the metric [2, 3]

$$ds^2 = a^2(t)\left[-(1+2A)\,dt^2 - 2\,B_i\,dtdx^i + \left[(1+2H_L)\,\delta_{ij} + 2H_{Tij}\right]\,dx^i dx^j\right], \tag{1.1}$$

expressed in conformal time t. The prefactor $a(t)$ is the *scale factor* associated to the expansion. A more convenient time variable is the redshift defined via $a = 1/(1+z)$. For simplicity, we neglect the vector and tensor modes that arise from the harmonic analysis and the Scalar-Vector-Tensor (SVT) decomposition of perturbations. Any vector field B_i can be decomposed in the combination of a (gradient of) scalar mode with a vector mode. In Fourier space, we can write $B_i = -\hat{k}_i\,B + \hat{B}_i$. The tensor modes are encoded in the tensor H_{ij}, whose decomposition yields two scalars, a vector mode and a purely tensorial mode. These tensor modes are generated from gravitational waves. The advantage of the SVT technique is that the scalar, vector and tensor modes decouple and evolve independently. In this Thesis, we focus on the scalar perturbations sector, parametrized by the scalar degrees of freedom denoted by A, B, H_L and H_{Tij}, where H_L is the scalar longitudinal mode of tensor perturbations and H_{Tij} is the scalar contribution to the trace of H_{ij}, defined as $H_{Tij} = (\hat{k}_i\hat{k}_i - \delta_{ij}/3)\,H_T$ in Fourier space. Hence, scalar fluctuations of the spacetime are completely determined by a set of four scalar modes, A, B, H_L and H_T, which are general functions of time and scale. Gauge invariance permits removing two of them allowing for a further simplification. With full generality, we can define two gauge-independent variables called the *Bardeen potentials* [4]

$$\Psi \equiv A + \frac{\mathcal{H}}{k} B + \frac{1}{k}\dot{B} - \frac{\mathcal{H}}{k^2}\dot{H}_T - \frac{1}{k^2}\ddot{H}_T, \tag{1.2}$$

$$\Phi \equiv -H_L - \frac{1}{3} H_L + \frac{\mathcal{H}}{k^2}\dot{H}_T - \frac{\mathcal{H}}{k} B, \tag{1.3}$$

where $\mathcal{H}(z) = (1+z)^{-1}H(z)$ is the conformal Hubble factor and k is the wave number of the Fourier mode. The dots denote a derivative with respect to conformal time, t. Choosing a gauge means to use specific functions for the scalar modes which determine the role of Ψ and Φ. The Bardeen potentials crucially depend on the theory of gravity. In General Relativity temporal and spatial perturbations are indistinguishable in any gauge, and hence we have $\Phi = \Psi$. However, this is not generally true for any theory of gravity. It is common to define the *anisotropic stress* or *gravitational slip* as the ratio between the Bardeen potentials. We adopt the convention

$$\eta = \frac{\Psi}{\Phi}. \tag{1.4}$$

In addition to the scalar modes of the metric, we will need two additional gauge independent variables for describing the density and velocity perturbations associated to the dark matter. As the Bardeen potentials, they can be defined in terms of the scalar modes by imposing gauge invariance and their precise physical meaning depends on the gauge choice. The simplest possibility is to work in the matter rest frame, i.e. the *comoving gauge*. Let us denote the matter density perturbations in this gauge by δ. Alternatively, we can work on the uniform curvature hypersurfaces frame. In a Friedman Universe, the constant curvature hypersurfaces are flat and density fluctuations in this frame are denoted by D_g. Let us note that different gauge choices lead to differences in the predicted power spectrum for the density fluctuations at scales near the horizon, $k \sim \mathcal{H}$ [5]. However, for measurements of matter and velocity perturbations taking place well inside the horizon, i.e. at scales $k \gg \mathcal{H}$, the differences between δ, D_g and any other density fluctuations variable are negligible. In any case, we formally change from one gauge to another by means of the linear relations between the gauge variables. The variable D_g is defined as

$$D_g = \delta - 3\Phi - 3\frac{\mathcal{H}}{k} V, \tag{1.5}$$

where V denotes the gauge-invariant variable encoding the peculiar velocity potential $\mathbf{V} = -\nabla V$, defined by

$$V = v - \frac{1}{k}\dot{H}_T. \tag{1.6}$$

Here v is the physical peculiar velocity. A very common choice in Cosmology studies, and the one we will adopt throughout this Thesis, is the so-called *longitudinal* or *Newtonian* gauge, defined by setting $B = H_T = 0$. In this gauge, the matter density fluctuations variable are denoted by D_s, defined as

$$D_s = D_g + 3\Phi, \tag{1.7}$$

$$D_s = \delta - 3\frac{\mathcal{H}}{k} V. \tag{1.8}$$

Note also that with $B = H_T = 0$, the Bardeen potentials thus reduce to be $\Psi = A$ and $\Phi = -H_L$ and the metric becomes

$$ds^2 = a^2(t)\left[-(1+2\Psi)\,dt^2 + (1-2\Phi)\,\delta_{ij}\,dx^i dx^j\right]. \tag{1.9}$$

Therefore, it is this gauge choice the one that endows the Bardeen potentials with a clear physical meaning: the potential Ψ encodes all the scalar perturbations to the time component of the metric, while the potential Φ represents the spatial fluctuations. In the non-relativistic limit of the theory, the latter is identified with the Newtonian potential, and hence the name given to this particular gauge choice. Let us also notice that eq.(1.6) implies that in the Newtonian gauge V directly identifies with the physical peculiar velocity of the galaxies, v. The Newtonian gauge offers a very natural interpretation and link between the gauge and physical variables. However, observables in physics must be gauge-independent, meaning it does not matter which particular gauge you choose to write down the expressions.

The perturbed Friedmann Universe is however not fully characterized without solving Einstein's equations. Separating the dynamical variables into a background contribution plus small perturbations allow for solving the corresponding evolution equations independently. The background contributions will obey the standard Friedmann equations (see refs. [1, 2]). The next-to-leading order perturbations of Einstein's equations are obtained similarly by determining the perturbed Einstein tensor $\delta G_{\mu\nu} = 8\pi G \delta T_{\mu\nu}$. They can be derived analytically by applying the well-known $3+1$ formalism of General Relativity and using the Cartan's formalism for the Riemann curvature [3].

At late-times, the Universe is filled with *dust* that evolves due to the struggle between gravitational interactions, which favours the clustering of matter, in an acceleratingly expanding flat background, which prevents clustering. Dust is a short-name for pressureless matter, with equation of state $\omega = 0$, and sound speed $c_s^2 = 0$. We initially consider the $\Lambda = 0$ case. Firstly, we find from the covariant derivative $T^{\mu\nu}_{\ ;\nu} = 0$ two constraint equations

$$\dot{D}_g + k\,V = 0, \tag{1.10}$$

$$\dot{V} + \mathcal{H}V - k\Psi = 0. \tag{1.11}$$

The first encodes energy conservation and receives the name of the *continuity equation*. The second one describes the gravitational acceleration. This is known as the *Euler equation*. Note that we wrote the former in terms of D_g for formal consistency with ref. [2]. However, as already discussed for measurements in sub-horizon scales we are safe to use $D_g \sim D_s \sim \delta$. In addition, from Einstein's equations spatial components $G_{ij} = 8\pi G T_{ij}$ we obtain a scalar equation

$$k^2(\Phi - \Psi) = 8\pi G a^2 \bar{P}\,\Pi. \qquad (i \neq j) \tag{1.12}$$

Here $\bar{P}$ is the pressure of the fluid and Π is the *scalar* mode of the anisotropic stress tensor. This one is defined as the traceless part of the stress-energy tensor perturbations. Formally, it also contains vector and tensor modes, which we neglect for simplicity. For a pressureless fluid we have $\Pi = 0$. Hence, for dust we indeed have $\Phi = \Psi$, i.e. there is no *anisotropic stress*. In addition, the components $G_{0\mu} = 8\pi G T_{0\nu}$ yield the *Poisson equation*, which in gauge-invariant form is written as

$$-k^2\Phi = 4\pi G a^2 \bar{\rho}_{\mathrm{m}}\left[D_g + 3\left(\Psi + \frac{\mathcal{H}}{k}V\right)\right] = 4\pi G a^2 \bar{\rho}_{\mathrm{m}}\,\delta, \tag{1.13}$$

where $\bar{\rho}_{\mathrm{m}}$ is the background matter density and in the second equality we have used eq. (1.5) together with the constraint eq.(1.12). Hence, the Poisson equation defines how the gravitational force affects the matter density perturbations. It is often convenient to rewrite the above in terms of the background matter density parameter $\Omega_{\mathrm{m}} = \bar{\rho}_{\mathrm{m}}/\rho_{\mathrm{c}}$ where

$$\rho_{\mathrm{c}}(t) = \frac{3\mathcal{H}^2}{8\pi G a^2}, \tag{1.14}$$

is the critical energy density in conformal time. We can thus recast eq.(1.13) into the form

$$k^2\Phi = -\frac{3}{2}\mathcal{H}^2(z)\Omega_{\mathrm{m}}(z)\,\delta. \tag{1.15}$$

These equations relate density, velocity and metric perturbations and define the hierarchy between the gauge invariant variables. In this Thesis, we will study the large-scale structure in the linear regime, where $\delta \ll 1$. Additionally, the measurements will be performed in sub-horizon scales, $k \gg \mathcal{H}$. Continuity equation (1.10) implies that the velocity perturbations are suppressed with respect to the density perturbations by a factor $V \sim (\mathcal{H}/k)\,\delta$. Similarly, Euler equation (1.11) mean that the temporal metric perturbations are suppressed with respect to the velocities by the same factor, $\Psi \sim (\mathcal{H}/k)\,V$. Finally, Poisson equation (1.13) states the hierarchy between metric and density perturbations as $\Psi \sim (\mathcal{H}/k)^2\,\delta$. These considerations will be relevant later in the following Section when computing the observables at linear order.

However, the previous are just a sub-set of equations solving the system given by $\delta G_{\mu\nu} = 8\pi G \delta T_{\mu\nu}$. Using the complete set of Einstein's and conservation equations, we can obtain an additional useful formula for the evolution of density perturbations. It turns out that for the dust case the same equation remains valid for the $\Lambda \neq 0$ case. It is therefore a crucial equation for describing the late-times Universe. Observations suggest that the present day Universe is dominated by a cosmological constant. Hence, the dynamics of dust perturbations in a ΛCDM universe is described by the equation

$$\ddot{\delta} + \mathcal{H}\,\dot{\delta} - \frac{3}{2}\mathcal{H}^2\Omega_{\mathrm{m}}(a)\,\delta = 0. \tag{1.16}$$

Note that the wave number k does not enter here. However, this equation is only valid in sub-horizon scales and hence it can only be used at late-times when all the observed perturbation modes are already inside the horizon. It is a second order differential equation in conformal time t. It shall be convenient to write it down as an equation in the variable $y = \ln a$

$$\delta'' + \left(1 - \frac{1}{2}\,\Omega_{\mathrm{m}}(a)\right)\,\delta' - \frac{3}{2}\Omega_{\mathrm{m}}(a)\,\delta = 0, \tag{1.17}$$

where $' = d/d\ln a$. In this form it is simpler to see that in matter domination $\Omega_{\mathrm{m}}(a) \approx 1$ we find a growing mode $D \propto a$, while for $\Omega_{\mathrm{m}} = 0$ we have a constant mode D. In a ΛCDM Universe, the amplitude of matter fluctuations undergoing pressureless growth is analytically given by

$$D_1(z) = \frac{5}{2}\frac{H_0\,\Omega_{\mathrm{m},0}}{H(z)}\int_0^{\frac{1}{1+z}} \frac{dx}{\left(\Omega_{\mathrm{m},0}/x + (1-\Omega_{\mathrm{m},0})x^2\right)^{3/2}}, \tag{1.18}$$

where $\Omega_{\mathrm{m},0}$, H_0 are the values of the matter density and Hubble parameters today, as measured e.g. by Planck [6]. The D_1 is known as the *growth function* of matter perturbations. During matter domination, these results that the linear growth of density perturbations can be described via the relation

$$\delta(k,z) = \frac{D_1(z)}{D_1(z_*)}\,\delta(k,z_*)\,, \tag{1.19}$$

mapping an initial time z_* to any posterior time z. Note that while density perturbations can be scale dependent, the D_1 is not for pure matter perturbations. Additionally, for measurements of the galaxy distribution it is often convenient to introduce the logarithmic growth rate, named the *growth rate*

$$f(z) \equiv \frac{\dot{D}_1}{\mathcal{H}\,D_1} = \frac{d\ln D_1}{d\ln a}\,. \tag{1.20}$$

Using the analytical expression for $D_1(z)$ in eq. (1.18), we can find the growth function in a ΛCDM Universe to be

$$f(z) = \frac{H_0^2}{\mathcal{H}^2(z)}\left[-\frac{3}{2}\Omega_{\mathrm{m},0}(1+z) + \frac{5}{2}\frac{\Omega_{\mathrm{m},0}}{D_1(z)}\right]\,. \tag{1.21}$$

Alternatively, people often introduce the matter density redshift evolution

$$\Omega_{\mathrm{m}}(z) = \frac{H_0^2\,\Omega_{\mathrm{m},0}\,(1+z)}{\mathcal{H}^2(z)}\,, \tag{1.22}$$

for which an approximate numerical solution of the growth rate is usually parametrized as

$$f(z) \simeq \Omega_{\mathrm{m}}^{\gamma}(z)\,, \tag{1.23}$$

where $\gamma = 0.55$ is the *growth index*. Interestingly, the continuity equation (1.10) can be recast into the form

$$V(k,z) = -\frac{\mathcal{H}}{k}f(z)\,\delta(k,z), \tag{1.24}$$

which reveals a link between density and velocity perturbations through $f(z)$, which is highly dependent on the theory of gravity. Measuring the growth rate of perturbations is actually the ingredient target GR tests based on observations of the LSS at late-times.

1.2 GALAXY NUMBER COUNTS: RELATIVISTIC EFFECTS

An observer who aspires to understand the distribution of galaxies on large scales needs to measure the number of galaxies in a pixel centered at the direction $\mathbf{n}$ at redshift z. Let us denote this quantity with $N(\mathbf{n},z)\,d\Omega_{\mathbf{n}}\,dz$, where $d\Omega_{\mathbf{n}}$ is the infinitesimal solid angle. Then, taking the average over angular coordinates provides the mean redshift distribution of galaxies, $\bar{N}(z)\,dz$. Let us now define the fractional fluctuation in the number of galaxies, also called *galaxy number counts*, as [5, 7]

$$\Delta(\mathbf{n},z) = \frac{N(\mathbf{n},z) - \bar{N}(z)}{\bar{N}(z)}. \tag{1.25}$$

The first instinct of any observer would be now to relate $\Delta(\mathbf{n}, z)$ to the dark matter density fluctuations. Using the galaxies as biased tracers of the underlying dark matter distribution, the number of galaxies is also $N(\mathbf{n}, z) = \rho(\mathbf{n}, z)\, V(\mathbf{n}, z)$, where ρ and V are the galaxy number density and the physical volume of the pixel, respectively. In a perturbed Friedman Universe, both the solid angle and the redshift are distorted inducing a perturbation in the volume. Moreover, the galaxy density local values generally depart from the average distribution. Let us see this explicitly by writing down the galaxy number counts fluctuations in terms of these two perturbed quantities

$$\Delta(\mathbf{n}, z) = \frac{\rho(\mathbf{n}, z) - \bar{\rho}(z)}{\bar{\rho}(z)} + \frac{\delta V(\mathbf{n}, z)}{\bar{V}(z)}. \tag{1.26}$$

The first term is directly the galaxy density fluctuations at fixed z, which we shall denote by $\delta_z(\mathbf{n}, z)$ (See refs. [5, 7]). Additionally, a Taylor expansion of $\bar{\rho}$ around the background redshift $z = \bar{z} + \delta z$ gives $\bar{\rho}(z) = \bar{\rho}(\bar{z}) + \partial_z \bar{\rho} \cdot \delta z$. Using this in eq. (1.26) we find

$$\Delta(\mathbf{n}, z) = \delta_{\mathrm{g}}(\mathbf{n}, z) - 3\,\frac{\delta z}{1+\bar{z}} + \frac{\delta V(\mathbf{n}, z)}{\bar{V}} = \delta_z(\mathbf{n}, z) + \frac{\delta V(\mathbf{n}, z)}{\bar{V}(z)}. \tag{1.27}$$

This equation explicitly shows that the observed galaxy number counts fluctuations are affected by a combination of the fluctuations in the galaxy density distribution, δ_{g}, fluctuations in the observed redshift and perturbations in the observed volume of each pixel.

Any observable in physics must satisfy the necessary condition of being *gauge independent* and our number counts fluctuations $\Delta(\mathbf{n}, z)$ cannot be an exception. The background density $\bar{\rho}$ is computed in a given Friedmann background so the comparison with the observed $\rho(\mathbf{n}, z)$ is thus gauge-dependent. The redshift fluctuations δz are also dependent on the chosen background and hence are gauge-dependent. However, it turns out that the combination $\delta_z(\mathbf{n}, z)$ is a gauge-independent quantity, and therefore a true observable. Moreover, the volume perturbations (last term in eq. (1.27)) turn out to be gauge invariant as well. This is naturally expected, as one can measure the volume perturbations with any other tracer different from galaxies.

Let us compute the explicit form of all the physical distortions contributing to $\Delta(\mathbf{n}, z)$, accounting for the gauge issue. For this task, we require of the fully relativistic calculation of the volume and redshift fluctuations. This program has been extensively studied in the literature and here we reproduce a summary of the steps (see refs. [5, 7–13]). The goal is to write down $\Delta(\mathbf{n}, z)$ only in terms of gauge invariant variables described in sec.1.1: the two *Bardeen potentials*, Φ and Ψ, the gauge invariant density fluctuations $D_g(\mathbf{n}, z)$ and the gauge invariant peculiar velocity $\mathbf{V}(\mathbf{n}, z)$.

1.2.1 *Redshift fluctuations*

The redshift fluctuations are derived by finding the solution to the null geodesic equation in a perturbed Friedmann Universe given by (1.1) and computing the change in energy of an incoming photon between emission and observation. Let us consider a photon emitted from a source S which is moving in direction $\mathbf{n}$. From the observer's O point of view, it is seen under the direction $-\mathbf{n}$. The redshift of the incoming photon is defined as the ratio

$$1 + z = \frac{(n \cdot u)_S}{(n \cdot u)_O}. \tag{1.28}$$

We need to solve the photon geodesic equation for $n = a^{-2}(1 + \delta n_0,\, \mathbf{n} + \delta \mathbf{n})$, where n is the lowest-order photon direction and δn terms are the perturbations to this direction. The four velocity is $u = a^{-1}(1 - A,\, \mathbf{v})$, where A is the temporal scalar perturbation and $\mathbf{v}$ is the peculiar velocity. We can now compute the redshift and write down the expression in terms of gauge invariant quantities

$$1 + z = \frac{a_0}{a_S}\left[1 + \left[H_L + \frac{1}{3}H_T + \mathbf{n}\cdot\mathbf{V} + \Phi + \Psi\right]_{t_S}^{t_0} - \int_{r_S}^{0} (\dot{\Psi} + \dot{\Phi})\, d\lambda\right], \tag{1.29}$$

where $a_0 = a(t_0)$ and $a_S = (t_S)$ are the scale factor at emission and arrival times and the overdots denote derivatives with respect to t. This simply gives $1 + \bar{z}$. Here Φ and Ψ are the Bardeen potentials, and $\mathbf{V}$ is the gauge-invariant velocity perturbation. Their precise physical meaning depends on the gauge choice, to which we will turn back later. Note that the second term has to be evaluated at observer's t_0 and emission t_S times. The terms evaluated at t_S are all dependent on $\mathbf{n}$ through the emission point which, to the lowest order, has coordinates $\mathbf{x}_s = \mathbf{x}_0 - \mathbf{n}(t_0 - t(\bar{z}_s))$. The dipolar term $\mathbf{n}\cdot\mathbf{V}(\mathbf{x}_0, t_0)$ is thus the only one dependent on the directions when evaluated at $\mathbf{x}_0$. The integral of the last term extends along the unperturbed photon trajectory with affine parameter λ. At emission point we set $\lambda = 0$, while at the observer's position $\lambda = t_0 - t_S = r_S$, r_S denoting the comoving distance between emitter and observer. The redshift perturbations $\delta z = z - \bar{z}$ take the form

$$\delta z = -(1+z)\left[\left(H_L + \frac{H_T}{3} + \mathbf{n}\cdot\mathbf{V} + \Phi + \Psi\right)(\mathbf{n}, z) + \int_{0}^{r_S} (\dot{\Psi} + \dot{\Phi})\, d\lambda\right]. \tag{1.30}$$

The terms related to the observer's position are missing on purpose in this last expression. They correspond to an unmeasurable monopole term and a dipole term which appears due to the fact that the observer's pick a particular observation direction [5]. Using this last result in eq. (1.27) and choosing an appropriate gauge-invariant definition for the density fluctuations we can write

$$\delta_z(\mathbf{n}, z) = D_g(\mathbf{n}, z) + 3(\mathbf{n}\cdot\mathbf{V})(\mathbf{n}, z) + 3(\Psi + \Phi)(\mathbf{n}, z) + 3\int_{t_S}^{t_0} (\dot{\Psi} + \dot{\Phi})(\mathbf{n}, z(t))\, dt. \tag{1.31}$$

Here we express the perturbation variables in direction $\mathbf{n}$ and redshift z in terms of its unperturbed positions and time, $f(\mathbf{n}, z) = f(\mathbf{x}(\mathbf{n}, z), t(z))$. Note that we have used the variable $D_g(\mathbf{n}, z)$ encoding the density fluctuations on the uniform curvature hypersurfaces. The expressions in other gauges can simply be found by using the linear relation between the gauge variables. To transform the expression to the Newtonian gauge, we shall use eqs. (1.7) and (1.8).

1.2.2 *Volume perturbations*

We now fix our gaze at the contributions from volume perturbations $\delta V/V$. As discussed, they can be measured with any tracer different to galaxies, and hence are gauge-invariant quantities on their own. Let us find the specific contributions in terms of the gauge-invariant variables. A source with four-velocity u^μ will see a volume element given by

$$dV = \sqrt{-g}\, \epsilon_{\mu\nu\alpha\beta}\, u^\mu\, dx^\nu dx^\alpha dx^\beta. \tag{1.32}$$

However, the observer will prefer to express the volume elements in its own language, parametrized in terms of the polar angles, θ_0 and ϕ_0, and the observed redshift z, so that $dV = \nu(z, \theta_0, \phi_0)\, dz d\theta_0 d\phi_0$, where

$$\nu(z, \theta_0, \phi_0) = \sqrt{-g}\, \epsilon_{\mu\nu\alpha\beta}\, u^\mu \frac{\partial x^\nu}{\partial z} \frac{\partial x^\alpha}{\partial \theta_S} \frac{\partial x^\beta}{\partial \phi_S} \left| \frac{\partial(\theta_S, \phi_S)}{\partial(\theta_0, \phi_0)} \right|, \tag{1.33}$$

is a differential density which determines the volume element perturbations

$$\frac{\delta V}{V} = \frac{\delta \nu}{\bar{\nu}} = \frac{\nu - \bar{\nu}}{\bar{\nu}}. \tag{1.34}$$

The term in between straight brackets is the determinant of the Jacobian of the transformation from angles seen by the source to the angles measured by the observer. Let us denote the angular components as $\boldsymbol{\theta}_i = (\theta_i, \phi_i)$ with $i = S, O$. In a perturbed Universe, the angles at the source are distorted with respect to the angles at the observer and can be written in a perturbative manner as $\theta_S = \theta_O + \delta\theta$ and $\phi_S = \phi_O + \delta\phi$. To first order, the Jacobian becomes

$$\left| \frac{\partial(\theta_S, \phi_S)}{(\theta_0, \phi_0)} \right| = 1 + \frac{\partial \delta\theta}{\partial \theta} + \frac{\partial \delta\phi}{\partial \phi}. \tag{1.35}$$

The length of the geodesics is also perturbed, which induces perturbations in the measured comoving distance $r = \bar{r} + \delta r$. Additional ingredients are the perturbed metric determinant $\sqrt{-g} = a^4(1 + A + 3H_L)$ and the four-velocity of the source. The volume element perturbation is then a combination of the scalar modes and coordinates fluctuations. In addition, we have to subtract the unperturbed differential density $\bar{\nu}$. To first order in perturbations, we find the volume perturbations to take the form

$$\begin{aligned} \frac{\delta\nu(\mathbf{n}, z)}{\bar{\nu}} = 3H_L &+ \left(\cot\theta_0 + \frac{\partial}{\partial\theta}\delta\theta \right) + \frac{\partial\delta\phi}{\partial\phi} - \mathbf{n}\cdot\mathbf{V} + \frac{1}{k^2} n^i \partial_i \dot{H}_T \\ &+ \frac{2\delta r}{r} - \frac{d\delta r}{d\lambda} + \frac{1}{\mathcal{H}(1+\bar{z})} \frac{d\delta z}{d\lambda} - \left(-4 + \frac{2}{\bar{r}\mathcal{H}} + \frac{\dot{\mathcal{H}}}{\mathcal{H}^2} \right) \frac{\delta z}{1+\bar{z}}, \end{aligned} \tag{1.36}$$

where λ is the affine parameter along the photon geodesic. In order to write the expression in terms of the gauge invariant variables we need to solve the null geodesic equation for the fluctuations δr, $\delta\theta$ and $\delta\phi$. This means to compute the deviation vector between the perturbed photon trajectory with the unperturbed one, $\delta x^\mu(\lambda) = x^\mu(\lambda) - \bar{x}^\mu(\lambda)$. We refer the reader to the foundational references of this chapter for the full derivation of these quantities [5, 7–12]. Let us just stress that the above expression also depends on δz (see eq. (1.30)) and its derivative with respect to the geodesic affine parameter, which gives

$$\begin{aligned} \frac{1}{\mathcal{H}(1+\bar{z})} \frac{d\delta z}{d\lambda} = \Phi + \Psi + H_L + \frac{H_T}{3} + \mathbf{n}\cdot\mathbf{V} + \int_0^{r_S} d\lambda (\dot{\Phi} + \dot{\Psi})\, d\lambda \\ - \frac{1}{\mathcal{H}} \left(\bar{n}^i\, \partial_i(\Phi + \Psi) + \frac{dH_L}{d\lambda} + \frac{1}{3}\frac{dH_T}{d\lambda} + \frac{d(\mathbf{n}\cdot\mathbf{V})}{d\lambda} \right). \end{aligned} \tag{1.37}$$

We can now add together eqs. (1.30), (1.36) and (1.37). We also have to perform several integrations by parts to arrive at the final form of the volume density fluctuations [5]. To first order in perturbations, we find

$$\begin{align}
\frac{\delta\nu(\mathbf{n},z)}{\bar{\nu}} = {}& -2(\Phi+\Psi) - 4\,\mathbf{n}\cdot\mathbf{V} + \frac{1}{\mathcal{H}}\left(\dot{\Phi} + \partial_r\Psi - \frac{d(\mathbf{n}\cdot\mathbf{V})}{dr}\right) \tag{1.38}\\
& + \left(\frac{\dot{\mathcal{H}}}{\mathcal{H}^2} + \frac{2}{r_S\,\mathcal{H}}\right)\left(\mathbf{n}\cdot\mathbf{V} + \Psi + \int_0^{r_S} dr'(\dot{\Phi}+\dot{\Psi})\right) \notag\\
& - 3\int_0^{r_S} dr'(\dot{\Phi}+\dot{\Psi}) + \frac{2}{r_S}\int_0^{r_S} dr'(\Phi+\Psi) \notag\\
& - \frac{1}{r_S}\int_0^{r_S} dr'\frac{r_S-r'}{r'}\Delta_\Omega(\Phi+\Psi). \tag{1.39}
\end{align}$$

Here we used that $d\lambda = dt = -dr$ in comoving coordinates and Δ_Ω denotes the Laplacian over the transverse directions (θ,ϕ), or the *angular* Laplacian. The functions are all to be evaluated at the source positions and time, and hence we will omit the subscript S in the following, $r_S \equiv r$, for simplicity.

We can now combine eqs. (1.31) and (1.38) to find the fully relativistic expression for the galaxy number counts fluctuations. Let us reorder the contributions according to their relevance for our purposes. At linear order in perturbation theory we find

$$\begin{align}
\Delta(\mathbf{n},z) = {}& D_s - \frac{1}{\mathcal{H}}\partial_r(\mathbf{n}\cdot\mathbf{V}) \tag{1.40}\\
& + \left(1 - \frac{\dot{\mathcal{H}}}{\mathcal{H}^2} - \frac{2}{r\mathcal{H}}\right)\mathbf{n}\cdot\mathbf{V} + \frac{1}{\mathcal{H}}\mathbf{n}\cdot\dot{\mathbf{V}} + \frac{1}{\mathcal{H}}\partial_r\Psi \notag\\
& - \frac{1}{r}\int_0^r dr'\frac{r-r'}{r'}\Delta_\Omega(\Phi+\Psi) + \frac{2}{r}\int_0^r dr'(\Phi+\Psi) \notag\\
& + \left(\frac{\dot{\mathcal{H}}}{\mathcal{H}^2} + \frac{2}{r\mathcal{H}}\right)\left(\Psi + \int_0^r dr'(\dot{\Phi}+\dot{\Psi})\right) + \Psi - 2\Phi + \frac{1}{\mathcal{H}}\dot{\Phi}. \notag
\end{align}$$

As discussed above, D_s are the density fluctuations in the Newtonian gauge describing the true galaxy density contrast linked to the fact that the matter distribution is not homogeneous. It is important to emphasize that the computation here is performed for the galaxy density perturbations. The reason is that, in practice, what we observe is not the dark matter but the galaxies. We regard galaxies as *biased tracers* of the underlying dark matter distribution, in the sense that they are subject to the same velocity field. As discussed in sec. 1.1, the link of the two is well-defined in the comoving gauge, where we can naturally introduce a *bias* model. For our purposes, it is sufficient to adopt a linear bias model, so that we can write $\delta_g = b\,\delta$. Here the bias factor b is generally a function of redshift $b(z)$. In particular, from eq. (1.8), we obtain the comoving gauge expression in real space by replacing above

$$D_s(\mathbf{n},z) = b\,\delta(\mathbf{n},z) + 3\mathcal{H}\nabla^{-2}\left(\nabla\mathbf{V}\right), \tag{1.41}$$

which we wrote in terms of the dark matter perturbations δ and the linear *galaxy bias* b. All the remaining terms arise from perturbations of the coordinate system used by the observer, $(\mathbf{n},z)$.

The second term in eq. (1.40) encodes the *redshift-space distortions* (RSD) due to the mapping from real to redshift space, on which the observations are performed. These two were originally found via a Newtonian computation in the original work by Kaiser [14] and are the next-to-leading order contributions to Δ (see also ref.[15]). Together with

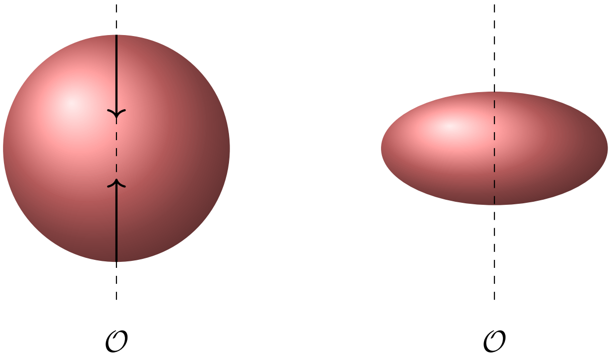

Figure 1.2: Diagram representing the Redshift-Space Distortion (RSD) effect (second term in eq. (1.42)). On linear scales, the net effect of the galaxies peculiar velocity components aligned with the observer's ($\mathcal{O}$) line-of-sight is to squeeze the observed volumes in redshift space. Galaxies moving towards $\mathcal{O}$ are observed closer, while galaxies receding away from $\mathcal{O}$ are observed further than predicted.

the density fluctuations, they are one of the main targets of current galaxy clustering analyses. Let us denote the combination of density fluctuations and RSD as the *standard* contributions

$$\Delta_{\rm ST}(\mathbf{n}, z) = b\delta - \frac{1}{\mathcal{H}}\partial_r(\mathbf{n}\cdot\mathbf{V}). \tag{1.42}$$

This is a well known combination that has already been measured in the redshift space power spectrum. The density term exhibits features called *baryon acoustic oscillations* (BAO) which are a relic of the acoustic waves generated in the plasma filling the Early Universe before the decoupling of baryons and photons [16, 17]. Given that we know very precisely the acoustic horizon, we can measure the angular diameter distance $d_A(z)$ from the angular scale of these oscillations [18–22]. The RSD term is a radial volume distortion due to the fact that galaxies with radial peculiar velocities are slightly more redshifted (or blueshifted) than expected according to their peculiar velocity component a long the line-of-sight (see fig.1.2). These volume distortions are actually measured in the 2-point correlation function and are used to constrain the linear growth rate of density fluctuations defined in eq.(1.20) [19, 23]. [2]

The second line contains three contributions already beyond the Newtonian limit, which are suppressed with respect to the standard contributions by a factor of $\mathcal{H}/k$. All together combine to form what we will call the *relativistic effects* in the following

$$\Delta_{\rm REL}(\mathbf{n}, z) = \left(1 - \frac{\dot{\mathcal{H}}}{\mathcal{H}^2} - \frac{2}{r\mathcal{H}}\right)\mathbf{n}\cdot\mathbf{V} + \frac{1}{\mathcal{H}}\mathbf{n}\cdot\dot{\mathbf{V}} + \frac{1}{\mathcal{H}}\partial_r\Psi. \tag{1.43}$$

The first one is a Doppler shift which has three ingredients. First, there is the so-called *light-cone effect* describing how the change of the redshift bin size causes that the peculiar velocity of galaxies changes the size of the time interval dt [24]. Secondly, a wrong estimation of the photons emission times induce a wrong estimation of the background expansion rate of the Universe at emission, taking into account that $\mathcal{H}$ is a time-evolving

---

[2] To be precise, current measurements of f are degenerate with the amplitude of density fluctuations inside a ball of radius 8 Mpc/h, parametrized by the variance σ_8^2. Hence, the quantity that current surveys are able to measure is actually $f\sigma_8$.

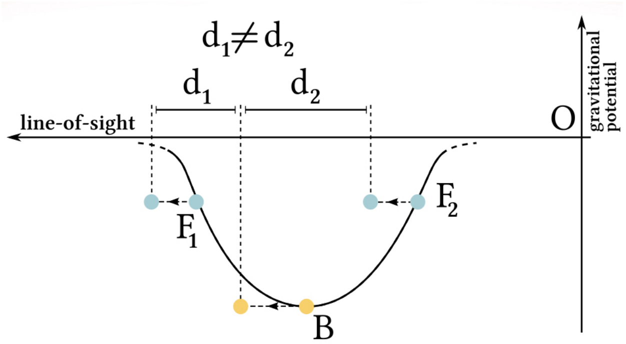

Figure 1.3: Symmetry breaking induced by the gravitational redshift (last term in eq. (1.58)). The apparent position of the galaxy sitting at the bottom of the potential well shifts more than the position of the galaxies sitting slightly upper. As a consequence, the bright galaxy appears to be closer to the galaxy in front of it and further away to the galaxy right behind along the line of sight, resulting in $d_1 \neq d_2$. This figure has been borrowed from ref. [24].

quantity. The third term in the first bracket was also found in the original Newtonian derivation. In addition, the term dependent on $\dot{\mathbf{V}}$ accounts from the fact that wrong estimations of t_S transform into wrong estimations of the galaxies peculiar velocities at emission time, and that velocities are also time-evolving quantities. Finally, the last term in eq. (1.43) is proportional to the gradient of the time distortions potential $\partial_r\Psi/\mathcal{H}$. This contribution account for the change in the comoving size of the redshift bin arising from the fact that the photons are emitted from galaxies sitting inside gravitational potential wells, receiving an additional contribution to their redshifts on their way to the observer's detector which is proportional to the depth of the potential. This translates into an asymmetry in the apparent separations between pairs of galaxies sitting at different 'heights' inside the wells (see fig. 1.3). It can be regarded as an equivalent of the standard redshift distortions, and hence we call it *gravitational redshift distortion*. Its study is one of the master pillars of this Thesis. Due to the gradient of Ψ it is of the same order of magnitude as the velocity terms.

A further simplification can be performed in theories of gravity that obey Euler equation. In terms of our gauge-invariant variables, the Euler's equation reads [3]

$$\mathbf{n}\cdot\dot{\mathbf{V}} + \mathcal{H}\,\mathbf{n}\cdot\mathbf{V} + \partial_r\Psi = 0, \tag{1.44}$$

which when combined with (1.43), the relativistic effects reduce to a simple Doppler distortion

$$\Delta_{\rm REL}(\mathbf{n},z) = -\left(\frac{\dot{\mathcal{H}}}{\mathcal{H}^2} + \frac{2}{r\mathcal{H}}\right)\mathbf{n}\cdot\mathbf{V}. \tag{1.45}$$

This last expression only differs with respect to the Newtonian result by the factor $\dot{\mathcal{H}}/\mathcal{H}^2$ (see ref. [7]).

The remaining terms in the third and fourth line of eq. (1.40) are also relativistic contributions, but we have taken the liberty of leaving them out from $\Delta_{\rm REL}$. The most important one is the first term of the third line, which quantifies the distortions generated by *gravitational lensing* on the solid angle of observation $d\Omega$: the presence of massive

---

[3] This is the configuration space counterpart of the Fourier expression given in eq.(1.11).

objects in between the observer and the source will induce distortions on the photons' trajectories in the transverse plane. This receives the name of *lensing magnification* [25, 26]

$$\Delta_{\rm LENS}(\mathbf{n}, z) = -\int_0^r dr' \frac{r - r'}{rr'} \Delta_\Omega(\Phi + \Psi). \tag{1.46}$$

We will come back later to this important effect and its relation to survey systematics. This contribution can be of the same order of magnitude as the standard terms. Roughly speaking, the Laplacian over the transverse directions cancels the $(\mathcal{H}/k)^2$ supression factor associated to the metric potentials. On the other hand, it consists in an integral along the line-of-sight which is enhanced at high redshifts, becoming comparable to density and RSD contributions [24, 27]. Nevertheless, it is expected to be subdominant at the redshift scales we will consider in Parts ii, iii and iv. On the other hand, the rest of the terms are directly proportional to the Bardeen potentials Φ and Ψ (or their time derivatives). Therefore, they are suppressed by a factor of $(\mathcal{H}/k)$ with respect to the Doppler and gravitational redshift terms and hence by a factor of $(\mathcal{H}/k)^2$ with respect to the Newtonian terms. We can summarize them into an additional correction term

$$\begin{aligned}\Delta_{\rm CORR}(\mathbf{n}, z) = \frac{2}{r}\int_0^r dr'(\Phi + \Psi) + 3\mathcal{H}\nabla^{-2}(\nabla \mathbf{V}) + \Psi - 2\Phi + \frac{1}{\mathcal{H}}\dot{\Phi} \\ + \left(\frac{\dot{\mathcal{H}}}{\mathcal{H}^2} + \frac{2}{r\mathcal{H}}\right)\left(\Psi + \int_0^r dr'(\dot{\Phi} + \dot{\Psi})\right),\end{aligned} \tag{1.47}$$

where the second term arises from writing D_s in the comoving gauge with eq. (1.8). These terms are due to distortions in the energy of the photons, the path of the geodesic and the time taken by the photons to travel from the source towards the observer's detector. Obviously, they have proper names and interesting features. The first term here is the *Shapiro time delay*, or gravitational time delay. In short and as its name suggests, the existence of gravitational potentials along the line of sight hinders the traveling photons, inducing a delay in their expected arrival times. This effect has been used to test General Relativity in the solar system using radar signals sent and received from Earth to Venus, providing an estimation of the time delay of photons due to the presence of a massive body like the Sun. In addition, the terms in the second line of eq. (1.47) are the Sachs-Wolfe contributions, which determine the amplitude of the gravitational field affecting the energy of the received photons. They split into the *ordinary Sachs-Wolfe* term accounting for the effect of Ψ at the last scattering surface, on which the CMB is measured, and the *integrated Sachs-Wolfe* effect which encodes the fluctuations induced by the time-varying potentials that photons have to cross on its path from the last-scattering surface to the observer's detector. Last, the remaining scalar potential terms are independent of the directions and are hence subdominant, monopolar contributions, which can safely be neglected against the density fluctuations in sub-horizon scales. However, for *ultra-large* scales, i.e. for very small values of k, they will come back as additional corrections to the main contributions. We will delve more into details about this fact in Part iv.

Importantly, the result derived in this section is incomplete. We omitted an important fact in the derivation of eq. (1.40) which is that, in practice, the redshift surveys on which Δ can be observed are magnitude limited. In other words, our detectors have a default luminosity threshold limiting the observational capacity: only galaxies above this

Figure 1.4: Image of the galaxy cluster SDSS J1038+4849, commonly known as the 'Cheshire Cat' or the 'Smiley', and the Einstein's rings due to strong lensing, as imaged by the HST. Borrowed from Loff, Sarah; Dunbar, Brian (10 February 2015). "Hubble Sees A Smiling Lens".

luminosity threshold can be detected. However, as discussed, inhomogeneities along the photons' trajectories can affect the number of galaxies we are able to detect. Due to gravitational lensing, galaxies behind overdense regions are distorted and *magnified*, and hence can enter in our detector threshold even if its intrinsic luminosity was too small in principle. Of course, the opposite effect is possible. In addition, we have neglected the possibility that the number of galaxies can change during the evolution of structures due to generation and merger of galaxies, clusters and such. Accounting for this feature is possible, but our expression (1.40) will require of a further refinement. These two systematic effects are relevant for the study of the relativistic effects Δ_{REL}. We will come back later to them and how to include them into our observable.

1.3 GRAVITATIONAL LENSING: THE CONVERGENCE FIELD

Gravitational Lensing is possibly one of the most interesting and visually beautiful phenomena existing in our Universe. Scientifically speaking, the study of gravitational lensing is an independent probe that provides crucial information about the LSS. As a direct consequence of the curvature of space-time on the propagation of light, as postulated by Einstein already at the time of establishing the pillars of GR, gravitational lensing effects contain crucial information to test gravity models. We can distinguish three different regimes on which gravitational lensing can happen: *strong*, *micro* and *weak*. The first happens when the *lens* is a very massive and compact object and the source is relatively close to it. This phenomenon is very rare but delights us with wonderful images: the bending of light due to the lens is so extreme that we are able to observe multiple images of the same source and, if by chance the source, lens and observer's camera are aligned, a unique figure called *Einstein's ring* will be seen (see fig. 1.4). In addition, the *micro lensing* is a physical effect that is exploited for observing small objects that emit from little to no light at all, such as the *exoplanets* or other transient sources. Last, the *weak lensing* is the one of most interest for this Thesis. Similarly as in the strong lensing case, the light coming from sources sitting behind massive objects is bent, distorting the photon's trajectories. In this case, weak lensing accounts for the stretching and distortion of source images through *shear*, or for their magnification through *convergence*. Although much smaller in amplitude than strong lensing, it is a much more common effect that has wide applications in the study of the statistical properties of the Universe, e.g. in the form of CMB lensing, which as of today conforms its own field of study and represents a powerful tool to probe the LSS at large redshifts $1 < z < 5$ [28, 29].

Let us now focus on the weak gravitational lensing and in particular in the study of the *convergence* field κ in a fully relativistic manner. We follow refs. [7, 30–32]. As in the case of the galaxy number counts fluctuations we adopt the metric for a perturbed Friedman Universe, and compute the distortion of a light beam by density perturbations between the source and the observer, i.e. we solve the Sachs equation. The weak lensing phenomenon can be described through a linear application called the *Jacobi map*. This is formally a $4x4$ matrix which relates the surface of the foreground galaxy to its projection at the observer's observation plane, which is presumably distorted due to gravitational perturbations induced by the lenses. In a first approximation, we can reduce the problem to a $2x2$ matrix called the *magnification matrix* mapping the angles at source and observer positions, by assuming that both the source and the image belong to the same two-dimensional subspace, i.e. the plane normal to the photon direction and to the observer four-velocity. For small angles, we can write $\boldsymbol{\theta}_S = \mathcal{A}\,\boldsymbol{\theta}_0$ where

$$\mathcal{A} = \begin{pmatrix} 1-\kappa+\gamma_1 & -\gamma_2 \\ -\gamma_2 & 1-\kappa-\gamma_1 \end{pmatrix}. \tag{1.48}$$

The *convergence* κ is the trace of the magnification matrix $\boldsymbol{\mathcal{A}}$, while the traceless part encodes the *complex shear*, defined as $\gamma = \gamma_1 + i\,\gamma_2$. Formally, both convergence and shear components are defined in terms of the so-called *lensing potential*

$$\Phi_W(\mathbf{n}, z) = \int_0^r dr' \frac{r-r'}{rr'} (\Phi + \Psi), \tag{1.49}$$

from where taking the Laplacian over the transverse directions we obtain the lensing convergence

$$\kappa = \frac{1}{2} \Delta_\Omega \, \Phi_W(\mathbf{n}, z), \tag{1.50}$$

and the shear components are given by the combinations

$$\gamma_1 = \frac{1}{2}(\partial_1\partial_1 - \partial_2\partial_2)\,\Phi_W(\mathbf{n}, z), \qquad \gamma_2 = \partial_1\partial_2\,\Phi_W(\mathbf{n}, z). \tag{1.51}$$

However, the source and observer's four-velocities generally differ, and hence the sources and images do not really belong to the same transverse plane. We can take account of this difference, but we need to modify the magnification matrix written above. Without getting into details, this modification will induce additional corrections to the shear which are second order in the peculiar velocities and hence too small to be observed. In addition, we also have to take into account that we measure quantities in redshift space, which generates additional contributions to the convergence in the form of redshift and volume fluctuations. These corrections are however relevant and

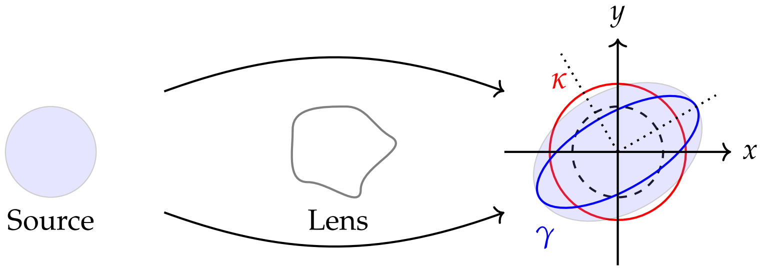

Figure 1.5: Diagram depicting the weak lensing effect produced by the existence of a large massive object in between the source and the observer. The figure on the right represents the linear order effects in the observer's focal plane. We identify a *magnification* effect (κ of eq. (1.52)), which produces a change in the apparenti size or magnitude of the objects, and a *cosmic shear* effect (γ, the combination of eqs.(1.51)), which encodes the distortion of the shape.

measurable at redshifts $z \lesssim 1$, and thus cannot be neglected. In summary, the relation between shear and convergence is affected by the galaxies' peculiar velocities. We jump over the detailed calculation of these contributions, which can be found in e.g. [30, 32]. The fully relativistic expression for the convergence at linear order, in terms of gauge-invariant variables takes the form

$$\kappa(\mathbf{n}, z) = \frac{1}{2r}\int_0^r dr' \, \frac{r-r'}{r'} \Delta_\Omega(\Phi+\Psi) - \frac{1}{r}\int_0^r dr'(\Phi+\Psi) \\ + \left(\frac{1}{r\mathcal{H}} - 1\right)\mathbf{n}\cdot\mathbf{V} + \left(1 - \frac{1}{r\mathcal{H}}\right)\left[\Psi + \int_0^r dr'(\dot{\Phi}+\dot{\Psi})\right] + \Phi. \tag{1.52}$$

We immediately identify a Doppler term in the second line indicating that the relative motion of a galaxy with respect to the observer changes its apparent size and luminosity in redshift space. The sign of this contribution, namely if the galaxy is *magnified* or *demagnified* clearly depends on the velocity direction through the product $\mathbf{n}\cdot\mathbf{V}$, but also on the sign of the prefactor (see discussion in ref. [7]). For a fixed redshift, a galaxy moving towards us (with $\mathbf{n}\cdot\mathbf{V} < 0$) is seen as further away than a galaxy with null peculiar velocity. At small redshifts, the term divided by $r\mathcal{H}$ dominates, leading to a demagnification of the galaxy, whereas at large redshift $1/r\mathcal{H} < 1$ producing a magnification effect on the galaxy. This velocity contribution is known under the name of *Doppler lensing*, and it has been extensively studied in the literature, where the reader might find it denoted by κ_v (see e.g. [31, 33, 34]).

Regarding the remaining terms in eq. (1.52), the first line contains the 'standard' gravitational lensing we found for the galaxy number counts fluctuations in eq. (1.40). This term is often denoted by κ_g. In principle, it is of the same order of magnitude as the Doppler lensing, but their relative importance depends again on the redshift. At small redshifts, the factor $1/r\mathcal{H}$ enhances the Doppler effect rendering the gravitational lensing term as the subdominant contribution. On the other hand, the integral nature of the standard gravitational lensing means that light deflections along the line of sight due to gravity accumulate for large redshifts, and hence it becomes the dominant term with respect to the Doppler lensing. The other terms in κ, encoding the relativistic corrections to the observed distances generated by the gravitational potentials Φ and Ψ, are suppressed by a factor $\mathcal{H}/k$ with respect to gravitational and Doppler lensing.

1.4 ACCOUNTING FOR SYSTEMATICS: EVOLUTION AND MAGNIFICATION BIAS

At this point, we hope the reader has become familiar with the relativistic effects affecting the apparent LSS of the Universe and how they modify our observables, in particular the galaxy number counts fluctuations $\Delta(\mathbf{n}, z)$ and the weak lensing convergence $\kappa(\mathbf{n}, z)$, for which we have provided the gauge-invariant expressions at linear order in perturbation theory. Looking back at our expression for $\Delta(\mathbf{n}, z)$ (1.40), we recall we had neglected two important details which depend on the specific survey on which we perform our observations: the *evolution* and *magnification* biases. In this sense, we regard them as *systematic effects* which are not generated out of gravitational perturbations but that induce additional modulations to the velocity perturbations. Therefore, they need to be included to obtain the true physical expression for the number counts fluctuations.

In the first place, we implicitly neglected the evolution of the background number density in the definition of $\Delta(\mathbf{n}, z)$, apart from the effect of dilution due to the Universe expansion. It is natural to expect that the evolution of structures, starting from a nearly homogeneous scenario at early-times and leading to the intricate configuration of filaments and voids characteristic of the late-times Cosmic Web, implies generation and merger of galaxies, clusters and all sorts of cosmic objects. Indeed, halo and galaxy formation and evolution lead to a non-conserved comoving number density which induces an additional modulation to the Doppler contribution in (1.40). We shall call this new correction as the *evolution bias*. Formally speaking, it arises as additional redshift (or comoving time) perturbations in Δ. Let us write $\bar{n}_\mathrm{g}(1 + \delta_\mathrm{g}(\mathbf{n}, z))d\Omega dz$, where $\bar{n}_\mathrm{g}(z)$ is the average comoving number density of sources and δ_g the galaxy density perturbations in the comoving gauge, directly measured from the survey at a fixed observed redshift $\bar{z}$. Let us relax the notation and omit the overbar on z, assuming all the quantities discussed here are evaluated at this background redshift. We can expand to first order the comoving galaxy number density as in ref. [11]

$$a^3(z)\, n_\mathrm{g}(z) = a^3(z)\, \bar{n}_\mathrm{g}(z)\, (1 + \delta_\mathrm{g}(\mathbf{n}, z)) - (1 + z)\frac{d(a^3 \bar{n}_\mathrm{g}(z))}{dz}\,\delta z. \tag{1.53}$$

The last term here encodes the so-called evolution bias. We will use the shorthand notation

$$f^{\mathrm{evol}}(z) \equiv -(1 + z)\frac{d}{dz}\ln\left(\frac{\bar{n}_\mathrm{g}(z)}{(1 + z)^3}\right) = \frac{1}{\mathcal{H}}\frac{d\,\ln\left(a^3 \bar{n}_\mathrm{g}(z)\right)}{dt}. \tag{1.54}$$

Hence, the evolution bias accounts for the difference between the redshift scaling of sources with respect to that of the mean density, which goes as $\bar{\rho} \sim (1 + z)^3$. Of course, $f^{\mathrm{evol}} = 0$ corresponds to the ideal case where the comoving number density of sources is conserved. This quantity is totally dependent on the tracer and has to be estimated independently for each survey [35]. In the Newtonian gauge, eq. (1.30) reduces to $\mathbf{n} \cdot \mathbf{V}$ (and the less relevant potential terms) and therefore the additional correction to the galaxy number counts fluctuations enter as an additional modulation to the Doppler contribution in Δ_{REL} in the form $f^{\mathrm{evol}}(z)\, \mathbf{n} \cdot \mathbf{V}$.

Secondly, there is the caveat that eq. (1.40) does not account for the fact that redshift surveys are limited in magnitude or luminosity. This means that we can only observe galaxies above a fixed flux threshold. It is crucial now to note that the weak lensing convergence discussed in sec. 1.3 plays a role around this limitation. What convergence does is to increase (or decrease) the apparent magnitude or luminosity of a source that is lensed by a gravitational distortion induced by a heavy object between source and observer. In general, galaxies with too small intrinsic luminosity to be detected can surpass the luminosity threshold if they are behind an overdense region. We say then that the galaxies have been *magnified*. The opposite effect can also happen: galaxies are *demagnified* when they live behind underdense regions, becoming undetectable. Note that the convergence-like contribution appearing in eq. (1.40) is not enough to account for this correction. In order to fully quantify this effect, we need to incorporate to Δ the relativistic corrections to κ. Let us define an additional correction to the number counts fluctuations of the form [36]

$$\Delta_{\rm MAG}(\mathbf{n},z) = 5\,s(z)\,\kappa(\mathbf{n},z), \tag{1.55}$$

where $s(z)$ is the *magnification bias* and κ takes the form of eq.(1.52). Alternatively, we could obtain the same contribution by computing the fluctuations in the luminosity distance [2, 37]. The magnification bias can be several ways, depending on the focus of the survey we are using. It is another astrophysical parameter that is obtained from the intrinsic source properties, more in particular from the luminosity function of the sources. Being $L_\star$ the luminosity cut of a given survey, the magnification bias can be defined in terms of the galaxy number density at the source $n_{\rm g}$ [35]

$$s(z) \equiv \frac{2}{5}\,\mathcal{Q}(z) = -\frac{2}{5}\frac{\partial \ln n_{\rm g}(z,L_\star)}{\partial \ln L_\star}, \tag{1.56}$$

which is intrinsically dependent on the survey luminosity cut. Here $\mathcal{Q}$ determines the number of galaxies that are gained at the observer's position due to magnification, i.e. for $\kappa > 0$, or lost due to demagnification, i.e. for $\kappa < 0$. Similarly as with $f^{\rm evol}$, we need to model $s(z)$ for each experiment separately. We refer the reader to some of the literature regarding estimation and modeling of the magnification and evolution bias for different surveys and different type of tracers [35, 38–40]. Later on in this Thesis, we will turn back to the modeling of these important systematic effects for spectroscopic surveys.

1.5 THE (PHYSICAL) GALAXY NUMBER COUNTS AT LINEAR ORDER

We have all the ingredients to write down the physical expression for the galaxy number counts fluctuations at linear order in perturbation theory. Schematically speaking, we can separate the contributions into

$$\Delta(\mathbf{n},z) = \Delta_{\rm ST} + \Delta_{\rm REL} + \Delta_{\rm LENS} + \Delta_{\rm CORR} \tag{1.57}$$

We can use eqs. (1.55), (1.52), and use the expansion (1.53) including $f^{\rm evol}$ to find that the magnification and evolution biases enter as additional Doppler modulations into eq. (1.40). Hence, the first term above is given by (1.42), whilst the relativistic contributions $\Delta_{\rm REL}$ are now

$$\Delta_{\rm REL}(\mathbf{n},z) = \left(1 - \frac{\dot{\mathcal{H}}}{\mathcal{H}^2} - 5\,s - \frac{2-5\,s}{r\mathcal{H}} + f^{\rm evol}\right)\mathbf{n}\cdot\mathbf{V} + \frac{1}{\mathcal{H}}\mathbf{n}\cdot\dot{\mathbf{V}} + \frac{1}{\mathcal{H}}\partial_r\Psi, \tag{1.58}$$

For completion, if we use the Euler equation (1.44) here, the simplified Doppler contribution including the systematic effects will be

$$\Delta_{\mathrm{REL}}(\mathbf{n},z) = -\left(\frac{\dot{\mathcal{H}}}{\mathcal{H}^2} + \frac{2-5s}{r\mathcal{H}} + 5s - f^{\mathrm{evol}}\right)\mathbf{n}\cdot\mathbf{V}. \tag{1.59}$$

Let us note that the gravitational lensing and gravitational potential terms in eq. (1.40) also pick corrections proportional to the magnification and evolution biases. The lensing contribution to in eqs. (1.46) is rewritten as

$$\Delta_{\mathrm{LENS}}(\mathbf{n},z) = \frac{5s-2}{2}\int_0^r dr'\frac{r-r'}{rr'}\,\Delta_\Omega(\Phi+\Psi). \tag{1.60}$$

Finally, the additional relativistic corrections encoded in (1.47) are recast to the form

$$\begin{aligned}\Delta_{\mathrm{CORR}}(\mathbf{n},z) = {}& \frac{2-5s}{r}\int_0^r dr'(\Phi+\Psi) + \left(3-f^{\mathrm{evol}}\right)\mathcal{H}\nabla^{-2}\left(\nabla\mathbf{V}\right) + \Psi + (5s-2)\Phi \\ & + \frac{1}{\mathcal{H}}\dot{\Phi} + \left(\frac{\dot{\mathcal{H}}}{\mathcal{H}^2} + \frac{2-5s}{r\mathcal{H}} + 5s - f^{\mathrm{evol}}\right)\left(\Psi + \int_0^r dr'(\dot{\Phi}+\dot{\Psi})\right).\end{aligned} \tag{1.61}$$

To conclude this Part, let us stress the main goal of this Thesis. The goal in all the projects included here is to evaluate the information contained in the relativistic effects using future galaxy surveys, in comparison with standard analyses which focus only on the standard terms Δ_{ST}. The relativistic contributions Δ_{REL} are systematically neglected due to limitations of current surveys, which do not reach the necessary sensitivity for their detection. Measurements of the galaxy number counts fluctuations can be the target of spectroscopic galaxy surveys and provide crucial information about the theory of gravity. We will demonstrate that these type of surveys represent the ideal playground from where to extract the information encoded in the Doppler and gravitational redshift effects. Henceforth, following the arguments regarding the order of magnitude hierarchy of the different contributions to Δ, the expression we will use in the text for the galaxy number counts fluctuations is thus the sum $\Delta(\mathbf{n},z) = \Delta_{\mathrm{ST}}(\mathbf{n},z) + \Delta_{\mathrm{REL}}(\mathbf{n},z)$ given eqs. (1.42) and (1.58), respectively (or (1.59) in a context where we can take the Euler equation to be valid). On the other hand, photometric surveys target the weak lensing effects that are better measured in angular scales. These are direct probes of cosmic shear field γ, which can be mapped to the lensing convergence term, κ_{g}, when neglecting relativistic effects in κ. These probes are sensitive to the total matter density distribution along the line-of-sight. Given that spectroscopic and photometric surveys are often independent and compatible probes, we will aim to consistently combine the information provided by both in order to develop meaningful gravity tests that include the most information possible. However, in practice, our observable quantities Δ and κ_{g} are not useful on their own to be confronted with the data provided by such experiments. The observer willing to go beyond theory has to rely on adapted statistical techniques for optimal extraction of the relevant information from each of the experiments, in order to meaningfully compare theory and observations. This will be the subject for the next Chapter.

2

SUMMARY STATISTICS OF COSMIC SURVEYS

Cosmology is probably entering its own Golden Age. The temperature anisotropies of the CMB have already been measured with astonishing precision by dozens of experiments and a new phase of new probes continues to grow. The late clustering of matter, i.e. the Cosmic Web, has already been demonstrated in several ways. In this case, the increasing trend does not fade away at all either. Following the success of galaxy redshift studies mapping the distribution of objects on the sky with the Sloan Digital Sky Survey (SDSS) and the Two Degree Field (2dF), the observers willing to study the Heavens through the propagation of light undertook photometric studies focusing on the galaxy lensing effects. Examples are the Kilo-Degree Survey (KiDS), the Dark Energy Survey (DES). There have been also spectroscopic extensions to SDSS, such as the Baryon Acoustic Spectroscopic Survey (BOSS). From the 2020s to the next decades, the IV-Stage galaxy surveys will dominate the scene. In the spectroscopic realm, the Dark Energy Survey Instrument (DESI) and the Square Kilometer Array (SKA) will provide high precision redshift data from about ~ 1 billion of galaxies. In the photometric field, we will have exquisite lensing maps from the Legacy Survey of Space and Time (LSST) at the Vera Rubin's Observatory. In addition, the Euclid satellite will provide both high quality spectroscopic and photometric data. Each of these experiments is expected to deliver datasets of unprecedented size and quality creating both new exciting challenges in the analysis on the technical side, but also new thrilling opportunities for testing the theory of gravity and possibly unveil the unsolved mysteries.

The increased precision and quality of the data open the door for new estimators and probes for sectors of the theory previously inaccessible. As a matter of fact, the relativistic effects Δ_{REL} have been known to exist for about a decade, but have been systematically neglected due to their subdominant nature. In short, the number of galaxies was not enough and shot-noise dominates over the signal arising from relativistic contributions. In this Thesis, we want to demonstrate that this will not be the case for future spectroscopic analysis. With a significant increase in number of detected galaxies, the shot-noise will no longer prevent us from detecting the relativistic effects with enough significance, and therefore neglecting them will be inconsistent. The fact that they can be useful to probe crucial general relativistic effects on large scales will turn out to be decisive for the task of testing gravity on large scales with minimal assumptions about the particular theory.

What we can really observe are the deviations with respect to a mean distribution, and the correlations between these deviations. Theoretically, we used perturbation variables to describe these deviations and computed the physical relations between them. We assumed these perturbations to have grown out of gravitational instabilities induced by small quantum fluctuations in the Early Universe. It is precisely the quantum nature of the primordial fluctuations what endows them with the crucial property of *Gaussianity*. The subsequent gravitational interactions making matter perturbations evolve linearly during matter domination are not changing this property. Henceforth, the perturbations variables at late-times can be assumed to be *Gaussian random fields*, δ, $\mathbf{V}$, Φ and Ψ. The beauty and utility of Gaussianity in this context is that such type of fields are fully characterized by the mean and covariance. In addition, the inherent structure of the data, if any, can be fully determined via the *correlation function* or its Fourier space counterpart, the *power spectrum*. No higher-order probabilistic moments are needed. If small departures from Gaussianity were present, it will be more precise to say that higher-order moments are strongly suppressed, but linear correlations will still be carrying most of the information. However, interestingly, higher-order moments such as the *bispectrum* have been used more frequently in the past years, in an attempt to evaluate the existence of deviations from Gaussianity and their observable effects [41]. These departures from Gaussianity can have various origins: they can be *primordial*, i.e. associated to the primordial fluctuations, but they can also be generated by non-linear evolution of small, non-linear scales.

Galaxy surveys mission is to gather data about the Cosmic Web. From this data, one can build maps of our cosmic environment such as that of fig. 1.1. Clearly, the data presented in this way has an inherent structure which seems very unlikely to have arisen from pure randomness. We, the observers, desire to understand the physical mechanisms that transformed the primordial tiny fluctuations into the intricate network of voids, filaments and sheets and probe if the most successful theory of gravity up to date can also explain what we see. In Chapter 1 we computed the observable quantities accounting for the fluctuations in the galaxy number counts Δ, and the changes in the apparent sizes and magnitude of galaxies due to weak-lensing convergence κ. The expressions are useful to identify the distinct effects affecting what we observe and where do they come from, but cannot be directly extracted from the cosmological datasets.

In this Chapter, we present the necessary tools to perform meaningful measurements from current and future cosmological datasets. The information from the three-dimensional galaxy clustering maps is analyzed using the 2-point correlation function (2pCF). In the photometric realm, we resort to the *angular power spectra* for analyzing the lensing maps. There we can obtain independent measurements of photometric clustering and shear and their correlations in the angular projections on the sky. Formally, in this Thesis, we will consider angular correlations of clustering and lensing contribution to the convergence, κ_g, which are inferred from cosmic shear measurements. [1]. This is commonly known within the photometric community as the 2×2pt analysis.

In addition, we review the inference techniques that we will require to connect the physical observables with the model parameters. Adopting a Bayesian approach, we can map a prior probability distribution on the observable quantities into a posterior probability distribution on the model parameters. In this context, we can infer the precision that we expect from the measurements, provided we know the survey specifications in two ways: we will perform a Fisher analysis, which require to assume the posterior distribution will also be Gaussian. However, if we cannot rely on this assumption, which is often the case, we will rather use a Monte Carlo Markov Chain (MCMC) algorithm to infer the parameter constraints.

---

[1] It is only between γ and κ_g (first term in (1.52)) for which an exact relation can be found. In practice, the additional relativistic effects in the full expression κ are usually neglected.

2.1 REDSHIFT-SPACE POWER SPECTRA

The gauge-invariant perturbation theory discussed in sec. 1.1 makes use of the harmonic decomposition for convenience. In Fourier space, the scalar, vector and tensor perturbation modes decouple and follow independent evolution equations, significantly simplifying the analysis. In this way, we arrive to the Fourier space expressions for the scalar perturbation variables and the correspondent Einstein equations. The real-space formulae are easily obtained by inverse Fourier transformations. However, since linear perturbations in Fourier space are simpler to analyze and one might be naturally tempted to estimate the statistical information directly there, where moreover the perturbation modes at different scales are uncorrelated. Assuming the perturbations to be Gaussian random fields, this is done by computing the *power spectrum*.

In general, all the perturbations modes in the Fourier realm are functions of the wave vector $\mathbf{k}$ and time. The standard approach within adiabatic perturbations is to express the perturbation variables in terms of an initial random field that was generated at early times from quantum fluctuations. People usually identify this variable to the *initial* Bardeen potential $\Psi_{\rm in}$. In this way, we can write the rest of the variables in terms of *transfer functions*, mapping their values at a given time to this $\Psi_{\rm in}$. Mathematically speaking, we define

$$\Psi(\mathbf{k},z) = T_\Psi(k,z)\,\Psi_{\rm in}(\mathbf{k}), \tag{2.1}$$

$$\delta(\mathbf{k},z) = T_\delta(k,z)\,\Psi_{\rm in}(\mathbf{k}), \tag{2.2}$$

$$V(\mathbf{k},z) = T_V(k,z)\,\Psi_{\rm in}(\mathbf{k}). \tag{2.3}$$

In this way, the statistical correlations of Fourier modes are characterized by the *primordial power spectrum* alone, encoding the (almost) Gaussian correlations of the primordial quantum fluctuations. We define

$$k^3\langle\Psi_{\rm in}(\mathbf{k})\Psi_{\rm in}(\mathbf{k}')\rangle = (2\pi)^3\delta(\mathbf{k}+\mathbf{k}')\,P_{\rm in}(k), \tag{2.4}$$

where it is explicit that different Fourier modes are uncorrelated. The primordial power spectrum $P_{\rm in}(k)$ is given by

$$P_{\rm in}(k) = \frac{1}{2\pi^2}\,A\left(\frac{k}{k_*}\right)^{n_s-1}, \tag{2.5}$$

where k_* is the pivot scale on which the amplitude of the primordial fluctuations A is measured and n_s is the spectral index. Note that A here is related to the Planck parameter A_s through $A = 8\pi^2 A_s/9$. The primordial power spectrum is completely determined by these two parameters that can be measured through CMB observations [6]. Thus, it is sufficient to determine the initial power spectrum and then to use the transfer functions to obtain the power spectrum of any other fluctuation variable.

The transfer functions T_X depend on the theory of gravity fixing the relations between matter and metric degrees of freedom. Importantly, they are deterministic functions that do not depend on the directions $\mathbf{k}$, in the sense that provide a map for any z assuming linear evolution is valid. In GR, we can make use of eqs. (1.10) (or (1.24)), (1.12) and (1.15) to relate the velocity and metric perturbations transfer functions to that associated to the matter perturbations

$$T_\Psi(k,z) = -\frac{3}{2}\left(\frac{\mathcal{H}}{k}\right)^2 \Omega_m(z)\, T_\delta(k,z), \tag{2.6}$$

$$T_\Phi(k,z) = T_\Psi(k,z), \tag{2.7}$$

$$T_V(k,z) = -\frac{\mathcal{H}}{k} f(z)\, T_\delta(k,z). \tag{2.8}$$

From eqs (2.6) and (2.7), we can easily find an additional transfer function associated to the Weyl potential

$$T_{\Phi+\Psi}(k,z) = 2T_\Phi(k,z) = -3\Omega_\mathrm{m}(z)\left[\frac{\mathcal{H}(z)}{k}\right]^2 T_\delta(k,z)\,. \tag{2.9}$$

At late-times, when all the relevant perturbation modes live inside the horizon, the matter transfer function can be split into a time-independent part and the growth function, which is independent of k. In this way, we can parametrize the link between the matter perturbations and the primordial potential in terms of the present values of $\Omega_{\mathrm{m},0}$ and H_0, as measured e.g. by Planck [6]

$$T_\delta(k,z) = -\frac{3}{5}\frac{k^2}{\Omega_{\mathrm{m},0}\, H_0^2}\frac{D_1(a)}{a}\, T(k). \tag{2.10}$$

With full generality, we can define the power spectrum encoding the statistical correlations between two perturbation variables A and B in the form

$$\langle \mathrm{A}(\mathbf{k},z)\, \mathrm{B}(\mathbf{k}',z)\rangle = (2\pi)^3\, P_\mathrm{AB}(k,z)\, \delta^3(\mathbf{k}+\mathbf{k}'), \tag{2.11}$$

which can be related to the primordial power spectrum via the transfer functions

$$P_\mathrm{AB}(k,z) = k^{-3}\, T_\mathrm{A}(k,z) T_\mathrm{B}(k,z)\, P_\mathrm{in}(k). \tag{2.12}$$

In sec. 1.1 we solved the equation for dust perturbations in a ΛCDM Universe in terms of the growth factor $D_1(z)$ mapping the solution at a given time z_* to any other z by a linear relation. This will be always valid during matter domination. We can do the same for the power spectrum defined here. Current Boltzmann solvers are fast in computing $T(k)$ and the matter power spectrum at any z_* using eq. (2.10). Hence, $P_{\delta\delta}(k,z_*)$ is fixed by the early Universe physics. Then, we can compute any other power spectrum contribution by linear evolution and the appropriate transfer functions, such that from

$$T_\delta(k,z) = \frac{D_1(z)}{D_1(z_*)}\, T_\delta(k,z_*), \tag{2.13}$$

the matter power spectrum at any redshift is easily obtained

$$P_{\delta\delta}(k,z) = \left(\frac{D_1(z)}{D_1(z_*)}\right)^2 P_{\delta\delta}(k,z_*), \tag{2.14}$$

where $D_1(z_*)$ is introduced to normalize the quantity at z_*. Hence, we are left with the computation of the time evolution for the quantities entering the transfer functions. If interested in transforming back to real-space, additional integrations over k will be needed.

2.1.1 *Galaxy number counts in Fourier Space*

The galaxy number count fluctuations power spectrum can be computed by using the previous considerations in the following manner. For full generality, we consider the case of two populations with different intrinsic properties, leading to different values of the population, magnification and evolution biases. We shall label each population of galaxies according to their luminosity, L, M. Let us define

$$\langle \Delta_{\rm L}(k',z)\,\Delta(k',z)_{\rm M}\rangle = (2\pi)^3\,P_{\rm LM}(k,z)\,\delta^3(\mathbf{k}+\mathbf{k}'), \tag{2.15}$$

where $\Delta(k,z)$ is the transfer function of the combination $\Delta = \Delta_{\rm ST} + \Delta_{\rm REL}$ (eqs. (1.42) and (1.58)). Using the convention in Appendix A.1 and $\mathbf{x} = r\mathbf{n}$, $\mathbf{k} = k\hat{\mathbf{k}}$ we have the formal relation

$$\Delta_{\rm L}(k,z) = \int d^3x\,\Delta_{\rm L}(\mathbf{n},z)\,e^{i(kr)\,\hat{\mathbf{k}}\mathbf{n}}. \tag{2.16}$$

However, in practice it is enough to take into account the transformation of the spatial derivatives to Fourier space, $\partial_r = -i\hat{\mathbf{k}}\mathbf{n}$. Time derivatives however commute with the Fourier transform operation. Hence, the galaxy number counts fluctuations for a population of galaxies with luminosity L becomes

$$\begin{aligned}\Delta_{\rm L}(\mathbf{k},z) = b_{\rm L}(z)\delta(\mathbf{k},z) &- \frac{k}{\mathcal{H}(z)}(\hat{\mathbf{k}}\cdot\mathbf{n})^2 V(\mathbf{k},z) \\ &+ i\,(\hat{\mathbf{k}}\cdot\mathbf{n})\left[\alpha_{\rm L}(z)V(\mathbf{k},z) + \frac{1}{\mathcal{H}(z)}\dot{V}(\mathbf{k},z) - \frac{k}{\mathcal{H}(z)}\Psi(\mathbf{k},z)\right],\end{aligned} \tag{2.17}$$

where we have defined the redshift dependent factor

$$\alpha_{\rm L}(z) = \left(1 - \frac{\dot{\mathcal{H}}(z)}{\mathcal{H}^2(z)} - 5\,s_{\rm L}(z) - \frac{2-5\,s_{\rm L}(z)}{r(z)\mathcal{H}(z)} + f_{\rm L}^{\rm evol}(z)\right) \tag{2.18}$$

and the velocity potential, V, is defined through $\mathbf{V}(\mathbf{k},z) = i\,\hat{\mathbf{k}}V(\mathbf{k},z)$. eq. (2.17) is valid only for a fixed line-of-sight direction $\mathbf{n}$ that has to be chosen from a given coordinate system. The product $(\hat{\mathbf{k}}\cdot\mathbf{n})$ represents the angle formed by the direction of observation and the wave vector, which depends on the chosen coordinate system. However, further considerations on this issue are better understood in configuration space and will be discussed in the next Section. For the time being, let us just mention that 'fixing' the $\mathbf{n}$ can be done by assuming the sources to be sufficiently far leading to a configuration called the *flat-sky limit*, such that incoming Fourier modes are described by plane waves. Using the definitions for the transfer functions given in eqs. (2.1)-(2.3) and (2.12), the power spectrum is then a linear combination of products of the quantities

$$\Delta^{\delta}(\mathbf{k},z) = b_{\rm L}(z)\,T_{\delta}(k,z), \tag{2.19}$$

$$\Delta^{\rm RSD}(\mathbf{k},z) = -\frac{k}{\mathcal{H}(z)}(\hat{\mathbf{k}}\cdot\mathbf{n})^2\,T_V(k,z), \tag{2.20}$$

$$\Delta^{\mathbf{V}}(\mathbf{k},z) = \alpha_{\rm L}(z)\,T_V(k,z), \tag{2.21}$$

$$\Delta^{\dot{\mathbf{V}}}(\mathbf{k},z) = \frac{1}{\mathcal{H}}\,T_{\dot{V}}(k,z), \tag{2.22}$$

$$\Delta^{\Psi}(\mathbf{k},z) = -\frac{k}{\mathcal{H}}\,T_{\Psi}(k,z), \tag{2.23}$$

where for $\dot{\mathbf{V}}(\mathbf{k},z) = d(T_V)/dt\,\Psi_{\rm in}(\mathbf{k})$ we have written $T_{\dot{V}} \equiv d(T_V)/dt$. In General Relativity, we might use the relations (2.6)-(2.10) to compute $P_{\rm LM}(k,z)$. In particular, using (2.8) we can find

$$T_{\dot{V}} = -\frac{d}{dt}\left(\frac{\mathcal{H}}{k}\,f(z)\,T_\delta(k,z)\right) \tag{2.24}$$

$$= -\frac{\mathcal{H}(z)}{k}\left(\dot{\mathcal{H}}(z)\,f(z) + \mathcal{H}(z)\,\dot{f}(z) + f^2(z)\right)\,T_\delta(k,z), \tag{2.25}$$

where we have used that in conformal time we have $\dot{D}_1 = \mathcal{H} f D_1$ which implies $\dot{T}_\delta = \mathcal{H} f T_\delta$.

In Fourier space, the contributions to the number counts fluctuations power spectrum naturally appear as a power series in the angle $(\hat{\mathbf{k}}\cdot\mathbf{n})$. Transforming this power series into an expression in terms of Legendre polynomials is then possible by using the definitions given in Appendix A.2. In this way, we can extract the multipoles of the power spectrum by exploiting some of their properties. Given that the Legendre polynomials form an orthogonal set, the *multipole* ℓ of $P_{\rm LM}$ can be extracted by weighting it with the Legendre polynomial $\mathcal{P}(x)$ of degree ℓ and integrating over $\mu = \hat{\mathbf{k}}\cdot\mathbf{n}$

$$P^{(\ell)}_{\rm LM}(k,z) = \frac{2\ell+1}{2}\int_{-1}^{1} d\mu\mathcal{P}_\ell(\mu)P_{\rm LM}(k,\mu,z)\,. \tag{2.26}$$

This technique permits to regard each $P^{(\ell)}_{\rm LM}(k,z)$ as an independent quantity directly measurable from cosmological datasets by a simple fitting operation. At this level, we could already construct an estimator out of the predicted multipoles from a given theory. From eq. (2.17) we will find a reduced set of three even multipoles ($\ell = 0$, 2, 4) and two odd multipoles ($\ell = 1$, 3). Interestingly, for an appropriate choice of the angle μ the latter will contain all the information of the relativistic effects contributions to the power spectrum, while the even multipoles encode the standard terms. The even multipoles have been shown to be optimal observables for measuring the growth rate of fluctuations and the population bias, and are widely used in current analysis. However, if we wish to include the odd multipoles tracking the relativistic corrections, estimators based on the redshift-space power spectrum suffer from an important limitation. In this context, the fixed line-of sight is only approximately valid and one needs to take into account corrections to the projections on the flat-sky. These corrections scale linearly with the separations between the correlated points d and depend on the angle $\hat{\mathbf{k}}\cdot\mathbf{n}$, becoming comparable in magnitude to the odd multipoles when including large separations. They thus affect the observables as a contamination. It turns out that in order to include this so-called *wide-angle corrections* it is necessary to work in configuration space, with the correlation function between two small volumes in the sky. As we will see in sec. 2.2, the wide-angle effects are originated by the standard terms and enter as additional corrections to the odd multipoles. Fortunately, it is possible to design estimators based on the correlation function that take into account the wide-angle effects making possible to remove them from the signal.

2.1.2 *Convergence field in Fourier space*

Additional difficulties also appear if we consider observables including integrated effects such as the convergence field $\kappa(\mathbf{n}, z)$. To leading order in perturbation theory, the dominant effect in eq. (1.52) is

$$\kappa(\mathbf{n}, z) = \frac{1}{2r} \int_0^r dr' \frac{r - r'}{r'} \Delta_\Omega(\Phi + \Psi). \tag{2.27}$$

Estimators including κ are probes of the *Weyl potential*, $(\Phi + \Psi)/2$, a combination which is subdominant for correlations using only pure number counts fluctuations at low redshift. However, we are free to combine gravitational lensing observables with galaxy number counts, the so-called *galaxy-galaxy lensing* correlations. In Fourier space, we might naively define the galaxy-galaxy lensing power spectrum as

$$\langle \Delta_{\mathrm{L}}(\mathbf{k}, z)\, \kappa(\mathbf{k}', z') \rangle = (2\pi)^2\, P_{\Delta\kappa}(k, z)\, \delta^3(\mathbf{k} + \mathbf{k}'). \tag{2.28}$$

The dominant contribution would be the term encoding the correlations with density and the transverse plane derivatives of the sum of the potentials. We shall denote $P_{\delta(\Phi+\Psi)}(k, z)$. Using our definitions for the transfer functions (2.6) and the fact that in GR we have $\Psi = \Phi$, we find a transfer function for the Weyl potential to be just $T_{\Phi+\Psi} = 2T_\Psi$. However, obtaining the fourier transform of $\kappa(\mathbf{n}, z)$ is more intricate than to compute $\Delta(k, z)$. The integral in κ has to be performed in a hypersurface of constant time that is only defined in the *past light-cone* of the observer. This makes the definition of $P_{\Delta\kappa}(k, z)$ above as ill-defined. However, the configuration space galaxy-galaxy lensing correlation is a well-defined quantity. In order to extract the correct $P_{\delta(\Phi+\Psi)}$ we are forced to work in configuration space and implement the Limber approximation when performing the Fourier transform. We will come back later to this important subtlety, but let us first to finally travel to configuration space and build the relevant estimators in a fully consistent way.

2.2 THE 2-PT CORRELATION FUNCTION OF SPECTROSCOPIC SURVEYS

In Statistics, the *correlation function* is generally defined as the quantity that encodes the statistical correlation between two or more random variables as a function of their spatial or temporal separation. Provided $\Delta(\mathbf{n}, z)$ is our random variable, the previous definition is no different in Cosmology. Given a random galaxy in a sky location, the 2-point correlation function describes the probability that another galaxy will be found within a given distance. In order for this to be entirely consistent in the statistical sense, we are required to compute the ensemble average of every pair in the distribution. However, in practice, statistical homogeneity and isotropy allow us to replace the ensemble average by an average over *pairs*. Hence, we just count pairs of galaxies separated by a certain distance in a given redshift range. What we demonstrated in Chapter 1 is that there are relativistic effects arising from gravitational perturbations in the propagation of light that affect the count. In fact, they leave an imprint in the Cosmic Web structure that is captured in the correlation function. Of course, a different gravity theory will lead to a distinct pattern in the observed galaxy distribution.

The galaxy 2-point correlation function compares the number of galaxies in a small volume of the sky, a *pixel*, at around redshift z_1 given by a small solid angle around direction $\mathbf{n}_1$ with another pixel at $(\mathbf{n}_2, z_2)$. With full generality, the pair of galaxies under consideration will exhibit different properties. Let us label the pairs according to e.g. their luminosity

$$\xi_{\mathrm{LM}}(\mathbf{n}_1, \mathbf{n}_2, z_1, z_2) \equiv \langle \Delta_{\mathrm{L}}(\mathbf{n}_1, z_1)\, \Delta_{\mathrm{M}}(\mathbf{n}_2, z_2) \rangle. \tag{2.29}$$

Statistical isotropy reduces the resulting correlation function to be only dependent on the separation between the points. We can write this down in terms of the angle θ between $\mathbf{n}_1$ and $\mathbf{n}_2$, through $\mathbf{n}_1 \cdot \mathbf{n}_2 = \cos\theta$. The comoving distance to each pixel is then denoted by $\mathbf{r}_i = r_i\, \mathbf{n}_i$.

We can compute the projection of ξ on the sky is by the expansion in Legendre polynomials of the angle θ [42]

$$\xi(\theta, z_1, z_2) = \frac{1}{4\pi} \sum_{\ell} (2\ell + 1) C_\ell(z_1, z_2) \mathcal{P}_\ell(\cos\theta), \tag{2.30}$$

where the $C_\ell(z_1, z_2)$ is the *angular-redshift power spectrum* and $\mathcal{P}_\ell$ denotes the Legendre polynomial of degree ℓ. The C_ℓ's are a way to estimate the correlations up to a given angular scale determined by ℓ. The larger the ℓ, the smaller the scales that are being included in the approximation. Small scales here mean to focus on small angles, which scale $\theta \sim 1/\ell \ll 1$. Theoretically speaking this is entirely satisfactory. We have precise and fast Boltzmann codes like CAMB and CLASS that are able to compute the C_ℓ's. Additionally, they are directly observable quantities. This is the standard technique to extract the information provided by photometric surveys where we analyze a dozen of redshift slices. However, it is not the optimal approach to study the correlations from spectroscopic information. Datasets from surveys like DESI, SKA or Euclid will require thousands of redshift slices leading to several million $C_\ell(z_1, z_2)$ for accurate reconstruction of the spectrum. This is highly inefficient from the computational point of view. In addition, each of those thin spectroscopic bins will only have a few thousands of galaxies and hence the spectra shot-noise, which scales as $\sim 1/N$, is expected to be very large. This limits the computation to very low values of ℓ, which dramatically narrows down the accuracy [42].

2.2.1 *The full-sky relativistic correlation function*

Alternatively, we can avoid the computation of thousands of C_ℓ's and obtain an exact expression for the correlation function by expanding $\xi_{\mathrm{LM}}(\theta, z_1, z_2)$ in Tripolar Spherical Harmonics [43, 44]. The resulting expression is called the *full sky* 2-point correlation function. Here we summarize a simplified version of the computation with the fully relativistic $\Delta(\mathbf{n}, z)$, following [42, 45, 46]. However, in contrast with the selected references, we will perform the computation for the more general situation of multiple populations with distinct luminosities. It is convenient to begin by computing the Fourier transform of the k-space correlations found in sec. (2.1), according to our convention (see Appendix A.1)

$$\xi_{\mathrm{LM}}(\mathbf{n}_1, \mathbf{n}_2, z_1, z_2) = \int \frac{d^3k_1\, d^3k_2}{(2\pi)^6}\, e^{-i(\mathbf{k}_1\mathbf{r}_1 + \mathbf{k}_2\mathbf{r}_2)} \langle \Delta_{\mathrm{L}}(\mathbf{k}_1, z_1)\, \Delta_{\mathrm{M}}(\mathbf{k}_2, z_2) \rangle \tag{2.31}$$

Using the properties of the Legendre polynomials and spherical Bessel functions summarized in Appendices A.2 and A.4, we find that the $C_\ell(z_1, z_2)$ are of the form

$$C_\ell^{\rm AB}(z_1, z_2) = 4\pi \int \frac{dk}{k}\, \Delta_\ell^{\rm A}(k, z_1)\, \Delta_\ell^{\rm B}(k, z_2)\, P_{\rm in}(k), \tag{2.32}$$

where $P_{\rm in}(k)$ is the power spectrum of primordial fluctuations as defined in eq.(2.5). The $\Delta_\ell(k, z)$ denote the multipoles of the (partial) Fourier-Bessel transforms for each contribution to eq.(2.17), labeled by the superscripts A and B (see eqs.(2.19)-(2.23)). For this Thesis, only the standard contributions, the relativistic doppler and gravitational redshift contributions are relevant. Hence, we have the set of contributions [42, 46]

$$\Delta_\ell^{\delta}(k, z) = b_{\rm L}(z)\, T_\delta(k, z)\, j_\ell(kr), \tag{2.33}$$

$$\Delta_\ell^{\rm RSD}(k, z) = \frac{k}{\mathcal{H}}\, T_V(k, z)\, j_\ell''(kr), \tag{2.34}$$

$$\Delta_\ell^{\rm V}(k, z) = \alpha_{\rm L}(z)\, T_V(k, z)\, j_\ell'(kr), \tag{2.35}$$

$$\Delta_\ell^{\dot{\rm V}}(k, z) = \frac{1}{\mathcal{H}}\, T_{\dot V}(k, z)\, j_\ell'(kr), \tag{2.36}$$

$$\Delta_\ell^{\Psi}(k, z) = -\frac{k}{\mathcal{H}}\, T_\Psi(k, z)\, j_\ell'(kr). \tag{2.37}$$

The $j_\ell(kr)$ are the spherical Bessel functions of wave number k and comoving distance $r(z)$. The $'$ denote derivatives with respect to the arguments. The functions $T_X(k, z)$ are the Fourier space transfer functions, which we computed in sec. 2.1. The factor in front of the Doppler term is given by eq. (2.18).

The hierarchy of the different contributions, discussed in secs. 1.1 and 1.2, is also manifest in this expressions. Let us note that in contrast with the expressions given in refs. [42, 46] here we do not use the Euler equation in order to maintain full generality. Additionally, we explicitly include the population-dependent parameters: galaxy bias, magnification bias and evolution bias. Using this expressions we can find a compact form for the correlation function ξ

$$\xi(\theta, z_1, z_2) = \sum_{\rm A,B} \int \frac{dk}{k}\, Q_k^{\rm AB}(\theta, z_1, z_2)\, P_{\rm in}(k), \tag{2.38}$$

where we defined [42, 46]

$$Q_k^{\rm AB}(\theta, z_1, z_2) \equiv \sum_\ell (2\ell + 1) \Delta_\ell^{\rm A}(k, z_1) \Delta_\ell^{\rm B}(k, z_2)\, \mathcal{P}_\ell(\mu). \tag{2.39}$$

Each Δ above has to be evaluated at a different redshift, which is implicit to the argument of the j_ℓ's functions, as $k\, r_i = k\, r(z_i)$. Importantly, isotropy is manifest after exploiting the properties of Legendre Polynomials and spherical Bessel functions summarized in Appendices A.2, A.3 and A.4. We define the comoving separations of the correlated pairs as

$$d \equiv |r_2 - r_1| = \sqrt{r_1^2 + r_2^2 - 2\, r_1 r_2 \cos\theta}. \tag{2.40}$$

Inserting eqs. (2.33)-(2.37) into eq. (2.39) we obtain sums over products of Legendre polynomials and spherical Bessel functions. For the j_ℓ's derivatives we shall use the recurrence relations allowing to express them in terms of lower-order functions (See Appendix A.5).

Formally speaking, the 2-pt correlation function of two populations can be written as

$$\xi_{\rm LM}(\theta,z_1,z_2)=\xi^{\rm ST}_{\rm LM}(\theta,z_1,z_2)+\xi^{\rm ST\times REL}_{\rm LM}(\theta,z_1,z_2)+\xi^{\rm REL}_{\rm LM}(\theta,z_1,z_2). \tag{2.41}$$

The last term encoding the auto-correlations of the relativistic terms is suppressed by a factor $(\mathcal{H}/k)^2$ with respect to the ST contributions and can safely be neglected, as the relativistic corrections contained thereby are too small to be detected. The contributions entering in the second term are the cross-correlation between ST and REL contributions. Being suppressed with respect to the dominant standard terms auto-correlations by a factor of $(\mathcal{H}/k)$, they turn out to be sufficiently large to be observed. Let us refer to this term as the *relativistic corrections to the 2-pt correlation function*. Let us also alleviate the notation by writing $\xi^{\rm ST\times REL}(\theta,z_1,z_2)\equiv\xi^{\rm REL}(\theta,z_1,z_2)$. Using eq. (2.39), the ST correlations are

$$\begin{aligned}\xi^{\rm ST}_{\rm LM}(\theta,z_1,z_2)=\int\frac{dk}{k}P_{\rm in}(k)\Bigg[&Q^{\delta\delta}_{\rm LM}(\theta,z_1,z_2)+Q^{\delta\,\rm RSD}_{\rm LM}(\theta,z_1,z_2)\\&+Q^{\rm RSD\,\delta}_{\rm LM}(\theta,z_1,z_2)+Q^{\rm RSD}_{\rm LM}(\theta,z_1,z_2)\Bigg].\end{aligned} \tag{2.42}$$

These contributions are completely symmetric under the exchange $z_1\to z_2$. Similarly, the relativistic corrections can be written as the k-integral

$$\begin{aligned}\xi^{\rm REL}_{\rm LM}(\theta,z_1,z_2)=\int\frac{dk}{k}P_{\rm in}(k)\Bigg[&Q^{\delta\,V}_{\rm LM}(\theta,z_1,z_2)+Q^{\delta\,\dot V}_{\rm LM}(\theta,z_1,z_2)\\&+Q^{\rm RSD\,V}_{\rm LM}(\theta,z_1,z_2)+Q^{\rm RSD\,\dot V}_{\rm LM}(\theta,z_1,z_2)\\&+Q^{\delta\,\Psi}_{\rm LM}(\theta,z_1,z_2)+Q^{\rm RSD\,\Psi}_{\rm LM}(\theta,z_1,z_2)\Bigg].\end{aligned} \tag{2.43}$$

The $Q^{\rm AB}_k$ are summarized in Appendix A.5. All together provide the exact expression for the two point correlation function in the full sky, including the relativistic corrections of order up to $(\mathcal{H}/k)$, in terms of the angle θ and the redshifts z_1 and z_2.

2.2.2 *The distant-observer approximation*

It is common to rewrite $\xi(\theta,z_1,z_2)$ in terms of the mean redshift $z=(z_1+z_2)/2$, the separation of the galaxies d and the relative orientation of the pair with respect to a fixed line-of-sight. In the discussion provided in ref. [42], this fixed line-of-sight is the line joining the observer with the midpoint of the separation and the correspondent angle is denoted by β (see fig. 2.1). In fact, we denote as $\mathbf{r}=(\mathbf{r}_1+\mathbf{r}_2)/2$ the comoving distance to the center of the pair, and with $\mathbf{n}$ the fixed direction of observation, i.e. $\mathbf{r}=r(z)\,\mathbf{n}$. For thin enough redshift bins, we have $z_1\approx z_2$ and the evolution of redshift dependent quantities can be safely neglected within the bin. This implies we can evaluate all the functions at the same redshift $F(z_1)\sim F(z_2)\sim F(z)$. In addition, for small angles there is no difference in choosing β or θ, i.e. $\theta\sim\beta$. To write down ξ in terms of the coordinates (d,μ,z), where $\mu=\cos\beta$, is mostly straightforward. In the distant-observer regime where $d\ll r$ the angles are indeed small and are approximately related by

$$\cos\theta\simeq 1-\frac{1}{2}\frac{d^2}{r^2}\left(1-\cos^2\beta\right)+\mathcal{O}\left(\frac{d^4}{r^4}\right). \tag{2.44}$$

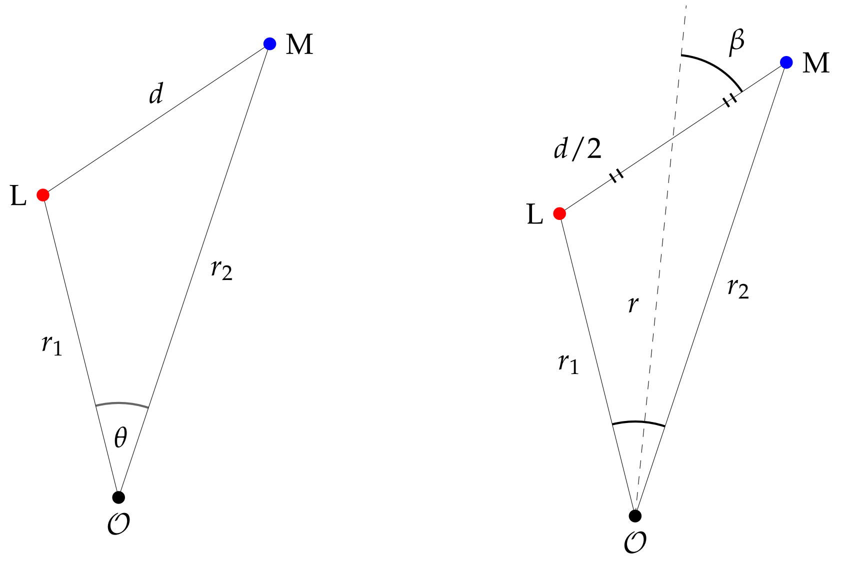

Figure 2.1: Coordinates systems used in the text to compute the correlation function. The right panel configuration is the preferred one. The information about the correlations is encoded in a reduced set of a few multipoles of the angle β. Also, the impact of the wide-angle effects is minimized. For further discussion about other possible choices see e.g. refs. [42, 47, 48]

The comoving distances are related through the expressions

$$r_{1,2} = r \mp \frac{1}{2} d \cos\beta. \tag{2.45}$$

Hence for $\beta \ll 1$ and $d \ll r$ we also have $r_i \sim r$. We are now able to rewrite the ζ^{ij} factors in terms of d, r and $\mu = \cos\beta$. This effectively transform our expressions into an expansion in powers of d/r, on which we only keep terms up to first order. Using the definitions of the Legendre polynomials, we can recast $\xi(d, \mu, z)$ in terms of $\mathcal{P}_\ell(\mu)$. This reorganizes the different contributions in a more useful manner that is easier to interpret, as a sum of the *multipoles* of the angle β. More precisely, we find that the ST contributions will be contained in three *even* multipoles (with $\ell = 0, 2, 4$), while the relativistic effects generate two *odd* multipoles (with $\ell = 1, 3$) [12, 24, 49, 50]. This is a significantly reduced set of observables if compared with the angular power spectra approach, and is the preferred technique for surveys that permit precise measurements of the redshift.

Hence, we find the general and exact expression for the standard contributions to the 2-pt correlation function to be

$$\begin{aligned}\xi^{\rm ST}_{\rm LM}(d,\mu,z) =& \frac{1}{2\pi^2}\int \frac{dk}{k}\, P_R(k) \times \\ & \times \Bigg[\left(b_{\rm L}\, b_{\rm M}\, T_\delta^2 - \frac{1}{3}\frac{k}{\mathcal{H}}(b_{\rm L}+b_{\rm M})T_\delta T_V + \frac{1}{5}\frac{k^2}{\mathcal{H}^2}T_V^2 \right) j_0(kd) \\ & + \left(\frac{2}{3}\frac{k}{\mathcal{H}}(b_{\rm L}+b_{\rm M})T_\delta T_V - \frac{4}{7}\frac{k^2}{\mathcal{H}^2}T_V^2 \right) \mathcal{P}_2(\mu)\, j_2(kd) \\ & + \frac{8}{35}\frac{k^2}{\mathcal{H}^2}T_V^2\, \mathcal{P}_4(\mu)\, j_4(kd) \Bigg],\end{aligned} \tag{2.46}$$

where we used $\mathcal{P}_0(\mu) = 1$. Therefore, matter perturbations and RSD generate even multipoles in the correlation function of galaxy number counts, i.e the *monopole* ($\ell = 0$), *quadrupole* ($\ell = 2$) and the *hexadecapole* ($\ell = 4$). They are completely symmetric contributions under the exchange of populations. In standard analysis however only one population is considered. By setting $b_{\mathrm{L}} = b_{\mathrm{M}} = b$ we recover the expressions for the single-population scenario.

In addition, the relativistic contributions are recast into the form

$$\begin{aligned} \xi^{\mathrm{REL}}_{\mathrm{LM}}(d,\mu,z) =& \frac{1}{2\pi^2}\int \frac{dk}{k}\, P_R(k)\times \\ &\times \Bigg[\Bigg(\frac{3}{5}\frac{k}{\mathcal{H}}(\alpha_{\mathrm{L}} - \alpha_{\mathrm{M}})\, T_V^2 - (b_{\mathrm{L}}\,\alpha_{\mathrm{M}} - b_{\mathrm{M}}\,\alpha_{\mathrm{L}})T_\delta T_V \\ &\qquad - \frac{1}{\mathcal{H}}(b_{\mathrm{L}} - b_{\mathrm{M}})T_\delta T_{\dot{V}} + \frac{k}{\mathcal{H}}(b_{\mathrm{L}} - b_{\mathrm{M}})T_\delta T_\Psi\Bigg)\, \mathcal{P}_1(\mu)\, j_1(kd) \\ &\qquad + \frac{2}{5}\frac{k}{\mathcal{H}}(\alpha_{\mathrm{L}} - \alpha_{\mathrm{M}})\, T_V^2\, \mathcal{P}_3(\mu)\, j_3(kd) \\ &\qquad + \frac{2}{5}\frac{d}{r}\frac{k}{\mathcal{H}}(b_{\mathrm{L}} - b_{\mathrm{M}})T_\delta T_V(\mathcal{P}_1(\mu) - \mathcal{P}_3(\mu))\, j_2(kd)\Bigg], \end{aligned} \tag{2.47}$$

where we can easily identify the *dipole* ($\ell = 1$) and the *octupole* ($\ell = 3$). Here $\alpha_{\mathrm{L,M}}$ are given by eq. (2.18). The last line contains terms of order (d/r) which actually arise from the standard contributions as additional corrections to the odd multipoles. [2] These receive the name of the *wide-angle corrections* and are expected to play a role at large separations, when they become comparable in magnitude to the leading contributions to dipole and octupole and can potentially bias any analysis that uses these quantities. Importantly, the wide-angle corrections appear only from distant-observer approximation when performed over the full-sky correlation function. They are not included in estimators based in the flat-sky power spectrum. If we desire to work in Fourier space, one should first compute the full-sky $\xi(d,\mu,z)$ and then compute the Fourier transform to find the power spectrum that includes those wide-angle effects. This operation lead to a wide-angle term generating dipole even for the single population case because of the effect of a window function needed for the calculation [51]. We also note that ξ^{REL} is antisymmetric under the exchange of populations, meaning it identically cancels out in the single-tracer case where, $\alpha_{\mathrm{L}} = \alpha_{\mathrm{M}}$ and $b_{\mathrm{L}} = b_{\mathrm{M}}$. Henceforth, the relativistic effects in the galaxy counts correlation function, i.e. the *dipole* and *octupole*, are only measurable when considering two distinct populations and induce a breaking of the symmetry of the 2-pt correlation function (see fig 1.3). However, let us note that this is only the case for multipoles of the angle β. Other choices of the coordinate system used to compute ξ actually lead to odd multipoles even for a single population (see e.g. [47, 48]). We have carefully chosen a configuration in which the symmetry of the 2-pt correlation function is only broken when considering two populations. Additionally, this configuration also minimizes the impact of the wide-angle effects [47, 48, 52].

---

[2] Similarly, the relativistic contributions also generate additional corrections to the even multipoles suppressed by a factor (d/r). However, they are subdominant at all scales with respect to the standard density and velocity contributions. We do not include them into the expressions.

Finally, we have to compute the k-integrals involving the transfer functions and the primordial power spectrum $P_R(k)$. We use the fact that for generic X and Y contributions we have $P_{XY}(k,z) = k^{-3}\, T_X T_Y P_R(k)$ and hence the integrals transform as

$$\int \frac{dk}{k}\, T_X T_Y\, P_R(k) \longrightarrow \int dk\, k^2 P_{XY}(k,z). \tag{2.48}$$

It is often more convenient to rewrite the expressions in terms of the density perturbations power spectrum $P_{\delta\delta}(k,z)$. In matter domination, where perturbations grow linearly this calculation can be done at a fixed redshift z_* and then mapped to any other z by linear relations given by the transfer functions. We then have to compute *once* the power spectrum at e.g. $z_* = 0$ with our favorite Boltzmann solver. We are free to choose z_* as long as matter domination can be assumed to be a good approximation. Using this, we are left with the computation of two types of integrals

$$\rho_\ell(d,z_*) = \frac{1}{2\pi^2}\int dk\, k^2\, P_{\delta\delta}(k,z_*)\, j_\ell(kd), \qquad \ell = 0,\, 2,\, 4 \tag{2.49}$$

$$\tau_\ell(d,z_*) = \frac{\mathcal{H}_0}{2\pi^2}\int dk\, k\, P_{\delta\delta}(k,z_*)\, j_\ell(kd), \qquad \ell = 1,\, 3 \tag{2.50}$$

where, $\mathcal{H}_0 = \mathcal{H}(z=0)$ is introduced to suppress the dimensions in the odd multipoles, which are proportional to $\mathcal{H}(z)$. This type of integrals is known as *Hankel transforms* of the power spectrum. They fully encode the dependance on the pairs separation of the 2-pt correlation functions due to statistical isotropy. The redshift evolution is given by the pre-factors containing the redshift-dependent quantities.

Let us finish this Section by writing down the final results for the multipoles of the galaxy 2-pt correlation function in General Relativity. First, let us emphasize on the usefulness of the three-dimensional multipoles versus the $C_\ell(z_1,z_2)$. From thousands of terms for accurate reconstruction of the angular power spectrum, the multipoles of the angle β are just a few terms that encode all the relevant contributions. Importantly, the projection on the sphere implies the loss of the radial information, which is kept by the three-dimensional multipoles. Similarly as the C_ℓ's, the multipoles of the 2-point correlation function are also observable quantities on their own right. We can individually extract them directly from the data by fitting with an appropriate weight

$$\xi^{(\ell)}_{\mathrm{LM}}(d,z) = \frac{2\ell+1}{2}\int_{-1}^{1} d\mu\, \xi_{\mathrm{LM}}(d,\mu,z)\, \mathcal{P}_\ell(\mu). \tag{2.51}$$

2.2.3 *The Even Multipoles in GR*

The generalized expressions for any theory of gravity and two populations for standard and relativistic correlation functions are given in eqs (2.46) and (2.47). Now, the relations needed to transform the expression in terms of the $P_{\delta\delta}(k,z)$ depend on the theory of gravity. We make use of the transfer functions found in sec. 2.1.1 to get the resulting equations for GR. In particular, in GR there is no anisotropic stress ($\Psi = \Phi$) and Euler (eq. (1.11)) and Continuity (eq. (1.10)) equations are valid for dark matter perturbations. Hence, using eqs. (2.6),(2.8) and the mapping (2.14) the generalized even multipoles take the form

$$\xi^{(0)}_{\mathrm{LM}} = \left(\frac{D_1(z)}{D_1(0)}\right)^2 \left(b_{\mathrm{L}}(z) b_{\mathrm{M}}(z) + \frac{1}{3}(b_{\mathrm{L}}(z) + b_{\mathrm{M}}(z))\, f(z) + \frac{1}{5} f^2(z)\right) \rho_0(d,0), \tag{2.52}$$

$$\xi^{(2)}_{\rm LM} = -\left(\frac{D_1(z)}{D_1(0)}\right)^2 \left(\frac{2}{3}(b_{\rm L}(z)+b_{\rm M}(z))\, f(z) + \frac{4}{7} f^2(z)\right) \rho_2(d,0), \tag{2.53}$$

$$\xi^{(4)}_{\rm T} = \frac{8}{35}\left(\frac{D_1(z)}{D_1(0)}\right)^2 f^2(z)\, \rho_4(d,0), \tag{2.54}$$

where we have set $z_* = 0$ and $f(z)$ is the growth rate of matter perturbations defined in eq. (1.20). This choice is appropriate for GR, but might not be accurate when considering other fiducial models. Given that the multipoles can be measured individually, the joint measurements of monopole, quadrupole and hexadecapole provide measurements of the growth rate and the population biases. Such measurements permit the construction of a variety of gravity tests based on f. [3] In particular, from the Euler equation (1.44) we can infer the gravitational potential. Comparing this with an independent measurement of the convergence field κ, which is sensitive to $(\Phi+\Psi)$, one can construct an estimator for the gravitational slip $\eta = \Psi/\Phi$. Another example is the E_g statistics designed to test deviations from the Poisson equation (see e.g. [53]).

2.2.4 The Odd Multipoles in GR

On the other hand, the relativistic corrections carry important additional information. Using the GR relations for the transfer function eqs. (2.6)-(2.10) with the linear mapping (2.14), the dipole and octupole take the form

$$\begin{aligned}\xi^{(1)}_{\rm LM} = \left(\frac{D_1(z)}{D_1(0)}\right)^2 \frac{\mathcal{H}}{\mathcal{H}_0}\Bigg(&\frac{3}{5}(\alpha_{\rm L}-\alpha_{\rm M})f^2 - (b_{\rm L}\alpha_{\rm M} - b_{\rm M}\alpha_{\rm L})f \\ &+ (b_{\rm L}-b_{\rm M})\left(\frac{\dot{\mathcal{H}}}{\mathcal{H}^2} + f + \frac{\dot f}{f\mathcal{H}}\right) f - \frac{3}{2}(b_{\rm L}-b_{\rm M})\Omega_m\Bigg)\tau_1(d,0) \\ &+ {\rm W.A.}^{(-)},\end{aligned} \tag{2.55}$$

$$\xi^{(3)}_{\rm LM} = \frac{2}{5}\left(\frac{D_1(z)}{D_1(0)}\right)^2 \frac{\mathcal{H}}{\mathcal{H}_0}(\alpha_{\rm L}-\alpha_{\rm M})f^2\,\tau_3(d,0) + {\rm W.A.}^{(+)}, \tag{2.56}$$

where $\alpha_{\rm L,M}$ are the Doppler pre-factors (2.18) and $\Omega_m(z)$ is the matter density parameter. We have denoted the wide-angle correction as

$${\rm W.A.}^{(\pm)} = \pm\frac{2}{5}\frac{d}{r}\left(\frac{D_1(z)}{D_1(0)}\right)^2 (b_{\rm L}-b_{\rm M}) f\,\rho_2(d,0). \tag{2.57}$$

Finally, we can further simplify eq. (2.55) by means of the Euler equation (1.44), which removes the terms with $\dot f$ and $\Omega_m(z)$. Taking into account simultaneously the full form for the α's (eq. (2.18)), we can recast the dipole into the simpler form

$$\begin{aligned}\xi^{(1)}_{\rm LM} = \left(\frac{D_1(z)}{D_1(0)}\right)^2 \frac{\mathcal{H}}{\mathcal{H}_0}\Bigg(&\frac{3}{5}(\beta_{\rm L}-\beta_{\rm M})f^2 - (b_{\rm L}\beta_{\rm M} - b_{\rm M}\beta_{\rm L})f \\ &+ (b_{\rm L}-b_{\rm M})\left(\frac{\dot{\mathcal{H}}}{\mathcal{H}^2} + \frac{2}{r\mathcal{H}}\right) f\Bigg)\tau_1(d,0) + {\rm W.A.}^{(-)},\end{aligned} \tag{2.58}$$

---

[3] To be completely precise, the growth rate is degenerate with the Amplitude of perturbations in a ball of radius 8 Mpc/h, which is typically parametrized by the variance σ_8. Hence, galaxy surveys at late times actually measure the combination $f(z)\,\sigma_8(z)$.

where we have defined the factor

$$\beta_{\rm L}(z) = 5\, s_{\rm L}(z) \left(\frac{1}{r(z)\mathcal{H}(z)} - 1 \right) + f_{\rm L}^{\rm evol}(z). \tag{2.59}$$

This expression is consistent with the prefactor in the simplified $\Delta_{\rm REL}$ terms (see eq. (1.59)), including the corrections due to magnification and evolution biases. Independent measurements of the dipole and the octupole thus carry additional information on the population bias and the growth rate in the sense of showing a different degeneracy between the parameters, which could be useful in principle. However, their impact on the global constraints on $b_{\rm L}$ and f is small as they are already well measured by the even multipoles. Interestingly, the additional corrections due to magnification and evolution bias are purely relativistic effects that are only present in the odd multipoles. The expressions (2.58) and (2.56) imply that, in a given theory of gravity e.g. GR and provided precise measurements of $b_{\rm L}$ and f, we could break some of the degeneracies between $s_{\rm L}$ and $f_{\rm L}^{evol}$, making possible to obtain independent constraints on these parameters from galaxy clustering observations. This is a potential application of the odd multipoles that we explore in Part iv.

Additionally, the dipole shall play a crucial role in testing the theory of gravity on large scales. From eq.(2.55) we see that when we do not use the Euler equation (1.44), the contributions from the time evolution of the growth rate and $\Omega_m(z)$ are explicit. The latter is of utmost importance for us. Let us note that this contribution comes from the term $Q_{\rm LM}^{\delta\Psi}$ encoding the correlations of the matter density perturbations with the gravitational redshift effect. The dependence on $\Omega_m(z)$ arises from the Poisson equation relating the potentials to the density perturbations, but this will not be the case in a modified theory of gravity. Interestingly, the relevance of the dipole relies on the fact that any deviation of gravity affecting this contribution can be isolated from the dipole, in combination with the even multipoles measuring b and the growth. Since the correlation $Q_{\rm LM}^{\delta\Psi}$ is directly proportional to the potential, a measurement of this quantity represents a direct measurement of Ψ, provided we introduce a smart parametrization. This is another interesting potential application for the dipole: we can extract a direct measurement of Ψ that do not rely on the validity of the Euler equation. In other words, we can probe the evolution of the time perturbations, and hence the gravitational redshift, in a truly model independent way. Such measurement can be used to construct a new estimator for the gravitational slip $\eta = \Psi/\Phi$ by the combination with convergence measurements. As discussed earlier, correlations of number counts with lensing convergence provide a way to measure the *Weyl potential*, $(\Phi + \Psi)/2$. We develop such a method to test gravity for future surveys in Part ii. Finally, if our interest is confined within a particular gravity model, we can exploit the information contained in the gravitational redshift to improve constraints on the model parameters. In a given model the dipole contributions will have an explicit dependency on one or more of the model parameters which is likely to be different to the degeneracies present in the even multipoles, and hence can help in improving constraints on the model. In Part iii, we adopt the Effective Theory of Interacting Dark Energy framework and study the strength of the dipole in breaking existing degeneracies between the model parameters.

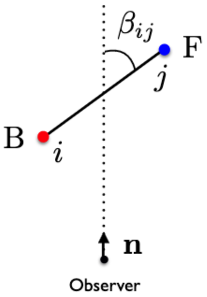

Figure 2.2: Reference system on which the dipole is measured. We depict the simplified situation after using the distant-observer approximation. In this coordinates, the dipolar contribution is zero when correlating two populations with the same luminosity. However, this is not the case in other reference systems (See ref. [47] for a discussion on this). We denoted the comoving separation between the points i and j as $d = |x_j - x_i|$. These diagrams are borrowed from refs. [7, 48]

2.2.5 *The estimator for the multipoles*

After finding the relevant observables affecting the large-scale distribution of galaxies at late-times, the observer must construct the appropriate estimators to isolate the different contributing effects, in a way that permits to combine them. As we have seen in the previous section, if we desire to probe the relativistic effects in the LSS we need to isolate the antisymmetric part of the 2-pt correlation function. This part will be non-zero only if we split the galaxy sample into multiple populations with different characteristics. We choose the main distinct characteristic to be the intrinsic luminosity. Then, the cross-correlation between two populations with L and M will be antisymmetric under the exchange of populations

$$\langle \Delta_L(\mathbf{x}_1, z_1)\Delta_M(\mathbf{x}_2, z_2)\rangle \neq \langle \Delta_L(\mathbf{x}_2, z_2)\Delta_M(\mathbf{x}_1, z_1)\rangle, \tag{2.60}$$

manifest by the existence of odd multipoles. The symmetric part is given by the even multipoles. The goal now would be to construct an *estimator* that isolate the different contributions. In order to extract the information from a galaxy survey map, we need to compute the correlation function for *all* the possible combinations of points in the sky. Let us label each sky pixel with i at which we count the number of galaxies at each luminosity, $N_\mathrm{L}(\mathbf{x}_i) = n_\mathrm{L}\mathcal{V}$, where $x_i = r_i\mathbf{n}_i$ is the position of the pixel in comoving coordinates, n_L denotes the number density and $\mathcal{V}$ is the survey volume. Note that we are neglecting the redshift evolution of the observables. All the quantities can be evaluated at the mean redshift, z, such that $n_\mathrm{L}(\mathbf{x}_i, z_i) \simeq n_\mathrm{L}(\mathbf{x}_i, z)$. We thus drop the dependency on z for clarity. The overdensity of galaxies with luminosity L at the pixel i is then

$$\delta n_\mathrm{L}(\mathbf{x}_i) = n_\mathrm{L}(\mathbf{x}_i) - d\bar{n}_\mathrm{L} = d\bar{n}_\mathrm{L} \cdot \Delta_\mathrm{L}(\mathbf{x}_i), \tag{2.61}$$

where $d\bar{n}_\mathrm{L}$ is the mean background number density of galaxies per pixel, with luminosity L, and $\Delta_\mathrm{L} = \Delta_\mathrm{L}^\mathrm{ST} + \Delta_\mathrm{L}^\mathrm{REL}$. Importantly, $d\bar{n}_\mathrm{L}$ depends on the size of the pixel, which we shall denote by l_p, as $d\bar{n}_{\rm L} = \bar{n}_{\rm L}\, l_p^3$ with $\bar{n}_{\rm L}$ denoting the background number density of L galaxies. The most general form for the estimator will thus be

$$\hat{\xi}_{\rm LM}(d,z) = \sum_{ij}\sum_{\rm LM} w_{ij{\rm LM}}\, \delta n_{\rm L}(\mathbf{x}_i)\delta n_{\rm M}(\mathbf{x}_j). \tag{2.62}$$

The kernel $w_{ij{\rm LM}}$ depends on the position of the pixels and on the luminosities. The specific properties will depend on the contribution we wish to extract. Generally speaking, it must be symmetric under the exchange of pixels i and j

$$w_{ij{\rm LM}} = w_{ji{\rm ML}}. \tag{2.63}$$

However, if the target is just the antisymmetric part we need the kernel to be antisymmetric under the exchange of positions and populations

$$w_{ij{\rm LM}} = -w_{ji{\rm LM}}, \tag{2.64}$$

$$w_{ij{\rm LM}} = -w_{ij{\rm ML}}. \tag{2.65}$$

In practice, we are interested in the multipoles of the estimator, which we can extract by the weighted integral (2.51). We consider the case of two populations, meaning L and M can only take two values. Respecting the antisymmetry in the odd multipoles, we can choose the kernel for the *multipoles estimator* such that

$$\hat{\xi}^{(\ell)}_{\rm LM}(d,z) = \frac{a^\ell_{\rm LM}}{2}\sum_{ij}\Big(\Delta_{\rm L}(\mathbf{x}_i)\Delta_{\rm M}(\mathbf{x}_j) + (-1)^\ell \Delta_{\rm M}(\mathbf{x}_i)\Delta_{\rm L}(\mathbf{x}_j)\Big) \times \mathcal{P}_\ell(\cos\mu_{ij})\delta_{\rm K}(d_{ij}-d), \tag{2.66}$$

where $\mu_{ij} = \cos\beta_{ij}$ is the angle formed by the line-of-sight $\mathbf{n}$ and the vector joining i and j in the distant-observer approximation (see fig. 2.2). The $a^\ell_{\rm LM}$ is a normalization factor that we need to choose carefully. We note that this estimator is a discrete quantity being $\delta_{\rm K}$ the Kronecker delta. The quantity we are after is the *mean* of the estimator, which represents the signal expected in a given survey, provided that the multipoles are written in term of Gaussian random fields. The mean of this estimator has to be understood as its expectation value, i.e. the average over all possible realizations. When taking the average, we have to insert the expectation values

$$\langle \Delta_{\rm L}(\mathbf{x}_i)\Delta_{\rm M}(\mathbf{x}_j)\rangle = \sum_{\ell=0}^{4} \xi^{(\ell)}_{\rm LM}(d_{ij})\,\mathcal{P}_\ell(\cos\beta_{ij}), \tag{2.67}$$

where $\xi^{(\ell)}_{\rm LM}(d_{ij})$ in GR are given by eqs. (2.52)-(2.56) (or eq.(2.58) for the simplified dipole). In addition, we take the continuous limit to solve the sum by replacing

$$\sum_{ij} \longrightarrow \frac{1}{l_p^6}\int d^3x_i\, d^3x_j, \qquad \delta_{\rm K}(d_{ij}-d) \longrightarrow l_p\,\delta^3(|\mathbf{x}_j - \mathbf{x}_i| - d), \tag{2.68}$$

where δ^3 is the three-dimensional Dirac delta. Then, after an appropriate change of variables to simplify the calculation, we find

$$\left\langle \hat{\xi}^{(\ell)}_{\rm LM}(d,z)\right\rangle = a^\ell_{\rm LM}\frac{2\pi\,\mathcal{V}\,d^2}{l_p^5}\sum_{\ell'=0}^{4}\xi^{(\ell')}_{\rm LM}(d,z)\int_{-1}^{1} d\mu\mathcal{P}_\ell(\mu)\mathcal{P}_{\ell'}(\mu). \tag{2.69}$$

The normalization factors are chosen by the requirement that the multipole ℓ has to be the expectation value of the estimator in the continuous limit, i.e. $\langle\hat{\xi}^{(\ell)}\rangle \to \xi^{(\ell)}$ when $N = \mathcal{V}/l_p^3 \to \infty$. Using the orthogonality relation for the Legendre polynomials (see Appendix A.2), we have for the normalization factors

$$a^{\ell}_{\mathrm{LM}} = \frac{(2\ell+1)}{4\pi}\frac{l_p^3}{\mathcal{V}}\left(\frac{l_p}{d}\right)^2 . \tag{2.70}$$

Here $\mathcal{V}$ denotes the volume of the survey under consideration. The multipole estimators represent the expected signal we might be able to detect from a spectroscopic survey. The even multipoles signals are thus isolated by setting $\ell = 0, 2, 4$ in the above expression. On the other hand, setting $\ell = 1, 3$ provide the isolated dipole and octupole signals including the wide-angle contaminations. An examination of the signs in eq. (2.57) indicates that wide-angle corrections decrease the effective dipole signal while increases the octupole signal, which might lead to biased estimations. We can actually use the other multipoles to remove them directly from the signal. In fact, we can construct an estimator for the factor $(b_{\mathrm{L}} - b_{\mathrm{M}})f$ out of separate measurements of the quadrupoles for the L and M populations. We are thus entitled to remove them from the signal observationally by modifying the dipole and octupole estimators given by eq. (2.69). For the dipole, we have [54]

$$\begin{aligned}\hat{\xi}^{(1)}_{\mathrm{LM}} =& \frac{3}{8\pi}\frac{l_p^3}{\mathcal{V}}\left(\frac{l_p}{d}\right)^2\sum_{ij}\left[\Delta_{\mathrm{L}}(\mathbf{x}_i)\Delta_{\mathrm{M}}(\mathbf{x}_j) - \Delta_{\mathrm{M}}(\mathbf{x}_i)\Delta_{\mathrm{L}}(\mathbf{x}_j)\right]\mathcal{P}_1(\mu_{ij})\delta_{\mathrm{K}}(d_{ij}-d) \\ &+ \frac{3}{10}\frac{5}{4\pi}\frac{d}{r}\frac{l_p^3}{\mathcal{V}}\left(\frac{l_p}{d}\right)^2\sum_{ij}\left[\Delta_{\mathrm{M}}(\mathbf{x}_i)\Delta_{\mathrm{M}}(\mathbf{x}_j) - \Delta_{\mathrm{L}}(\mathbf{x}_i)\Delta_{\mathrm{L}}(\mathbf{x}_j)\right]\mathcal{P}_2(\mu_{ij})\delta_{\mathrm{K}}(d_{ij}-d).\end{aligned} \tag{2.71}$$

The second line here completely removes the wide-angle corrections in the dipole. Similarly, we can remove the wide-angle corrections from the octupole as well by adding the same factor with opposite sign to the octupole estimator. This result is completely general and does not depend on the theory of gravity, but rather on how the information is spread across the multipoles. We have exploited the fact that multipoles are observationally independent so that we are allowed to combine them to isolate the sectors that are of more interest for us. Note that the second line in eq. (2.71) is built from $\langle\hat{\xi}^{(2)}_{\mathrm{LL}}\rangle$ (up to a prefactor $3d/(10r)$ introduced to match the prefactor in front of the wide-angle corrections in eq.(2.57)), which estimates the auto-correlations of a given population of galaxies.

2.3 HARMONIC POWER SPECTRA OF PHOTOMETRIC SURVEYS

The large-scale structure probes discussed so far, i.e. the galaxy clustering and the fluctuations in the number counts, contain crucial information about the theory of gravity on large scales, but they suffer from a subtle downside. They both probe the distribution of galaxies, i.e. *baryonic matter* alone, and not the total mass distribution. The way out discussed in sec. 1.2 was to introduce an additional free coefficient linking galaxies and matter, the galaxy bias. However, this connection needs to be modeled apart and can only be trusted on large scales.

The gravitational lensing effects discussed in sec. 1.3, distorting the shapes, positions and apparent magnitudes of distant galaxies, are other powerful probes of gravity which are sensitive to the entire total distribution along the line-of-sight. Interestingly, weak lensing statistics can be used to probe gravity with high accuracy even if the precise position of sources and lenses is uncertain. This task is possible thanks to current and future large imaging surveys, also known as *photometric surveys*. The term photometric comes from the fact that these type of surveys perform observations in several color bands that can trivially be assigned to the galaxies. These colors are then transformed into approximate redshift estimates, which receive the name of *photometric redshifts*. Hence, instead of a precise redshift measurement we have a probability distribution on where the objects in a given band might be located, possibly with a significant scatter around the true redshift. Consequently,in terms of comoving distances we work with a distribution formally given by [1, 2]

$$W(r) = \frac{1}{\mathrm{N_g}}\frac{d\mathrm{N_g}}{dr}, \tag{2.72}$$

where $\mathrm{N_g}$ denotes the total number of galaxies. This is often called *window* or *selection* function which enter as a weighting kernel into the observables equations. $W(r)$ is normalized to unity over the interval $r \in [0, \infty)$. However, phenomenologically speaking, the distribution drops to zero below and above some minimum and maximum distances. At low redshifts there are only a few galaxies just because the available volume is small. In addition, galaxies at very large distances are too faint to be detected. Let us note that we are ignoring the technical difficulties in obtaining the photometric redshifts and hence the distribution over distances $W(r)$. This is a challenging task that we assume has been adequately managed by the experimentalists.

The weak lensing maps provided by photometric surveys are also analyzed by means of correlation functions. However, in contrast with spectroscopic datasets, here we do not look at the three-dimensional 2-pt functions, but their *projections* on the sky. This is achieved by expanding in spherical harmonics (or in terms of Legendre polynomials) as in eq. (2.30). Hence, the quantities of interest here are the angular power spectra, or *harmonic power spectra*, denoted by $C_\ell(z_1, z_2)$ (see eq. (2.32)). The shape of the C_ℓ's will depend on the type of correlations under consideration. Importantly, the projection on the sky is actually restricted to the *light-cone*, which in turn imply that the harmonic power spectra generally involves the *unequal time* correlations. In addition, the Fourier transforms in the light-cone are not trivial and demand of an additional approximation.

2.3.1 *Photometric clustering and the Limber's approximation*

Let us consider the computation of the galaxy density angular power spectrum as an example. We denote by $\Delta_\mathrm{g}(\mathbf{n}, z)$ the projected overdensity of galaxies, which we write now as a superposition of many slices of the 3D galaxy density field at different distances r, weighted by the distance distribution

$$\Delta_\mathrm{g}(\mathbf{n}, z) = \int_0^\infty dr\, W(r)\, \delta_\mathrm{g}(r(z)\mathbf{n}, z). \tag{2.73}$$

We then take the 2-pt correlation function as $\langle \Delta_\mathrm{g}(\mathbf{n}_1, z_1)\Delta_\mathrm{g}(\mathbf{n}_2, z_2)\rangle$ and compute the sky projection according to eq. (2.30) in the configuration of fig. 2.1. We also Fourier-transform the density fields. The galaxy density harmonic power spectrum takes the form [1, 2]

$$C_\ell^{\rm gg}(z_1,z_2) = \frac{2}{\pi}\int_0^\infty dk\,k^2 \int_0^\infty dr_1\,W(r_1)j_\ell(kr_1)\int_0^\infty dr_2\,W(r_2)j_\ell(kr_2) \\ \times P_{\rm gg}(k,z_1,z_2), \quad (2.74)$$

where $P_{\rm gg}(k,z_1,z_2)$ is the more general unequal time galaxy density power spectrum. This expression is *exact* and general: given the three-dimensional power spectra and the selection function we can always compute the C_ℓ's using the above. However, it involves three nested integrals of the convolution of rapidly oscillatory functions with the full, unequal time power spectra which makes the calculation intricate. We proceed by using an approximation akin to the distant-observer approximation worked out in sec. 2.2. On small angular scales, $\ell \gg 1$, the angle subtended by the galaxy pairs contributing to $C_\ell^{\rm g}$ is roughly $\theta \sim 1/\ell$. In addition, for large ℓ the product of j_ℓ's has a sharp peak at $kr_1 \sim kr_2 \sim \sqrt{\ell(\ell+1)} \approx \ell + 1/2$. Provided that $P_{\rm gg}$ varies slowly within the narrow range over which the j_ℓ are non-zero, given by $\Delta k \sim 1/(\ell r)$, we can consider it has an approximately constant value. This is the so-called *Limber's approximation* [55–57]. A systematic derivation as a series expansion in powers of $(\ell+1/2)^{-1}$ is possible, here we just consider the approximation at first order [58]. Physically speaking, the Limber's approximation relies on the fact that large longitudinal modes do not contribute to the correlations due to cancellations along the line of sight. Only longitudinal modes with wave numbers of $\mu_k k \lesssim 1/r$ contribute, but they are much smaller than the relevant transverse wavenumbers, of order $1/r$. We can thus safely neglect the former and consider only the transverse modes, significantly simplifying by setting $r_1 = r_2$. Hence, we can take $P_{\rm gg}(k,z)$ out of the integral over k above and use the closure relation of spherical Bessel functions to find (see Appendix A.4)

$$C_\ell^{\rm g}(k_\ell,z) = \int_0^\infty \frac{dr}{r^2}\,W^2(r)\,P_{\rm gg}\left(k_\ell,z\right), \qquad k_\ell = \frac{\ell+1/2}{r}. \quad (2.75)$$

Here k_ℓ denotes the transverse modes. This is expected to be a good approximation for scales $\ell \geq 100$ [59]. An additional subtlety here is that the $P_{\rm gg}\left(k_\ell,z\right)$ entering here must include non-linear scales, at least to certain extent. While theoretical modeling the non-linear scales is a cumbersome task, it turns out that weak lensing measurements are sensitive to a non-negligible amount of information that is there hidden. The state-of-the-art on this topic is to extract the fully non-linear matter power spectrum from simulations, and use it to compute the predictions for the observables. We shall get back to this issue a bit later. Finally, having the C_ℓ we can compute the angular correlation function by computing the sum of the multipoles. On small scales, we can interpret the C_ℓ as the multipoles of the two-dimensional power spectrum on a plane and hence write the correlation function as

$$w^{\rm g}(\theta,z) = \int_0^\infty \frac{dl}{2\pi}\,\ell\,C_\ell^{\rm g}(k_\ell,z)\,J_0(\ell\theta). \quad (2.76)$$

This quantity is the projected correlation function measured by DES [60, 61]. In principle, it probes the same physics as the galaxy clustering $\xi(z,d)$, but the information is spread differently due to the projection within wide redshift slices. It has however a very large signal-to-noise thanks to the increased number of galaxies in a given z-slice. Interestingly, the BAO feature is in the angular correlation function is smoothed out due to the projection, but nevertheless still detectable [21]. In any case, the main interest of this projected clustering correlation function will be the combination with other weak lensing observables. As a final remark, here we are just mentioning Δ_g due to the fact that RSD and relativistic effects are strongly suppressed in photometric samples. The former have been added to the anlyses only very recently to assess their impact on future surveys, such as in Euclid [62]. On the other hand, the lensing contribution is significant and adding it to the signal has become the standard approach.

2.3.2 *The* 3×2*pt analysis*

More generally, we can define the angular power spectra associated to the correlations between any cosmological field similarly as in eq. (2.32). Let us denote by A and B the line-of-sight projections of the fields for which we compute the correlation function $\langle A(\mathbf{n}, z) B(\mathbf{n}, z') \rangle$. We have seen already how the theory of gravity always allows us to write any A and B in terms of the matter density field. Hence, by analogy with eq. (2.73) each component needs to be weighted with its correspondent window function $W^{\mathrm{A,B}}$. We are again obliged to introduce again a linear bias as the link between matter and galaxy density fluctuations, as we did in the spectroscopic analysis, $\delta_{\mathrm{g}}(\mathbf{n}, z) = b(z)\, \delta(\mathbf{n}, z)$. Using the Limber's approximation, we will find

$$C_\ell^{\mathrm{AB}}(k_\ell, z) = \int dz\, \frac{W^{\mathrm{A}}(z) W^{\mathrm{B}}(z)}{(1+z)\mathcal{H}(z) r^2(z)}\, P_{\delta\delta}(k_\ell, z), \tag{2.77}$$

where kernels $W^{\mathrm{A,B}}$ are defined by the mapping of each contribution to the matter power spectrum, and we have written the integral in terms of the redshift. We shall find them in brief. Also, $P_{\delta\delta}(k_\ell, z)$ here is the non-linear matter power spectrum, to which only transverse modes are considered.

In practice, photometric galaxy surveys provide a finite, small number of redshift bins given defined by the distributions extracted from the colors. We call them *tomographic bins*. Ideally, we will evaluate the information considering the correlations across different tomographic bins, which might be non-zero due to overlapping between the redshift distributions of adjacent bins. However, the z distributions are generally different. Hence, we need to compute the unequal-time angular power spectra $C^{\mathrm{AB}}(z_i, z_j)$ where i, j are labels denoting the individual tomographic bin. Mathematically, we can define

$$C_\ell^{\mathrm{AB}}(z_i, z_j) = \int dz\, n_i(z) \int dz'\, n_j(z')\, C_\ell^{\mathrm{AB}}(z, z') \tag{2.78}$$

The calculation can be done by using the definition of eq. (2.32) for the $C_\ell^{\mathrm{AB}}(z, z')$ in the integrand. By applying the Limber's approximation, the calculation will reduce to integrals over the redshift distributions as given by eq. (2.77). This is the theoretical basis to construct the widely known 3×2pt method to extract information out of weak lensing surveys, as done by DES collaboration (see e.g. [61, 63]). The number 3 means that three probes are being considered: the cosmic shear encoding the correlations in the shapes of galaxies, galaxy clustering and the cross-correlation between them, which receive the name of *galaxy-galaxy lensing* correlations.

In this work, we are mainly interested in the last two. We already discussed photometric galaxy clustering at the beginning of this Chapter. Starting from eq. (2.32) we

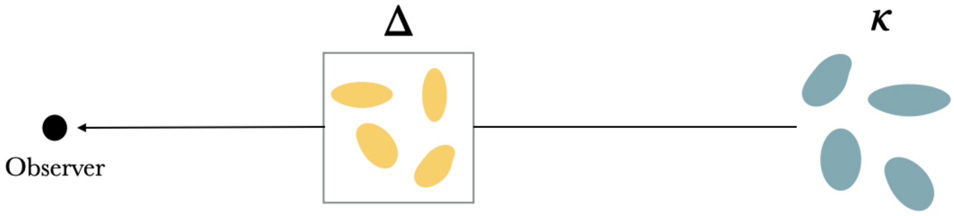

Figure 2.3: Schematic representation of galaxy-galaxy lensing correlations. The blue bubbles represent the galaxies that are lensed by the yellow ones, changing their apparent sizes and shapes. The information about this effect is described by a Gaussian field we call *convergence*, $\kappa(\mathbf{n}, z)$. We can then evaluate the convergence field κ (see eq. (1.52)) and the number counts fluctuations Δ (given by eq. (1.42)) at the redshifts of the lenses (yellow bubbles) to compute the galaxy-galaxy lensing correlator.

introduce eq.(2.33) and implement the Limber's approximation as for eq. (2.74). We will find the following kernel

$$W_i^{\delta}(z) = (1+z)\mathcal{H}(z)\, n_i(z)\, b_i(z), \tag{2.79}$$

to be introduced in eq. (2.77) to compute the photometric clustering. Here, $n_i(z)$ is the true galaxy distribution at the i-th bin and b_i the associated linear and scale-independent galaxy bias. Note that we are only considering the leading contribution to Δ, i.e. the correlations between κ and the density perturbations. The correlations between κ and RSD are subdominant for thick tomographic bins, and hence can be safely neglected (see ref. [59]). The same applies to the correlations involving the relativistic corrections due to Doppler terms and gravitational potentials appearing in eq. (1.52).

On top of photometric clustering, we will consider the so-called galaxy-galaxy lensing correlations. Observationally, we already have high significance measurements from several surveys, e.g. from DES [60, 61, 63, 64]. Conceptually speaking, these correlations probe the entire mass distribution around the lenses by correlating the lenses density with the shapes or magnification of the background galaxies. We can depict the situation as in fig. 2.3. In this work, our interest lies on the correlations of the convergence field with the galaxy number counts fluctuations given by eqs. (1.52) and (1.58), respectively. The only relevant contributions turn out to be the correlations between the first term in both equations, i.e. $\langle \delta(\mathbf{n}, z)\kappa(\mathbf{n}, z)\rangle$, as suggested by the discussion in sec.2.1.2. To be completely precise, in practice, surveys measure the shear, which can be linked to the lensing convergence term in κ when neglecting the relativistic effects, finding an exact relation between γ and κ_{g} (see sec. 1.3). Let us relax the notation in the subsequent discussion by using κ, but keeping in mind that we refer just to the lensing convergence term (first term in eq. (1.52)). In the 3×2pt formalism, we compute the quantity

$$C_\ell^{\delta\kappa}(z_i, z_j) = \int dz\, n_i(z) \int dz'\, n_j(z')\, C_\ell^{\delta\kappa}(z, z'), \tag{2.80}$$

where in $C_\ell^{\delta\kappa}(z, z')$ we introduce eq. (2.19) and the Fourier-Bessel transform of κ (first term in eq. (1.52)), given by

$$\Delta_\ell^{\kappa}(k, z) = -\frac{\ell(\ell+1)}{2} \int_0^r dr' \frac{r - r'}{r\, r'}\, T_{\Phi+\Psi}(k, z)\, j_\ell(kr'). \tag{2.81}$$

The factor $\ell(\ell+1)$ here arises from the action of the transverse Laplace operator Δ_Ω on the associated Legendre polynomial when projecting $\langle\delta\kappa\rangle$ on the sky via (2.30). (see Appendix A.3) This quantity is sensitive to the sum of the two metric potentials, often summarized as the Weyl potential $(\Phi+\Psi)/2$. Using the Poisson equation (1.15) and assuming no anisotropic stress such that $\Phi=\Psi$, it is easy to map the Weyl potential to the matter density distribution. This is explicit via the transfer function (2.9). Implementing the Limber's approximation and writing the resulting expression into the form of eq. (2.77), we find the kernel of the galaxy-galaxy lensing correlations to be

$$W_i^\kappa(z) = \frac{3}{2}\,\Omega_m(z)\mathcal{H}^2(z)\,r(z)\int_z^{z_{\max}} dz'\,n_i(z')\left(1-\frac{r(z)}{r(z')}\right), \tag{2.82}$$

The integral term here is weighted by the galaxy distribution in the correspondent tomographic bin, which is confined within a given $z_{\max}$. Everything together permits the calculation of the relevant power spectra, namely $C_\ell^{\delta\delta}$ and $C_\ell^{\delta\kappa}$. In the current 3×2pt analysis, the latter is obtained by combining eqs. (2.79) and (2.82) into (2.77), which gives the analytic form of the observables in GR. It is often parametrized in terms of the values of the cosmic parameters, using $\Omega_m(z)\mathcal{H}^2(z) = H_0^2\,\Omega_{m,0}(1+z)$ above (see e.g.[61]). In $C_\ell^{\delta\kappa}$ we find a degeneracy between the total matter density and the linear bias. However, the combination with $C_\ell^{\delta\delta}$ might break this degeneracy. In principle, we would also need to compute the $C^{\kappa\kappa}$ correlations to complete the 3×2pt recipe method, but it will not be necessary for our purposes. In fact, in Part ii we will show haw combining only the two probes discussed here permits us to construct an estimator for the evolution of the Weyl potential, which will be combined later with measurements of the gravitational potential Ψ from the multipoles of the spectroscopic 2-pt correlation function. However, it will be necessary to incorporate the treatment of the so-called *intrinsic alignments* (IA), which are usually regarded as contaminants to weak lensing measurements. In short, the IA encode correlations between galaxy shapes and the underlying distribution which are not due to propagation effects, but rather naturally arise from the galaxy formation processes. Therefore, they are *intrinsic* to the gravitational structure [65–67].

2.4 VARIANCE OF THE MULTIPOLES

The theory of Probability and Statistics establishes that the properties of any Gaussian field are completely characterized by the mean and the covariances of its variables. The latter encodes the joint variability of two random variables. It is said that when the covariance is positive these two random variables are linearly related and grow or decrease jointly, i.e they are *correlated*. In contrast, when the covariance is negative the linear relation between the variables imply that larger values of one correspond to smaller values of the second, i.e. they are *anti-correlated*. The generalization of this notion to multiple dimensions (for n Gaussian variables) leads to the *covariance matrix*. This must be a square, symmetric and semi-definite positive $n\times n$ matrix. The diagonal elements contain the variance of each variable (the covariance of each element with itself), while the off-diagonal terms encode the covariance between each pair of variables.

As we have extensively proved, the multipoles of the galaxy 2-pt correlation function are nothing else than combinations of the initial Gaussian random variables δ, $\mathbf{V}$, Ψ and Φ. Therefore, they are the signals we can directly measure from data. This signal is the mean of the correspondent estimators, given by eq. (2.69). Conceptually speaking, in Cosmology we can only probe one Universe, and more precisely a limited part of it. We are therefore using discrete tracers of the fields, and hence the estimators will never be exactly equal to their expectation values. The variation with respect to the mean is precisely encoded in the variances and covariances between the observables. We now turn to the computation of the associated covariance matrix encoding the joint variability of each pair of multipoles. We will follow refs. [46, 48, 54, 68, 69] but we aim to provide the generalized formulae for the two-populations scenario.

The covariance matrix is generally defined as the expectation value of the product of their deviations with respect to the product of their means. In the language of the multipoles estimators presented here, we define the multipoles covariance matrix as

$$\mathrm{COV}\left(\hat{\xi}^{(\ell)}_{\mathrm{LM}}, \hat{\xi}^{(\ell')}_{\mathrm{NP}}\right)(d,d') = \left\langle \hat{\xi}^{(\ell)}_{\mathrm{LM}}(d)\, \hat{\xi}^{(\ell')}_{\mathrm{NP}}(d') \right\rangle - \left\langle \hat{\xi}^{(\ell)}_{\mathrm{LM}}(d) \right\rangle \left\langle \hat{\xi}^{(\ell')}_{\mathrm{NP}}(d') \right\rangle . \tag{2.83}$$

Let us remind about the dependency on redshift we have previously neglected for simplicity, is of course present here. Using eq. (2.66) and the help of permutation rules for exchanging the pixel positions respecting the asymmetry property, i.e. $\mathcal{P}_\ell(\mu_{ij}) = (-1)^\ell \mathcal{P}_\ell(\mu_{ji})$, the second term above reduces to be:

$$\begin{aligned}\left\langle \hat{\xi}^{(\ell)}_{\mathrm{LM}}(d) \right\rangle \left\langle \hat{\xi}^{(\ell')}_{\mathrm{NP}}(d') \right\rangle = a^{\ell}_{\mathrm{LM}} a^{\ell'}_{\mathrm{NP}} \sum_{ijkq} &\left\langle \Delta_{\mathrm{L}}(\mathbf{x}_i)\Delta_{\mathrm{M}}(\mathbf{x}_j)\right\rangle \left\langle \Delta_{\mathrm{N}}(\mathbf{x}_k)\Delta_{\mathrm{P}}(\mathbf{x}_q)\right\rangle \\ &\times \mathcal{P}_\ell(\mu_{ij})\mathcal{P}_{\ell'}(\mu_{kq})\, \delta_{\mathrm{K}}(d_{ij}-d)\delta_{\mathrm{K}}(d_{kq}-d').\end{aligned} \tag{2.84}$$

The first term is an expectation value of four Δ, i.e. a 4th-order moment. However, using the Isserli's theorem of probability theory, better known in fundamental physics as the Wick's theorem when applied to quantum field operators, we can decompose any 4th-order moment as a sum of three products of 2-pt correlations, one of which cancels out with the products of means. This allows to write down the generalized expression for the multipoles covariance matrix in the form

$$\begin{aligned}\mathrm{COV}\left(\hat{\xi}^{(\ell)}_{\mathrm{LM}}, \hat{\xi}^{(\ell')}_{\mathrm{NP}}\right)(d,d') &= \frac{(2\ell+1)(2\ell'+1)}{(4\pi)^2}\frac{l_p^6}{\mathcal{V}^2}\left(\frac{l_p}{d}\right)^2\left(\frac{l_p}{d'}\right)^2 \\ \times \sum_{ijkq}\Big[&\left\langle \Delta_{\mathrm{L}}(\mathbf{x}_i)\Delta_{\mathrm{N}}(\mathbf{x}_k)\right\rangle \left\langle \Delta_{\mathrm{M}}(\mathbf{x}_j)\Delta_{\mathrm{P}}(\mathbf{x}_q)\right\rangle + (-1)^{\ell'}\left\langle \Delta_{\mathrm{L}}(\mathbf{x}_i)\Delta_{\mathrm{P}}(\mathbf{x}_k)\right\rangle \left\langle \Delta_{\mathrm{M}}(\mathbf{x}_j)\Delta_{\mathrm{N}}(\mathbf{x}_q)\right\rangle\Big] \\ &\times \mathcal{P}_\ell(\mu_{ij})\mathcal{P}_{\ell'}(\mu_{kq})\, \delta_{\mathrm{K}}(d_{ij}-d)\delta_{\mathrm{K}}(d_{kq}-d').\end{aligned} \tag{2.85}$$

In practice, the expectation values $\left\langle \Delta_{\mathrm{L}}(\mathbf{x}_i)\Delta_{\mathrm{M}}(\mathbf{x}_j)\right\rangle$ are not taken into account the fact that real surveys can only detect a finite number of objects. This demands the inclusion of an additional contribution called *Poisson term*, or simply *shot-noise* contribution, which scales with the inverse of the number of objects in a given pixel. In the two population scenario on which we work out the calculations, we assume that the populations are independent. Hence, we can write the observed 2-point correlation function as

$$\left\langle \Delta_{\mathrm{L}}(\mathbf{x}_i)\Delta_{\mathrm{M}}(\mathbf{x}_j)\right\rangle = C_{\mathrm{LM}}(d_{ij}) + \frac{1}{d\bar{n}_{\mathrm{L}}}\delta_{ij}\delta_{\mathrm{LM}}, \tag{2.86}$$

separating the pure *cosmic* contributions and the Poisson term. Here $d\bar{n}_{\mathrm{L}}$ is the background number density of galaxies with luminosity L *per pixel*. The product of two correlation functions in eq. (2.85) gives rise to three contributions. The first contribution is the *cosmic variance*, built upon products of the correlation function as defined in eq. (2.67). Conceptually speaking, the cosmic variance arises from the fact that we observe a finite volume. In most of previous analyses only the standard terms where considered in the computation of the covariance, finding a vanishing cosmic variance for the dipole (see e.g. [54]). However, a recent analysis shows that the odd multipoles pick a non-zero cosmic variance arising from the cross-correlation between relativistic and standard terms, which is dominant at large separations [39]. The second contributions to the covariance are the products $C_{\mathrm{LM}}(d_{ij})\,\delta_{kq}\delta_{\mathrm{NP}}/d\bar{n}_{\mathrm{N}}$, called the *mixed terms*, which combine cosmic variance and shot-noise. Finally, the pure shot-noise terms scaling with $1/n^2$ only contribute to the diagonal of the covariance matrix.

2.4.1 *Cosmic variance*

Let us provide the recipe for calculating the covariance matrix of the multipoles for the more general case of arbitrary populations. Inserting eq.(2.86) into (2.85) we find for the generic expression for the cosmic variance contributions

$$
\begin{aligned}
\mathrm{COV}_{\mathrm{CC}}\left(\hat{\xi}^{(\ell)}_{\mathrm{LM}}, \hat{\xi}^{(\ell')}_{\mathrm{NP}}\right)(d,d') = {} & \frac{(2\ell+1)(2\ell'+1)}{(4\pi)^2}\,\frac{l_p^6}{\mathcal{V}^2}\left(\frac{l_p}{d}\right)^2\left(\frac{l_p}{d'}\right)^2 \\
& \times \sum_{ijkq}\Big[C_{\mathrm{LN}}(d_{ik})C_{\mathrm{MP}}(d_{jq}) + (-1)^{\ell'} C_{\mathrm{LP}}(d_{ik})C_{\mathrm{MN}}(d_{jq})\Big] \\
& \qquad \times \mathcal{P}_{\ell}(\mu_{ij})\mathcal{P}_{\ell'}(\mu_{kq})\,\delta_{\mathrm{K}}(d_{ij}-d)\delta_{\mathrm{K}}(d_{kq}-d').
\end{aligned}
\tag{2.87}
$$

The computation of the even and odd multipoles cosmic variances can be performed separately. In fact, the cross-variances between even and odd multipoles are zero by construction.

Let us write down the pure cosmic term arising from the standard terms as

$$
\begin{aligned}
C^{\mathrm{ST}}_{\mathrm{LM}}(d_{ij}) &= \left\langle \Delta^{\mathrm{ST}}_{\mathrm{L}}(\mathbf{x}_i)\Delta^{\mathrm{ST}}_{\mathrm{M}}(\mathbf{x}_j)\right\rangle \\
&= \sum_a \frac{1}{(2\pi)^3}\int d^3k\, e^{i\mathbf{k}(\mathbf{x}_j-\mathbf{x}_i)}\,P_{\delta\delta}(k)\,\mathcal{C}^{\mathrm{ST}}_a(\mathrm{L},\mathrm{M})\mathcal{P}_a(\mu),
\end{aligned}
\tag{2.88}
$$

where $a = 0,\,2,\,4$. The dependency on redshift is encoded in the population-dependent coefficients

$$\mathcal{C}^{\mathrm{ST}}_0(\mathrm{L},\mathrm{M}) = b_{\mathrm{L}}b_{\mathrm{M}} + (b_{\mathrm{L}}+b_{\mathrm{M}})\frac{f}{3} + \frac{f^2}{5}, \tag{2.89}$$

$$\mathcal{C}^{\mathrm{ST}}_2(\mathrm{L},\mathrm{M}) = \frac{2}{3}(b_{\mathrm{L}}+b_{\mathrm{M}})f + \frac{4}{7}f^2, \tag{2.90}$$

$$\mathcal{C}^{\mathrm{ST}}_4(\mathrm{L},\mathrm{M}) = \frac{8}{35}f^2. \tag{2.91}$$

Hence, the symmetry under the exchange of L, M explicitly shows that $\mathrm{COV}_{\mathrm{CC}}$ vanishes for $\ell = 1,\,3$. However, from the crossed correlations between standard and relativistic contributions, we find

$$
\begin{aligned}
C^{\mathrm{REL}}_{\mathrm{LM}}(d_{ij}) &= \left\langle \Delta^{\mathrm{ST}}_{\mathrm{L}}(\mathbf{x}_i)\Delta^{\mathrm{REL}}_{\mathrm{M}}(\mathbf{x}_j)\right\rangle + \left\langle \Delta^{\mathrm{REL}}_{\mathrm{L}}(\mathbf{x}_i)\Delta^{\mathrm{ST}}_{\mathrm{M}}(\mathbf{x}_j)\right\rangle \\
&= \sum_a \frac{1}{(2\pi)^3}\int d^3k\, e^{i\mathbf{k}(\mathbf{x}_j-\mathbf{x}_i)}\,P_{\delta\delta}(k)\left(i\frac{\mathcal{H}}{k}\right)\mathcal{C}^{\mathrm{REL}}_a(\mathrm{L},\mathrm{M})\mathcal{P}_a(\mu),
\end{aligned}
\tag{2.92}
$$

where $a = 1, 3$ and the correspondent redshift dependent factors take the form

$$\mathcal{C}_1^{\mathrm{REL}}(\mathrm{L},\mathrm{M}) = \left[\tilde{\alpha}_{\mathrm{L}}\left(b_{\mathrm{M}} + \frac{3}{5}f\right) - \tilde{\alpha}_{\mathrm{M}}\left(b_{\mathrm{L}} + \frac{3}{5}f\right)\right], \tag{2.93}$$

$$\mathcal{C}_3^{\mathrm{REL}}(\mathrm{L},\mathrm{M}) = \frac{2}{5}(\tilde{\alpha}_{\mathrm{L}} - \tilde{\alpha}_{\mathrm{M}})f. \tag{2.94}$$

Here $\tilde{\alpha}_{\mathrm{L}} = 1 - \alpha_{\mathrm{L}}$ is given by eq. (2.18). We explicitly see the antisymmetry characteristic of the relativistic contributions. C^{REL} vanishes in the single population case where the biases are equal. Additionally, the cosmic variance due to the relativistic corrections is also zero for covariances of the even multipoles with distinct populations. Inserting eq. (2.88) or (2.92) into (2.87) and taking the continuum limit we can compute the sums over pixels positions. The calculation involves some change of variables and tricks exploiting the properties of exponential, delta functions and Spherical harmonics. Precise details can be found in ref.[46]. In summary, we find a compact expression for the standard terms contribution to the cosmic variance

$$\begin{aligned}\mathrm{COV}_{\mathrm{CC}}^{\mathrm{ST}}\left(\xi_{\mathrm{LM}}^{(\ell)}, \xi_{\mathrm{NP}}^{(\ell')}\right)(d,d') &= \frac{1}{\mathcal{V}}\left(\frac{D_1(z)}{D_1(0)}\right)^2 (-1)^{\frac{\ell-\ell'}{2}}(-1)^{\ell+\ell'} \\ &\times \frac{1}{4}\sum_{ab}\left[\mathcal{C}_a^{\mathrm{ST}}(\mathrm{L},\mathrm{N})\mathcal{C}_b^{\mathrm{ST}}(\mathrm{M},\mathrm{P}) + \mathcal{C}_a^{\mathrm{ST}}(\mathrm{L},\mathrm{P})\mathcal{C}_b^{\mathrm{ST}}(\mathrm{M},\mathrm{N})\right]\mathcal{G}(\ell,\ell',a,b)\,\mathcal{I}(d,d'),\end{aligned} \tag{2.95}$$

where ℓ, ℓ', a, b run only over the even values 0, 2, 4. In addition, we have defined the integrals

$$\mathcal{G}(\ell,\ell',a,b) = \int_{-1}^{1} d\mu\, \mathcal{P}_\ell(\mu)\mathcal{P}_{\ell'}(\mu)\mathcal{P}_a(\mu)\mathcal{P}_b(\mu), \tag{2.96}$$

$$\mathcal{I}(d,d') = \frac{(2\ell+1)(2\ell'+1)}{\pi^2}\int dk k^2\, P_{\delta\delta}^2(k, z_* = 0)\, j_\ell(kd) j_{\ell'}(kd'). \tag{2.97}$$

The last one encodes the information about separation scales, and it has been written in terms of the power spectrum at $z_* = 0$. Let us recall that we can compute it at any redshift by using the linear scaling involving the growth factor of matter perturbations (2.14).

A similar expression can be found for the relativistic contributions to the cosmic variance

$$\begin{aligned}\mathrm{COV}_{\mathrm{CC}}^{\mathrm{REL}}\left(\xi_{\mathrm{LM}}^{(\ell)}, \xi_{\mathrm{NP}}^{(\ell')}\right)(d,d') &= \frac{1}{\mathcal{V}}\left(\frac{D_1(z)}{D_1(0)}\right)^2\left(\frac{\mathcal{H}}{\mathcal{H}_0}\right)^2 (-1)^{\frac{\ell-\ell'}{2}}(-1)^{\ell+\ell'} \\ &\times \frac{1}{4}\sum_{ab}\left[\mathcal{C}_a^{\mathrm{REL}}(\mathrm{L},\mathrm{N})\mathcal{C}_b^{\mathrm{REL}}(\mathrm{M},\mathrm{P}) - \mathcal{C}_a^{\mathrm{REL}}(\mathrm{L},\mathrm{P})\mathcal{C}_b^{\mathrm{REL}}(\mathrm{M},\mathrm{N})\right]\mathcal{G}(\ell,\ell',a,b)\,\mathcal{J}(d,d'),\end{aligned} \tag{2.98}$$

where ℓ, ℓ', a, b run only over the odd values 1, 3, and we have defined the last integral to be

$$\mathcal{J}(d,d') = \frac{(2\ell+1)(2\ell'+1)}{\pi^2}\int dk \mathcal{H}_0^2\, P_{\delta\delta}^2(k, z_* = 0)\, j_\ell(kd) j_{\ell'}(kd'). \tag{2.99}$$

Here we have introduced the factor $\mathcal{H}_0^2$ to suppress the dimensions of $\mathcal{H}$. Comparing with eq.(2.97), we see that the integrand of $\mathcal{I}(d,d')$ is k^2 times larger, which makes $\mathcal{J}(d,d')$ much smaller. This of course means that even for the non-zero combinations in a multiple population scenario, we are mostly entitled to neglect $\mathrm{COV}_{\mathrm{CC}}^{\mathrm{REL}}$ against $\mathrm{COV}_{\mathrm{CC}}^{\mathrm{ST}}$. This is not the case however for the odd multipoles, where $\mathrm{COV}_{\mathrm{CC}}^{\mathrm{REL}}$ will be comparable to the mixed term contributions at small separations.

2.4.2 *Mixed contributions*

The product between 2-pt functions and the shot-noise gives rise to the mixed terms contributions to the covariance. It is easy to see that the insertion of eq.(2.86) into (2.85) gives two sums that can be reduced to one by permutations of i, j and k, q indices. In addition, one of the original sum indices is suppressed by the δ_{ij} in the Poisson terms. This yields

$$
\begin{aligned}
\mathrm{COV}_{\mathrm{CP}}\left(\xi^{(\ell)}_{\mathrm{LM}}, \xi^{(\ell')}_{\mathrm{NP}}\right)(d, d') = {} & \frac{(2\ell+1)(2\ell'+1)}{(4\pi)^2}\frac{l_p^6}{\mathcal{V}^2}\left(\frac{l_p}{d}\right)^2\left(\frac{l_p}{d'}\right)^2 \\
& \times \sum_{ijk}\Bigg[\frac{\delta_{\mathrm{MP}}}{d\bar{n}_{\mathrm{M}}}C_{\mathrm{LN}}(d_{ik}) + (-1)^{\ell'}\frac{\delta_{\mathrm{MN}}}{d\bar{n}_{\mathrm{M}}}C_{\mathrm{LP}}(d_{ik}) \\
& \qquad + (-1)^{\ell+\ell'}\left(\frac{\delta_{\mathrm{LN}}}{d\bar{n}_{\mathrm{L}}}C_{\mathrm{MP}}(d_{ik}) + (-1)^{\ell'}\frac{\delta_{\mathrm{LP}}}{d\bar{n}_{\mathrm{L}}}C_{\mathrm{MN}}(d_{ik})\right)\Bigg] \\
& \qquad \times \mathcal{P}_{\ell}(\mu_{ij})\mathcal{P}_{\ell'}(\mu_{kj})\,\delta_{\mathrm{K}}(d_{ij}-d)\delta_{\mathrm{K}}(d_{kj}-d').
\end{aligned}
\tag{2.100}
$$

where the factor $(-1)^{\ell+\ell'}$ arises from the permutation of indices. In contrast with the cosmic variance which depends only on the survey volume $\mathcal{V}$, the mixed terms scale with the inverse of the average number density of galaxies per pixel. Moreover, it is only linear in C_{LN}, and hence linear in the power spectrum.

We solve the sum by going to the continuum limit. In this case, the relativistic corrections to the variance are strongly subdominant at all redshifts and separations with respect to the standard terms contributions, which are present in both even and odd multipoles. Hence, we just consider C^{ST} as defined in eq.(2.88). After a similar calculation than for the cosmic variance, we find

$$
\begin{aligned}
\mathrm{COV}_{\mathrm{CP}}\left(\xi^{(\ell)}_{\mathrm{LM}}, \xi^{(\ell')}_{\mathrm{NP}}\right)(d, d') = {} & \frac{l_p^3}{\mathcal{V}}\left(\frac{D_1(z)}{D_1(0)}\right)^2(-1)^{\frac{\ell-\ell'}{2}}(-1)^{\ell+\ell'} \\
& \times \frac{1}{8}\sum_{a}\Bigg[\frac{\delta_{\mathrm{MP}}}{d\bar{n}_{\mathrm{M}}}\mathcal{C}^{\mathrm{ST}}_{a}(\mathrm{L},\mathrm{N}) + (-1)^{\ell'}\frac{\delta_{\mathrm{MN}}}{d\bar{n}_{\mathrm{M}}}\mathcal{C}^{\mathrm{ST}}_{a}(\mathrm{L},\mathrm{P}) \\
& \qquad + (-1)^{\ell+\ell'}\left(\frac{\delta_{\mathrm{LN}}}{d\bar{n}_{\mathrm{L}}}\mathcal{C}^{\mathrm{ST}}_{a}(\mathrm{M},\mathrm{P}) + (-1)^{\ell'}\frac{\delta_{\mathrm{LP}}}{d\bar{n}_{\mathrm{L}}}\mathcal{C}^{\mathrm{ST}}_{a}(\mathrm{M},\mathrm{N})\right)\Bigg] \\
& \times \mathcal{G}(\ell,\ell',a,0)\,\mathcal{K}(d,d').
\end{aligned}
\tag{2.101}
$$

Here a runs over the even values and ℓ, ℓ' can take any value between 0 and 4. However, orthogonality of the Legendre polynomials implies that the cross-correlations between odd and even multipoles are zero. In addition, we have defined the integrals

$$
\mathcal{K}(d,d') = \frac{2(2\ell+1)(2\ell'+1)}{\pi^2}\int dk k^2\, P_{\delta\delta}(k, z_* = 0)\, j_{\ell}(kd) j_{\ell'}(kd'). \tag{2.102}
$$

This is therefore subdominant with respect to $\mathcal{I}(d,d')$, which is quadratic in the power spectrum. Similarly, the balance between integrating $k^2 P_{\delta\delta}$ or $P^2_{\delta\delta}$ gives the hierarchy between the relativistic cosmic variance and the mixed terms, respectively. In this case, the former is comparable to the latter at small separations, but becomes subdominant at large separations $(d,\ d')$.

2.4.3 *Pure shot-noise*

The 'square' of the Poisson term in eq.(2.86) generates the shot-noise contributions to the covariance matrix. This contribution scales with the inverse of the number of objects. Future surveys are expected to significantly reduce the impact of the shot-noise thanks to a significant increase in the number of detected objects. However, we need to take into account this additional source of variance to be fully consistent. The odd multipoles will still be very sensitive to shot-noise at large redshifts, due to the reduced number of pairs. The last contribution to COV obtained from the insertion of eq.(2.86) into (2.85) takes the form

$$\begin{aligned} \mathrm{COV_P}\left(\xi^{(\ell)}_{\mathrm{LM}}, \xi^{(\ell')}_{\mathrm{NP}}\right)(d,d') &= \frac{(2\ell+1)(2\ell'+1)}{(4\pi)^2}\frac{l_p^6}{\mathcal{V}^2}\left(\frac{l_p}{d}\right)^2\left(\frac{l_p}{d'}\right)^2 \qquad (2.103) \\ &\times \sum_{ik}\frac{1}{d\bar{n}_{\mathrm{L}}d\bar{n}_{\mathrm{M}}}\left[\delta_{\mathrm{LN}}\delta_{\mathrm{MP}} + (-1)^{\ell'}\delta_{\mathrm{LP}}\delta_{\mathrm{MN}}\right]\mathcal{P}_\ell(\mu_{ik})\mathcal{P}_{\ell'}(\mu_{ik})\delta_{\mathrm{K}}(d_{ik}-d)\delta_{\mathrm{K}}(d_{ik}-d'). \end{aligned}$$

The sums over four indices are reduced to sums over two indices thanks to the products $\delta_{ij}\delta_{kq}$. We thus transform the sum to integrals by taking the continuum limit. Using the orthogonality relation of the Legendre polynomials, we find the shot-noise contributions for generic populations to be

$$\mathrm{COV_P}\left(\xi^{(\ell)}_{\mathrm{LM}}, \xi^{(\ell')}_{\mathrm{NP}}\right)(d,d') = \frac{2\ell+1}{4\pi}\frac{l_p^5}{\mathcal{V}}\frac{1}{d\bar{n}_{\mathrm{L}}d\bar{n}_{\mathrm{M}}}\frac{\delta_{\ell\ell'}\delta_{dd'}}{d^2}\left[\delta_{\mathrm{LN}}\delta_{\mathrm{MP}} + (-1)^{\ell'}\delta_{\mathrm{LP}}\delta_{\mathrm{MN}}\right]. \qquad (2.104)$$

This result shows that the shot-noise is a diagonal contribution which is only non-zero in the multipoles variances ($\ell = \ell'$). Additionally, from the δ's inside the square brakets we see that for distinct populations there is no shot-noise contribution to the multipoles covariance. This is true provided we have assumed the population to be independent, but it shall not be the case if the populations are not completely independent of each other. In Part iv we will adopt a more general scenario in which we consider a set of populations that overlap to some extent. This modifies the shot-noise and mixed terms contributions, while the cosmic variance terms remain the same.

Importantly, we computed here the multipoles covariance matrix in General Relativity. The matrix structure is implicit in the integrals with arguments (d, d'). However, the derivation presented here is completely general in the theory sense. The covariance matrix in any other gravity model is computed by finding the $\mathcal{C}_a^{\mathrm{ST,REL}}$ coefficients according to the alternative model's 2-pt correlation function. Even so, in practice we will assume that the fiducial covariance matrix is that of GR, regardless if the signal fiducial model is obtained from any other gravity theory. Assuming Gaussianity, the GR covariance matrix remains valid if we limit our scope to analyses using fiducials sufficiently close to GR.

Finally, let us mention that we are not including here the analytic computation of the covariance matrix associated to the harmonic power spectra, $C_\ell(z, z')$. The formal definition is analogous to eq. (2.83), replacing $\left\langle \xi^{(\ell)}_{\mathrm{LM}} \right\rangle(z, d)$ by the correspondent estimators for the $C_\ell(z, z')$. Similar techniques and integrals are involved in the calculation. However, the covariance of the harmonic power spectra involves a few thousands of ℓ's. Nevertheless, we will rely on well-tested and accurate numerical codes that are able to compute both of these covariances fast and with high accuracy when needed.

2.5 INFERENCE AND ANALYSIS

The properties of the Large-Scale structure at late times can thus be inferred from the data by using the estimators $\left\langle \xi^{(\ell)}_{\mathrm{LM}} \right\rangle (z, d)$ to extract the spectroscopic signal, or estimators based on the $C_\ell(z_i, z_j)$ to measure the photometric spectra. In addition, the covariance matrix incorporates the information regarding the relations between the observables and the uncertainty on the estimators. Then, provided we have at our disposal a galaxy survey dataset, we can measure the theory parameters and construct tests to probe the properties of gravity. This can be done e.g. by adopting a Bayesian approach, i.e. assuming a *prior* knowledge about the expected measurements we can obtain a *posterior* probability distribution for the parameters, encoding the measured parameters' mean values and how much they are allowed to vary with respect to the mean, while maintaining the consistency of the theory. [4] However, we do not always have an appropriate dataset. In this case, we can still test our theory by creating mock data (e.g. from simulations). Alternatively, if we know the technical specifications of a survey, we can *forecast* the expected precision in constraining the theory's parameter space. This is still of importance in assessing if we are able to distinguish gravity models even if we cannot know the precise parameter values.

In this Thesis, we adopt the Bayesian approach and perform *forecasts* for future surveys, with the aim to investigate the capability of the 2-point correlation function odd multipoles in constraining gravity models. Current surveys are not able to measure them, but the coming generation of Stage IV galaxy surveys will. It is thus of utmost interest to study in advance which kind of physics we will be able to test from these new observations, modulo observational systematics and difficulties with which we trust the experimentalists will be able to deal with. We devote this section to introduce the two techniques we adopted for this task across the projects included in this work.

Generally speaking, the crucial ingredient of any Bayesian analysis is the *likelihood function*. This is the name given to the joint probability density of observing some dataset $\mathcal{X}$ assuming $\boldsymbol{\theta}$ is the set of parameter values. It is thus a conditioned probability, often denoted by $\mathcal{L}(\mathcal{X}|\boldsymbol{\theta})$. Then, given that we have a prior probability distribution on $\boldsymbol{\theta}$, the posterior probability distribution is such that

$$P(\boldsymbol{\theta}|\mathcal{X}) \propto \mathcal{L}(\mathcal{X}|\boldsymbol{\theta})\, P(\boldsymbol{\theta}). \tag{2.105}$$

Here $P(\boldsymbol{\theta}|\mathcal{X})$ is read as the probability of measuring the parameters $\boldsymbol{\theta}$ provided $\mathcal{X}$ is the dataset. When we do not have a dataset, we can take the theoretical prediction as the expected signal. Therefore, constraining the parameter space is done through the likelihood function, from which we will then extract the actual constraints on the model parameters.

2.5.1 *Fisher Analysis*

A first approximation to Bayesian inference can be to study the *Fisher information* of the observables. This is defined as the amount of information that any given combination of random variables carry about the parameter space defined by the underlying model. In

---

[4] The alternative would be to adopt the *frequentist* approach, which assumes the model parameters as fixed and aims to predict a decision drawn out a significance test or a confidence interval.

other words, the Fisher information encodes the variance of the observed parameters. Formally speaking, the Fisher information is evaluated by means of the *Fisher matrix*, defined as the Hessian of the likelihood. We have thus to compute the expectation value of the second derivative of the logarithm of the likelihood with respect to the parameters of the model:

$$\mathcal{F}_{\alpha\beta} = \left\langle -\frac{\partial^2 \ln(\mathcal{L})}{\partial\theta_\alpha \partial\theta_\beta} \right\rangle . \tag{2.106}$$

Here θ_α are the elements of the parameter vector $\boldsymbol{\theta}$. Assuming we work with a Gaussian likelihood, the Fisher matrix can be written in terms of the observables covariance matrix [5]

$$\mathcal{F}_{\alpha\beta} = \sum_{ij} \frac{\partial \bar{\mathcal{X}}_i}{\partial\theta_\alpha} \left(\mathrm{COV}^{-1}\right)_{ij} \frac{\partial \bar{\mathcal{X}}_j}{\partial\theta_\beta} , \tag{2.107}$$

where $\bar{\mathcal{X}}$ is the mean of the data vector (or the signal vector) and COV is the covariance matrix of the observables. These correspond to the multipoles of the 2-point correlation function in spectroscopic galaxy clustering analysis. We computed both signals and covariance analytically in the previous sections. In the case of photometric surveys, the signal vector will be formed by the $C_\ell(z,z')$'s and COV will be the correspondent covariance matrix. More details about the relevant datasets and covariances in each of the projects will be discussed in the correspondent Parts of this Thesis. However, let us stress here that, because of our assumption of the ΛCDM model as our fiducial, we always use GR to compute these covariances and assume it is reasonable to use it even if we consider fiducials that are not too far apart from GR. This is a way to assume that the correlations between the observers will not be strongly dependent on the theory of gravity, although a different amplitude can be expected.

The Fisher matrix is thus an interesting mathematical object encoding the variance of the target parameters. In fact, the inverse of the Fisher information is a lower bound on the variance of an estimator. This is the so-called *Cramér-Rao bound* in Statistics. One can show that we can simply estimate the covariance matrix of the model parameters as the inverse of the Fisher matrix

$$\mathrm{C}_{\alpha\beta} = \left(\mathcal{F}^{-1}\right)_{\alpha\beta} . \tag{2.108}$$

In the language of Statistics theory, this covariance corresponds to the combination of parameters that maximize the likelihood function, i.e. the values that are more likely to be observed provided the given data. The diagonal of C contains the square of the variance of the parameters. Hence, the forecasted 1σ uncertainty on a given parameter θ_α is computed by taking the square root

$$\sigma(\theta_\alpha) = \sqrt{\mathrm{C}_{\alpha\alpha}}. \tag{2.109}$$

In addition, the off-diagonal terms of C encode the covariances between the parameters, which provide an estimate for the confidence regions constraining the size of the parameter space to the hypervolume allowed by the data. However, let us stress the importance

---

[5] We also assume that the covariance of the observables is not dependent on the model parameters, which is actually not true. However, the leading order contribution will still be this equation. We assume the additional corrections due to the dependency of the covariance on the model parameters to be negligible.

of the assumption of Gaussianity (both on the prior and posterior distributions) is crucial for taking as valid the constraints given by a Fisher analysis. On top of that, in eq. (2.107) we have also implicitly assumed that the derivatives of the data vector $\bar{\mathcal{X}}$ are smooth and well-behaved functions. However, it is often the case that this idealistic fully Gaussian scenario does not apply. If the actual posterior distribution for the parameters is far from Gaussianity, $\mathcal{F}$ will not be valid, and we cannot trust anymore the forecasted constraints. If this is the case, we need to adopt a more sophisticated approach to obtain the expected confidence regions.

2.5.2 *MCMC*

An alternative (but compatible) Bayesian inference technique is to estimate the posterior probability distributions and the correspondent credible intervals via the likelihood function with the so-called *Markov Chain Monte Carlo* methods. The idea is to explore numerically the parameter space defined by a set of continuous random variables by drawing samples from a given probability distribution in a stochastic manner [6], and assign a probability for each sample to belong to the physical model. Computing the probabilities for each set of samples, known in this context as *chains* or *walks*, means to estimate the likelihood function. This is computationally expensive, as it requires to compute the expected signal at each point in the parameter space and compare the theoretical prediction with the data.

Assuming that the likelihood is Gaussian and neglecting the dependency of the observables covariance matrix on the theory parameters, one can show that the log likelihood can be written as

$$\ln \mathcal{L}(\mathcal{X}|\boldsymbol{\theta}) = -\frac{1}{2}\left(\hat{\mathcal{X}} - \bar{\mathcal{X}}^{\rm th}\right)^T \mathrm{COV}^{-1}\left(\hat{\mathcal{X}} - \bar{\mathcal{X}}^{\rm th}\right). \tag{2.110}$$

Here $\hat{\mathcal{X}}$ represents the observed, or estimated, signal and $\bar{\mathcal{X}}^{\rm th}$ is the theoretical prediction for the mean, i.e. the signal as a function of the model parameters. From the likelihood function, it is easy to compute the probability density for each sample by using Bayes theorem. Then, an example of such an algorithm is the so-called *Metropolis-Hastings algorithm*, which works as follows. We randomly pick a point in the parameter space and evaluate the likelihood to compute the probability density via the Bayes theorem. Next, a second point is randomly drawn following a chosen distribution (e.g. uniform or Gaussian distribution) with respect to the initial point. [7] Then, we compute the likelihood for the second sample and compare with the first. If the probability for the second sample is larger or equal to the probability density for the first sample, we add it to the chain and continue from 'here'. If not, we jump to the next point and check the ratio of probabilities. The algorithm goes on drawing samples and comparing probability densities until a stationary state is reached. This stationary state tends to the target distribution, i.e. the posterior, for sufficiently large number of samples in the chain, and we say that the algorithm has *converged*. Also, stochasticity ensures that the algorithm

---

[6] Stochasticity in this context is what provides *Markov Chain* part of the name. A markov chain is a particular type of stochastic process in which the probability of an event depends solely in the immediately previous event.

[7] This feature is the origin of the *Monte Carlo* part of the name. We 'throw a die', i.e. use a random number generator, to produce the samples.

has *no memory*, so that the last elements of the chain are uncorrelated with the initial ones.

Finally, the parameter covariance matrices and the forecast uncertainties can be extracted from the posterior distribution of the parameters once the chains have converged. If the converged chain has n samples, then the *best fit* parameter is approximately given by the mean of the predicted values for each sample (when n is large), that comes together with the correspondent sample variance

$$\bar{\theta}_\alpha = \frac{1}{n}\sum_{i=1}^{n}\theta_\alpha^i, \qquad \sigma(\theta_\alpha) = \frac{1}{n-1}\sum_{i=1}^{n}(\theta_\alpha^i - \bar{\theta}_\alpha)^2. \tag{2.111}$$

In the context of the projects presented in this Thesis, each sample is a particular combination of model parameters values. At each point in the parameter space, we will need to compute the multipoles of the correlation function (or the C_ℓ's) and compare the prediction with the fiducial model. In contrast with the Fisher analysis approach, the MCMC does not need the assumption that the posterior distributions are Gaussian, because the algorithm itself provides the posterior distributions, on top of the mean and variances of the parameters. In this sense, when expecting intricate degeneracies among the model parameters, the MCMC is the preferred approach due to its ability to properly capture them. We can then construct the parameters covariance matrices out of the $\sigma(\theta_\alpha)$ and the associated Fisher matrix by computing the inverse. This approach will be used in Parts ii and iii. In the first application, we will use an MCMC algorithm to compute the parameters covariances out of the harmonic power spectra, needed to construct an anisotropic stress estimator that combines the predictions on the evolutions of Ψ and the Weyl potential. Secondly, the MCMC turns to be necessary to extract constraints on the Effective Theory of Interacting Dark Energy from galaxy clustering observations, where the algorithm requires the computation of the multipoles of the 2-pt correlation function.

Part II

MEASURING THE ANISOTROPIC STRESS WITH RELATIVISTIC EFFECTS

3

TESTING GRAVITY AT LATE-TIMES

This Part is based on publications 1, 2 and 3 listed in the preamble.

Two fundamental mysteries are latent at the core of current research in cosmology: what is causing the observed accelerated expansion of the Universe; and what is the nature of dark matter. The standard model of cosmology, the ΛCDM model, postulates that the accelerated expansion is due to a cosmological constant, and that dark matter is a perfect non-relativistic fluid which interacts only gravitationally with the normal baryonic matter.

Testing the law of gravity at cosmological scales is one of the main science driver for the coming generation of large-scale structure surveys. At large scales, the geometry of our Universe can be consistently described by two metric potentials, Φ and Ψ, describing the geometry perturbations around a homogeneous and isotropic background. Testing the law of gravity therefore requires to test the relations between these two potentials and the energy-momentum tensor describing the content of our Universe, in particular the matter density fluctuation, δ, and the galaxy peculiar velocity, $\mathbf{V}$.

Two approaches can be used for this. The first one consists in assuming a specific model or class of models of gravity (e.g. Horndeski models [70]), determine how the four fields, Φ, Ψ, δ and $\mathbf{V}$, depend on the parameters of the model, and use observations (which depend on the four fields) to constrain the parameters. This approach has the obvious disadvantage that it has to be performed separately for each model or class of models.

The second approach consists in building model-independent tests, that allow to probe directly the relations between the four fields without assuming any model, see e.g. [53, 54, 71–77]. The outcome of these tests can then be used to determine the validity of any theory of gravity. This second approach, which is more powerful, is however suffering from an important limitation: the fact that our observables at late time are sensitive to only three combinations of the four fields, namely δ and $\mathbf{V}$ (through redshift-space distortions, see e.g. [19, 78]) and $\Phi + \Psi$ (through cosmic shear [79, 80], CMB lensing [29, 81–83] or Integrated Sachs Wolfe [84]). This means that current observations are not able to test all relations between the four fields. The standard way of overcoming this problem is to assume that some of the relations between the four fields are known. Typically, one usually assumes that the continuity equation for dark matter holds: there is no exchange of energy between dark matter and dark energy; and that Euler equation for dark matter holds: there is no fifth force acting on dark matter, which consequently follows geodesics. Under these conditions, a measurement of $\mathbf{V}$ can be translated into a measurement of Ψ, which can then be compared to $\Phi + \Psi$ to test if the two metric potentials are the same, i.e. to test for the presence of anisotropic stress [72, 85–87] (see fig. 3.1). This is a key test for modified theories of gravity since in General Relativity (GR) and for large classes of dark energy models, $\Phi = \Psi$ at late time [1], whereas very generally in modified theories of gravity $\Phi \neq \Psi$, see e.g. [90].

$$\begin{tikzcd} b\,\delta \arrow[r, leftrightarrow, "\text{Poisson eq.}"] \arrow[d, leftrightarrow, "\text{Continuity eq.}"'] & (\Phi + \Psi) \\ \mathbf{V} \arrow[r, leftrightarrow, "\text{Euler eq.}"'] & \Psi \end{tikzcd}$$

Figure 3.1: Diagram describing the relations between the four observable fields Φ, Ψ, δ and $\mathbf{V}$ and the equations connecting them. Note that we include the bias factor b in front of the matter density fluctuation. The actual observable is the overdensity of galaxies, which we assume to be biased tracers of the underlying dark matter distribution.

Deviations from ΛCDM are often studied separately by different communities: some studies concentrate on models beyond General Relativity (see e.g. [91, 92] for a review), assuming that dark matter obeys the weak equivalence principle; while other studies explore non-standard dark matter models subjected to a dark fifth force (see e.g. [93–97]), assuming the validity of General Relativity (GR). In practice however, since we do not know if GR is valid, and we do not know if dark fifth forces exist, we would like to use observations to distinguish between these different scenarios. More precisely, if we observe deviations from the ΛCDM model, it is legitimate to ask ourselves if they are due to a modification of the theory of gravity, or to a fifth force acting on dark matter [2].

One key observable in large-scale structure surveys is the growth rate of perturbations f, that can be measured in a model-independent way from redshift-space distortions (RSD), see e.g. [101]. While this growth of structure provides a powerful way of unveiling deviations from ΛCDM, it cannot unambiguously distinguish between modifications of gravity and dark fifth forces since they impact the way matter is clustering in a very similar way [102–104]. A key difference between modifications of gravity and dark fifth force models however, is the fact that in modified gravity theories, very generically the two gravitational potentials encoding spatial (Φ) and temporal (Ψ) distortions are different (see e.g. [90]), whereas in GR these potentials are the same at late time. This property remains of course valid in the presence of a dark fifth force acting on dark matter (only very exotic models of dark matter with a non-zero anisotropic stress would modify this.) Hence, measuring the relation between Φ and Ψ, the so-called anisotropic stress, is often referred to as a *smoking gun* for modified gravity, i.e. a way of distinguishing a dark fifth force from a true deviation from GR [75, 105, 106].

As discussed in [104], however, this test cannot be performed with current methods. The reason for this is that, besides RSD, we are currently only able to measure the sum of the two gravitational potentials, $\Phi + \Psi$, through gravitational lensing (cosmic shear or

---

[1] Note that neutrinos also generate a non-zero anisotropic stress, which is however very small [88, 89].

[2] Note that there are also models where gravity is modified and in addition the equivalence principle is broken since dark matter and baryons are coupled differently to the new degree of freedom [98, 99]. In other models the equivalence principle is valid at the microscopic level, but the modifications of gravity generate an effective breaking of the equivalence principle due to screening [100].

CMB lensing) [61, 107]. We have no individual measurements of Φ or Ψ. The only way to measure the anisotropic stress is therefore to use measurements of the galaxy velocity V from RSD, and translate these into measurements of Ψ assuming the validity of Euler equation [75]. While this procedure is perfectly valid in models of modified gravity, it clearly does not work in models with a dark fifth force, that break the equivalence principle. Wrongly assuming Euler equation in this case would lead us to measure an effective difference between Φ and Ψ, and to erroneously conclude that gravity is modified even if it is not.

An alternative method to constrain the anisotropic stress consists in looking at the speed of propagation of gravitational waves (GWs). In scalar-tensor theories of gravity (Horndeski theories [70]), one of the parameters that generates a non-zero anisotropic stress also governs the speed of propagation of GWs. Combining the constraints on this speed obtained through the GW and electromagnetic observations of the binary neutron stars system GW170817 [108], with the consideration that dark energy perturbations in Horndeski may become unstable in the presence of GWs [109] (which may further limit the parameter space), leads to constraints on the anisotropic stress of the order of a few percent [110]. This elegant method, which combines GWs propagation with large-scale structure, is however applicable only to a specific class of modified gravity theories and is therefore not model-independent. As before, it relies on the validity of the weak equivalence principle in Horndeski theories. Moreover, it assumes that the speed of GWs is independent of frequency and of time, something that has not been validated observationally.

Therefore, a truly model independent *smoking gun* for modified gravity requires of very specific rounds: we need an independent measurement of the time distortions Ψ, or the spatial distortions Φ. Interestingly, among the relativistic effects affecting the LSS there exists one that is proportional to Ψ, the so-called *gravitational redshift*. As we demonstrated in Chapter 2, this effect leaves an impact on the distribution of galaxies [5, 8, 10], and can be measured by looking for a dipole in the cross-correlation of populations of different luminosity. In essence, one typically splits the galaxy population into two groups labelled as *bright* and *faint* galaxies [7, 12, 24, 47, 48, 50, 111, 112]. Gravitational redshift is an effect predicted by [113], which postulates that time passes at a slower rate in a gravitational potential well. It has been measured in a variety of systems: around earth, by comparing clocks at different distances from the ground, i.e. at different values of Ψ [114, 115]; in white dwarf, by looking at the reddening of light due to its escape from the gravitational field of the star [116, 117]; and in clusters of galaxies and non-linear structures by looking at the difference in redshift between galaxies at the centre of the structure and galaxies away from the centre [118–120]. So far, all these measurements have confirmed the validity of GR. However, this effect (and consequently the potential Ψ) has never been measured at cosmological scales.

In this Part, we develop a model independent test of gravity relying on a new technique for measuring the time distortions metric potential Ψ directly from Large-Scale Structure observations, building upon refs. [121–123]. In Chapter 4, we develop the method to isolate the evolution of Ψ by combining the multipoles of the power spectrum. This quantity affects the redshifts of incoming photons due to the existence of varying gravitational potentials along the line-of-sight. We continue to introduce a new estimator for the gravitational slip, defined as the ratio $\eta = \Phi/\Psi$ in Fourier space, which combines the previous observable with cosmic shear observations, which are sensitive to the

Weyl potential, $(\Phi + \Psi)/2$. In Chapter 5, we develop the same technique isolating the gravitational redshift in configuration space by means of the multipoles of the galaxy 2-pt correlation function, which naturally includes the wide-angle effects. We then introduce the appropriate parametrization for measuring the gravitational redshift and the evolution of the Weyl potential from galaxy surveys in a model independent manner. This allows us to produce Fisher forecasts for these two observables and predict the constraints on the anisotropic stress expected from the upcoming Stage-IV galaxy surveys. Finally, in Chapter 6 we explain the methodology and surveys specifications adopted for the Fisher analyses and discuss the results. We conclude this part in Chapter 7.

4

ESTIMATOR FOR THE ANISOTROPIC STRESS: FOURIER SPACE

In this chapter, we introduce a novel model-independent test for the anisotropic stress, which does not rely on any assumption for dark matter, i.e. which does not rely on the validity of the continuity or Euler equation. We shall denote the correspondent estimator by O^{stress}. To build this test we use the fact that galaxy number counts are affected by gravitational redshift, a relativistic effect that is directly proportional to the evolution of the field Ψ along the line-of-sight [5, 8, 10, 11], as described in sec.1.2. This effect changes the redshifts of the incoming photons that propagate throughout the Universe traveling across gravitational wells generated by heavy objects. We develop a method to isolate Ψ from galaxy number counts observations. More precisely, we build an observable which measures the correlations between the matter density fluctuations and the gravitational potential Ψ: $O^{\delta\Psi} \propto \langle \delta\Psi \rangle$. We then compare this with lensing observations, which provide a measurement of $O^{\delta(\Phi+\Psi)} \propto \langle \delta(\Phi+\Psi) \rangle$. Our test is then simply given by the ratio between these two observables:

$$O^{stress} \equiv \frac{O^{\delta(\Phi+\Psi)}}{O^{\delta\Psi}} = 1 + \eta \,, \tag{4.1}$$

where η relates the two metric potentials, $\Phi = \eta\Psi$. In ΛCDM, the two metric potentials are equal and therefore $O^{stress} = 2$ at all scales and redshifts. Any observed deviation from 2 would therefore unambiguously mean that the anisotropic stress is non-zero in our Universe, which is a strong indication for deviations from GR. The discussion below is fully based in ref. [121].

4.1 GALAXY NUMBER COUNTS IN FOURIER SPACE

Spectroscopic redshifts surveys are able to map the distribution of galaxies in the sky, providing precise measurements of their position. This permits the reconstruction of sky maps on which we can measure the galaxy number counts fluctuations, $\Delta(\mathbf{n}, z)$. This observable can be consistently defined in a gauge invariant form following the discussion presented in Chapter 1. Let us recall here that, at linear order in perturbation theory, the dominant contributions to Δ are the density and RSD contributions (see eq. (1.42)), into which the linear galaxy bias $b(z)$ enters. In addition, we also consider the relativistic distortions of eq. (1.58). Their amplitude depends on the magnification and evolution biases, $s(z)$ and $f^{\mathrm{evol}}(z)$. The lensing magnification is neglected, as we expect this term to be negligible for our test, at least below $z = 1.5$ [77]. In Fourier space, the galaxy number counts fluctuations for a population of galaxies with luminosity L becomes into the form given by eq. (2.17). This is valid only in the flat-sky approximation, where $\mathbf{n}$ can be considered as fixed. The product $(\hat{\mathbf{k}} \cdot \mathbf{n})$ represents the angle formed by the direction of observation and the direction of the Fourier modes. Note also that here we can use z as the time variable, since the corrections generated by the difference between a surface of constant time and a surface of constant redshift have been consistently included in the expression for Δ.

Finally, note that eq. (2.17) are valid at linear order in perturbation theory. In the non-linear regime, other terms have been shown to contribute to the observable Δ, modifying the RSD contribution [41, 124], and also the relativistic effects (like transverse Doppler effects [111, 125–127]). Hence, test proposed in this chapter is valid only in the linear regime, where the impact from non-linear corrections can be neglected.

4.2 ESTIMATOR FOR THE GRAVITATIONAL REDSHIFT

The aim of our work is to isolate the contribution from gravitational redshift given by the last term in eq. (2.17), $k\Psi/\mathcal{H}$, since it is directly proportional to the time component of the metric Ψ. The optimal way of targeting this contribution is to cross-correlate two populations of galaxies with different luminosities, such that this term contributes to odd multipoles [12, 24, 49, 50].

The statistical properties of the correlations between a bright, $\mathrm{L}=\mathrm{B}$, and a faint, $\mathrm{L}=\mathrm{F}$, population of galaxies in Fourier space are given by the power spectrum. Following our line of reasoning in sec. 2.1.1, we can define

$$\langle \Delta_{\mathrm{B}}(\mathbf{k},z)\Delta_{\mathrm{F}}(\mathbf{k}',z)\rangle = (2\pi)^3 P_{\mathrm{BF}}(k,\mu,z)\delta_D(\mathbf{k}+\mathbf{k}')\,,$$

where $P_{\mathrm{BF}}(k,\mu,z)$ is the total power spectrum. In Fourier space, the different contributing terms naturally appear as a power series of the flat-sky angle $\mu = \hat{\mathbf{k}}\cdot\mathbf{n} = \cos\beta$ (See fig. 2.2). Using the definitions of the Legendre polynomials contained in Appendix A.2 up to $\mathrm{L}=4$ and replacing $x=\mu$, we can recast the power spectrum into the form

$$\begin{aligned} P_{\mathrm{BF}} =\, & b_{\mathrm{B}} b_{\mathrm{F}} P_{\delta\delta} - \frac{1}{3}(b_{\mathrm{B}}+b_{\mathrm{F}})\frac{k}{\mathcal{H}}P_{\delta V} + \frac{1}{5}\left(\frac{k}{\mathcal{H}}\right)^2 P_{VV} \\ & + \left[-\frac{2}{3}(b_{\mathrm{B}}+b_{\mathrm{F}})\frac{k}{\mathcal{H}}P_{\delta V} + \frac{4}{7}\left(\frac{k}{\mathcal{H}}\right)^2 P_{VV}\right]\mathcal{P}_2(\mu) + \frac{8}{35}\left(\frac{k}{\mathcal{H}}\right)^2 P_{VV}\mathcal{P}_4(\mu) \\ & + \left[(b_{\mathrm{F}}\alpha_{\mathrm{B}} - b_{\mathrm{B}}\alpha_{\mathrm{F}})P_{\delta V} + (b_{\mathrm{F}}-b_{\mathrm{B}})\frac{1}{\mathcal{H}}P_{\delta\dot{V}} + \frac{3}{5}(\alpha_{\mathrm{F}}-\alpha_{\mathrm{B}})\frac{k}{\mathcal{H}}P_{VV}\right] i\mathcal{P}_1(\mu) \\ & + \frac{2}{5}(\alpha_{\mathrm{F}}-\alpha_{\mathrm{B}})\frac{k}{\mathcal{H}}P_{VV}\, i\,\mathcal{P}_3(\mu) + (b_{\mathrm{B}}-b_{\mathrm{F}})\frac{k}{\mathcal{H}}P_{\delta\Psi}\, i\,\mathcal{P}_1(\mu)\,. \end{aligned} \tag{4.2}$$

Here $\mathcal{P}_\ell$ denotes the Legendre polynomial of degree ℓ the contributing power spectra are defined through relations of the form

$$\langle X(\mathbf{k},z)Y(\mathbf{k}',z)\rangle = (2\pi)^3 P_{XY}(k,z)\delta_D(\mathbf{k}+\mathbf{k}')\,, \tag{4.3}$$

for $X,Y=\delta, V, \dot{V}, \Psi$. The terms of the first line of eq. (4.2) are the contributions to the monopole ($\mathcal{P}_0=1$). The terms with $\mathcal{P}_2$ and $\mathcal{P}_4$ correspond to the quadrupole and the hexadecapole, respectively. The relativistic effects, encoded in the companion terms to $i\,\mathcal{P}_1(\mu)$ and $i\,\mathcal{P}_3(\mu)$, generate imaginary contributions to the power spectrum. Note however that these terms are proportional to $(b_{\mathrm{B}}-b_{\mathrm{F}})$ and $(\alpha_{\mathrm{F}}-\alpha_{\mathrm{B}})$ and therefore vanish for correlations involving a single population of galaxies. As we saw in sec. 2.2.2, this translates into symmetry-breaking contributions to the correlation function in configuration space. In fact, by Fourier-transforming back to configuration space and introducing the relevant transfer functions for each P_{XY}, we find eq. (4.2) to be consistent with the (sum of the) integrands of eqs.(2.46) and (2.47), except for the wide-angle corrections that cannot be taken into account directly in the flat-sky Fourier space.

Our aim is to isolate the last term in eq. (4.2), which is proportional to $P_{\delta\Psi}$. The anisotropic stress can then be directly measured by dividing this contribution with the so-called galaxy-galaxy lensing correlation, which is proportional to $P_{\delta(\Phi+\Psi)}$ [64]. To isolate $P_{\delta\Psi}$, we first extract the dipole of $P_{\rm BF}$ which contains terms proportional to $P_{\delta\Psi}, P_{\delta V}, P_{\delta\dot{V}}$ and P_{VV}. We then look for combinations of the other multipoles in order to cancel the $P_{\delta V}, P_{\delta\dot{V}}$ and P_{VV} contributions.

Given that the Legendre polynomials form an orthogonal set, the multipole ℓ of $P_{\rm BF}$ can be extracted by weighting it with the Legendre polynomial $\mathcal{P}(x)$ of degree ℓ and integrating over μ via eq. (2.26) In this way, each $P^{(\ell)}_{\rm BF}(k,z)$ represent an independent observable quantity one can easily extract from the data. We are therefore free to combine them '*à volonté*' to isolate and probe the relative impact of each contribution.

In the case of our particular test, we need to measure the monopole and quadrupole of the bright and faint populations, the hexadecapole of the whole population. The hexadecapole is independent of the population bias. Therefore, we cannot distinguish a hexadecapole contribution for each population. In addition, we also require of measurements of the dipole and octupole of the cross-correlation between bright and faint. In Fourier space, the multipoles of the angle β take the form

$$P^{(0)}_{\rm LM} = b_{\rm L} b_{\rm M} P_{\delta\delta} - \frac{1}{3}(b_{\rm L}+b_{\rm M})\frac{k}{\mathcal{H}}P_{\delta V} + \frac{1}{5}\left(\frac{k}{\mathcal{H}}\right)^2 P_{VV}\,, \tag{4.4}$$

$$P^{(2)}_{\rm LM} = -\frac{2}{3}(b_{\rm L}+b_{\rm M})\frac{k}{\mathcal{H}}P_{\delta V} + \frac{4}{7}\left(\frac{k}{\mathcal{H}}\right)^2 P_{VV}\,, \tag{4.5}$$

$$P^{(4)}_{\rm T} = \frac{8}{35}\left(\frac{k}{\mathcal{H}}\right)^2 P_{VV}\,, \tag{4.6}$$

$$\begin{aligned} P^{(1)}_{\rm BF} = -i\Bigg[&(b_{\rm B}\alpha_{\rm F} - b_{\rm F}\alpha_{\rm B})P_{\delta V} + (b_{\rm B}-b_{\rm F})\frac{1}{\mathcal{H}}P_{\delta\dot{V}} \\ &- \frac{3}{5}(\alpha_{\rm F}-\alpha_{\rm B})\frac{k}{\mathcal{H}}P_{VV}\Bigg] + i(b_{\rm B}-b_{\rm F})\frac{k}{\mathcal{H}}P_{\delta\Psi}\,, \end{aligned} \tag{4.7}$$

$$P^{(3)}_{\rm BF} = i\,\frac{2}{5}(\alpha_{\rm F}-\alpha_{\rm B})\frac{k}{\mathcal{H}}P_{VV}\,, \tag{4.8}$$

with L=B, F. Of course, they are the Fourier transform of the configuration space multipoles computed in sec. 2.2 (see eqs. (2.52)-(2.56) for the GR expressions). From these observed multipoles we construct the following independent observables:

$$\begin{aligned} O^{\delta\delta}_{\rm L}(k,z) &\equiv P^{(0)}_{\rm L} - \frac{1}{2}P^{(2)}_{\rm L} + \frac{3}{8}P^{(4)}_{\rm L} \\ &= b^2_{\rm L}\,P_{\delta\delta}(k,z)\,, \end{aligned} \tag{4.9}$$

$$\begin{aligned} O^{\delta V}_{\rm L}(k,z) &\equiv \frac{3}{4}P^{(2)}_{\rm L} - \frac{15}{8}P^{(4)} \\ &= -b_{\rm L}\frac{k}{\mathcal{H}}\,P_{\delta V}(k,z)\,, \end{aligned} \tag{4.10}$$

$$\begin{aligned} O_{\mathrm{L}}^{\delta\dot{V}}(k,z) &\equiv -(1+z)\sqrt{O_{\mathrm{L}}^{\delta\delta}(k,z)}\frac{d}{dz}\left[\frac{O_{\mathrm{L}}^{\delta V}(k,z)}{\sqrt{O_{\mathrm{L}}^{\delta\delta}(k,z)}}\right] \\ &= b_{\mathrm{L}}\frac{k}{\mathcal{H}}\left[\frac{\dot{\mathcal{H}}}{\mathcal{H}^2}P_{\delta V}(k,z)-\frac{1}{\mathcal{H}}P_{\delta\dot{V}}(k,z)\right]. \end{aligned} \tag{4.11}$$

To obtain the last line in eq. (4.11) we use the fact that, in generic theories of gravity, the density and velocity fields in the linear regime can be written as $\delta(\mathbf{k},z) = D(k,z)\delta(\mathbf{k},0)$ and $V(\mathbf{k},z) = G(k,z)\delta(\mathbf{k},0)$, where $\delta(\mathbf{k},0)$ is a constant and denotes the present dark matter density, while $D(k,z)$ and $G(k,z)$ are functions of k and z mapping $\delta(\mathbf{k},0)$ into the past [1]. With this we can easily verify that

$$\sqrt{P_{\delta\delta}(k,z)}\frac{d}{d\tau}\left(\frac{P_{\delta V}(k,z)}{\sqrt{P_{\delta\delta}(k,z)}}\right) = D(k,z)\dot{G}(k,z)P_{\delta\delta}(k,0) = P_{\delta\dot{V}}(k,z)\,,$$

which gives rise to expression (4.11). From eqs. (4.9), (4.10) and (4.11) it's clear we can measure the galaxy biases and the velocity contributions. We are now able to isolate $P_{\delta\Psi}$ with the following combination

$$\begin{aligned} O^{\delta\Psi}(k,z) \equiv\, & i\,\frac{\mathcal{H}}{k}\left[\frac{3}{2}P^{(3)}_{\mathrm{BF}} - P^{(1)}_{\mathrm{BF}}\right] - \left(\frac{\mathcal{H}}{k}\right)^2\left[O_{\mathrm{B}}^{\delta\dot{V}}(k,z) - O_{\mathrm{F}}^{\delta\dot{V}}(k,z)\right] \\ & - \left(\frac{\mathcal{H}}{k}\right)^2\left[1-\frac{2}{r\mathcal{H}} - 5s_{\mathrm{F}}\left(1-\frac{1}{r\mathcal{H}}\right) + f_{\mathrm{F}}^{\mathrm{evol}}\right] O_{\mathrm{B}}^{\delta V}(k,z) \\ & + \left(\frac{\mathcal{H}}{k}\right)^2\left[1-\frac{2}{r\mathcal{H}} - 5s_{\mathrm{B}}\left(1-\frac{1}{r\mathcal{H}}\right) + f_{\mathrm{B}}^{\mathrm{evol}}\right] O_{\mathrm{F}}^{\delta V}(k,z) \\ =\, & (b_{\mathrm{B}} - b_{\mathrm{F}})P_{\delta\Psi}(k,z)\,. \end{aligned} \tag{4.12}$$

We see that $O^{\delta\Psi}(k,z)$ can be measured from the galaxy number counts, without making any assumption on the theory of gravity. It depends indeed on:

- The multipoles of the power spectrum, which are observable.
- The background quantities $\mathcal{H}/k$ and $r\mathcal{H}$. These two combinations can be inferred from background observations. For example, observations of type Ia supernovae provide a measurement of the luminosity distance, up to a multiplicative constant [2]: $\hat{d}_L \equiv d_L\mathcal{H}_0$, from which one can infer the ratio $\mathcal{H}(z)/\mathcal{H}_0$. We then have

  $$r\mathcal{H} = \frac{\hat{d}_L}{1+z}\frac{\mathcal{H}}{\mathcal{H}_0}\,,\quad \text{and} \quad \frac{\mathcal{H}}{k} = \frac{\mathcal{H}}{\mathcal{H}_0}\frac{1}{\hat{k}}\,, \tag{4.13}$$

  where $\hat{k} \equiv k/\mathcal{H}_0$ is independent of h for k in units $\mathrm{Mpc}^{-1}h$.
- The magnification bias, s, and evolution bias, f^{evol}, of the bright and faint populations. These quantities can be directly measured from the two populations of galaxies. The magnification bias requires a measurement of the number of galaxies as a function of luminosity [25], whereas the evolution bias requires a measurement of the number of galaxies as a function of redshift [10, 128].

---

[1] These relations are valid in theories of gravity where mode couplings are negligible in the linear regime.

[2] This is due to the fact that the absolute intrinsic luminosity of supernovae is unknown, so that only ratios of luminosity distances at different redshifts are independent of normalization.

The observable $O^{\delta\Psi}$ is on its own a very interesting quantity. It probes directly the correlations between density perturbations and the metric gravitational potential Ψ. Therefore, it provides a way of measuring these correlations at cosmological scales, for the first time.

This observable relies on the dipole and octupole of the power spectrum, that are too small to be measured with current surveys [47]. The signal-to-noise ratio (SNR) of the dipole has however been forecasted for the upcoming generation of surveys (in configuration space), and is expected to reach 9.6 for the DESI survey (7.4 for the Bright Galaxy Sample and 6.2 for the emission line galaxies and luminous red galaxies [48]), and 46.4 for the SKA phase 2 [54]. The octupole is between 2 to 5 times smaller than the dipole [24], and its SNR is therefore expected to be reduced accordingly (its variance should indeed be similar, since it is dominated by density and RSD). The octupole may therefore degrade the overall SNR of $O^{\delta\Psi}$. If this is the case, this could be circumvented by replacing the octupole with the hexadecapole, which is similarly sensitive to P_{VV}, see eq. (4.6). Due to the relatively large SNR of the dipole for DESI and the SKA, we expect $O^{\delta\Psi}$ to be well measured in future surveys.

Let us mention that one limitation of the observable $O^{\delta\Psi}$ is to rely on the flat-sky approximation. Since relativistic effects may be of similar order as wide-angle effects, this approximation may not be accurate enough and wide-angle effects may modify the form of eq. (4.12). To study the importance of wide-angle effects, one needs to work in configuration space, where these effects can be consistently included [24]. In particular, in configuration space one can construct estimators that remove wide-angle effects directly from the signal [54, 69], without relying on any theoretical modelling. Adapting the observable $O^{\delta\Psi}$ to configuration space will not change its form nor meaning, and we defer this study to Chapter 5. Let us first continue the discussion towards our final result for the anisotropic stress estimator.

4.3 GALAXY-GALAXY LENSING

To extract the anisotropic stress from $O^{\delta\Psi}$, we need in addition a measurement of $P_{\delta(\Phi+\Psi)}$. This can be obtained by correlating gravitational lensing with galaxy number counts, the so-called galaxy-galaxy lensing correlations [64]. In terms of the arguments presented in Chapter 1, we already know that observations of galaxy shapes provide a measurement of the convergence field $\kappa(\mathbf{n}, z)$, whose dominant term, i.e. the lensing magnification, is directly sensitive to the Weyl potential (see eq. (1.52)). It actually implies an integral of the transverse Laplacian of $(\Phi + \Psi)$ on a hypersurface of constant time. Such an integral only meaningful on the past light-cone of the observer. Therefore, as discussed in sec. 2.1.2, we have first to define the correlation function in configuration space, and then extract the power spectrum from this well-defined quantity.

The observable $O^{\delta\Psi}$ depends on the bias difference between the bright and faint populations, $b_{\mathrm{B}} - b_{\mathrm{F}}$. In order to cancel this dependence we consider the following galaxy-galaxy lensing correlation (see also fig. 2.3)

$$\begin{aligned}\xi^{\mathrm{BF}}_{\Delta\kappa} &\equiv \langle \Delta_{\mathrm{B}}(\mathbf{n}, z)\kappa(\mathbf{n}', z')\rangle - \langle \Delta_{\mathrm{F}}(\mathbf{n}, z)\kappa(\mathbf{n}', z')\rangle \\ &= (b_{\mathrm{B}} - b_{\mathrm{F}}) \int_0^{r'} ds \frac{(r'-s)s}{2r'} \langle \delta(\mathbf{n}, z)\Delta_\Omega(\Phi+\Psi)(\mathbf{n}', z')\rangle\,,\end{aligned} \tag{4.14}$$

where $r' \equiv r(z')$ and s is the dummy integration variable. We see how Fourier transforming δ and $\Phi+\Psi$ and using Limber approximation [55, 57], we obtain

$$\xi^{\rm BF}_{\Delta\kappa} = -(b_{\rm B}-b_{\rm F})\frac{(r'-r)r}{2r'}\Theta(r'-r)\,\frac{1}{2\pi}\int_0^\infty dk_\perp k_\perp^3 P_{\delta(\Phi+\Psi)}(k_\perp,z)J_0(k_\perp\Delta x_\perp). \quad (4.15)$$

Here J_0 is the Bessel function of order zero, $k_\perp = |\mathbf{k}_\perp|$ is the amplitude of the wavenumber contribution perpendicular to the line-of-sight, $\Delta x_\perp = |\Delta\mathbf{x}_\perp|$ denotes the amplitude of the vector joining the pixel in which $\Delta_{\rm L}$ is measured and the pixel in which κ is measured, projected in the plane orthogonal to the line-of-sight, and Θ is the Heaviside function, accounting for the fact that the correlation between $\Delta_{\rm L}$ and κ is non-zero only if κ is behind $\Delta_{\rm L}$. Note that $\langle\Delta_{\rm L}\kappa\rangle$ contains also a lensing-lensing contribution, due to the first term of the third line in eq. (1.40) [129]. However, this contribution does not depend on the galaxy population and vanishes therefore in $\xi^{\rm BF}_{\Delta\kappa}$. Moreover, the correlation between κ and the velocity contributions in eq. (1.40), which are projection effects along the line-of-sight, exactly vanishes in the Limber approximation.

Since $\xi^{\rm BF}_{\Delta\kappa}$ depends on $P_{\delta(\Phi+\Psi)}$, on the bias difference $b_{\rm B}-b_{\rm F}$ and on the observable quantities r and r', we could directly compare it with $O^{\delta\Psi}$ to extract the anisotropic stress. However, to build a more direct test, it is convenient to Fourier transform the correlation function and define

$$\begin{aligned} O^{\delta(\Phi+\Psi)}(k_\perp,z) &\equiv -\frac{4\pi}{\Delta r k^2}\int_0^\infty d\Delta x_\perp \Delta x_\perp \xi^{\rm BF}_{\Delta\kappa}(\Delta r,\Delta x_\perp,z)J_0(k_\perp\Delta x_\perp) \\ &= (b_{\rm B}-b_{\rm F})P_{\delta(\Phi+\Psi)}(k_\perp,z). \end{aligned} \quad (4.16)$$

Here the correlation function is expressed in terms of the transverse separation, $\Delta x_\perp$, and the radial separation, Δr, between $\Delta_{\rm L}$ and κ. To obtain the second equality in eq. (4.16) we have used the orthogonality relation for J_0

$$\int_0^\infty d\Delta x_\perp \Delta x_\perp J_0(k_\perp\Delta x_\perp)J_0(k'_\perp\Delta x_\perp) = \frac{1}{k_\perp}\delta_D(k_\perp - k'_\perp)\,. \quad (4.17)$$

Equation (4.16) contains an integral over $\Delta x_\perp$ going from 0 to ∞. In practice, since the correlation function and the Bessel function go to zero at large separation, the integral can be cut at some maximum transverse separation $\Delta x_\perp^{\rm max}$. The observable $O^{\delta(\Phi+\Psi)}$ depends only on the transverse wave number $k_\perp$ (in the Limber approximation, the radial modes do not contribute to the correlation function $\xi^{\rm BF}_{\Delta\kappa}$). Therefore, to compare with $O^{\delta\Psi}$, we have to evaluate $O^{\delta(\Phi+\Psi)}$ at $k = k_\perp$.

The galaxy-galaxy lensing correlations have already been measured with high significance in several surveys, e.g. by the Dark Energy Survey [60, 64]. To build $O^{\delta(\Phi+\Psi)}$ we need to measure these correlations for two different populations of galaxies and to take their difference. In sec. 6.2.2, we study the performance of this observable with the upcoming generation of surveys.

Note that $O^{\delta(\Phi+\Psi)}$ has been built to cancel the bias difference of $O^{\delta\Psi}$, see eq. (4.12). This is however only possible if the galaxy-galaxy lensing correlations are measured from the same galaxy populations as the clustering correlations. It requires therefore a spectroscopic survey and a lensing survey that cover the same part of the sky [130]. This is for example the case for Euclid, which will measure spectroscopic redshifts and photometric galaxy images over the same sky area [59]. Similarly, one can combine the spectroscopic redshifts measured by DESI [131], with the galaxy images measured by the

DESI Legacy Imaging Survey [132]. Otherwise, the combination of lensing and clustering surveys targeting different underlying populations requires the knowledge about the cross-variance between the different datasets.

4.4 ANISOTROPIC STRESS ESTIMATOR

In ΛCDM and for large classes of dark energy models, the two metric potentials are the same at late times, and we have therefore

$$O^{stress} = \frac{O^{\delta(\Phi+\Psi)}}{O^{\delta\Psi}} = 2\,. \tag{4.18}$$

On the other hand, in theories of modified gravity, the metric potentials are generally different. This difference is usually parameterized by the variable η through the generalized relation $\Phi(\mathbf{k}, z) = \eta(k, z)\Psi(\mathbf{k}, z)$, where one allows for redshift and, possibly, scale dependence. This leads to

$$O^{stress} = \frac{O^{\delta(\Phi+\Psi)}}{O^{\delta\Psi}} = 1 + \eta\,. \tag{4.19}$$

The observable $O^{\delta\Psi}$ provides therefore a direct way of measuring η. In particular, if the ratio in eq. (4.19) is different from 2 at any redshift or scale k, then ΛCDM is ruled out, as well as all classes of dark energy models with no anisotropic stress, at least beyond that redshift or k-scale.

To emphasize the robustness of our test compared to standard methods, let us consider the following model, widely used in the literature: we parameterize deviations from GR by two functions, $\eta(k, z)$ (introduced above) and $Y(k, z)$, which encodes modifications to Poisson equation [72]

$$-k^2\Psi(\mathbf{k}, z) = \frac{3}{2}\mathcal{H}^2\Omega_m(z)Y(k, z)\delta(\mathbf{k}, z)\,, \tag{4.20}$$

where $\Omega_m(z)$ is the matter density parameter at redshift z. The function $Y(k, z)$ (sometimes called μ in the literature) reduces to 1 in GR (see eq. (1.15)). In addition to these functions, we allow for another departure from GR by modifying Euler equation (1.11)

$$\dot{V}(\mathbf{k}, z) + \mathcal{H}V(\mathbf{k}, z) - k\Psi(\mathbf{k}, z) = \hat{E}^{\text{break}}(\mathbf{k}, z)\,, \tag{4.21}$$

where $\hat{E}^{\text{break}}$ is a generic function encoding deviations from geodesic motion for dark matter. For example, in models where dark matter experiences a fifth force due to a non-minimal coupling to a scalar field, $\hat{E}^{\text{break}}$ takes the form $\hat{E}^{\text{break}} = k\,\Gamma(z)\Psi(\mathbf{k}, z)$, where Γ is the amplitude of the fifth force [54].

We now apply the test developed in [72] to this particular model. By doing this we clearly use the test outside its domain of validity, since in [72] it is explicitly assumed that Euler equation is valid. However, since in practice we do not know if dark matter obeys Euler equation or not, it is relevant to see what happens in this case. The evolution equation for the density contrast becomes

$$\delta'' + \left(2 + \frac{H'}{H}\right)\delta' = -\frac{k^2}{(aH)^2}\Psi - \frac{k}{(aH)^2}\hat{E}^{\text{break}}\,, \tag{4.22}$$

where $H(z) = \mathcal{H}(z)(1+z)$ and a prime denotes a derivative with respect to $N = \ln a$. The violation of the equivalence principle modifies therefore the way structures grow as a function of time, see also discussion in [133]. The combination of observables proposed in [72] to measure the anisotropic stress becomes then

$$\frac{3(1+z)^3 P_2}{2E^2\left(P_3 + 2 + \frac{E'}{E}\right)} - 1 = \eta + \frac{k}{(aH)^2}\frac{(1+\eta)}{f' + f^2 + \left(2 + \frac{E'}{E}\right)f}\frac{\hat{E}^{\text{break}}}{\delta} \neq \eta\,. \tag{4.23}$$

Here P_2 and P_3 are the ratios of observables defined in [72] (see their eqs. (14) and (15)), f is the growth rate and $E \equiv H/H_0$.

From eq. (4.23) we see that the test developed in [72] is not a measurement of η when Euler equation is not valid. In other words, a non-trivial outcome of this test can either mean that the anisotropic stress is non-zero, or that dark matter does not obey Euler equation. While we can use it as an estimator to test deviations from General Relativity, we will not be able to distinguish if these deviations are originated from the anisotropic stress or the breaking of the Euler equation for dark matter from it alone, without an additional estimator for the $\hat{E}^{\text{break}}$. In this case, we might be able to infer η from the combination of the two.

In conclusion, we have constructed an observable, $O^{\delta\Psi}$, which is directly proportional to the time component of the metric Ψ. This observable is constructed from the multipoles of the galaxy number counts, Δ, and it relies only on observable quantities. We have then shown how this novel observable can be used to measure directly the anisotropic stress, i.e. the difference between the two metric potentials Φ and Ψ.

This test, O^{stress}, has the strong advantage that it does not rely on any assumption about the theory of gravity, apart from the fact that photons propagate on null geodesics. In particular, O^{stress} does not assume that dark matter obeys the continuity or Euler equation. This differs from standard measurement of the anisotropic stress, which rely on the validity of the continuity and Euler equations. As an example, we have shown how the test proposed in [72] will fail if Euler equation is not valid: instead of measuring directly η, the combination of observables defined in [72] contains an additional term proportional to the deviation from Euler equation. This limitation simply follows from the fact that standard observables are insensitive to Ψ. The only way to test the relation between Ψ and $\Phi + \Psi$ with the current tests is then to translate a measurement of V into a measurement of Ψ assuming that dark matter obeys Euler equation. Importantly, this restricts the validity of current tests to the theories in which this assumption is valid.

Our test, O^{stress}, overcomes this limitation by using an observable sensitive to relativistic effects, which allows a direct measurement of Ψ. Of course, the price to pay is that O^{stress} will be more difficult to measure than standard tests, since relativistic effects are more challenging to measure than RSD. In the following Chapter, we will study in more detail the sensitivity of O^{stress} for the upcoming Stage-IV generation of large-scale structure surveys. In particular, we will analyze the performance of our test on the Phase 2 of the Square Kilometer Array survey (SKA2) and the Vera C. Rubin's Observatory Legacy Survey of Space and Time (LSST). The first is expected to provide high quality spectroscopic data, crucial for measuring Ψ, while the second will deliver a huge amount of exquisite photometric data crucial to galaxy lensing measurements.

Finally, let us note that our test, O^{stress}, is highly complementary to the well-known E_g statistics [53, 71, 134], which measures the ratio between density-lensing correlations, $\langle\delta(\Phi + \Psi)\rangle$, and density-velocity correlations, $\langle\delta V\rangle$. Similarly to our test, the E_g statistics does not rely on the validity of Euler equation, and is therefore truly model-independent. It provides however constraints on the combination of parameters: $Y(1+\eta)/f$. An observed deviation from the ΛCDM value in E_g can therefore either be due to a non-zero anisotropic stress (suggesting a modification of the theory of gravity) or to a growth rate which differs from ΛCDM (which also happens in simple models of dark energy). Having a test which directly and uniquely targets the anisotropic stress is therefore of high importance to test the theory of gravity.

5

MEASURING THE ANISOTROPIC STRESS IN CONFIGURATION SPACE

In this chapter, we revisit the method for measuring Ψ directly from large-scale structure observations explained ref. [121]. In practice, the most efficient approach for extracting information from galaxy surveys is to apply summary statistics such as the configuration space correlation function. So far, we introduced the Fourier space method in Chapter 4. This was useful to understand the technique extracting an estimator for Ψ, but suffers from the important limitation that it does not account for the so-called *wide-angle* corrections, arising in the flat-sky approximation only when performed in configuration space. The relativistic effects we are after might be of the same order of magnitude as these wide-angle effects and hence ignoring them lead to biased estimations [24]. However, we note that the power spectrum is just the Fourier transform of the correlation function, and hence the arguments and conclusions of Chapter 4 remain valid.

Therefore, we now travel to the realm of positions and redshifts and develop the method to isolate the correlation of Ψ with the density δ by combining the multipoles of the galaxy three-dimensional 2-pt correlation function. We develop the theoretical model and introduce a model-independent parametrization of the evolution of Ψ. We then propose a new parametrization for the evolution of the Weyl potential $(\Phi+\Psi)/2$ to be used for gravitational lensing measurements. Finally, we reconstruct the estimator for the anisotropic stress as the ratio of measurements of the time distortions and the Weyl potential. The present chapter is based in refs. [122, 123].

5.1 EVOLUTION OF THE TIME DISTORTIONS: Ψ

We start by parameterizing the evolution of the gravitational potential encoding the time distortions in a model-independent way. We assume that at early time, well in the matter era, the Universe is well described by GR and Cold Dark Matter (CDM). This has been tested with great precision by CMB measurements. We link therefore deviations from the CDM model to the onset of the accelerated expansion of the Universe. In this context, in sec. 2.1 we modelled the perturbations variables in Fourier space by means of the transfer functions connecting them to the primordial gravitational potential generated by inflation, Ψ_{in}, which depend on the Fourier mode wave number, k, and on the redshift, z. The matter density fluctuations are given by $T_\delta(k,z)$ (eq. (2.10)) and it is related to the velocity and potential perturbations by the Einstein's equations. Under the assumption that deviations from GR appear only at late time, we can compute $T_\delta(k,z)$ by linear evolution from $T_\delta(k,z_*)$ with eq. (2.13). The growth function $D_1(k,z)$ describes the growth of structure at late time and depends consequently on the theory of gravity and on the model of dark energy. At z_*, where GR is recovered and radiation is negligible, this function is independent on k. [1]

The velocity transfer function is usually related to the density transfer function using the continuity equation for matter, to find eq. (2.8) in terms of the growth rate $f(k,z)$. Under the same assumption about the deviations from GR, the velocity transfer function evolves at late time as

$$T_V(k,z) = \frac{\mathcal{H}(z)f(k,z)D_1(k,z)}{\mathcal{H}(z_*)f(z_*)D_1(z_*)} T_V(k,z_*) \,. \tag{5.1}$$

If the continuity equation is not valid, this standard parametrization breaks down. This would happen for example if dark matter exchanges energy with dark energy [135]. Since we want here to be agnostic about the theory of gravity and the behavior of dark matter, we parametrize instead the growth of velocity at late time with a new function $G(k,z)$ such that

$$T_V(k,z) = \frac{\mathcal{H}(z)G(k,z)}{\mathcal{H}(z_*)f(z_*)D_1(z_*)} T_V(k,z_*) \,. \tag{5.2}$$

Finally, the potential transfer function can be related to the density transfer function, using the Poisson equation and assuming that there is no anisotropic stress via eq. (2.6). Additionally, the matter density transfer function is usually split into a linear part and a boost factor, B, which accounts for the nonlinear evolution of matter fluctuations at small scales

$$T_\delta(k,z) = T_\delta^{\text{lin}}(k,z)\sqrt{B(k,z)} \,. \tag{5.3}$$

One can extract this non-linear boost factor from simulations by comparing the predicted signal with the linear regime theoretical prediction. Under the same assumptions as for the velocity equation above, we can write the late-times evolution of the gravitational potential in the form

$$T_\Psi(k,z) = \frac{\mathcal{H}^2(z)\Omega_m(z)D_1(k,z)}{\mathcal{H}^2(z_*)D_1(z_*)} \sqrt{\frac{B(k,z)}{B(k,z_*)}}\, T_\Psi(k,z_*) \,, \tag{5.4}$$

where we have used that $\Omega_m(z_*) = 1$. Again, in order to be agnostic about the theory of gravity, we replace this standard evolution with a new free function $I(k,z)$ which encodes the evolution of the gravitational potential Ψ at late time:

$$T_\Psi(k,z) = \frac{\mathcal{H}^2(z)I(k,z)}{\mathcal{H}^2(z_*)D_1(z_*)} \sqrt{\frac{B(k,z)}{B(k,z_*)}}\, T_\Psi(k,z_*) \,. \tag{5.5}$$

The functions $D_1(k,z)$ and $G(k,z)$ have been measured via redshift-space distortions. The function $I(k,z)$ on the other hand has never been measured at cosmological scales. In the next section we present the method to measure I using the multipoles of the 2-pt galaxy clustering correlation function. Later on Chapter 6, we forecast the precision for measuring $\hat{I}(z)$ with the coming generation of surveys. Note that for the forecasts we will

---

[1] The only scale-dependence within general relativity (GR) is indeed due to massive neutrinos and it is very small (see, e.g., [59]).

use the quasi-static approximation where we can drop the k-dependence. We also restrict the correlation function to separations chosen such that non-linearities are negligible, i.e. that the boost B plays no role. However, we included it here for consistency with the derivation of secs. 5.3 and 5.5 for the evolution of the Weyl potential and the anisotropic stress estimator.

5.2 GALAXY CLUSTERING 2-PT CORRELATION FUNCTION

As shown in Chapter 4, the evolution of Ψ can be measured by cross-correlating the over-density, Δ, of two populations of galaxies, e.g., a bright and a faint population. Ψ contributes to the galaxy over-density through the effect of gravitational redshift, which shifts to the red the spectrum of galaxies situated in a gravitational potential well. This effect adds to the density and RSD in eq. (1.42) and generates a contribution of the form $\partial_r\Psi/\mathcal{H}$ in Δ [7]. This term has the particularity to produce asymmetries in the distribution of galaxies [24] (see fig. 1.3). Hence, it was proposed to measure it by fitting for a dipole in the cross-correlation of bright and faint galaxies [24, 49, 50]. However, since Doppler effects also contribute to such a dipole, one needs a method to disentangle the two types of contributions.

Recovering the discussion presented in sec.2.2, we recall that galaxy surveys are able to map the distribution of galaxies in the sky. From this maps, we can reconstruct the galaxy number counts fluctuations, $\Delta(\mathbf{n}, z)$, as a function of the direction of observation, $\mathbf{n}$ and the redshift, z. We computed the analytical expression at linear order in perturbation theory in sec.1.2. Our conclusion there was that we will consider first line the standard density and redshift-space distortions (RSD) contributions (eq. (1.42)) and the relativistic effects (eq. 1.58). Among those, the first two terms are Doppler contributions [2]. Finally, the last term of the latter is the contribution from gravitational redshift, which depends directly on Ψ and is the target of our study.

In practice, from the discussion in Chapter 2 we learned that the standard approach to extract information from the galaxy distribution maps is to measure the statistical moments of the galaxy distribution. Assuming the fields describing the Universe are random Gaussian variables, all the relevant information will be contained in the 2-point correlation function and the variances between the variables. Generally speaking, the Gaussian fields are functions of position and time. In Cosmology, it is more convenient to define the 2-pt correlations in terms of the direction of observation $\mathbf{n}$ and the redshift z. Hence, we take two points in the sky and compute the 2-pt correlation function of Δ, $\xi_{\mathrm{LM}}(z, d, \mu) = \langle\Delta_{\mathrm{L}}(\mathbf{n}, z)\Delta_{\mathrm{M}}(\mathbf{n}', z')\rangle$, where d is the comoving distance between the 2 points in the sky and $\mu = \mathbf{k}\cdot\mathbf{n}$ is an angle. The function ξ depends on the specific shape of the triangle formed by the observer and the two points, and its final dependence is determined by the property of isotropy. This correlation measures the probability of finding a galaxy at the position $(\mathbf{n}', z')$ provided that there is a galaxy at the position $(\mathbf{n}, z)$. In addition, it is convenient to work in the distance-observer regime, assuming $d \ll r$ where $r(z)$ is the comoving distance to the pair. In this approximation, we have $r(z') \sim r(z)$ and one can take as reference point the center of the line joining the two points. Then $\mu = \cos\beta$ is the relative angle between the line-of-sight and the orientation

---

[2] Note that other relativistic distortions contribute to Δ [5, 8, 10], but their impact on the multipoles of the correlation function is negligible [27]. Gravitational lensing also contributes to Δ, but its impact becomes important only at large redshifts [27, 136], where we will see that I cannot be measured anymore.

of the pair (see fig. 2.2). This computation was done in sec. 2.2, where we computed the correlation function for the more general scenario of distinct populations of galaxies.

Interestingly, we have shown that in the distant-observer approximation performed in sec. 2.2.2 the density and RSD contributions in Δ generate a monopole, quadrupole and hexadecapole in the correlation function. These contributions have been measured with various surveys, see e.g. [101]. The contributions from gravitational redshift and Doppler effects generate additional terms on these multipoles as well, but they are suppressed by a factor of $(\mathcal{H}/k)\,(d/r)$ and are strongly subdominant, i.e. they can safely be neglected [27]. However, these relativistic effects generate a dipole in the correlation function, which can only be measured by correlating two distinct populations of galaxies, for example bright and faint galaxies [24]. We found the GR expressions for the even and odd multipoles in secs. 2.2.3 and 2.2.4. However, for our test we require to rewrite the expressions in terms of the new parametrization introduced above, i.e. the functions D_1, G and I of sec. 5.1. The even multipoles take the form

$$\xi^{(0)}_{\mathrm{LM}}(z,d) = \left[\hat{b}_{\mathrm{L}}\hat{b}_{\mathrm{M}}(z) + \frac{1}{3}\left(\hat{b}_{\mathrm{L}}(z)+\hat{b}_{\mathrm{M}}(z)\right)\hat{G}(z) + \frac{1}{5}\hat{G}^2(z)\right]\mu_0(z_*,d)\,, \tag{5.6}$$

$$\xi^{(2)}_{\mathrm{LM}}(z,d) = -\left[\frac{2}{3}\left(\hat{b}_{\mathrm{L}}(z)+\hat{b}_{\mathrm{M}}\right)\hat{G}(z) + \frac{4}{7}\hat{G}^2(z)\right]\mu_2(z_*,d)\,, \tag{5.7}$$

$$\xi^{(4)}(z,d)_{\mathrm{T}} = \frac{8}{35}\hat{G}^2(z)\,\mu_4(z_*,d)\,, \tag{5.8}$$

where

$$\hat{b}_{\mathrm{L}}(z) \equiv b_{\mathrm{L}}(z)\sigma_8(z)\,, \tag{5.9}$$

$$\hat{G}(z) \equiv G(z)\frac{\sigma_8(z)}{D_1(z)} = G(z)\frac{\sigma_8(z_*)}{D_1(z_*)}\,, \tag{5.10}$$

and

$$\mu_\ell(z_*,d) = \frac{1}{2\pi^2}\int dk k^2 \frac{P_{\delta\delta}(k,z_*)}{\sigma_8^2(z_*)} j_\ell(kd)\,. \tag{5.11}$$

The functions $\mu_\ell(z_*,d)$ depend on the matter power spectrum at $z=z_*$, well in the matter era, and are therefore determined by physics in the early Universe, which is tightly constrained by CMB observations [6]. These functions will be therefore considered as fixed for this analysis. Measuring the even multipoles provides consequently direct measurements of the biases, $\hat{b}_{\mathrm{L,M}}(z)$, and of the function $\hat{G}(z)$ [101] (which reduces to $f(z)\sigma_8(z)$ under the assumption that the continuity equation (1.10) is valid).

The dipole in the cross-correlation of bright and faint galaxies reads

$$\begin{aligned}\xi^{(1)}_{\mathrm{BF}}(z,d) = \frac{\mathcal{H}}{\mathcal{H}_0}\Bigg\{ & 3\left(\frac{1}{r\mathcal{H}}-1\right)\left(s_{\mathrm{B}}(z)-s_{\mathrm{F}}(z)\right)\hat{G}^2(z) \\ & +5\left(\frac{1}{r\mathcal{H}}-1\right)\left(\hat{b}_{\mathrm{F}}(z)s_{\mathrm{B}}(z)-\hat{b}_{\mathrm{B}}(z)s_{\mathrm{F}}(z)\right)\hat{G}(z) \\ & +\left(\hat{b}_{\mathrm{B}}(z)-\hat{b}_{\mathrm{F}}(z)\right)\left[\left(\frac{2}{r\mathcal{H}}-1\right)\hat{G}(z)-\frac{\dot{\hat{G}}(z)}{\mathcal{H}}\right] \\ & +\frac{3}{2}\left(\hat{b}_{\mathrm{B}}(z)-\hat{b}_{\mathrm{F}}(z)\right)\hat{I}(z)\Bigg\}\,\nu_1(z_*,d)\,,\end{aligned} \tag{5.12}$$

which is only non-zero when correlating two distinct populations of galaxies [3]. Note that the dipole is explicitly dependent on the time evolution of the modified growth factor and on the gravitational redshift. This is only the case if we do not use the Euler equation in the calculation. We have defined

$$\hat{I}(z) \equiv I(z)\frac{\sigma_8(z)}{D_1(z)} = I(z)\frac{\sigma_8(z_*)}{D_1(z_*)}\,, \tag{5.13}$$

and

$$\nu_1(z_*, d) = \frac{\mathcal{H}_0}{2\pi^2}\int dkk\frac{P_{\delta\delta}(k, z_*)}{\sigma_8^2(z_*)}j_1(kd)\,. \tag{5.14}$$

As before, the function $\nu_1(z_*, d)$ which depends on z_* will be considered fixed in the analysis. Note also that we have parametrized the expressions in terms of $\sigma_8(z)$ instead of $D_1(z)$ as in sec. (2.1). In doing that we have used the fact $\sigma_8/\sigma_8(z_*) \approx D_1/D_1(z_*)$. This is more convenient from the observational point of view, as σ_8 is degenerate with the quantities we want to measure. Hence, combining the dipole with the even multipoles provides a way of measuring directly the function $\hat{I}(z)$, which encodes the evolution of the gravitational potential Ψ, and the evolution of the velocities $\hat{G}(z)$ in a model-independent way.

The function $\hat{I}$ is a new parameter encoding the z-evolution of the gravitational potential. If galaxies obey Euler's equation, which is the case if the weak equivalence principle for dark matter and baryonic matter is valid, then $\hat{I}$ can be related to $\hat{f} = f\sigma_8$ through

$$\hat{I} = \frac{2}{3}\hat{f}\left[\frac{\mathcal{H}'}{\mathcal{H}} + \frac{\hat{f}'}{\hat{f}} + 1\right]\,. \tag{5.15}$$

It is therefore possible to reconstruct the evolution of Ψ from RSD, as has been shown in [75]. On the other hand, if Euler's equation is not valid, for example if dark matter is sensitive to a fifth force, or if baryons and dark matter are not coupled in the same way to gravity, then eq. (5.15) is not valid [138]. In this case, $\hat{I}$ has to be considered as an independent function, that cannot be inferred from RSD measurements. The dipole is therefore an important new observable, since it will allow us to measure $\hat{I}$ directly, without having to assume anything on the behavior of dark matter. With current surveys, the dipole is unfortunately not detectable [47]. Forecasts show however that the coming generation of surveys, like DESI and SKA2, will be able to measure it robustly [54, 111, 112].

Finally, let us stress that in our derivation we have assumed that the k-dependence of D_1, G and I is negligible, so that we can take them out of the integrals in eqs. (5.11) and (5.14). This is a common assumption, that is used in many analyses, see e.g. [101], and that is motivated by the fact that in the quasi-static approximation the k-dependence

---

[3] Note that the dipole is also affected by wide-angle effects, which generate a contribution of the form $-2/5(\hat{b}_B - \hat{b}_F)\,\hat{G}\,(d/r)\,\mu_2(z_*, d)$. This is a contamination arising from the even multipoles in the distant-observer approximation. The relativistic effects are suppressed by a factor $(\mathcal{H}/k)$ with respect to the even multipoles, which is a factor roughly of the same order as (d/r). This contribution can however be removed by constructing an appropriate estimator, as has been shown in sec. 2.2.5 (see also [24, 54, 69]). For simplicity we have set here the evolution biases to zero $f_B^{\text{evol}} = f_F^{\text{evol}}$. In practice these parameters will be measured from the galaxy populations, see e.g. [137].

can often be neglected [98, 99, 139]. However, for some theories of gravity this assumption may not be valid [140]. Relaxing it would slightly complicate the forecasts, but would not invalidate our method.

5.3 EVOLUTION OF THE WEYL POTENTIAL: $\Phi + \Psi$

The standard method to model the evolution of the two gravitational potentials consists in relating them to the matter density, allowing for a non-zero anisotropic stress and a modification to Poisson's equation. Here we develop a different method, which, as we will show, allows us to measure directly the evolution of $\Phi + \Psi$ with redshift.

We start by reviewing how $\Phi + \Psi$ evolves with redshift in ΛCDM. The correspondent transfer function of the Weyl potential can be related to that of the matter density via the Poisson equation and assuming $\Psi = \Phi$, i.e. no anisotropic stress, which is the case for General Relativity ($\eta = 1$). We found the expression in eq. (2.9) Once more, the matter density transfer function is usually split into a linear part and a boost factor, B, which accounts for the non-linear evolution of matter fluctuations at small scales (see eq. (5.3)).

As stated earlier, in ΛCDM the growth of matter density fluctuations in the linear regime is scale-independent at late times, and we can therefore relate the transfer function at redshift z to a redshift z_* through the growth function $D_1(z)$. Inserting (2.13) into (2.9) we find the relation

$$T_{\Phi+\Psi}(k,z) = \frac{\mathcal{H}^2(z)\Omega_{\rm m}(z)D_1(z)}{\mathcal{H}^2(z_*)\Omega_{\rm m}(z_*)D_1(z_*)}\sqrt{\frac{B(k,z)}{B(k,z_*)}}\,T_{\Phi+\Psi}(k,z_*)\,. \tag{5.16}$$

Equation (5.16) tells us that, in ΛCDM, the evolution of $\Phi + \Psi$ is governed by $\Omega_{\rm m}(z)D_1(z)$, i.e. that $\Phi + \Psi$ follows directly the evolution of the *total* matter density.

In the case of modified gravity, however, the two equalities present in eq. (2.9) are generically modified: first Φ and Ψ can be different from each other due to the anisotropic stress, and second Φ may not be related to the density, δ, via Poisson's equation. Therefore, generically, the evolution of $\Phi + \Psi$ will differ from the evolution of the density, governed by D_1. To account for this, without restricting ourselves to any particular model of gravity, we replace $\Omega_{\rm m}(z)D_1(z)$ in eq. (5.16) by an agnostic function $J(k,z)$. This function encodes the growth of $\Phi + \Psi$, and by treating it as a *new degree of freedom*, that can be directly measured from the data and that is independent of the growth function D_1, we effectively allow for any deviations from GR.

Since here we want to generically parametrize gravity modifications at late-times, we define the pivot redshift z_* to be well in the matter era, before the accelerated expansion of the Universe started. We assume that, at that redshift, GR is recovered. In other words, we expect structures to grow as in GR, when the background evolution of the Universe behaves as in GR. We therefore set $J(k,z_*) = \Omega_{\rm m}(z_*)D_1(z_*) = D_1(z_*)$, since $\Omega_{\rm m}(z_*) = 1$ in the matter era. With this, the transfer function for $\Phi + \Psi$ evolves as

$$T_{\Phi+\Psi}(k,z) = \frac{\mathcal{H}^2(z)J(k,z)}{\mathcal{H}^2(z_*)D_1(z_*)}\sqrt{\frac{B(k,z)}{B(k,z_*)}}\,T_{\Phi+\Psi}(k,z_*)\,. \tag{5.17}$$

Combining eq. (5.17) with eqs. (5.3) and (2.13), and using that at z_* GR is recovered, i.e.

$$T_\delta^{lin}(k,z_*) = -\frac{1}{3}\left[\frac{k}{\mathcal{H}(z_*)}\right]^2 T_{\Phi+\Psi}(k,z_*)\,, \tag{5.18}$$

we can relate the transfer function of $\Phi + \Psi$ to the density transfer function at z_* via

$$T_{\Phi+\Psi}(k,z) = -3\left[\frac{\mathcal{H}(z)}{k}\right]^2 J(k,z)\sqrt{B(k,z)}\,\frac{T_\delta^{\rm lin}(k,z_*)}{D_1(z_*)}\,. \tag{5.19}$$

5.4 HARMONIC POWER SPECTRA: THE 2×2PT ANALYSIS

Let us now determine how the function J can be measured with gravitational lensing. Gravitational lensing can be measured either through shear-shear correlations or through density-shear correlations (the so-called galaxy-galaxy lensing). In this chapter we focus on the latter, since, as we will see, it allows us to probe directly the function J at the redshift of the lenses. In addition, we include in our analysis the galaxy-galaxy correlations since it allows us to break the degeneracy between the galaxy bias and the function J. In summary, we exploit a reduced '2×2pt formalism' as explained in sec.2.3.

Let us find the generalized version of the 2×2pt observables in terms of our new parametrization. The harmonic power spectra of galaxy-galaxy lensing correlations can be computed using eq. (2.78)

$$\begin{aligned} C_\ell^{\Delta\kappa}(z_i,z_j) &= \int \mathrm{d}z\, n_i(z) b_i(z) \int \mathrm{d}z' n_j(z') C_\ell^{\delta\kappa}(z,z') \\ &= -\frac{A}{\pi}\int \mathrm{d}z\, n_i(z) b_i(z) \int \mathrm{d}z' n_j(z') \int \frac{\mathrm{d}k}{k}\left(\frac{k}{k_*}\right)^{n_s-1} \\ &\quad \times T_\delta(k,z) j_\ell(kr) \frac{1}{r'}\int_0^{r'} \mathrm{d}r'' \frac{r'-r''}{r''}\ell(\ell+1) T_{\Phi+\Psi}(k,r'') j_\ell(kr'')\,. \end{aligned} \tag{5.20}$$

Here Δ denotes the galaxy over-density, evaluated at the effective redshift of the tomographic bin i

$$\Delta(z_i,\mathbf{n}_i) = b_i \delta(z_i,\mathbf{n}_i) + \frac{1}{\mathcal{H}}\partial_r(\mathbf{V}\cdot\mathbf{n}_i)\,, \tag{5.21}$$

where $\mathbf{n}_i$ is the direction of the pixel i, $\mathbf{V}$ is the galaxy peculiar velocity, b_i is the linear bias, and ∂_r denotes a derivative with respect to the comoving distance r. Here κ represents the lensing convergence [4], evaluated in pixel j with effective redshift z_j. It is related to the Weyl potential by

$$\kappa(z_j,\mathbf{n}_j) = \int_0^{r_j} dr\, \frac{r_j - r}{2 r_j\, r}\,\Delta_\Omega(\Phi+\Psi)(r,\mathbf{n}_j)\,, \tag{5.22}$$

where $r_j \equiv r(z_j)$ and Δ_Ω is the Laplace operator on the sphere surface. On top of that, n_i and n_j denote the galaxy distribution function of the lenses and sources, respectively, and j_ℓ stands for the spherical Bessel function of order ℓ. The parameters A, n_s, and k_* denote the amplitude, spectral index, and pivot scale of the primordial power spectrum defined through[5] $k^3\langle\Psi_{in}(\mathbf{k})\Psi_{in}(\mathbf{k}')\rangle = (2\pi)^3 A (k/k_*)^{n_s-1}\delta(\mathbf{k}+\mathbf{k}')$. Note that in eq. (5.20), we

---

[4] Let us remind that this is just κ_g (first term in eq. (1.52)) as discussed in sec. 2.3. We remind that what galaxy surveys measure is the shear γ, which can be identified with κ_g. In other words, the full κ field of eq. (1.52) entering in the magnification matrix (1.48) can be identified with γ when neglecting the relativistic effects, which we do in this context. Therefore, we allow ourselves for an abuse of our own notation and hereby use κ when actually referring to κ_g.

[5] Note that A is related to the amplitude A_s defined in Planck through $A = 8\pi^2 A_s/9$.

have neglected the correlation between the convergence and RSD (the second term in eq. (5.21)), as is done, e.g., in [59], since those are subdominant for thick tomographic bins. We also neglect correlations involving the Doppler lensing, which is only relevant at small z and wide-angles (i.e. very large separations) [31, 34].

Using the Limber approximation and inserting eq. (5.19), (5.3), and (2.13) into eq. (5.20) we find the harmonic power spectra to take the form

$$C_\ell^{\Delta\kappa}(z_i,z_j) = \int \mathrm{d}z\, n_i(z) b_i(z) \int \mathrm{d}z' n_j(z') \frac{r'-r}{rr'} \\ \times \frac{3\ell(\ell+1)}{2(\ell+1/2)^2} \mathcal{H}^2(z) \frac{J(z)}{D_1(z)} P_{\delta\delta}\left(k_\ell, z\right) , \tag{5.23}$$

where $k_\ell \equiv (\ell+1/2)/r$. Notice that this is consistent with the insertion of eqs. (2.79) and (2.82) into eq. (2.77). The background quantities are evaluated at the same effective redshift. Once more, we have neglected the k-dependence of the functions D_1 and J. However, the methodology could be generalized to include the scale-dependence in case of need, as in the galaxy clustering case. From eq. (5.23), we see that J is evaluated at the redshift of the lenses, whose distribution is given by $n_i(z)$.

Writing now the density power spectrum as

$$P_{\delta\delta}\left(k_\ell, z\right) = \left[\frac{D_1(z)}{D_1(z_*)}\right]^2 P_{\delta\delta}^{\mathrm{lin}}\left(k_\ell, z_*\right) B\left(k_\ell, z\right) , \tag{5.24}$$

we can rewrite eq. (5.23) as

$$C_\ell^{\Delta\kappa}(z_i,z_j) = \frac{3}{2} \int \mathrm{d}z\, n_i(z) \mathcal{H}^2(z) \hat{b}_i(z) \hat{J}(z) \\ \times B\left(k_\ell, z\right) \frac{P_{\delta\delta}^{\mathrm{lin}}\left(k_\ell, z_*\right)}{\sigma_8^2(z_*)} \int \mathrm{d}z' n_j(z') \frac{r'(z')-r(z)}{r(z)r'(z')} , \tag{5.25}$$

where we have defined

$$\hat{J}(z) \equiv \frac{J(z)\sigma_8(z)}{D_1(z)} = \frac{J(z)\sigma_8(z_*)}{D_1(z_*)} , \tag{5.26}$$

and

$$\hat{b}_i(z) \equiv b_i(z)\sigma_8(z) . \tag{5.27}$$

From eq. (5.25), we see that galaxy-galaxy lensing is affected by four distinct ingredients:

1. The background expansion of the Universe, through the Hubble function $\mathcal{H}(z)$ and the comoving distance $r(z)$.
2. The density fluctuations at redshift z_*, before acceleration started.
3. The nonlinear boost factor B.
4. The evolution of density and gravitational potential at late times, through the two functions $\hat{b}$ and $\hat{J}$.

Ingredients 1 and 2 are tightly constrained by cosmic microwave background (CMB) measurements. In the analysis we will therefore fix them, for simplicity, using the latest Planck ΛCDM values for A_{s}, n_{s}, $\Omega_{\mathrm{m},0}$, $\Omega_{\mathrm{b},0}$, and h [6] [6]. But we note that the methodology described in this work would allow for a combination of galaxy survey data with CMB observations to constrain all parameters together, including the cosmological and the $\hat{J}$ and $\hat{b}$ parameters. Ingredient 3 depends in principle on the theory of gravity. However, the standard method to infer the nonlinear boost is by generating cosmological simulations, which require the choice of a specific modified gravity model. Therefore, it is not possible to obtain a general nonlinear boost factor for our parametrization. In this work, we follow the approach considered in the Dark Energy Survey analysis [63] and keep the standard halofit nonlinear boost [141], while limiting the range of scales used in the analysis to avoid entering deeply into the nonlinear regime. We also consider a more stringent scale cut to assess the impact of this choice of boost in our results, showing that it is subdominant and constitutes, therefore, an acceptable approximation. Finally, ingredient 4 is what we want to measure in this work. In practice, we assume $\hat{J}$ and $\hat{b}$ to be free parameters with a constant value within each tomographic bin, and we focus on constraining them.

As can be seen from eq. (5.25), once we consider $\hat{J}$ and $\hat{b}$ as free parameters with a constant amplitude in each tomographic bin, their product is fully degenerate. Therefore, as mentioned at the beginning of the section, we do not consider galaxy-galaxy lensing measurements alone, but rather their combination with galaxy clustering, using the same photometrically-selected lenses.

The harmonic power spectra for galaxy clustering, using the Limber approximation, was computed in sec. (2.3). Here we just transform the expression in terms of our parametrization. Using the Limber's approximation, we combine eqs.(2.77) and (2.79) to find the expression for the photometric clustering

$$C_\ell^{\Delta\Delta}(z_i, z_j) = \int \mathrm{d}z\, n_i(z) n_j(z) \frac{\mathcal{H}(z)(1+z)}{r^2(z)}\, \hat{b}_i(z)\hat{b}_j(z)\, B\left(k_\ell, z\right) \frac{P^{lin}_{\delta\delta}\left(k_\ell, z_*\right)}{\sigma_8^2(z_*)}\,. \tag{5.28}$$

Combining this expression for the galaxy clustering observable with the galaxy-galaxy lensing observable in eq. (5.25), we can break the degeneracy between $\hat{J}$ and $\hat{b}$ and constrain both sets of parameters at the same time.

This procedure allows us to measure the evolution of the gravitational potentials, $\Phi + \Psi$, in a model-independent way. The only assumption underlying such an analysis is that at high redshift z_*, before acceleration started, we recover GR. Note that this procedure is similar to the one used in RSD measurements, where the density power spectrum at z_* is constrained by CMB measurements, and RSD are used to measure $\hat{b}$ and $\hat{f} \equiv f\sigma_8$ in a model-independent way in each redshift bin, see, e.g., [101].

---

[6] Note that here we assume that the background evolution is consistent with ΛCDM predictions, since this has been so far confirmed by observations. This assumption is common in large-scale structure analyses, see, e.g., [101].

$\mu-\Sigma$ approach	Our approach
$A_s,\ n_s,\ \Omega_{\rm b,0},\ \Omega_{\rm m,0},\ h$	$A_s,\ n_s,\ \Omega_{\rm b,0},\ \Omega_{\rm m,0},\ h$
$b(z)$	$\hat{b}(z)=b(z)\sigma_8(z)$
$\Sigma(z)$	$\hat{J}(z)=\Sigma(z)\Omega_{\rm m}(z)\sigma_8(z)$
$\mu(z)$	adding RSD: $\hat{f}(z)=f(z)\sigma_8(z)$

Table 5.1: Comparison of the parameters used in the standard $\mu-\Sigma$ approach and in our approach. On top of those, let us remind we also have an independent measurement for Ψ via the parameter $\hat{I}$, that should be added into the column of the right.

5.4.1 *Comparison with the standard $\mu-\Sigma$ parametrization*

Before moving to the Fisher analyses, let us compare our approach with the standard parametrization used in weak lensing analyses. Modifications to GR are usually encoded into two phenomenological functions, $\mu(k,z)$ and $\eta(k,z)$, that modify Poisson's equation and the relation between the two gravitational potentials:

$$k^2\Psi = -4\pi G a^2\,\mu(z,k)\,\bar{\rho}_m\delta\,, \tag{5.29}$$

$$\Phi = \eta(z,k)\,\Psi\,. \tag{5.30}$$

The sum of the gravitational potentials can then be written as

$$k^2(\Phi+\Psi) = -3\mathcal{H}^2(z)\Omega_{\rm m}(z)\Sigma(z)\delta(k,z), \qquad \Sigma=\frac{\mu}{2}(1+\eta). \tag{5.31}$$

With this the galaxy-galaxy lensing power spectra and the galaxy clustering power spectra become

$$C_\ell^{\Delta\kappa}(z_i,z_j) = \frac{3}{2}\int {\rm d}z\, n_i(z)\mathcal{H}^2(z)\Omega_{\rm m}(z)b_i(z)\Sigma(z) \times B\left(k_\ell,z\right)P_{\delta\delta}^{\rm lin}\left(k_\ell,z\right)\int {\rm d}z' n_j(z')\frac{r'(z')-r(z)}{r(z)r'(z')}\,, \tag{5.32}$$

$$C_\ell^{\Delta\Delta}(z_i,z_j) = \int {\rm d}z\, n_i(z)n_j(z)\frac{\mathcal{H}(z)(1+z)}{r^2(z)}\,b_i(z)b_j(z)\,B\left(k_\ell,z\right)P_{\delta\delta}^{lin}\left(k_\ell,z\right)\,. \tag{5.33}$$

The galaxy-galaxy lensing power spectra depend directly on the function $\Sigma(z)$. In addition, both the galaxy-galaxy lensing power spectra and the clustering power spectra depend on μ, since the evolution of δ, and consequently the matter power spectrum at redshift z, are sensitive to μ.

Comparing eq. (5.32) with eq. (5.25) we see that

$$\hat{J}(z) = \Sigma(z)\Omega_{\rm m}(z)\sigma_8(z)\,. \tag{5.34}$$

In table 5.1, we list the set of free parameters in the standard $\mu-\Sigma$ parametrization and in our parametrization. The parameters in the first line are the standard cosmological parameters that are best determined by the CMB, and that are the same in both cases. In our forecasts, we will keep them fixed for simplicity, but in practice, in both approaches, one can combine lensing with CMB measurements to constrain these parameters. In addition to these standard parameters, the $\mu - \Sigma$ parametrization has three free parameters per redshift bin (b, Σ, μ), whereas our parametrization has two free parameters per redshift bin $(\hat{b}, \hat{f})$. One could conclude that the $\mu - \Sigma$ parametrization is more powerful since it allows us to measure one more parameter at each redshift. This is however not the case, since b, Σ, and μ are strongly degenerated in eq. (5.32) and (5.33). To break the degeneracy it is necessary to add new information, through RSD, which are sensitive to μ and b. In our approach, adding RSD would add one new free function $\hat{f}(z) = f(z)\sigma_8(z)$, that can directly be measured from RSD and leads to the same number of free parameters in both approaches.

From this we see that the first key property of our approach is that it separates clearly the information that can be measured with the 2×2pt lensing measurements, from the information that can be measured from RSD. The 2×2pt data measure the evolution of $\Phi + \Psi$ and the evolution of the galaxy density, whereas RSD measure the evolution of the velocity (and again the evolution of the galaxy density). In the standard $\mu - \Sigma$ parametrization this separation cannot be applied since the parameters b, Σ, and μ can only be measured by combining lensing with RSD.

The second specificity of our approach is to allow for a direct measurement of the parameters $\hat{f}$ and $\hat{b}$ in each redshift bin. In contrast, in the $\mu - \Sigma$ approach, it is not straightforward to measure $\mu(z)$ in each redshift bin. The reason for this is that μ enters in eqs. (5.32) and (5.33) through its impact on the matter power spectrum, $P_{\delta\delta}(k, z)$, which depends on the whole time evolution of $\mu(z)$. In other words, to constrain $\mu(z)$ from the 2x2pt data and RSD, we need to solve the modified version evolution equation for the matter density δ (eq. (1.16)), which reads

$$\delta''(k, a) + \left(1 + \frac{\mathcal{H}'(a)}{\mathcal{H}(a)}\right)\delta'(k, a) - \frac{3}{2}\frac{\Omega_{\mathrm{m},0}}{a}\left(\frac{\mathcal{H}_0}{\mathcal{H}(a)}\right)^2 \mu(a)\,\delta(k, a) = 0\,, \tag{5.35}$$

where a prime denotes derivatives with respect to $\ln a$. This means that to measure μ in the bin z_i, it is not enough to measure clustering at z_i and weak lensing at (z_i, z_j). We need instead measurements of these quantities in a variety of redshifts larger than z_i. Two methods have been used to account for this fact. The simplest way is to assume a given evolution for μ with a, for example, see [101, 142]

$$\mu(a) = 1 + \mu_0 \frac{\Omega_\Lambda(a)}{\Omega_{\Lambda,0}}\,, \tag{5.36}$$

where only μ_0 is a free parameter, that is constrained from the data. However, if μ does not evolve in this way, the constraints on μ_0 are not valid. Another possibility is to parametrize μ and Σ in terms of their values in a number of redshift nodes, and then interpolate between the nodes to obtain continuous functions, that can be used to solve eq. (5.35), see [139]. This method does not assume any time evolution, but it depends on the chosen interpolation method, which introduces arbitrary correlations between the nodes. For example, using a cubic spline tends to suppress sharp changes in these functions [139]. In contrast, in our approach, since no evolution equation needs to be solved, no interpolation is needed: $\hat{f}$ can be measured directly in each redshift bin. A theory prior on the evolution of $\hat{f}$ with redshift can be introduced if we want, for example, to reduce the number of free parameters, but this is not required.

Finally, our approach has the advantage to be fully model-independent: we directly measure $\hat{f}$, i.e. the evolution of $\Phi + \Psi$, without any assumption on the theory of gravity or on the behavior of dark matter. This is not the case for the standard $\mu - \Sigma$ approach, which relies on the validity of eq. (5.35) to find δ for a given μ. As shown in [103], if dark matter couples differently than baryonic matter to gravity, or if dark matter is affected by a fifth (non-gravitational) force [138], this equation is modified and the constraints on μ and Σ are not valid.

Measuring $\hat{J}$ is therefore much more direct and robust than measuring Σ and μ. It is actually completely equivalent to measuring $\hat{f} = f\sigma_8$ from RSD. These measurements can indeed also be done in a completely model-independent way, in each of the redshift bins of the survey. In contrast, going from $f\sigma_8$ to μ requires to solve the evolution equation (5.35) for δ. In the next section, we will present an example where measuring $\hat{J}$ is very useful and allows us to measure η redshift bin by redshift bin, without having to assume anything on the evolution of μ, and, as stated previously, without having to assume a specific behavior for dark matter. Note that from table 5.1, we expect the relative constraints on $\hat{J}$ and $\hat{f}$ to be of similar amplitude as the relative constraints on Σ and μ.

To finish this section of comparison with other parametrizations, it is worth considering the recent analysis presented in [143]. The author considers a template-fitting approach to constrain the growth of matter perturbations with cosmic shear analyses in a model-independent way, which is similar to our goal. There is however an important difference with respect to our approach, which is that in [143], GR is assumed, and therefore eq. (2.9) is used to relate the evolution of $\Phi + \Psi$ to the evolution of the density. The main goal of this method is therefore to measure the growth of density, without being affected by the bias. Hence, the free function that is fitted from the data is $\Omega_{\mathrm{m}}(z)\sigma_8(z)$. In our case, on the other hand, we use lensing to measure directly the evolution of $\Phi + \Psi$, i.e. $\hat{J}(z)$, without assuming GR. Note that because of that, we choose our reference power spectrum at $z = z_*$ (where we assume GR to be recovered) instead of $z = 0$, as is done in [143]. Furthermore, we assume the shape of the template power spectrum to be given by CMB measurements, instead of assuming a fiducial cosmology and accounting for it with an Alcock-Paczyński parameter. We also differ in the fact that we use mildly nonlinear scales with a GR nonlinear boost factor. Finally, another relevant difference is that in [143] the author considers the cosmic shear observable and, because of this, he includes the BNT nulling technique proposed in [144]. Such technique allows the author to obtain localized cosmic shear kernels and therefore constrain the growth at different redshift bins. In our analysis, we consider the galaxy-galaxy lensing observable. Therefore, the agnostic $\hat{J}$ function only appears at the level of the lenses, which are already localized.

Other recent model-independent analyses to test modified gravity that are worth mentioning are the Dark Energy Survey Year 1 analysis splitting between growth and geometry [145] and the Dark Energy Survey Year 3 (DES Y3) analysis binning σ_8 as a function of redshift [63]. The former considered a split of a subset of cosmological parameters, such that one parameter was sensitive to the growth of perturbations and the other one was sensitive to the geometry of the Universe. Within ΛCDM, the two parameters should agree and provide the same value. In the Year 3 analysis, a successor of this method was considered by introducing a set of amplitudes (one per redshift bin) that scale the linear power spectrum. These translate into the value of σ_8 at redshift 0 based on the amplitude of structure in a given redshift bin. These methods can be seen as consistency tests of ΛCDM, where any deviation would consist in an indication for beyond-ΛCDM physics. Instead, our method focuses on directly measuring the evolution of the gravitational potentials and the anisotropic stress as a function of redshift in a model-independent way. Finally, a recent measurement of $\hat{J}$ using DES Y3 data has been performed in ref. [146], showing that DES Y3 data prefers high values of the primordial fluctuations and a slow evolution of the Weyl potential. The authors also show that this feature lies at the core of the well-known σ_8 tension. Let us emphasize that the technique for measuring $\hat{J}$ is model-independent and can therefore be compared with any theory of gravity.

5.5 ANISOTROPIC STRESS

Now that we have derived the parametrization of the gravitational lensing and gravitational redshift observables, we can combine them to measure the anisotropic stress, or gravitational slip, defined as the ratio between the two Bardeen potentials, $\eta = \Phi/\Psi$. The combination of the two redshift dependent functions accounting for the evolution of Ψ and the Weyl potential provides a redefinition of the anisotropic stress estimator

$$O^{stress} \equiv \frac{\hat{I}(z)}{\hat{J}(z)} = \frac{T_{\Phi+\Psi}(k, z_*)}{T_\Psi(k, z_*)}\frac{T_\Psi(k, z)}{T_{\Phi+\Psi}(k, z)} = \frac{2\Psi}{\Phi+\Psi} = \frac{2}{1+\eta}, \tag{5.37}$$

where in the first equality we use eqs. (5.17) and (5.5). The boost, $B(k, z)$, cancels in the ratio since it is expected to affect in the same manner the evolution of Ψ and of $\Phi + \Psi$ (it encodes indeed the nonlinear evolution of matter density – see eq. (5.3)). Moreover, in the second equality we use that $(\Phi + \Psi)(z_*) = 2\Psi(z_*)$, since GR is recovered at z_*.

We note that we consider the ratio of $\hat{I}$ over $\hat{J}$, or equivalently the ratio of Ψ over the Weyl potential, instead of the inverse, because our constraints on Ψ are weaker, as we will see in the following sections. The fact of having weaker constraints allows Ψ to become compatible with a null value, which introduces numerical instabilities in the inverse of eq. (5.37).

Equation (5.37) is a novel estimator of the anisotropic stress, η, in configuration space, which is fully model-independent. It is directly built from measurements of the functions $\hat{J}$ and $\hat{I}$ in the bins of the surveys. If the ratio $\hat{I}/\hat{J}$ differs from 1, we can then unambiguously conclude that gravity is modified. In other words, if a value $O^{stress} \neq 1$ is measured, we will have strong evidence that gravity is purely modified by an anisotropic stress, meaning that the time and spatial perturbations of the metric, encoded in Ψ and Φ, respectively, behave differently on large scales at late-times. In contrast, the standard $\mu - \Sigma$ approach does not allow us to measure η in a model-independent way. In particular, with the standard approach, we could detect an apparent deviation from GR: $\eta \neq 1$, even if gravity is not modified and $\Psi = \Phi$. As has been discussed in [138], this is due to the fact that if dark matter is affected by a fifth force, RSD do not provide a measurement of the true μ. As a consequence, the observed η, which is inferred from a measurement of Σ and μ, will not be the true η (see sec. (4.4) for the discussion regarding the breaking of the Equivalence Principle for dark matter). Our method is therefore crucial for being able to interpret a measurement of $\eta \neq 1$ as a true smoking gun for modified gravity.

6

FORECASTS FOR FUTURE GALAXY SURVEYS

In this Chapter, we discuss the analysis for the novel method to measure the anisotropic stress, which has the key advantage of being model-independent. As explained in Chapters 4 and 5, our method combines direct measurements of the time distortion, Ψ, which can be detected via the effect of gravitational redshift, with measurements of the Weyl potential from gravitational lensing, to *directly* probe the relation between Ψ and Φ. This method does not rely on a specific model of gravity, nor on a particular behavior of dark matter: it uses the data in a completely agnostic way to extract measurable quantities and compare them. In particular, contrary to current measurements from RSD and weak lensing, this method is also valid if the weak equivalence principle is violated, i.e. if dark matter obeys a fifth force.

Our analysis follows the method presented in [121], where it was shown that combining multipoles of the galaxy power spectrum with the galaxy-galaxy lensing power spectrum provides a direct model-independent determination of $\eta \equiv \Phi/\Psi$. We include forecasts for the expected precision on the novel redshift evolution parametrizations for the time distortion Ψ and the Weyl potential $(\Phi+\Psi)/2$. In addition, we apply the method to the coming generation of surveys to determine the precision with which η can be measured. Note that we use here the correlation function and the angular power spectrum, instead of the power spectrum, to properly account for wide-angle effects [24, 42]. Our forecasts show that combining measurements of gravitational redshift from the Square Kilometer Array with measurements of the Weyl potential from the Legacy Survey of Space and Time of the Vera C. Rubin Observatory (LSST) will allow us to constrain the anisotropic stress with a precision of $\sim 20\,\%$, through the relation

$$O^{stress} \equiv \frac{2}{1+\eta} = \frac{2}{1+\Phi/\Psi}. \tag{6.1}$$

The rest of the chapter, based on ref. [122, 123], is organized as follows: in sec. 6.1 we present the specifications of the future galaxy surveys considered, and the methodology used to forecast the constraints on the different parameters under study. We then present and discuss the main results of the analysis in sec. 6.2 for both observables and their combination. We leave the conclusions for the following Chapter 7.

6.1 METHODOLOGY

In this section we present the methodology used to forecast the constraints on the observables presented in Chapter 5. We first describe the galaxy surveys considered and their settings, and then briefly explain the Fisher matrix forecast used in this work.

6.1.1 *Gravitational redshift with SKA*

Future Stage-IV galaxy surveys will provide us with precise spectroscopic data probing the galaxy clustering in our Universe. An example of such a survey is the Phase 2 of the Square Kilometer Array (SKA) [1], expected to be in full operational capacity by 2030, with which we will be able to observe close to a billion of galaxies between redshifts $z = 0.1$ and $z = 2.0$. It is expected that this new data will drastically improve our measurements of the growth history, achieving sub-percent measurements of $f(z)\sigma_8(z)$ [147] using the even multipoles of the galaxy clustering correlation function. In this Chapter we want to show that by combining the measurement of the even multipoles with the dipole we will be able to measure the gravitational redshift at late times.

We set $z_* = 10$, well in the matter era, and as described in Section 5.2 we assumed that the functions $\mu_\ell(z_*, d)$ and $\nu_1(z_*, d)$ are fixed by CMB constraints. Therefore, we vary only $\hat{G}$, $\hat{I}$ and the biases of the bright and faint populations in each redshift bin [2]. We split the galaxies into a bright and faint population with same number of galaxies per redshift bin.

We consider the number density and volume specifications presented in [147] and follow the approach used in [122] to split the populations of galaxies between faint and bright such that we have the same number of each luminosity type per redshift bin. For the fiducial of the galaxy biases we use the exponential fitting functions

$$b_{\rm B} = c_{\rm B}\, e^{d_{\rm B}\, z} + \frac{\Delta b}{2}\,, \tag{6.2}$$

$$b_{\rm F} = c_{\rm F}\, e^{d_{\rm F}\, z} - \frac{\Delta b}{2}\,, \tag{6.3}$$

for the bright and faint populations, respectively, with fiducial values of $c_{\rm B} = c_{\rm F} = 0.554$ and $d_{\rm B} = d_{\rm F} = 0.783$, following [147]. As in [122], we assume a difference between the two galaxy biases of $\Delta b = 1$. This is consistent with the $\mathcal{O}(1)$ difference that has been measured for BOSS in [47]. In our forecasts, we then treat $b_{\rm B}$ and $b_{\rm F}$ as free parameters in each redshift bin and marginalize over them. For the magnification bias, we use the model developed in [103], and we neglect the evolution bias for the two populations. Once data will be available, both the evolution bias and the magnification bias of the two populations will be directly measurable from the average galaxy distribution, although it will be highly non-trivial and completely dependent in the selection criteria. Therefore, we keep these values fixed in our forecasts.

In the first place, we forecast the uncertainties on the different parameters relevant to the observables described in sec. 6.2.1.1 using the SKA Phase 2 specifications. We assume as our independent parameters the values of the functions $\hat{I}$, $\hat{G}$ and the population biases b_B, b_F at each redshift bin. In summary, the parameters considered for the measurements of the distortions of time are given by the vector:

$$\theta_{\hat{I}} = \{\hat{I}_i, \hat{G}_i, \hat{b}_{{\rm B},j}, \hat{b}_{{\rm F},j}\}\,, \tag{6.4}$$

where i runs over the spectroscopic redshift bins. We consider 12 bins of size $\Delta z = 0.1$ in the interval ranging from $z = 0.1$ to $z = 1.3$. From eq. (5.12) we see that the dipole depends not only on $\hat{G}$ in each redshift bin, but also on its time derivative $\dot{\hat{G}}$. Since we

---

[1] https://www.skatelescope.org

[2] Note that the derivatives in the Fisher matrix can be computed analytically for our set of parameters.

do not want to assume anything regarding the evolution of $\hat{G}$, we choose to write this time derivative in a given z-bin in terms of the value of $\hat{G}$ at the neighbour bins. For this purpose, we use the five-point Stencil method

$$\begin{aligned}\dot{\hat{G}}(z_i) =& -(1+z_i)\mathcal{H}(z_i)\frac{d\hat{G}(z_i)}{dz_i}\\ =& -\frac{(1+z_i)\mathcal{H}(z_i)}{12\Delta z}\left[-G(z_{i+2})+8G(z_{i+1})-8G(z_{i-1})+G(z_{i-2})\right]. \end{aligned} \tag{6.5}$$

We have checked that for redshift bins of size $\Delta z = 0.1$, the five-point stencil method allows us to reconstruct $\dot{\hat{G}}(z_i)$ with a precision of 0.1 percent. On the other hand, if we use only two bins to reconstruct the time derivative we would make an error of up to 129 percent at low redshift, due to the fact that $\dot{\hat{G}}$ changes sign. Such a large mistake in $\dot{\hat{G}}$ may bias the measurement of $\hat{I}$.

Secondly, we assume a specific time evolution for the $\hat{I}(z)$ and $\hat{G}(z)$ functions akin to the approach used in standard RSD analysis for constraining deviations from GR. One common assumption is to link the deviations to the amount of dark energy $\Omega_\Lambda(z)$ (see e.g [148]). This is an elegant way to enforce the assumption that any gravity modification can only be relevant at late times, after dark energy begins to dominate the evolution of the Universe. Here we consider the two following models for the evolution of $\hat{G}$ and $\hat{I}$:

$$\hat{G}(z) = f(z)\sigma_8(z)\left[1+\hat{G}_0\,X(z)\right], \tag{6.6}$$

$$\hat{I}(z) = \Omega_m(z)\sigma_8(z)\left[1+\hat{I}_0\,X(z)\right], \tag{6.7}$$

with $X(z) = 1$ for $z \in [0,2]$ in the first model and $X(z) = \Omega_\Lambda(z)/\Omega_\Lambda(z=0)$ in the second model. With this, the analysis is significantly simplified since $\dot{\hat{G}}$ is directly determined by eq. (6.6). Moreover, in this case, instead of considering one free bias parameter per redshift for each population, we assume that the biases evolve as in eqs. (6.2) and (6.3), with four free parameters $c_\mathrm{B}, c_\mathrm{F}, d_\mathrm{B}$ and d_F. The parameters vector will be then

$$\theta_0 = \{\hat{I}_0, \hat{G}_0, c_\mathrm{B}, c_\mathrm{F}, d_\mathrm{B}, d_\mathrm{F}\}. \tag{6.8}$$

Finally, we shall perform two forecasts by choosing different values for the minimum separations between galaxies. This $d_{\mathrm{m}in}$ must be set at the scale on which the linear regime is a good approximation. Following [77], for an optimistic scenario, we choose $d_{\mathrm{m}in} = 20\,\mathrm{M}pc/h$, while for the pessimistic case we set $d_{\mathrm{m}in} = 32\,\mathrm{M}pc/h$. In this regime, the boost in eq. (5.5) plays a negligible role and can therefore be set to 1 in our forecasts. In addition, we set the maximum separation such that it is consistent with the size of our smallest redshift bin, $d_{\mathrm{m}ax} = 120\,\mathrm{M}pc/h$, in all of our bins.

6.1.2 *Gravitational lensing with LSST*

In the following years we will also have access to a huge amount of exquisite photometric data from the future Stage-IV galaxy surveys. Some examples are the Vera C. Rubin Observatory that will carry out the Legacy Survey of Space and Time (LSST[3], [149]), the Euclid satellite[4] [150], or the Nancy G. Roman Space Telescope[5] [151]. In this work we

---

[3] https://www.lsst.org

[4] https://www.euclid-ec.org

[5] https://roman.gsfc.nasa.gov

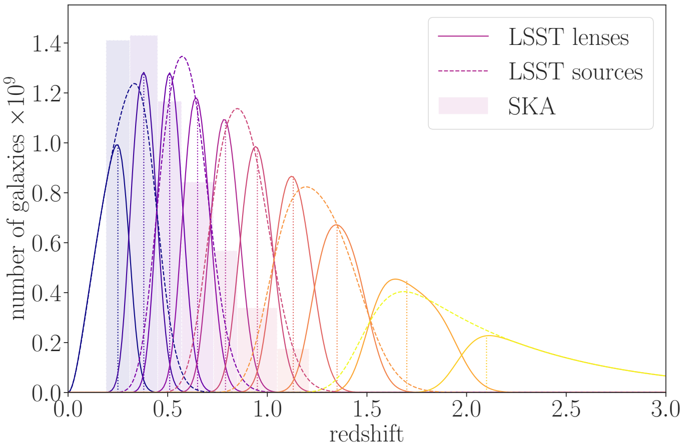

Figure 6.1: Number of galaxies as a function of redshift for the different samples considered. The solid lines stand for the LSST lenses, the dashed lines represent the LSST sources, and the bars represent the SKA spectroscopic top-hat bins, that have been adapted to the LSST lenses. The effective redshift for each tomographic bin is represented with a vertical dotted line.

focus on LSST, whose main science objective from a cosmological perspective is to probe dark energy and dark matter. In order to achieve this, the baseline survey will cover 18 000 square degrees of the Southern sky during 10 years to obtain accurate photometry in multiple optical bands. Such a survey will allow us to obtain accurate photometric redshifts and weak lensing shear measurements for about 27 galaxies per arcmin^2. This will enable precise photometric galaxy clustering, cosmic shear, and galaxy-galaxy lensing cosmological analyses, also called 3×2pt analyses.

In more detail, we consider the survey settings provided with the public version of `CosmoSIS` [152]. These consist in five equipopulated tomographic bins for the sources and ten equipopulated tomographic bins for the lenses with a total of 27 galaxies per arcmin^2, for both sources and lenses. We represent the galaxy distributions in fig. 6.1. Additionally, we consider a linear galaxy bias model with a constant fiducial set to $b = 2$, but treated as a nuisance parameter in each tomographic bin and marginalized over [6]. We also consider the nonlinear alignment model for intrinsic alignments [65, 66] with a fiducial amplitude set to $A_{IA} = 1$ but allowed to vary. We note that we limit our analysis to multipoles between $\ell = 20$ and $\ell = 2627$ in the optimistic scenario and between $\ell = 20$ and $\ell = 750$ in the pessimistic scenario. In both cases we do not go too deep into the non-linear regime, and therefore the linear modeling for galaxy bias and intrinsic alignment can still be assumed as good approximations for our forecasts. Finally, we consider an ellipticity total dispersion of $\sigma_\epsilon = 0.3$.

It is important to mention that we assume GR is valid at small scales where intrinsic alignments are important, that is, we include the intrinsic alignment contribution using a standard GR modeling, even when constraining $\hat{J}$. The main reason for this choice is the lack of intrinsic alignment models for modified gravity theories. However, we marginalize over the amplitude of this effect to account for its impact. We neglect some observational systematic uncertainties, like a shear calibration bias, or biases in the mean

---

[6] We note that a realistic galaxy bias might have some redshift dependence. However, since we marginalize over its value at each redshift bin, we have verified that a different fiducial value for the galaxy bias does not change the size of the final constraints. We therefore keep $b = 2$ as fiducial, for simplicity.

of our galaxy distributions. Moreover, we neglect some contributions to the signal like the impact of magnification or RSD for photometric galaxy clustering and galaxy-galaxy lensing observables. This is also the approach followed in [59], for example. Note that we do not expect magnification to alter the measurement of $\hat{b}$ and $\hat{J}$ at small redshift, where its contribution to the signal is strongly subdominant. Since, as we will see, η is only well measured at small redshift with our estimator, our analysis should be independent of this contamination. Also, RSD are partially washed out in thick tomographic bins and therefore a subdominant contribution to the total signal. In any case, this analysis focuses on determining whether a model-independent measurement of the anisotropic stress can be performed with future observations. Therefore, our first aim is to check its feasibility in an optimistic scenario where the main systematic uncertainties are under control. Obviously this analysis will need to fully account for all observational uncertainties once real observations are available in order to obtain precise and unbiased predictions.

Once we have our theoretical predictions for the observable $\hat{J}$ derived in sec. 5.4 with the specifications provided above, we can forecast the uncertainties on the different parameters using a Fisher matrix formalism. We summarize the parameters considered in our analysis, together with their fiducial values, in tables B.1 and B.2 in the Appendix, but for simplicity our vector of free parameters is given by

$$\theta_{\hat{J}} = \{\hat{J}_i, \hat{b}_i, A_{\mathrm{IA}}, \hat{I}_j, \hat{f}_j, \hat{b}_{\mathrm{B},j}, \hat{b}_{\mathrm{F},j}\}\,, \tag{6.9}$$

where i runs over the ten tomographic bins for LSST and j runs over the seven bins for SKA2. Notice that, in the later case, the effective number of bins on which we can constrain $\hat{I}$ is limited due to the usage of the five-point Stencil method to infer the evolution of $\hat{G}$ (see eq. (6.5)). Hence, even though we use 11 bins, we can only constrain $\hat{I}$ in 7 of them. On top of that, we limit the spectroscopic analysis to the redshift range over which we found meaningful constraints.

6.1.3 *Combining the probes*

In final analysis, we use the measurements on $\hat{J}$ and $\hat{I}$ to build an estimator for the anisotropic stress by comparing the functions $\hat{I}(z)$ and $\hat{J}(z)$ of eq. (5.13) and eq. (5.26), respectively. Importantly, we need to modify the redshift bins considered in the previous section (see also [122]) for $\hat{I}(z)$, in order to obtain constraints at the same effective redshifts than those for $\hat{J}(z)$. These are the redshifts of the lenses. This can easily be done for SKA2, thanks to the very precise determination of redshift. The new top-hat galaxy distributions and the effective redshifts are shown in fig. 6.1. Let us remind that these new redshift bins corresponde to those on which we can extract constraints on $\hat{I}$, but that we need at least four more in order to infer the evolution of $\hat{G}$. After computing the forecast constraints for both $\hat{J}$ and $\hat{I}$, we can combine them and place constraints on the anisotropic stress η. Following the methodology described in Sections 6.1.2 and 6.1.1 and after marginalizing over the last three tomographic bins for $\hat{J}$, we generate a mock chain of 50 000 points for $\hat{J}$ and another one for $\hat{I}$. In each point we compute the ratio presented in eq. (5.37) and compute the posterior at each redshift bin.

6.1.4 *Fisher matrix forecasts*

We estimate the constraints on the parameters by means of the Fisher formalism described in sec. 6.1.4. We compute the Fisher matrices $\mathcal{F}$ using eq. (2.106), where $\bar{\mathcal{X}}$ is the mean of the data vector and COV is the covariance matrix of the data. These will correspond to the galaxy-galaxy lensing and galaxy clustering harmonic spectra for LSST, and to the correlation function multipoles for SKA2. We consider a Gaussian covariance for the former, meaning that we account for the cosmic variance and shape/shot noise, but neglect non-Gaussian terms like the super-sample covariance, as was done in [59]. For SKA2, we include shot noise and cosmic variance in the variance of the multipoles and account for cross-correlations between the different combinations of luminosity pairs. Details on the multipoles covariance matrix are given in sec. 2.4. Importantly, we do not include the non-zero cosmic variance associated to the dipole, arising from the relativistic corrections (given by eq. (2.92)). This has mostly a publication timing reason, as ref. [39] is posterior to refs. [122, 123]. Nevertheless, it's impact on the results should be small for the separations considered in these works. We note that, because of our ΛCDM fiducial, we use GR to compute these covariances. Once the Fisher matrix is computed, we estimate the covariance matrix of the model parameters as the inverse of the Fisher matrix (see eq. (2.108)).

In practice, we use `CosmoSIS` to call the `CAMB` Boltzmann solver [153, 154] and compute the Fisher matrix for the $\hat{J}$ parameters. We then use the same Boltzmann solver to build the Fisher matrix for the $\hat{I}$ parameters from the correlation function multipoles. We note that our gravitational lensing observable is also sensitive to $\hat{b}$ and the amplitude of intrinsic alignments, while our gravitational redshift observable depends on the generic growth function $\hat{G} = f\sigma_8$ [7] and galaxy biases $\hat{b}_{\mathrm{B}} = b_{\mathrm{B}}\sigma_8$ and $\hat{b}_{\mathrm{F}} = b_{\mathrm{F}}\sigma_8$. These additional parameters are considered nuisance parameters and we marginalize over them when providing constraints on $\hat{J}$ or $\hat{I}$. We also remind the reader that these observables depend on the cosmological parameters providing the spectrum of matter perturbations at $z = z_*$, but we consider the cosmology fixed.

In addition to the forecast constraints on $\hat{J}$ and $\hat{I}$, sensitive to $\Phi + \Psi$ and Ψ, respectively, we want to combine them to constrain the anisotropic stress. Instead of building a Jacobian transformation to move from one set of parameters to another one, and to keep the non-linearities that may arise in the transformation, we generate synthetic chains from the individual Fisher matrices. In more detail, given a Fisher matrix for the $\hat{J}$ parameters and a Fisher matrix for the $\hat{I}$ parameters, we invert them to obtain the covariances of the parameters. Then, for each one of them, we generate a mock chain centered at our fiducial and with random points drawn from a multidimensional Gaussian distribution with the corresponding covariance. We finally generate a third chain from the ratio of the other two at each point, which provides the posterior on $\hat{I}/\hat{J} = 2/(1+\eta)$. It is important to mention that for the joint analysis we only consider seven redshift bins for $\hat{I}$, while we use ten redshift bins for $\hat{J}$, as can be seen in fig. 6.1. The main reason for this choice is the lack of constraining power on $\hat{I}$ at higher redshifts. Therefore, we further marginalize over the last three tomographic bins for the gravitational lensing observable when it is combined with the gravitational redshift.

---

[7] Note that we treat $\hat{G}$ as a free function, with unknown time evolution. In particular, we do not assume that $f = \frac{d \ln D_1}{d \ln a}$, since this is only true if the continuity equation for dark matter is valid. Since we want to remain agnostic about the behavior of dark matter, we do not assume that this equation is valid.

	z	0.35	0.45	0.55	0.65	0.75	0.85	0.95	1.05
$d_{\rm min}$	$\hat{I}$	0.23	0.24	0.28	0.33	0.39	0.48	0.60	0.77
20	$\hat{G}$	0.002	0.002	0.003	0.003	0.003	0.004	0.004	0.005
$d_{\rm min}$	$\hat{I}$	0.27	0.28	0.32	0.37	0.45	0.55	0.69	0.87
32	$\hat{G}$	0.004	0.004	0.005	0.006	0.006	0.007	0.008	0.009

Table 6.1: 1σ constraints on $\hat{I}$ and $\hat{G}$ relative to their corresponding fiducial value, marginalized over the bias parameters. We show the results for two values of the minimal separation d_{min}, in Mpc/h.

6.2 RESULTS

In this section, we present the main results of the analysis. We first focus on the gravitational redshift and explain the results on Ψ coming from the dipole of the galaxy clustering 2-pt correlation function. We then present the results on gravitational lensing observable and the constraints on $\Phi + \Psi$. Finally, we derive the constraints on the anisotropic stress from the combination of the two observables.

6.2.1 *Gravitational redshift*

We present the first forecast of the gravitational redshift on cosmological scales in a model-independent manner. This effect is proportional to the time distortions potential Ψ and hence represents a measurement on the field itself. As explained in Chapter 5, we can do this by combining the measurement of the even multipoles with a measurement of the dipole of the galaxy clustering 2-point correlation function. This technique will allow to measure the gravitational redshift in a future survey such as SKA2 with a precision of $10 - 30\%$ at late times (see [122]) in bins of size $\Delta z = 0.1$.

We performed two analysis following distinct approaches. For the first example, we propose to measure the evolution of Ψ and the peculiar velocity field. For this purpose, we assume as free parameters the values of the functions $\hat{I}$ and $\hat{G}$ at each of the 12 redshift bins. The population biases of the bright and faint population are treated as independent nuisance parameters we marginalize over. In the second analysis we introduce a fixed redshift evolution for $\hat{I}$, $\hat{G}$ (see eqs. (6.6) and (6.7)) and the galaxy biases (see eqs. (6.2) and (6.3)) which simplify the analysis effectively reducing the number of relevant and nuisance parameters.

6.2.1.1 *Constraints per redshift bin*

In table 6.1, we show the 1σ constraints on $\hat{I}$ and $\hat{G}$, marginalized over the bias parameters. Note that due to the five-point stencil method we cannot constrain $\hat{I}$ in the first two and in the last two redshift bins, since in these four bins $\dot{\hat{G}}$ is not constrained. We show therefore the constraints starting at $z = 0.35$. We compute the constraints starting at two different minimum separations: $d_{\rm min} = 20\,$Mpc/h and $d_{\rm min} = 32\,$Mpc/h, since non-linearities have been shown to become relevant around those scales [77]. Since the signal-to-noise ratio peaks around 30 Mpc/h and then slowly decreases with

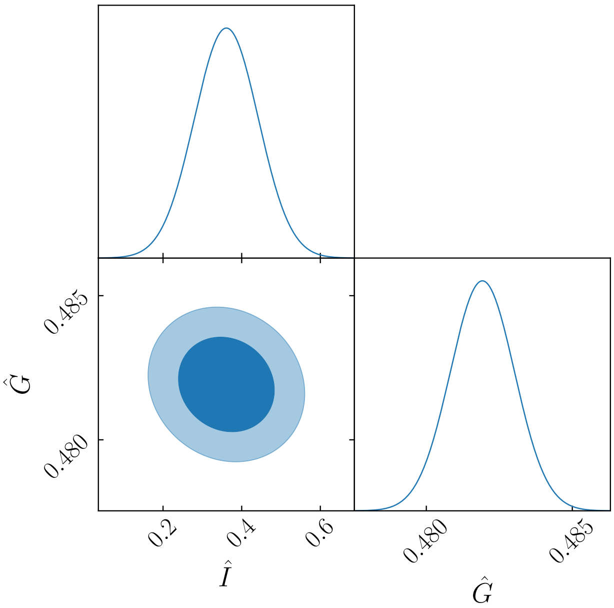

Figure 6.2: Joint constraints of $\hat{I}$ and $\hat{G}$ at $z = 0.35$, with $d_{\text{min}} = 20\,\text{Mpc}/h$.

separation (see e.g. fig. 5 in [54]), separations above $d_{max} = 160\,\text{Mpc}/h$ are irrelevant. The constraints are therefore obtained from separations well inside the horizon, which justifies the use of the quasi-static approximation.

We see that at low redshift, the constraints on $\hat{I}$ are very good, providing a direct measurement on the evolution of the potential Ψ with a precision of 20-30 percent. Combining such a measurement with gravitational lensing will allow us to distinguish unambiguously between deviations from GR and dark fifth force models. Comparing with current tests of gravity, we see that the precision with which Ψ will be measured with the coming generation of survey is similar to the precision with which the evolution of the velocity field is currently measured: in [101], for example, the combination $f(z)\sigma_8(z)$ is measured with a precision of 10-30 percent in various redshift bins. The future constraints on $\hat{G}$ are tighter than those on $\hat{I}$ by almost two order of magnitude. This is not surprising since $\hat{G}$ is constrained by the even multipoles, which will be measured with exquisite accuracy with SKA2, whereas $\hat{I}$ is constrained only by the dipole, which has a significantly lower signal-to-noise ratio. Interestingly, the constraints on $\hat{I}$ are only mildly degraded (by $14-18\%$) when increasing d_{min} from 20 to 32 Mpc/h. In contrast, the constraints on $\hat{G}$ are degraded by 100%. This is due to the fact that the gravitational potential is much less affected by non-linearities than density and RSD.

In fig. 6.2 we show the joint constraints on $\hat{G}$ and $\hat{I}$ at $z = 0.35$. We see that the parameters are almost not degenerate. This is due to the fact that the even multipoles are only sensitive to $\hat{G}$ and can therefore efficiently break the degeneracy between $\hat{G}$ and $\hat{I}$ in the dipole.

Finally, we have also performed forecasts for the parameter $\tilde{I} \equiv (\hat{b}_{\text{B}} - \hat{b}_{\text{F}})\hat{I}$ which directly enters into the dipole. The constraints on this parameter are only very slightly better than those on $\hat{I}$ (by 0.1 percent). Hence, even though $\hat{I}$ seems to be completely degenerate with the galaxy biases in the dipole (see eq. (5.12)), these biases are so well constrained by the even multipoles, that the degeneracy is completely broken. Regarding

	No evolution		Evolution	
$d_{\rm min}[{\rm Mpc}/h]$	20	32	20	32
$\hat{I}_0$	0.10	0.11	0.15	0.18
$\hat{G}_0$	0.001	0.002	0.002	0.003

Table 6.2: 1σ constraints on $\hat{I}_0$ and $\hat{G}_0$, marginalized over the bias parameters, for the two models described after eq. (6.7).

the magnification and evolution bias, we emphasize on that we have not included them into the current analysis, assuming they shall be directly measurable from the specific galaxy samples.

6.2.1.2 *Constraints from a specific time evolution*

When constraining deviations from GR, standard RSD analyses usually assume a specific time evolution for the functions encoding these deviations. One common assumption is to use that the deviations evolve proportionally to the amount of dark energy $\Omega_\Lambda(z)$, (see e.g [148]). We introduced the functional form of this time evolution in sec. 6.1.1. In practice, we are now left with two free parameters encoding the amplitude of the gravitational potential and the peculiar velocities *today*, $\hat{I}_0$ and $\hat{G}_0$ respectively. Additionally, we also simplified the population biases by assuming as nuisance parameters the four $c_{\rm B,F}$ and $d_{\rm B,F}$ of eqs. (6.2) and (6.3).

The marginalized constraints on $\hat{G}_0$ and $\hat{I}_0$ are shown in table 6.2. For the constant model, we reach a precision of 10% on $\hat{I}_0$, which decreases to 15% for the dynamical model.

6.2.2 *Gravitational lensing*

In the top panel of fig. 6.3 we present the $1\,\sigma$ forecast uncertainties for $\hat{J}$ with respect to their fiducial value as a function of redshift. We show the optimistic scenario in red, corresponding to scale cuts $\ell_{max} = 2627$, and the pessimistic scenario in blue, corresponding to $\ell_{max} = 750$. A given offset has been added in the x-axis for illustrative purposes.

As can be seen in fig. 6.3, there is a degradation of the constraints on $\hat{J}$ as a function of redshift. This behavior is essentially due to two effects. First, at high redshift, the tomographic bins are wider, which implies that there is a more significant smoothing of the galaxy clustering distribution along the line-of-sight. Because of this, the amplitude of the galaxy-galaxy lensing spectra decreases, leading to worse constraints on $\hat{J}$. Second, at high redshift, the lenses are necessarily closer to the sources, which decreases the lensing kernel, and in addition, the lenses are correlated with a smaller number of bins, which decreases the number of independent measurements of $\hat{J}$ at that redshift. Let us for example consider the tomographic bin number two for the lenses in fig. 6.1, which is centered at redshift $z \sim 0.4$. The lensing efficiency will peak at roughly the double of this redshift, implying that the sources in the third tomographic bin, which is centered at redshift $z \sim 0.9$, will provide a high signal-to-noise measurement. In addition, this

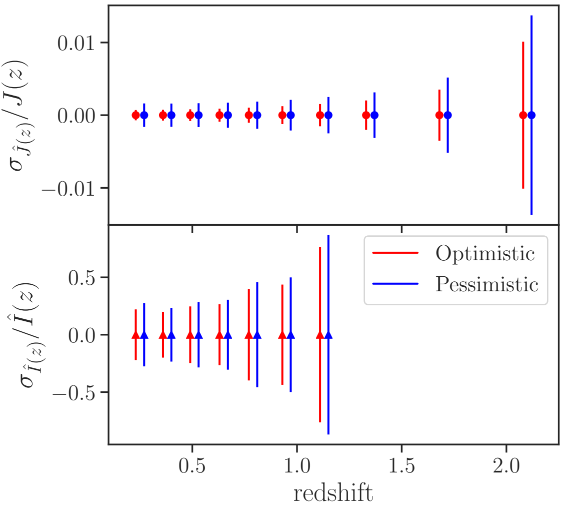

Figure 6.3: Forecast $1\,\sigma$ uncertainties for $\hat{J}$ (top panel) and $\hat{I}$ (bottom panel) with respect to their fiducial value for each tomographic bin. The red (light gray) error bars correspond to the optimistic scenario, while the blue (dark gray) error bars represent the pessimistic settings described in the text.

second bin is also correlated (albeit less strongly) with the bins number two, four, and five of the sources, providing four independent measurements of $\hat{J}$ at $z \sim 0.4$. On the other hand, if we consider the high-redshift lenses, like tomographic bins number seven or higher (effective redshifts higher than $z \sim 1.2$), there are no sources at the double of these effective redshifts, where the signal would be the strongest. This means that only the very low-redshift tail of the lenses distributions will be close to half the effective redshift of the sources. Therefore, this will lead to a decrease of the lensing kernel and thus a decrease of the galaxy-galaxy lensing signal. Furthermore, since the lenses are not correlated with the sources at lower redshift, the lenses bin number seven is only correlated with the sources bin number four and five, which provides only two independent measurements of $\hat{J}$. All together, these effects lead to worse constraints on $\hat{J}$ at high redshift. We note that all tomographic bins have the same number of galaxies with the same ellipticity dispersion. Therefore, the shape and shot noise are the same for all redshifts. Cosmic variance is instead a bit smaller at high redshift, given the larger volume, but not enough to compensate the effects mentioned above. However, even accounting for the degradation as a function of redshift, LSST will be able to constrain $\hat{J}$ as a function of redshift at less than percent level, and therefore probe the Weyl potential with very high precision.

Let us mention that we have validated our method to measure $\hat{J}$, by comparing it with the standard method, assuming ΛCDM. For this we have proceeded in the following way. First, we have verified that replacing the standard ΛCDM harmonic power spectra by the ones provided in eqs. (5.25, 5.28) with the $\hat{J}$ and $\hat{b}$ values in eqs. (5.26-5.27), we recover the same constraints on the cosmological parameters at the level of 0.1 %. We note that in this test we have fixed the values of $\hat{J}$ and $\hat{b}$ and constrained the cosmological parameters, with the goal of testing the implementation of the new harmonic spectra against the standard method. In a second step, we have assumed $\hat{J}$ and $\hat{b}$ to be constant within each redshift bin and moved them out of the integral. Their values have then been fixed according to eqs. (5.26-5.27) at the effective redshift of the corresponding bin. Under this assumption, the recovered constraints on the cosmological parameters degrade by a factor between 1 and 3.5 compared to the constraints obtained with the standard approach. Such a discrepancy is expected, since by fixing the value of $\hat{J}$ and $\hat{b}$ in each redshift bin, we remove the information coming from the evolution of these quantities inside the bins. Performing the same test with twice the number of redshift bins, we have found that the degradation reduces to a factor between 1 and 1.8, showing that as we increase the number of bins and the approximation of constant $\hat{J}$ and $\hat{b}$ is more valid, we recover the standard constraints with our new implementation.

Besides validating our methodology, this test also shows the level of degradation on the cosmological constraints due to our requirement of model-independence. Since we want to measure the evolution of the Weyl potential without assuming a specific theory of gravity, we are limited by the size of the tomographic bins. Contrary to standard methods, where the evolution within a redshift bin is given by the model, here we can only measure the value of the Weyl potential at the effective redshift of the bins, therefore loosing part of the information.

6.2.3 *Anisotropic stress with the combination of probes*

Measuring the anisotropic stress employing the technique proposed in sec. 5.5 requires of the combination of spectroscopic and photometric data. Ideally, we need to measure the evolution of time distortions Ψ and of the Weyl potential $(\Phi + \Psi)/2$ from the same underlying sample. In practice, we forecast the precision of the spectroscopic data SKA2 for measuring $\hat{I}$ and of the photometric data provided by LSST for measuring $\hat{J}$. The anisotropic stress estimator O^{stress} is then simply defined as the ratio $\hat{J}/\hat{I}$ (see eq. (6.1)).

Let us first focus on the spectroscopic side of the analysis with the dipole measurements. We present the main results for $\hat{I}$ in the bottom panel of fig. 6.3. As for $\hat{J}$ in the top panel, we present the $1\,\sigma$ forecast uncertainty on $\hat{I}$ with respect to their fiducial value as a function of redshift. We present both the optimistic (red) and pessimistic (blue) scenarios, which correspond to $d_{\rm min} = 20\,\text{Mpc}/h$ and $d_{\rm min} = 32\,\text{Mpc}/h$, respectively. As for the gravitational lensing observable, the uncertainties on $\hat{I}$ increase as a function of redshift. This is due to the fact that the signal decreases with increasing redshift, given the decreasing growth at higher redshifts. Moreover, shot-noise increases quickly as a function of redshift, as can be seen in the drop of the number of galaxies in fig. 6.1.

Overall, SKA2 will be able to constrain $\hat{I}$ as a function of redshift at the level of $\sim 20\%$. These results are consistent with the forecasts presented in sec. 6.2.1.1 (see also [122]), although different redshift bins have been considered for this re-analysis. Let us recall that we needed to adapt the z binning so that we compare $\hat{I}$ and $\hat{J}$ at the redshifts of the gravitational lenses. It is important to note that the constraining power on $\hat{J}$ is much stronger than on $\hat{I}$, but this is an expected result. The signal-to-noise ratio (SNR) of the galaxy-galaxy lensing observable is already of 148 with current observations [155], while the expected SNR for gravitational redshift is much lower. Using the bins defined in this analysis, the SNR can be computed as

$$SNR^{\Psi} = \sum_{z} \sum_{ij} \xi_1^{\Psi}(d_i, z) \text{COV}^{-1}(d_i, d_j, z) \xi_1^{\Psi}(d_j, z)\,, \tag{6.10}$$

where $\xi_1^{\Psi}(d_i, z)$ is the gravitational redshift contribution to the dipole, i.e. the contribution from the last term in eq. (5.12), evaluated at separation d_i and in the redshift bin z, and

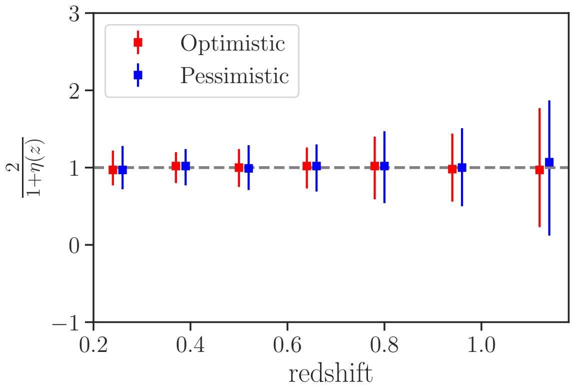

Figure 6.4: Reconstruction of $2/(1+\eta)$ as a function of redshift. The dashed horizontal line represents the fiducial, while the vertical error bars show the optimistic (red, light gray) and pessimistic (blue, dark gray) forecast uncertainties.

$\mathrm{cov}(d_i, d_j, z)$ stands for its covariance at separations d_i and d_j and redshift bin z. Summing from 20 to 120 Mpc/h, we find a total SNR of 8. Note that the SNR of the dipole is significantly larger, due to the Doppler effects, but these terms do not contribute to the constraints on $\hat{I}$. Therefore, it is not surprising that the constraints obtained with gravitational lensing will be much more stringent. However, the particularity of the dipole is that it allows us to directly constrain $\hat{I}$ and therefore directly probe Ψ in a model-independent way, something that cannot be done with any other observable at cosmological scales.

In addition, let us stress that the constraining power on $\hat{I}$ directly depends on the magnitude of the bias difference between the bright and the faint population. In this analysis, we assumed a bias difference of 1, consistent with what has been measured for BOSS in [47]. If the bias difference turns out to be smaller [8], the constraints presented in this analysis worsen by a factor of ~ 2. However, the final results still provide stringent constraints.

Finally, we present in fig. 6.4 the $1\,\sigma$ uncertainties on $2/(1+\eta)$ as a function of redshift for both the optimistic (red) and pessimistic (blue) scenarios. Again, an offset in the x axis has been included for illustrative purposes. As it was the case for $\hat{J}$ and $\hat{I}$, there is a degradation of the constraining power as a function of redshift, which is given by the same physical effects since we are computing the ratio of the two quantities. We can appreciate a more significant degradation compared to the $\hat{J}$ case, but this is due to the fact that the uncertainties are driven by the uncertainties on $\hat{I}$. Overall, the combination of LSST and SKA2 will allow us to constrain the anisotropic stress, through the relation $2/(1+\eta)$, in a model-independent way as a function of redshift and at the level of $\sim 20\,\%$ in the optimistic scenario ($\sim 30\,\%$ in the pessimistic case). Note again that if the bias difference is of order $\mathcal{O}(0.5)$, the final constraints on η worsen by a factor of ~ 2. Finally, let us mention that since the uncertainties are essentially dominated by the dipole, we do not expect a significant gain on the constraints if we add cosmic shear into the analysis.

---

[8] See, e.g., the analysis of [120], which finds a bias difference of order $\mathcal{O}(0.5)$. See also ref. [39] for an study for the Dark Energy Spectroscopic Instrument (DESI), where they find bias differences slightly smaller than $\mathcal{O}(1.0)$ and a strong dependence on the proportion between bright and faint galaxies.

7

SUMMARY AND CONCLUSION

In this Part we have addressed the question of how well future surveys will be able to constrain the laws of gravity. Given how open this question is, one way to answer it is by comparing the two gravitational potentials encoding the time distortion and the spatial distortion, that is Ψ and Φ, respectively. This comparison is a key test of the validity of GR, since it compares directly the two independent degrees of freedom of the Universe's geometry. In contrast, the growth of structure is less direct: a deviation from the ΛCDM prediction can indeed be generated not only by modified gravity, but also by a fifth force acting on dark matter, or by a dark energy component that is clustering. Because of this, measuring $\eta \neq 1$ is often regarded as the smoking gun of modified gravity.

Many analyses exist in the literature constraining the anisotropic stress, η, with current observations [63, 101, 110, 142], or forecasting the expected constraints with future surveys [72, 75, 86]. However, these analyses all rely on the validity of the weak equivalence principle. Hence, they are simply not valid if dark matter obeys a fifth force. In this work we have built a new estimator, which does not rely on the behavior (or even on the existence) of dark matter, and we have forecast the expected constraints from future galaxy surveys.

In Chapter 4, we introduced a new model-independent test of gravity in a proof-of-concept manner. Our method relies on two basic ingredients: the first ingredient are the multipoles of the galaxy clustering power spectrum, which are essentially sensitive to the density perturbations δ, the peculiar velocities of galaxies $\mathbf{V}$, and the time distortions potential Ψ; the second ingredient is the (angular) power spectrum of the galaxy-galaxy lensing correlations, i.e. the correlations between cosmic shear and galaxy clustering. We show that the dipole of the galaxy clustering power spectrum is directly sensitive to an effect called gravitational redshift, which affects the light reaching to us from the bottom of gravitational potential wells. This effect takes the form of $-k/\mathcal{H}\Psi$ in Fourier space, which means that its measurement is actually a measurement of Ψ. We show how an adequate combination of the dipole with the even multipoles (which are probes of δ, $\mathbf{V}$ or the growth $\sigma_8 f$ and the population biases b) isolates the gravitational redshift contribution. We next show that the combination of this new estimator for Ψ in conjunction with galaxy-galaxy lensing data can be used to construct a novel estimator for the anisotropic stress. This new estimators are completely general and do not rely on any assumption about dark matter. In particular, in contrast with current analysis, they represent a true test of gravity even if the Euler equation for dark matter is not valid. However, we argue that starting from the power spectrum complicates the inclusion of the so-called wide-angle effects arising from the widely used distant-observer approximation about the plane-parallel limit ($d \ll r$). These wide-angle effects are of the same order as the relativistic effects in the odd multipoles, and hence are regarded as a contamination to the dipole signal that might lead to biased constraints if neglected.

Subsequently, in Chapter 5 we revisit the novel gravity test working directly in configuration space. We compute the galaxy clustering three-dimensional 2-point correlation function and perform an expansion in multipoles of the angle $\mu = \mathbf{k} \cdot \hat{n}$. Similarly, as with the Fourier space counterpart, the combined measurements of the even multipoles with the dipole provide a measurement of the time distortions potential Ψ, parametrized through a k-independent function $\hat{I}(z)$. In addition, we introduce a novel parametrization that we have developed for the galaxy-galaxy lensing observable, which allows us to directly measure the evolution of the Weyl potential $(\Phi + \Psi)/2$, encoded in a free function $\hat{J}$, in each tomographic bin. We have also shown that combining the harmonic power spectra of galaxy-galaxy lensing with the galaxy clustering of the photometrically-detected galaxies allows us to break the degeneracy between this new function and the galaxy bias. Importantly, this novel parametrization has the strong advantage of being fully model-independent, contrary to the standard $\mu - \Sigma$ parametrization, which relies on the validity of the weak equivalence principle to measure μ and Σ from weak lensing observables [103, 138]. We end the chapter with the redefinition of the anisotropic stress estimator O^{stress} in configuration space as the ratio between the two functions parameterizing the evolution of Ψ and the Weyl potential.

This Part finishes with forecasts on the precision we expect to achieve for our observables with the upcoming generation of spectroscopic and photometric surveys. In sec. 6.2, we use the Fisher matrix formalism to demonstrate that a SKA2-like survey will be able to measure directly the evolution of the gravitational potential, Ψ, with an accuracy of 10–30%. Such a measurement will be a game changer to distinguish modified theories of gravity from models with a dark fifth force, since it is fully complementary to current measurements that are sensitive to the matter density and velocity, and to the sum of the two gravitational potentials. Measuring $\hat{I}$ is however not free of difficulties. We discuss that the evolution of Ψ is degenerate with the time derivative of the velocity, which is itself unknown. However, we have shown that future surveys will be able to measure the velocity in thin redshift bins, so that this can be used to reconstruct, in a model-independent way, the time derivative of the velocity and consequently break the degeneracy with Ψ. The possibility of measuring Ψ on cosmological scales in a model-independent way represents a significant development for testing gravity. Note that current measurements of Ψ are instead performed through RSD, assuming that the equivalence principle is valid. More precisely, Ψ is inferred from the velocity, using Euler's equation. In contrast, our method allows for a direct measurement of the evolution of Ψ from galaxy clustering spectroscopic data, without the requirement of assuming the validity of the Euler's nor the continuity equation for dark matter.

Comparing our forecasts with current constraints on modified gravity, we see that future constraints on Ψ are roughly of the same order of magnitude as current constraints on the velocity V, and worse by two orders of magnitude than future constraints on V. This is simply due to the fact that the dipole (which is sensitive to Ψ) has a signal-to-noise ratio which is significantly lower than that of the even multipoles (which constrain V). However, it is worth mentioning that the very tight constraints expected on V do not directly translate into tight constraints on modified gravity parameters, like for example μ_0 (which encodes a modification to Poisson equation [156]). As shown in [103], if one does not assume that dark matter obeys the weak equivalence principle, μ_0 can only be constrained with a precision of 15% with a survey like SKA2, which is very similar to the constraints we found here on Ψ. This seems therefore to be the level at which modifications to GR can be tested in a model-independent way.

As discussed, the first application of the novel measurement of Ψ can be to use it in combination with gravitational lensing information to measure the anisotropic stress. We have then applied again the Fisher matrix formalism to study the constraining capability of LSST and determined the uncertainties on $\hat{J}$ as a function of redshift (see fig. 6.3). We have observed an expected degradation of the constraining power toward higher redshifts, but the overall constraints are at less than percent level, showing that LSST will be able to provide very precise model-independent constraints of the late-time growth of the Weyl potential. This degradation is also observed for $\hat{I}$, for which we obtain significantly weaker constraints compared to $\hat{J}$. This is also expected given the difficulty to measure the relativistic dipole of the correlation function. Nevertheless, we revisit the analysis for the gravitational redshift to find SKA2 will be able to put constraints of the order of $20\,\%$ on $\hat{I}$, therefore directly constraining the gravitational potential Ψ. These results are consistent with those presented in sec. 6.2.1.1 (see also ref. [122]), although a different redshift binning has been considered for the combination with $\hat{J}$. The new redshift binning adapts de measurements of $\hat{I}$ to be performed at the same redshifts as the measurements of $\hat{J}$, that is, at the redshift of the LSST lenses.

Finally, we have combined the constraints on $\hat{J}$ from LSST and the constraints on $\hat{I}$ from SKA2 to constrain the anisotropic stress. More precisely, we have considered the ratio between both quantities, which translates into the combination $2/(1+\eta)$, and shown that the combination of data provided by these two future galaxy surveys will be able to constrain η at the $\sim 20\,\%$ level in a direct and model-independent way. This level of precision is similar to current constraints on η obtained through the $\mu - \Sigma$ parametrization. The latest DES analysis does indeed constrain μ_0 with a precision of 20% and Σ_0 with a precision of 5% [63], leading to a derived constraint on η_0 of the order of 25%. However, as explained before, these constraints are not valid if dark matter obeys a fifth force. Moreover, they assume a given time evolution for μ and Σ, meaning that only η_0, i.e. the value of η today can be constrained with this method. If this time evolution is not correct, then the constraints that are obtained are invalid. In contrast, in our case, η is measured independently in each of the redshift bins of the surveys.

To conclude, let us mention that our analysis has considered a simple Fisher matrix formalism, accounting for some astrophysical systematic uncertainties, like galaxy bias or intrinsic alignments. However, an analysis using real observations should go beyond this proof-of-concept and account for additional observational systematics, that we have assumed here to be under control. Finally, let us stress we have combined two different surveys such as the SKA2 and LSST samples. Ideally, it would be of interest to use a survey which provides simultaneously both spectroscopic and photometric data, such as the Euclid satellite. However, the Euclid spectroscopic survey probes galaxy clustering for redshifts ranging from $z = 0.84$ to $z = 1.88$ [1], values of z at which the dipole variance is already dominated by shot-noise. This causes a significant decrease of the dipole effective SNR for this survey. As discussed in sec. 6.2 (see also lower panel of fig. 6.3), it is therefore not possible to measure $\hat{I}$ beyond redshift $z \sim 1.0$ even with the upcoming generation of galaxy surveys.

---

[1] `https://www.euclid-ec.org/public/core-science/`

Part III

GRAVITATIONAL REDSHIFT CONSTRAINTS ON THE EFFECTIVE THEORY OF INTERACTING DARK ENERGY

8

INTRODUCTION

This Part is based on publication 4 listed in the preamble.

In recent years, a considerable amount of both theoretical and observational work in Cosmology has focused on testing gravity on scales larger than individual galaxies, in the quest to unveil the unknown mechanism driving the accelerated expansion of the Universe. Following the line of argument of this Thesis, a powerful observational tool to achieve this consists in employing maps of galaxies in redshift space, which are directly sensitive to the peculiar velocities of the galaxies. Since different theories of gravity generate different velocity fields, comparing these measurements with theoretical predictions provides an efficient way of testing models beyond General Relativity (GR). However, the difficulty of such studies lies in the huge number of theories that have been proposed, making it impractical to compare them against the data one by one. In Part ii, we opted to avoid this Herculean task by adopting a model-agnostic approach. Using minimal assumptions about the theory of gravity, we designed new model-independent measurements of the time distortions potential Ψ and the Weyl potential $(\Phi + \Psi)/2$. We show that we can extract the former directly from measurements of the galaxy clustering 2-pt correlation function multipoles. In particular, the dipole is sensitive to Ψ through the gravitational redshift effect. The evolution of the Weyl potential can be measured from the harmonic power spectra of the galaxy-galaxy lensing correlations. Additionally, the combination of the two new independent measurements can be used to build a new test of gravity tracking directly the anisotropic stress, or gravitational slip, defined as the ratio $\eta = \Phi/\Psi$. In contrast with current tests that rely in the validity of the Euler's equation, a detection of $\eta \neq 1$ using the estimator proposed in this Thesis can be considered as a genuine *smoking-gun* for modified gravity. However, it is not telling us much about the underlying theory which we should focus on to explain the departure from General Relativity.

From now on, we move away from the agnostic approach to more specific model testing using the information contained in the multipoles of the galaxy clustering 2-pt correlation function. A powerful approach is provided by the *effective field theory (EFT) of dark energy* [157–165], which encompasses a large class of theories in a unified formalism, describing a rich phenomenology beyond GR.[1] This formalism is based on a model-independent construction at the level of the action, providing a description of linear cosmological perturbations in scalar-tensor theories of gravity around a homogeneous and isotropic background. In particular, it covers Horndeski models [70], which constitute the most general class of Lorentz-invariant scalar-tensor theories with second-order

---

[1] An alternative model-independent framework, which was developed to test gravity with cosmological observations on linear scales, is the Parameterized Post-Friedmann approach, see refs. [166–168].

equations of motion (this comprises e.g. $f(R)$ gravity [169], quintessence [170, 171], Brans-Dicke models [172], kinetic braiding [173], Galileons/generalized Galileons [174–176]). In this Part, we will focus on models of this class, where four functions of time fully describe the perturbations [159, 162, 164]: the kineticity α_{K}, the braiding α_{B}, the Planck-mass run rate α_{M} and the tensor speed excess α_{T}.[2] Observational as well as theoretical constraints have been put on these free functions, combining the Cosmic Microwave Background (CMB), large-scale structure data and gravitational-wave detections [6, 109, 110, 182–189]. However, at the moment only the parameter α_{T} is tightly restricted to its GR value of zero by the gravitational-wave event GW170817 and its electromagnetic counterpart, GRB170817A [190]. Even if this already restricts the allowed space of theories [182–185], a wide range of allowed models remains, and data from next-generation surveys are necessary to put stringent constraints on the remaining free functions [99, 191, 192].[3]

Moreover, the aforementioned constraints are based on the assumption of a universal coupling of the gravitational sector to the various matter species. This means that the validity of the weak equivalence principle (WEP) is preserved. However, the universality of fifth force effects, mediated by additional degrees of freedom associated to deviations from GR, is yet untested. More specifically, fifth force effects on baryons and photons are strongly constrained (see e.g. ref. [198–202]), while those on cold dark matter (CDM) could be significant and indeed occur in various theories [93–95, 97, 100, 203–207], leading to a breaking of the WEP. To include such theories with distinct couplings, the effective treatment can be broadened to an extension known as *effective theory of interacting dark energy*. This framework has been introduced in ref. [98] in the context of Horndeski theories and further developed in refs. [181, 208] to include more general classes of scalar-tensor theories. Within this formalism, ref. [99] considered a WEP-breaking scenario where photons and baryons have standard couplings to the metric, whereas CDM has a non-minimal coupling described by a single additional free function γ_c. The capability of future galaxy surveys to constrain the parameters of this framework was forecasted through a Fisher matrix approach based on a combination of the galaxy power spectrum in redshift space, the tomographic weak-lensing shear power spectrum, and the correlation between the integrated Sachs-Wolfe effect and the galaxy distribution. This analysis highlighted strong degeneracies between the effects of a fifth force and the other modifications.

As shown in ref. [103] using a phenomenological approach, these degeneracies are due to the fact that the growth of structure is affected in a similar manner by modifications in the Poisson and Euler equations. Both these equations determine how matter falls into a gravitational potential and consequently how it clusters, so their respective modifications cannot be distinguished through redshift-space distortion (RSD) analyses, which only probe the growth of structure. Gravitational lensing does not help to disentangle the two effects, since it does not probe the spatial distortion of the geometry and the time distortion separately [104]. Luckily, ref. [103] has demonstrated that a measurement of the distortion of time through the effect of gravitational redshift on cosmological scales

---

[2] An additional function of time, α_{H}, is required to describe "beyond Horndeski" theories [177, 178], while four further functions are necessary to describe degenerate higher-order theories (DHOST, see refs. [179–181]).

[3] Note that other bounds exist for functions describing theories beyond Horndeski, which further motivates our choice of restricting to Horndeski theories here. In particular, imposing the absence of gravitational-wave-induced instabilities in the dark energy sector places a tight bound of $|\alpha_{\mathrm{H}}| \lesssim 10^{-20}$ [109]. Free functions of DHOST models can be constrained by astrophysical observations [193–197].

can break the degeneracies, since it provides a way of testing both the Euler equation (by comparing the distortion of time with the galaxy velocity), and the relation between the temporal and spatial distortion (by comparing the distortion of time with gravitational lensing [121–123]).

At this stage of the present Thesis, we have become familiar with the gravitational redshift effect. As predicted by GR [113] it induces a change of wavelength when photons travel across gravitational potentials. Let us emphasize that gravitational redshift has been measured by several means in the laboratory [209], from solar observations [210], on astrophysical scales from stacked galaxy clusters [127, 211–215], as well as in the non-linear regime of large-scale structure [120, 216]. This strongly confirms the prediction of its existence. The main motivation of this Thesis is to show that measuring the gravitational redshift on large scales it will be possible with the next generation of cosmic surveys, a measurement that will be complementary to those mentioned here. By way of reminder, we focus on cosmological scales described within linear perturbation theory and consider the two-point correlation function of galaxies as an observable. Together with other relativistic corrections, we learned in sec. 2.2 how the gravitational redshift generates a dipolar modulation in the correlation function. (or similarly an imaginary part in the power spectrum, see Chapter 4), which only appears by cross-correlating two populations of galaxies with different clustering properties, for example bright and faint galaxies. As introduced in Chapter 5, combining the relativistic dipole with the even multipoles generated by RSD makes it possible to isolate the contribution due to gravitational redshift [121]. While the even multipoles of the correlation function have been successfully measured with various surveys, see e.g. [19, 23, 101, 217], the dipole is too small to be detected by current data in the linear regime [47]. Detailed forecasts have however shown that it will be measurable by upcoming galaxy surveys, such as the Dark Energy Spectroscopic Instrument (DESI) [48, 111] and the Square Kilometer Array (SKA) [54, 112]. In particular, SKA is expected to observe close to a billion galaxies up to $z = 2$, allowing for a detection of the dipole with signal-to-noise of 80 (see sec. 11.2.1.2).

In this Part, we investigate the constraining power of gravitational redshift within the framework of the effective theory of interacting dark energy, as established in refs. [98, 99]. With this approach, we provide forecasts on constraints on fundamental parameters that enter at the level of the Lagrangian and cover a wide range of modified gravity theories, more specifically all Horndeski theories with an additional breaking of the WEP for CDM. Using a Monte Carlo Markov Chain (MCMC) analysis as described in sec. 2.5.2, we forecast the expected constraints from a survey like SKA phase 2 (SKA2) [147]. We show that, without gravitational redshift, the parameters are strongly degenerated, leading to wide contours with two branches in most 2-dimensional projections. Such degeneracies leading to highly non-Gaussian posteriors cannot be captured by a Fisher analysis and require an MCMC approach. We show that the inclusion of gravitational redshift significantly alleviates the degeneracies and tightens the constraints on all parameters, reducing the $1\,\sigma$ error bars by up to ~ 50 percent when the bias difference between the two populations is assumed to be 1, which is a reasonable value for current and upcoming galaxy surveys [47]. This is truly remarkable, since gravitational redshift can be extracted from the same data as the growth rate of structure by measuring a dipole from the cross-correlation of galaxies in addition to the standard even multipoles.

This Part is structured as follows: In Chapter 9, we revise the effective theory of interacting dark energy developed in refs. [98, 99], while highlighting differences to the original work in our implementation of the formalism. Moreover, in sec. 9.4 we state the relation between our model parameters and commonly employed, phenomenologically-motivated parameters, The expressions for the observables used for our analysis, in particular the galaxy clustering dipole arising from the general relativistic time distortion, are given in Chapter 10. In sec. 11.1, we discuss the survey specifications and our numerical implementation of the effective theory approach in the `EF-TIGRE` (*Effective Field Theory of Interacting dark energy with Gravitational REdshift*) Python code [4]. Finally, we present the results on the constraining power of gravitational redshift in sec. 11.2, and we conclude in Chapter 12. We also refer the reader to Appendix C which contains supplementary plots supporting the discussion. The Chapters conforming this Part of the Thesis are entirely based in ref. [218].

---

[4] The `EF-TIGRE` code developed for this project is publicly available on Github at github.com/Mik3M4n/EF-TIGRE. The version used for this work is available on Zenodo at 10.5281/zenodo.10606418.

9

EFFECTIVE THEORY OF INTERACTING DARK ENERGY

In this Chapter, we adopt the effective theory of interacting dark energy established in refs. [98, 99]. This comprehensive formalism allows to describe a wide class of modified gravity models encompassing all Horndeski theories, while allowing for different couplings of the matter sector to gravity due to interactions in the dark sector. In particular, this enables us to consider a breaking of the WEP for the unknown CDM component. We summarize our approach in the following, referring to refs. [98, 99] for details and highlighting the differences with respect to the original setup.

9.1 GRAVITATIONAL AND MATTER SECTOR

As in refs. [98, 99], we assume that the gravitational sector is described by a four-dimensional metric $g_{\mu\nu}$ and a scalar field ϕ, with an action corresponding to the class of Horndeski theories [70]. The action can be written in the unitary gauge, where the constant-time hypersurfaces coincide with the uniform scalar field ones. In the Arnowitt-Deser-Misner (ADM) formalism [219], the metric can be written as [1]

$$ds^2 = -N^2 d\tau^2 + h_{ij}\left(dx^i + N^i d\tau\right)\left(dx^j + N^j d\tau\right) , \tag{9.1}$$

where N is the lapse function, N^i is the shift and h_{ij} the 3-dimensional spatial metric. Note that here we are using the physical time τ. The gravitational action can then be expressed in the general form

$$S_g = \int d^4x \sqrt{-g}\, L(N, K_{ij}, R_{ij}, h_{ij}, D_i; \tau) , \tag{9.2}$$

with K_{ij} being the extrinsic curvature tensor and R_{ij} the Ricci tensor associated to the constant time hypersurfaces.

The contribution from the matter action can be generically written as

$$S_m = \sum_I^{N_S} S_I , \qquad S_I = \int d^4x \sqrt{-\check{g}^{(I)}} L_I\left(\check{g}^{(I)}_{\mu\nu}, \psi_I\right) , \tag{9.3}$$

with each of the N_S particle species being minimally coupled to the gravitational sector by a generally different effective metric $\check{g}^{(I)}_{\mu\nu}$. In this work, we consider contributions to the total energy density arising from baryons, CDM and radiation. We assume that the coupling of CDM to the gravitational sector is different from the one of baryons and radiation, leading to a breaking of the WEP. Thus, we cannot identify a global Jordan

---

[1] We work in units where the speed of light c is set to 1.

frame, but we choose to work in the Jordan frame of baryons and radiation, defining the corresponding metric as the gravitational metric $g_{\mu\nu}$. In this frame, CDM is allowed to be non-minimally coupled to $g_{\mu\nu}$. We denote baryons, CDM and radiation by the subscripts b, c and r respectively.

9.2 BACKGROUND

We consider a homogeneous and isotropic background described by the Friedmann-Lemaître-Robertson-Walker (FLRW) metric

$$ds^2 = -d\tau^2 + a^2(\tau)\delta_{ij}dx^i dx^j \,, \tag{9.4}$$

where $a(\tau)$ is the scale factor and τ is the physical time. In the following, a bar denotes the 0-th order quantities, and we assume spatial flatness. The background evolution equations can be obtained by taking variations of the homogeneous action $\bar{S}_g + \bar{S}_m$.

We use the logarithm of the scale factor $\ln(a)$ as a time variable, denoting the corresponding derivatives with a prime, and write the Friedmann equations as (see eqs. (2.12)–(2.13) of ref. [98])

$$H^2 = \frac{1}{3M^2}\left(\bar{\rho}_b + \bar{\rho}_c + \bar{\rho}_r + \bar{\rho}_{\rm DE}\right) \,, \tag{9.5}$$

$$\zeta \equiv \frac{H'}{H} = -\frac{3}{2} - \frac{1}{2M^2H^2}\left(\bar{p}_{\rm DE} + \bar{p}_r\right) \,. \tag{9.6}$$

Here, ρ denotes the energy density and p the pressure, and we assume that baryons and CDM are pressureless, $p_b = p_c = 0$. H is the Hubble parameter and M denotes the effective Planck mass, which in this framework is a function of time. Its time evolution is determined by the function $\alpha_{\rm M}$, defined by

$$\alpha_{\rm M} \equiv \frac{d\ln M^2}{d\ln(a)} \,. \tag{9.7}$$

The equations governing the energy densities of baryons, CDM and radiation follow from the invariance of the matter action under arbitrary diffeomorphisms. These are given in eqs. (4.2)–(4.4) of ref. [98] and read

$$\bar{\rho}_b' = -3\,\bar{\rho}_b \,, \tag{9.8}$$

$$\bar{\rho}_c' = -3(1-\gamma_c)\bar{\rho}_c \,, \tag{9.9}$$

$$\bar{\rho}_r' = -4\bar{\rho}_r \,. \tag{9.10}$$

Hence, baryons and photons evolve in a standard way, as perfect fluids with pressure $p_b = 0$ and $p_r = \rho_r/3$ respectively, while the evolution of CDM is modified by its non-minimal coupling to gravity, encoded in the free function γ_c. [2] Equations (9.5)–(9.6) define the energy density and pressure of the dark energy component. The dark energy equation of state is then given by $w_{\rm DE} \equiv \bar{p}_{\rm DE}/\bar{\rho}_{\rm DE}$, and is included as a free parameter in

---

[2] The function γ_c is given by a combination of the two functions governing the conformal and disformal coupling of CDM to gravity, see eqs. (2.24) and (2.16)–(2.17) of ref. [99]. As a consequence, in this framework it is not possible to distinguish between conformal and disformal couplings. These would be distinguishable only for a component with pressure, see section 5 of ref. [98].

the model. Inserting this into eqs. (9.5)–(9.6), we see that the dark energy density evolves as

$$\bar{\rho}'_{\rm DE} = -3(1+w_{\rm DE})\bar{\rho}_{\rm DE} - 3\gamma_c\bar{\rho}_c + \alpha_{\rm M}(\bar{\rho}_b + \bar{\rho}_c + \bar{\rho}_r + \bar{\rho}_{\rm DE})\,. \tag{9.11}$$

It is convenient to introduce the dimensionless density parameters $\Omega_X \equiv \frac{\bar{\rho}_X}{3M^2H^2}$, and rewrite the evolution equations for $\bar{\rho}_b$, $\bar{\rho}_c$ and $\bar{\rho}_r$ as

$$\Omega'_b = -\Omega_b\left[\alpha_{\rm M} - 3w_{\rm DE}\Omega_{\rm DE} - \Omega_r\right], \tag{9.12}$$

$$\Omega'_c = -\Omega_c\left[\alpha_{\rm M} - 3\gamma_c - 3w_{\rm DE}\Omega_{\rm DE} - \Omega_r\right], \tag{9.13}$$

$$\Omega'_r = -\Omega_r[1 + \alpha_{\rm M} - 3w_{\rm DE}\Omega_{\rm DE} - \Omega_r]\,. \tag{9.14}$$

In the above equations, $\Omega_{\rm DE}$ is defined via eq. (9.5) by $\Omega_{\rm DE} = 1 - \Omega_b - \Omega_c - \Omega_r$. The Hubble parameter can be calculated from the solutions of eq. (9.12) to (9.14) by writing eq. (9.6) as

$$\zeta = -\frac{3}{2}\left(1 + \frac{1}{3}\Omega_r + w_{\rm E}\Omega_{\rm DE}\right)\,, \tag{9.15}$$

and integrating this expression while fixing as initial condition the value H_0 at present time (see section 11.1 for a discussion about the value of H_0),

$$H(z) = H_0 \exp\left[\frac{3}{2}\int_{\ln(a(z))}^{0} {\rm d}\ln a' \left(1 + \frac{1}{3}\Omega_r + w_{\rm DE}\Omega_{\rm DE}\right)\right]\,. \tag{9.16}$$

9.3 PERTURBATIONS

To compute the equations of motions for linear perturbations, the gravitational Lagrangian in eq. (9.2) must be expanded up to second order. The coefficients of the second-order expansion can be conveniently factorized in three dimensionless combinations denoted by $\alpha_{\rm B}$, $\alpha_{\rm K}$ and $\alpha_{\rm T}$ (see section 2.3 of ref. [98] for details). The most general quadratic action leading to second-order equations of motion can consequently be written as

$$S^{(2)}_{\rm g} = \int d^3x\, d\tau\, a^3 \frac{M^2}{2}\left[\delta K^i_j \delta K^j_i - \delta K^2 + R\,\delta N + (1+\alpha_{\rm T})\,\delta_2\!\left(\sqrt{h}R/a^3\right)\right. \\ \left. + \alpha_{\rm K} H^2 \delta N^2 + 4\alpha_{\rm B} H \delta K \delta N\right]\,. \tag{9.17}$$

Here, δ_2 denotes the second-order term in a perturbative expansion. The gravity modifications entering eq. (9.17) are thus parameterized by four time-dependent functions: the tensor speed excess $\alpha_{\rm T}$, the kineticity $\alpha_{\rm K}$, the braiding $\alpha_{\rm B}$,[3] and the effective Planck mass M, whose evolution is encoded in the parameter $\alpha_{\rm M}$ defined in eq. (9.7). The parameter $\alpha_{\rm T}$ is directly related to the speed of propagation of tensor modes $c_{\rm T} \equiv 1 + \alpha_{\rm T}$, which was constrained to match the speed of light up to $\sim 10^{-15}$ by the multi-messenger observation of the binary neutron star merger GW170817 in conjunction with the gamma-ray

---

[3] Note that the parameter $\alpha_{\rm B}$ used here corresponds to the one used in refs. [98, 99], but needs to be divided by a factor -2 to obtain the parameter $\alpha_{\rm B}$ originally introduced in ref. [164].

burst GRB 170817A in 2017 [190]. Therefore, we set $\alpha_{\mathrm{T}} = 0$ throughout our analysis. [4] We are thus left with the three free functions α_{M}, α_{K} and α_{B}, which take the values $\alpha_{\mathrm{K}} = \alpha_{\mathrm{B}} = \alpha_{\mathrm{M}} = 0$ in the special case of GR.

In order to write the perturbations equations, it is convenient to adopt the Newtonian gauge for the linearly perturbed FLRW metric,

$$ds^2 = -(1+2\Psi)d\tau^2 + a^2(\tau)(1-2\Phi)\delta_{ij}\,dx^i dx^j\,. \tag{9.18}$$

We work in the quasi-static approximation, following the approach of ref. [223], where a hierarchy of terms is introduced based on the assumption that time derivatives are smaller than spatial ones. With these assumptions, the action in eq. (9.2) leads to the following Euler equations for baryons and CDM (see eqs. (4.16) and (4.18) in ref. [98], where Φ and Ψ are interchanged),[5]

$$V_b' + V_b - \frac{k}{\mathcal{H}}\Psi = 0\,, \tag{9.19}$$

$$V_c' + V_c\,(1+3\gamma_c) - \frac{k}{\mathcal{H}}\Psi\left(1 + \frac{6\gamma_c}{c_s^2\alpha\mu}\,(\alpha_{\mathrm{B}} - \alpha_{\mathrm{M}} + 3\gamma_c\omega_c b_c)\right) = 0\,. \tag{9.20}$$

Here, $V_{b,c}$ are the velocity potentials of baryons and CDM in Fourier space, related to the velocity fields by $\mathbf{V}_{b,c} = -i\mathbf{k}/k\,V_{b,c}$, and the quantities $c_s^2\alpha$ and μ are defined below. The modified Poisson equation reads (see eq. (4.19) in ref. [98])

$$-\frac{k^2}{a^2}\Psi = 4\pi G\mu(k,z)\,\delta_{\mathrm{m}}\,\bar{\rho}_m\,, \tag{9.21}$$

i.e. the Newton constant G is replaced by an effective Newton constant, $G\mu$, which depends on the gravity modifications and the non-minimal coupling γ_c (see eq. (9.25) below). Combining eq. (9.21) with the continuity equation and the Euler equations gives rise to second-order evolution equations for the density (see eqs. (4.23) and (4.24) in ref. [98]),

$$\delta_b'' = -\,(2+\zeta)\,\delta_b + \frac{3}{2}\Omega_m\left[1 + \frac{2}{c_s^2\alpha}\,(\alpha_{\mathrm{B}} - \alpha_{\mathrm{M}})\,(\alpha_{\mathrm{B}} - \alpha_{\mathrm{M}} + 3\gamma_c\omega_c b_c)\right]\,, \tag{9.22}$$

$$\begin{aligned}\delta_c'' = &-\,(2+\zeta+3\gamma_c)\,\delta_c \\ &+ \frac{3}{2}\Omega_m\left[1 + \frac{2}{c_s^2\alpha}\,(\alpha_{\mathrm{B}} - \alpha_{\mathrm{M}} + 3\gamma_c)\,(\alpha_{\mathrm{B}} - \alpha_{\mathrm{M}} + 3\gamma_c\omega_c b_c)\right]\,.\end{aligned} \tag{9.23}$$

Here, Ω_{m} and δ_{m} refer to the total matter contribution,

$$\Omega_{\mathrm{m}} = \Omega_b + \Omega_c\,, \qquad \delta_{\mathrm{m}} = (\Omega_b\delta_b + \Omega_c\delta_c)/\Omega_{\mathrm{m}}\,, \tag{9.24}$$

and $\omega_c \equiv \Omega_c/\Omega_{\mathrm{m}}$ and $b_c \equiv \delta_c/\delta_{\mathrm{m}}$ denote the fraction of CDM at the level of the background and perturbations respectively. The Euler, evolution and Poisson equations depend on the function ζ given in eq. (9.6), and on the function μ defined as

$$\mu \equiv 1 + \frac{2}{c_s^2\alpha}\,(\alpha_{\mathrm{B}} - \alpha_{\mathrm{M}})\,(\alpha_{\mathrm{B}} - \alpha_{\mathrm{M}} + 3\gamma_c\omega_c b_c)\,. \tag{9.25}$$

---

[4] An open possibility is that the propagation speed of GWs exhibits a frequency dependence such that the GR value is recovered in the frequency range where the LIGO-Virgo detectors operate, while deviating from GR at lower frequencies [220]. This effect can be constrained with LISA or multi-band GW observations [221, 222]. In this work, we assume a frequency-independent GW speed.

[5] The velocity potentials $v_{b,c}$ in ref. [98] are related to the quantities $V_{b,c}$ used here as $v_{b,c} = -aV_{b,c}/k$.

Moreover, the evolution equations contain the quantity $c_s^2\alpha$, involving the speed of sound of scalar perturbations c_s (given by eq. (2.39) of ref. [98]),

$$c_s^2\alpha = -2\left[(1+\alpha_{\rm B})\left(\zeta-\alpha_{\rm M}+\alpha_{\rm B}\right)+\alpha_{\rm B}'+\frac{3}{2}\Omega_{\rm m}+2\Omega_r\right]. \tag{9.26}$$

The quantity α, defined in eq. (2.36) of ref. [98], contains a combination of the functions $\alpha_{\rm K}$, $\alpha_{\rm B}$ and $\alpha_{{\rm D},c}$, where the latter arises from a disformal coupling of CDM to the metric $g_{\mu\nu}$. However, we note that the combination $c_s^2\alpha$ in eq. (9.26) does not depend on $\alpha_{\rm K}$ and $\alpha_{{\rm D},c}$. This is a consequence of the quasi-static approximation and implies that the kineticity $\alpha_{\rm K}$ remains unconstrained when adopting this limit.[6] Finally, the absence of ghost and gradient instabilities requires $c_s^2\alpha \geq 0$, and we note that a major advantage of the EFT formalism is that these theoretical constraints can be easily incorporated in the analysis, leading to a large restriction of the parameter space [189]. We will include this condition in our analysis.

In the following, we will investigate the potential of upcoming galaxy surveys to constrain the functions $\alpha_{\rm M}$, $\alpha_{\rm B}$, γ_c and $w_{\rm DE}$, highlighting the fundamental role played by gravitational redshift.

9.4 RELATION TO THE PHENOMENOLOGICAL PARAMETERS

The effective theory of interacting dark energy adopted in this work only contains a limited number of free functions ($\alpha_{\rm M}$, $\alpha_{\rm B}$, γ_c and $w_{\rm DE}$), which all have a simple theoretical interpretation and enter at the level of the Lagrangian. However, another common approach to investigate the impact of modified gravity and dark energy on cosmological observables consists in introducing some phenomenologically-motivated free functions, entering directly in the Poisson and Euler equations (see e.g. refs. [102, 156, 224–228]). In this appendix, we state the relation between the two sets of parameters arising from these different approaches.

To parameterize modifications in the Poisson equation, the gravitational constant G is usually multiplied by a free function μ, as done in eq. (9.21). Indeed, μ can be expressed using the free functions $\alpha_{\rm M}$, $\alpha_{\rm B}$ and γ_c, see eq. (9.25). In the phenomenological approach, the difference between the two potentials Φ and Ψ is expressed by the gravitational slip $\eta = \Phi/\Psi$. The gravitational slip is obtained by combining eqs. (4.26) and (4.27) of ref. [98] (note that their Φ and Ψ are interchanged compared to our notation), and translates into

$$\eta = \frac{c_s^2\alpha + 2\alpha_{\rm B}(\alpha_{\rm B}-\alpha_{\rm M}+3\gamma_c\omega_c b_c)}{c_s^2\alpha + 2(\alpha_{\rm B}-\alpha_{\rm M})(\alpha_{\rm B}-\alpha_{\rm M}+3\gamma_c\omega_c b_c)}. \tag{9.27}$$

Apart from the phenomenologically-motivated functions μ and η, ref. [54] has introduced the free functions Θ and Γ encompassing a breaking of the WEP for CDM. They appear as a friction and fifth force term in the Euler equation,

$$V_{\rm c}' + (1+\Theta)V_{\rm c} - \frac{k}{\mathcal{H}}(1+\Gamma)\Psi = 0. \tag{9.28}$$

---

[6] We note that, even when the full set of perturbations equations beyond the quasi-static limit is considered, the kineticity is hardly constrained by CMB, baryon acoustic oscillations, and RSD data, and in general it can be fixed to arbitrary values without affecting the results for the remaining parameters [188].

Comparing this with the Euler equation of the effective theory of interacting dark energy given in eq. (9.20), we obtain

$$\Theta = 3\gamma_c\,, \tag{9.29}$$

and

$$\Gamma = \frac{6\gamma_c\left(\alpha_{\mathrm{B}} - \alpha_{\mathrm{M}} + 3\gamma_c\omega_c b_c\right)}{c_s^2\alpha + 2(\alpha_{\mathrm{B}} - \alpha_{\mathrm{M}})\left(\alpha_{\mathrm{B}} - \alpha_{\mathrm{M}} + 3\gamma_c\omega_c b_c\right)}\,. \tag{9.30}$$

Note that these phenomenological modifications enter the perturbation equations as follows (see ref. [103]),

$$\delta_b'' + (2+\zeta)\delta_b' - \frac{3}{2}\Omega_{\mathrm{m}}\delta_{\mathrm{m}}\,\mu = 0\,, \tag{9.31}$$

$$\delta_c'' + (2+\zeta+3\gamma_c)\delta_c' - \frac{3}{2}\Omega_{\mathrm{m}}\delta_{\mathrm{m}}\,\mu(\Gamma+1) = 0\,, \tag{9.32}$$

which, combined with eqs. (9.25), (9.29) and (9.30), indeed recover eqs. (9.22) and (9.23).

Galaxy surveys have provided constraints on the free functions μ and η through gravitational lensing [6, 63, 142] and RSD measurements [101]. The combination of data from the CMB, baryon acoustic oscillations, supernovae, weak lensing and RSD recently allowed for a reconstruction of their redshift evolution [229] as well as their joint redshift and scale dependence [230]. Reference [103] pointed out that the standard RSD-based constraints on μ are strongly degenerate with the parameters Θ and Γ describing a breaking of the WEP, and forecasted constraints when taking gravitational redshift into account.

We emphasize that, despite the existence of analytical expressions relating the free functions of the phenomenological and effective theory framework, these two approaches are fundamentally different. First, in the phenomenological approach, the free functions μ, η, Γ and Θ are usually assumed to be independent. However, we see in eqs. (9.25), (9.27), (9.29) and (9.30) that they in fact display dependencies through more fundamental, theory-based free functions. Moreover, while we assume that the theory-based functions evolve according to the dark energy density, see eq. (11.1), their interplay in the equations for the phenomenologically-motivated functions leads to a different time dependence. Hence, a time evolution of μ, η, Γ and Θ proportional to the dark-energy density (as applied e.g. in refs. [6, 101, 103, 142]) cannot be maintained in our effective theory framework.

To summarize, a direct, quantitative comparison between the constraints in our work to those obtained employing the phenomenologically-motivated parameters cannot be performed. However, some qualitative results are reflected in both these approaches. Most importantly, the role of gravitational redshift in breaking degeneracies that was pointed out in ref. [103] is also maintained in our effective theory approach, as extensively discussed in section 11.2.

10

GALAXY CLUSTERING OBSERVABLES IN THE EFT FORMALISM

The theoretical framework presented in the previous section can be constrained through observations of the distribution of galaxies across the sky. Galaxy surveys provide measurements of the number of galaxies N as a function of redshift z and angular position $\hat{\mathbf{n}}$ in the sky. As of now, we recognize these observations as necessary to reconstruct the number count fluctuations observable, $\Delta(\mathbf{n}, z)$. In Chapter 1, we computed the quantity Δ at linear order in perturbation theory [5, 8, 10, 11, 13], finding[1] we can separate the contributions into groups as $\Delta(\mathbf{n}, z) = \Delta^{\rm st}(\mathbf{n}, z) + \Delta^{\rm rel}(\mathbf{n}, z)$, given by eqs. (1.42) and (1.58) respectively. Let us remind that these equations are valid in any metric theory of gravity and only rely on the assumption that photons travel along null geodesics of the metric $g_{\mu\nu}$. In addition, we note that s is the magnification bias (see e.g. refs. [10, 24]) arising from magnitude cuts imposed in the sample selection. Here we shall neglect the impact of the evolution bias, whose contribution is expected to be subdominant [39].[2]

Once again, we resort to summary statistics for analyzing the galaxy clustering data. Let us consider again the galaxy two-point correlation function, $\xi \equiv \langle \Delta(\hat{\mathbf{n}}, z)\Delta(\hat{\mathbf{n}}', z')\rangle$, and its multipole expansion in powers of μ, i.e. the cosine angle between the line of sight and the separation between the correlated galaxies (see figs. 2.2 for an illustration. See eqs.(2.52)-(2.56) for the mathematical expressions in GR). This provides a set of independent observables that are functions of z, the comoving separation between galaxies, d and the population dependent parameters such as the galaxy bias, magnification bias and evolution bias. We denoted them by $\xi^{(\ell)}_{\rm L,M}(z, d)$.

In the distant-observer regime, the standard contributions (density fluctuations and RSD) generate three even multipoles: a monopole ($\ell = 0$), a quadrupole ($\ell = 2$) and a hexadecapole ($\ell = 4$), which were measured by various surveys, see e.g. ref. [101]. These are given by (2.52)-(2.54), in which all the spatial information comes from the integrals $\rho_\ell(z, d)$ involving the matter power spectrum $P_{\delta\delta}(k, z)$ at a given redshift. We defined them in eq. (2.49), in terms of the reference redshift $z_\star$, but they are easily redefined to any z by the linear mapping (2.14). However, importantly, here the relevant $P_{\delta\delta}(k, z)$

---

[1] For a derivation of the relativistic effects at second order, see e.g. [231–233].

[2] The evolution bias $f^{\rm evol}$ depends on the redshift evolution of the populations of sources. It can be directly measured from the average number of galaxies once data become available (see ref. [35] for a forecast using SKA specifications). However, as it does not affect the terms proportional to x_c encoding the breaking of the WEP, we neglect it here, since we do not expect it to impact the constraining power of the dipole. Note that in general the contribution of $f^{\rm evol}$ to the dipole is suppressed with respect to the other contributions for two reasons. First, from eq. (8) in ref. [39], we see that the contributions proportional to the magnification bias difference is boosted at low redshift over those proportional to the evolution bias by a factor $\left(1 - \frac{1}{r\mathcal{H}}\right)$. Secondly, following the argument in section 4.1 of ref. [39], we see that the term depending on the difference $f^{\rm evol}_{\rm B} - f^{\rm evol}_{\rm F}$ vanishes, further reducing the impact of the evolution bias.

needs to be computed by solving eqs. (9.22)–(9.23) for a given combination of the EFT parameters. Aside from this subtlety, the formal expressions for the even multipoles remain the same in the EFT formalism. The dependency on the specific model is hidden in the matter power spectrum and the growth rate of density perturbations, as we will see shortly.

On the other hand, the cross-correlation of Δ^{rel} with the standard terms breaks the symmetry of the two-point function ξ (see sec. 2.2), generating a dipole moment.[3] To extract this dipole from galaxy surveys, it is necessary to cross-correlate two differently biased populations of galaxies, for example a bright (B) and a faint (F) sample. In contrast with the even multipoles, the explicit expression for $\xi^{(1)}_{\rm BF}$ turns out to be explicitly dependent on the EFT parameters. Employing the Poisson equation (9.21) and the Euler equations (9.19)–(9.20), we obtain the following expression for the dipole,

$$\begin{aligned}\xi_1^{\rm BF}(z,d) =& \frac{\mathcal{H}}{\mathcal{H}_0}\tau_1(d,z)\Bigg\{-3(s_{\rm B}-s_{\rm F})\,f^2\left(1-\frac{1}{r\mathcal{H}}\right)+(b_{\rm B}-b_{\rm F})\,f\left(\frac{2}{r\mathcal{H}}+\frac{\dot{\mathcal{H}}}{\mathcal{H}^2}\right)\\ &+5f\,(b_{\rm B}s_{\rm F}-b_{\rm F}s_{\rm B})\left(1-\frac{1}{r\mathcal{H}}\right)\\ &+3\,x_c\,(b_{\rm B}-b_{\rm F})\,\gamma_c\left[f-(1+z)\left(\frac{\mathcal{H}_0}{\mathcal{H}}\right)^2\frac{3\,\Omega_{\rm m,0}}{c_s^2\alpha}(\alpha_{\rm B}-\alpha_{\rm M}+3\gamma_c\omega_c b_c)\right]\Bigg\}\\ &-\frac{2}{5}(b_{\rm B}-b_{\rm F})\,f\,\frac{d}{r}\rho_2(d,z)\,. \end{aligned}\tag{10.1}$$

Here, x_c is the fraction of CDM mass in a galaxy (which in general can differ from the background CDM fraction ω_c as well as from the fraction $b_c \equiv \delta_c/\delta_{\rm m}$ at the level of perturbations), and $\tau(d,z)$ is given by eq. (2.50) (including the linear mapping (2.14)). The third line in eq. (10.1) arises from the first and last two terms of $\Delta^{\rm rel}$ in eq. (1.58), which are related to the density through the modified Poisson equation (9.21) and the Euler equation for CDM (9.20). These terms vanish if $\gamma_c = 0$, i.e. if CDM is minimally coupled to the scalar field, thus obeying the Euler equation. Their combination is weighted by a factor x_c due to the fact that the WEP is only broken for CDM, but not for baryons. The remaining Doppler contributions in eq. (1.58) lead to the first and second line of eq. (10.1). The fourth line contains the wide-angle effect, a contamination to the dipole from RSD due to the fact that the sky is not flat [24]. Even though this term is suppressed by d/r, it is of the same order as the contributions in the first three lines, since it is proportional to $\rho_2(d)$, which is enhanced by a factor $k/\mathcal{H}$ with respect to $\tau_1(d)$. We note that the dipole in eq. (10.1), including the wide-angle effect, exactly vanishes for a single galaxy population. This would not be the case if we had chosen to align the line-of-sight direction along the line towards one of the correlated galaxies instead of along the median direction between the galaxies. In this case, one would have a remaining “large-angle effect" even for a single population of galaxies, as described in refs. [47, 52].[4]

Finally, there is an additional consideration regarding the growth function f when comparing with the results in previous Chapters. Here, a breaking of the Equivalence

---

[3] The cross-correlation between standard and relativistic terms also generates an octupole, which is however not sensitive to gravitational redshift [121] and thus does not help in breaking degeneracies in our analysis. We will therefore not consider it in the following.

[4] When considering the galaxy power spectrum instead of the correlation function, the wide-angle term generates a dipole for a single population of galaxies because of the effect of the window function [51].

principle is allowed, meaning dark matter and baryons might experience different velocity potentials. In other words, cold dark matter and baryons perturbations might grow and cluster differently. Therefore, in the context of the EFT formalism presented here, the galaxy velocity **V** appearing in eqs. (1.42) and (1.58) is thus a weighted average of the velocities of baryons and CDM [99],

$$\mathbf{V} = x_c \mathbf{V}_c + (1 - x_c)\mathbf{V}_b \,. \tag{10.2}$$

The velocity potentials $V_{b,c}$ can be related to the density fields $\delta_{b,c}$ via

$$V_{b,c} = -\frac{\mathcal{H}}{k}\, f_{b,c}(a)\, \delta_{b,c}(a, \mathbf{k})\,, \tag{10.3}$$

where $f_{b,c}(a) \equiv \mathrm{d}\ln(\delta_{b,c})/\mathrm{d}\ln(a)$ is the growth rate of the respective species. Equation (10.3) corresponds to the linear-order continuity equation, remaining valid for all particle species in the effective theory of interacting dark energy (see eqs. (4.15) and (4.17) in ref. [98]). The galaxy velocity potential then becomes

$$V = -\frac{\mathcal{H}}{k}\left[x_c\, f_c\, \delta_c + (1 - x_c)\, f_b\, \delta_b\right] = -\frac{\mathcal{H}}{k} f\, \delta_{\mathrm{m}}\,, \tag{10.4}$$

where the *effective* growth rate of galaxies f is related to that of baryons and CDM through

$$f = x_c f_c b_c + (1 - x_c) f_b b_b \,. \tag{10.5}$$

In the following secs., we forecast the constraints on the effective theory of interacting dark energy arising from measurements of the even multipoles of $\xi(z, d)$, and we compare them with the constraints obtained when the dipole is added to the analysis.

11

MCMC ANALYSIS

11.1 METHODOLOGY

The effective theory framework and the galaxy clustering observables presented in the previous sections form the foundation for our work. Here, we discuss additional preliminaries necessary for the numerical analysis with our `EF-TIGRE` Python package. There, we implemented an MCMC algorithm following the guidelines given in sec. 2.5.2. We define the survey specifications and choice of time evolution for the parameters we constrain. Moreover, we specify the set of observables and the fiducial models used in our analysis, and outline further details of our numerical implementation.

11.1.1 *Survey specifications*

We consider a survey similar to SKA2, covering 30,000 square degrees and ranging from $z = 0$ to $z = 1.5$. We divide this redshift range into 15 bins of size $\Delta z = 0.1$ and in each of these bins we consider the survey specifications given in table 3 in ref. [147].[1] Then, the sample modeling is analogous to the adopted in sec. 6.1.1. We split the sample of galaxies into two populations with the same number of galaxies in each redshift bin and model the bias of each population with the fitting function from ref. [147], using eqs. (6.2) and (6.3) for the bright ($\mathrm{L} = \mathrm{B}$) or faint ($\mathrm{L} = \mathrm{F}$) populations, respectively. We vary the four parameters c_B, c_F, d_B and d_F, around fiducial values $c_\mathrm{L} = 0.554$ and $d_\mathrm{L} = 0.783$ following ref. [147]. We fix $\Delta b = 1$, which is consistent with the bias difference obtained from the measurement of BOSS [47]. This quantity could in principle be different for SKA2, but once the data become available, various possibilities of splitting the galaxy sample can be explored in order to boost the bias difference [111, 234], and thus the dipole signal from eq. (10.1). The magnification biases s_B and s_F will be measurable from the average number of galaxies within the SKA2 survey, and for the purpose of our forecast we fix their values according to Appendix B of ref. [103].

11.1.2 *Choices of parametrizations and time evolution of the free functions*

In addition to the galaxy and magnification bias parameters, our observables depend on four free functions of time, which are the main focus of our work: the braiding α_B, the running of the Planck mass α_M, the parameter γ_c encoding a non-minimal coupling

---

[1] The highest five redshift bins between $z = 1.5$ and $z = 2.0$ stated in table 3 of ref. [147] could as well be included in our analysis, but we omit them for numerical efficiency as they do not provide a significant improvement to our constraints.

of CDM to the metric $g_{\mu\nu}$, and the dark energy equation of state parameter $w_{\rm DE}$. In order to extract constraints on these functions, it is necessary to either assume a parameterized time evolution for them, or to resort to non-parametric models, typically consisting in constraining the free functions in redshift bins [229]. Due to the large dimensionality of the parameters space and the strong correlations between the free functions, in this work we choose to adopt the first strategy and assume a specific time evolution. Hence, we assume that $w_{\rm DE}$ is constant in time, whereas $\alpha_{\rm B}$, $\alpha_{\rm M}$ and γ_c decay proportionally to the dark energy density when going backwards in cosmic history, in line with much previous literature (see e.g. refs. [99, 103, 188, 191, 235]). This time parametrization is motivated by the fact that the scalar field drives the accelerated expansion of the Universe, and that its impact should therefore be negligible well before acceleration started. In practice, for each parameter $p \in \{\alpha_{\rm B}, \alpha_{\rm M}, \gamma_c\}$, we write

$$p = p_0 \, \frac{1 - \Omega_{\rm m}^{\Lambda CDM} - \Omega_{\rm r}^{\Lambda CDM}}{1 - \Omega_{\rm m,0}^{\Lambda CDM} - \Omega_{\rm r,0}^{\Lambda CDM}} \,, \tag{11.1}$$

where the superscript ΛCDM denotes quantities evaluated in ΛCDM, i.e. explicitly

$$\Omega_{\rm m}^{\Lambda CDM} = \Omega_{\rm m,0}^{\Lambda CDM} \left(\frac{H_0}{H^{\Lambda CDM}(z)} \right)^2 e^{-3 \ln a} \tag{11.2}$$

$$\Omega_{\rm r}^{\Lambda CDM} = \Omega_{\rm r,0}^{\Lambda CDM} \left(\frac{H_0}{H^{\Lambda CDM}(z)} \right)^2 e^{-4 \ln a} \,. \tag{11.3}$$

Note that here we parametrize the time evolution using the fiducial ΛCDM evolution for simplicity. Given that the background evolution is expected to be close to ΛCDM and that the choice of time parametrization involves a degree of arbitrariness, there is no compelling reason to introduce a more intricate evolution. With these assumptions, the degrees of freedom reduce to three free parameters $\alpha_{\rm B,0}$, $\alpha_{\rm M,0}$ and $\gamma_{c,0}$, denoting the present-time values of the functions. The final constraints on these parameters are sensitive to our choice of time parametrization, but we will argue in section 11.2 that this does not affect the main message of our work, i.e. that the inclusion of gravitational redshift breaks several degeneracies among the parameters.

Our choice of time parametrization is the same as in ref. [99] for $\alpha_{\rm M}$ and $\alpha_{\rm B}$, but it differs concerning γ_c. In ref. [99], the authors assumed a constant value for the combination $\beta_\gamma = 3\sqrt{2}\gamma_c/(c_s\alpha^{1/2})$ and provided constraints on this quantity.[2] Instead, here we assume that also γ_c evolves according to eq. (11.1), thus ensuring that all free functions entering the evolution equations for the perturbations, eqs. (9.22)–(9.23), share the same time dependence. This is important, since assuming distinct time evolutions could artificially break the degeneracies between parameters, thus enhancing the constraining power of our observables. Our choice of constraining γ_c instead of β_γ also simplifies the numerical implementation in comparison to ref. [99], as the expression for $c_s^2\alpha$ in eq. (9.26), combined with ζ in eq. (9.6), is directly given in terms of the free functions. To summarize, the relevant degrees of freedom are $\alpha_{\rm B,0}$, $\alpha_{\rm M,0}$, $\gamma_{c,0}$ and $w_{\rm DE}$, which in the following we refer to as EFT parameters.

---

[2] This parametrization was adopted to make an analogy to the standard assumption made for coupled quintessence models [236, 237].

11.1.3 *Observables*

We consider as our observables all possible auto- and cross-correlations between the bright and faint galaxy samples, which we expand in multipoles. This yields a total of three monopoles and three quadrupoles (bright-bright, faint-faint and bright-faint). Since the hexadecapole, as in eq. (2.54), is independent of population-specific biases, no additional information is obtained by considering various samples, so we only include the hexadecapole of the total galaxy population. Thus, we have in total seven even multipoles, which are evaluated at each redshift bin. We compare the constraints obtained from these even multipoles with an analysis where we also include the dipole in the cross-correlation between the bright and faint populations, which includes the effect of gravitational redshift. Note that the dipole is strictly zero for two populations with equal galaxy and magnification bias, as can be seen from eq. (10.1), and therefore no bright-bright or faint-faint dipole exists. We fix the minimum separation between galaxy pairs to $d_{\mathrm{m}in} = 20\,\mathrm{Mpc}/h$, such that the impact of non-linearities is negligible [39]. Moreover, after testing that going beyond this range does not improve the resulting constraints, we fix the maximum separation to $d_{\mathrm{m}ax} = 160\,\mathrm{Mpc}/h$.

Our choice of time parametrization for the modifications ensures that we recover GR at high redshift, well before the cosmic acceleration started. As a consequence, the constraints from the CMB on the parameters Ω_{m}, Ω_{b}, Ω_{r} at early time as well as on the primordial parameters A_s and n_s remain valid. Hence, we fix the values of these parameters according to the Planck values [6] and start solving the background equations at recombination.

On the other hand, the dark energy equation of state parameter w_{DE} affects the late-time evolution of the Universe and can differ from -1 in Horndeski theories. We therefore keep it as a free parameter, and we cannot directly set a Planck prior on it, as the Planck constraints on this parameter were obtained assuming the validity of GR at late times. We thus introduce an indirect constraint arising from the distance to last scattering, which is inferred in a model-independent manner from the position of the peaks in the CMB angular power spectrum. More precisely, we consider the Planck measurement of the comoving angular diameter distance D_{M} at recombination,[3] which is given by the ratio between the sound horizon at recombination, r_*, and the angular scale of the first peak of the CMB, θ_*. We include the quantity D_{M} as an independent observable in addition to the multipoles, with a central value and variance determined by Planck [6]. The expected value is obtained by integrating the inverse of the Hubble parameter from today up to the redshift z_* of recombination,

$$D_{\mathrm{M}} = \int_0^{z_*} \frac{\mathrm{d}z}{H(z)} \,. \tag{11.4}$$

Note that this implies that, unlike for the constraints obtained in ref. [99], we need to include radiation in the background evolution, as it becomes relevant at high redshift. On the other hand, since the multipoles are only observed at late time, it is sufficient to solve the perturbation equations starting at $z_{\mathrm{i}n} = 10$, where we can neglect the impact of radiation.

Lastly, we fix the value of the Hubble constant today, H_0, since it can be determined in a model-independent way from local measurements of the expansion rate. In practice, we

---

[3] The distance D_{M} is related to the usual angular diameter distance by $D_{\mathrm{M}} = (1+z)D_{\mathrm{A}}$.

should use the best-fit value obtained from supernova and Cepheid measurements [238], but since local measurements are currently in tension with the value inferred from Planck data, such a choice would mean that the fiducial cosmology is not ΛCDM. In particular, if H_0 differs from the Planck value, the theory of gravity should also be modified to ensure that the background evolution yields a distance to last scattering compatible with Planck. We therefore consider two separate fiducial models (see section 11.1.4): a ΛCDM fiducial model, based on the assumption that the H_0 tension is due to systematic effects and will disappear in the future, where we choose H_0 to be compatible with the Planck constraints; and a modified gravity fiducial model, where the values of the parameters are compatible with $D_{\rm M}$ measured from Planck and with H_0 measured from supernovae and Cepheids.

11.1.4 *Choice of fiducial models*

We consider the three following cases:

1. ΛCDM fiducial with EFT parameters,

$$\alpha_{\rm M,0}^{fid} = \alpha_{\rm B,0}^{fid} = \gamma_{c,0}^{fid} = 0\,, \quad w_{\rm DE}^{fid} = -1\,. \quad (\Lambda\text{CDM fiducial}) \tag{11.5}$$

   Here we fix $H_0 = 67.66\,{\rm k}m\,s^{-1}\,Mpc^{-1}$ according to the Planck measurement [6].

2. *Modified gravity with large modifications* (MGI). In this case, we assume that $H_0 = 73.04\,{\rm k}m\,s^{-1}\,Mpc^{-1}$ is given by the local measurement of ref. [238]. In order for the distance to last scattering to match the Planck value, other parameters affecting the background evolution must be modified, i.e. at least one among $\alpha_{\rm M,0}^{fid}$, $\gamma_{c,0}^{fid}$ and $w_{\rm DE}^{fid}$ should be different from the ΛCDM value. At the same time, the stability condition in eq. (9.26) must be satisfied, which in general requires modifying at least two of these parameters. Once we adopt a modified gravity fiducial, the most general choice is that all parameters deviate from their ΛCDM values, unless some fine-tuning is present. We thus choose fiducial values $\alpha_{\rm M,0}^{fid}$, $\alpha_{\rm B,0}^{fid}$ and $\gamma_{c,0}^{fid}$, which lie between the 1 and $2\,\sigma$ constraints of the ΛCDM fiducial model. Then, the value of $w_{\rm DE}^{fid}$ is fixed such that the distance to last scattering matches the Planck measurement when assuming $H_0 = 73.04\,{\rm k}m\,s^{-1}\,Mpc^{-1}$. In summary, we choose for the EFT parameters

$$\alpha_{\rm M,0}^{fid} = -0.1\,, \quad \alpha_{\rm B,0}^{fid} = -0.5\,, \quad \gamma_{c,0}^{fid} = 0.15\,, \quad w_{\rm DE}^{fid} = -1.41\,. \quad (\text{MGI fiducial}) \tag{11.6}$$

   Note that $w_{\rm DE} < -1$ does not lead to instabilities in Horndeski theories, since the effect of the equation of state on the sound speed can be counterbalanced by other parameters to keep $c_s^2\alpha > 0$ (see eq. (11.10) below).

3. *Modified gravity with small modifications* (MGII). The values of the MGI fiducial model correspond to quite large deviations from ΛCDM. For comparison, we also consider a fiducial model with smaller deviations, to investigate the impact on the constraints with and without the gravitational redshift. We therefore include a third fiducial model defined by

$$\alpha_{\rm M,0}^{fid} = -0.01\,, \quad \alpha_{\rm B,0}^{fid} = -0.1\,, \quad \gamma_{c,0}^{fid} = 0.01\,, \quad w_{\rm DE}^{fid} = -1.01\,. \quad (\text{MGII fiducial})$$

(11.7)

In this case, H_0 is fixed to the Planck value, $\alpha_{\mathrm{M},0}^{fid}$, $\alpha_{\mathrm{B},0}^{fid}$ and $\gamma_{c,0}^{fid}$ are chosen arbitrarily, and w_{DE}^{fid} is determined from the distance to last scattering.

We always fix the values of A_s and n_s and the density parameters Ω_{m}, Ω_{b}, Ω_{r} at z_* according to the Planck constraints [6]. We show the galaxy correlation multipoles in the three fiducial models in figure 11.1. The deviation of the even multipoles with respect to ΛCDM is due to a shift in the growth rate f, which is reduced in MGI and increased in MGII. The monopole is less affected by gravity modifications because it is dominated by the density contribution, which is less sensitive to deviations from GR than the velocity contribution. The dipole is additionally affected by the term due to gravitational redshift in eq. (10.1), which is zero in ΛCDM and positive in both MGI and MGII.

In addition to the equation of state and EFT parameters, the observables are affected by the fraction of CDM within a galaxy, x_c, defined in eq. (10.2), which is generally unknown. The most straightforward possibility would be to assume that this fraction is equal to the fraction of CDM at the background level, as was done in ref. [99]. However, this is not necessarily the case. Therefore, we include a free parameter X in our analysis, capturing the deviation of x_c from the background CDM fraction ω_c. In particular, we assume that the fractions of mass in CDM and baryons in each galaxy (denoted as x_c, x_b respectively) are related to the respective background energy fractions ω_b, ω_c as

$$x_c = X\omega_c\,, \qquad x_b = X\omega_b + 1 - X\,, \tag{11.8}$$

so that the condition $x_c + x_b = 1$ is always satisfied. The parameter X can have values $X \in [0, 1 + \omega_b/\omega_c]$, corresponding to the extreme cases $x_c = 1$, $x_b = 0$ for $X = 1 + \omega_b/\omega_c$, and $x_c = 0$, $x_b = 1$ for $X = 0$.[4] The fiducial value is assumed to be $X = 1$, in which case the fraction of CDM inside a galaxy corresponds to the background one.

11.1.5 *MCMC analysis*

In summary, our model is characterized by the following set of parameters:

$$(\alpha_{\mathrm{B},0},\ \alpha_{\mathrm{M},0},\ \gamma_{c,0},\ w_{\mathrm{DE}},\ X,\ c_{\mathrm{B}},\ d_{\mathrm{B}},\ c_{\mathrm{F}},\ d_{\mathrm{F}})\,. \tag{11.9}$$

For each fiducial model in section 11.1.4, we generate mock values for the observables described above assuming zero noise. Then, we perform an MCMC analysis proceeding as follows. First, we evaluate the background quantities Ω_{m}, Ω_c and Ω_{r} by solving the system of equations given in eqs. (9.12)–(9.14). We then obtain $H(z)$ by integrating eq. (9.16) with initial condition $H(z=0) = H_0$, and compute the combination $c_s^2\alpha$ from eq. (9.26) with ζ given by eq. (9.6). Note that the derivative α_{B}' can be expressed using the time evolution specified in eq. (11.1). If $c_s^2\alpha$ is negative, signaling the presence of an instability, the point is rejected. Otherwise, we insert the background solutions into the perturbations equations, solve the resulting system of equations in eqs. (9.22) and (9.23), and compute the expected values of all the observables.

---

[4] Note that, if the WEP is satisfied, then ω_b, ω_c are constant, and the domain of X is fixed by the initial conditions. In our case, however, baryons and CDM can evolve differently, so the upper bound for X depends on the background evolution and in particular on the value of γ_c. In practice, during the MCMC analysis, at each step we reject the sample if X lies outside the range $[0, 1 + \omega_b/\omega_c]$.

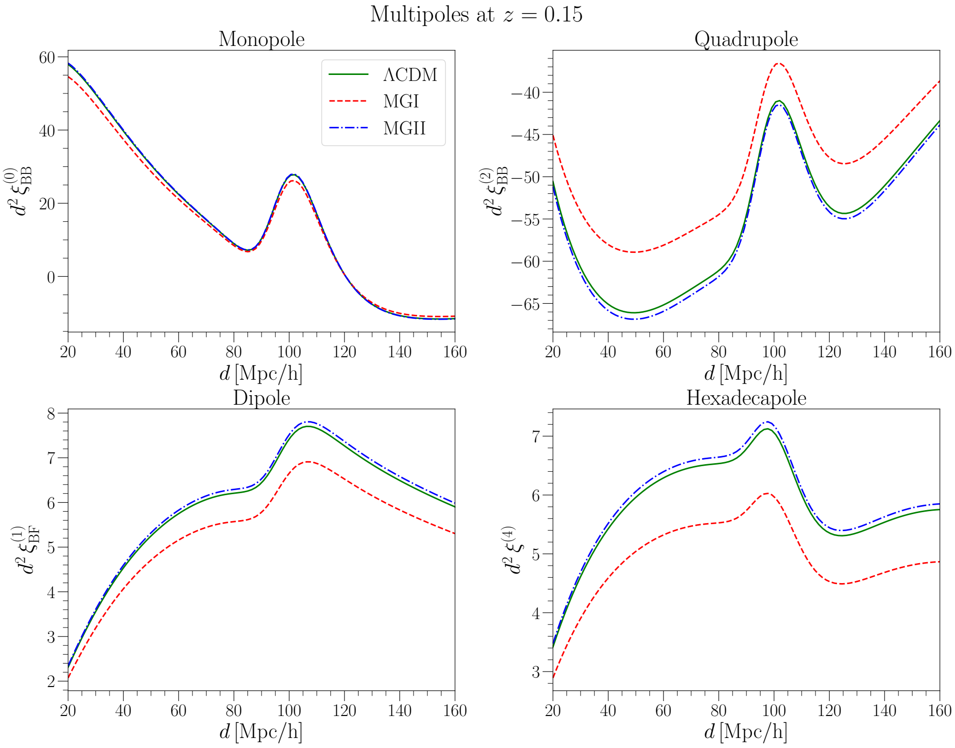

Figure 11.1: Multipoles of the galaxy correlation function as a function of separation, d, for ΛCDM (green) and the modified gravity fiducial models MGI (red) and MGII (blue), evaluated at the center of the first SKA redshift bin, $z = 0.15$.

The likelihood for the galaxy clustering observables is given by a multivariate Gaussian centered on the fiducial values. The respective covariance matrix includes cosmic variance due to the finite survey volume as well as shot noise arising from the finite number of observed galaxies (see sec. 2.4 for details). We include the non-vanishing cross-correlations between the even multipoles as well as between the bright and faint sample of galaxies. We also consider the pure cosmic variance contribution to the dipole from relativistic effects following ref. [39], where the robustness of the full theoretical expression for the covariance was thoroughly tested.[5] For the angular diameter distance to the CMB, we assume a Gaussian likelihood centered on the Planck value $D_{\rm M} = r_*/\theta_*$, where r_* and θ_* are taken from Planck 2018 [6]. The variance is computed by propagating the error accordingly. We adopt large priors on all variables except for X, which is restricted to its physical range as already described in section 11.1.4.

We use the ensemble slice sampler `zeus` [239, 240] [6] with 18 walkers, ensuring that the length of the chains is at least 50 times the autocorrelation time, and further excluding a burn-in phase equal to the correlation length and thinning by the autocorrelation time.

---

[5] In particular, ref. [39] performed a comparison to the simulation-based jackknife covariance in the case of DESI, showing that the theoretical covariance that we also adopt here slightly underestimates the errors due to the impact of non-linearities. This only leads to a mild difference in the detectability of the dipole in the case of DESI. For SKA2, we expect a similar impact in the low-redshift sample, but a lower impact at high redshifts where non-linearities have less importance. Note that the complete expression for the covariance should also contain the impact of the survey mask. This can be evaluated once the survey is performed.

[6] Note that this sampler uses the Ensemble Slice Sampling (ESS) algorithm, and not the Metropolis-Hastings algorithm described in sec.2.5

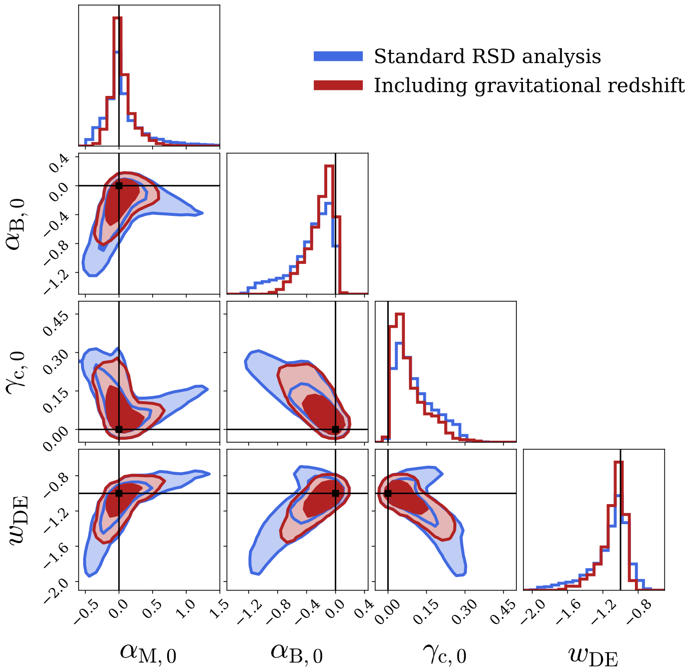

Figure 11.2: Constraints around a ΛCDM fiducial model.

11.2 RESULTS

In this section, we present the constraints obtained on the EFT parameters $\alpha_{\mathrm{M},0}$, $\alpha_{\mathrm{B},0}$, $\gamma_{c,0}$ and w_{DE}. We discuss the results for the three fiducial models introduced in section 11.1.4 (ΛCDM and two modified gravity fiducials) and we additionally study the impact of restricting the parameter space to specific subclasses of models. We compare the analysis solely based on the even multipoles of the galaxy two-point correlation function (standard RSD analysis) with the constraints obtained when also including the dipole, which contains the contribution of gravitational redshift.

11.2.1 *Constraints around a ΛCDM fiducial model*

Choosing ΛCDM as our fiducial model, we show in figure 11.2 the constraints on the EFT parameters, marginalized over the biases and the parameter X. The results obtained with a standard RSD analysis are presented in blue, while those that also include gravitational redshift are in red. In both cases, we also consider the angular diameter distance in our set of observables. In table 11.1, we report the marginal median values and credible intervals for the EFT parameters, both with and without the gravitational redshift (“Dipole" and “No dipole" columns).

11.2.1.1 *Standard RSD analysis including even multipoles only*

When considering the even multipoles only, the constraints arise from the galaxy velocity field and the angular diameter distance to last scattering, where the latter depends on the integral of the inverse Hubble parameter $H^{-1}(z)$ from today to the

	Median		Width of the 68% credible interval		
	No dipole	Dipole	No dipole	Dipole	Reduction
$\alpha_{\mathrm{M},0}$	0.01	0.01	$[-0.18, 0.31]$	$[-0.11, 0.17]$	43%
$\alpha_{\mathrm{B},0}$	-0.26	-0.17	$[-0.37, 0.19]$	$[-0.24, 0.13]$	34%
$\gamma_{\mathrm{c},0}$	0.09	0.06	$[-0.05, 0.11]$	$[-0.04, 0.09]$	19%
w_{DE}	-1.06	-1.05	$[-0.27, 0.12]$	$[-0.16, 0.08]$	38%

Table 11.1: Median values and 68% credible intervals for the ΛCDM fiducial model both for the standard RSD analysis (no dipole) and when adding the dipole that contains gravitational redshift. We also show the percent reduction on the credible interval obtained by including the dipole.

redshift of decoupling. In the following, we discuss the respective constraints (blue contours in figure 11.2) for each parameter pair.

- $w_{\mathrm{DE}} - \alpha_{\mathrm{M},0}$ contour: These two parameters affect directly the evolution of $H(z)$ and consequently the angular diameter distance to the CMB. From eq. (9.16) we see indeed that $H(z)$ is directly sensitive to w_{DE}, and that it also depends on α_{M} through the evolution of the radiation density Ω_{r}, see eq. (9.14). This leads to a strong degeneracy between $\alpha_{\mathrm{M},0}$ and w_{DE}, as can be seen in figure 11.2. For example, an equation of state $w_{\mathrm{DE}} < -1$ leads to a dark energy pressure more negative than in ΛCDM, increasing the distance to last scattering. This can be compensated by a negative α_{M}, which makes radiation decay more slowly than in ΛCDM: the increase in radiation pressure counteracts the negative pressure of dark energy, keeping the distance in agreement with CMB constraints. On the other hand, when $w_{\mathrm{DE}} > -1$, the opposite occurs, favoring a positive $\alpha_{\mathrm{M},0}$. This leads to the two branches in the contours in figure 11.2. Note that the direction of the $w_{\mathrm{DE}} - \alpha_{\mathrm{M},0}$ degeneracy changes when w_{DE} passes through -1. This is due to the fact that an equation of state significantly smaller than -1 can be easily compensated by increasing the pressure of radiation. On the other hand, an equation of state too close to zero would lead to no cosmic acceleration, which could not be compensated by a very low pressure from radiation.

- $\alpha_{\mathrm{M},0} - \alpha_{\mathrm{B},0}$ and $w_{\mathrm{DE}} - \alpha_{\mathrm{B},0}$ contours: We obtain a first branch with $w_{\mathrm{DE}} < -1$ and $\alpha_{\mathrm{M}} < 0$, in which case the stability of the perturbations requires $\alpha_{\mathrm{B}} < 0$. Indeed, linearizing eq. (9.26) around ΛCDM and applying eq. (9.15), we find that

  $$c_s^2\alpha = 2\alpha_{\mathrm{M}} + 3(1 + w_{\mathrm{DE}})\Omega_{\mathrm{DE}} + (1 + \Omega_{\mathrm{r}} - 3\Omega_{\mathrm{DE}})\alpha_{\mathrm{B}} - 2\alpha_{\mathrm{B}}' \,. \tag{11.10}$$

  Since $1 + \Omega_{\mathrm{r}} - 3\Omega_{\mathrm{DE}} < 0$ at low redshift, we see that $\alpha_{\mathrm{B}} < 0$ is needed to keep $c_s^2\alpha > 0$ when the first two terms are negative (note that α_{B}' has the same sign as α_{B} with our chosen time evolution). Moreover, since Ω_{DE} and α_{M} both decay at high redshift, while the term in front of α_{B} increases at high redshift (it becomes less negative), a strongly negative $\alpha_{\mathrm{B},0}$ is necessary to maintain $c_s^2\alpha > 0$ at higher redshift.[7] This is clearly visible in the $\alpha_{\mathrm{M},0} - \alpha_{\mathrm{B},0}$ and $w_{\mathrm{DE}} - \alpha_{\mathrm{B},0}$ contours of figure 11.2.

On the other hand, we have a second branch with $w_{\mathrm{DE}} > -1$ and $\alpha_{\mathrm{M}} > 0$, which both contribute positively to the sound speed. Since the term proportional to α_{B} in eq. (11.10) dominates over the first two at high redshift, $\alpha_{\mathrm{B},0}$ needs to be negative also in this branch to keep $c_s^2\alpha > 0$ in the past. In this case, however, the absolute value of $\alpha_{\mathrm{B},0}$ does not need to be as large as in the other branch, as is visible from figure 11.2.

- Contours involving the parameter $\gamma_{c,0}$: In addition to the distance to last scattering and the stability condition, the parameters are constrained by the even multipoles, which are directly sensitive to the galaxy growth rate f. The growth rate depends on the evolution of the dark matter and baryon density given in eqs. (9.22) and (9.23), providing a constraint on the combination

$$\frac{1}{c_s^2\alpha}(\alpha_{\mathrm{B}} - \alpha_{\mathrm{M}} + 3\gamma_c)(\alpha_{\mathrm{B}} - \alpha_{\mathrm{M}} + 3\gamma_c\omega_c b_c)\,. \tag{11.11}$$

This explains the behavior of $\gamma_{c,0}$ along the aforementioned two branches. Along the first branch, $\alpha_{\mathrm{M},0}$ and $\alpha_{\mathrm{B},0}$ are negative, and $|\alpha_{\mathrm{B},0}| > |\alpha_{\mathrm{M},0}|$ (to ensure stability also in the past). To counterbalance this, and keep the growth rate close to ΛCDM, it is necessary to have $\gamma_{c,0} > 0$. Along the second branch, we have $\alpha_{\mathrm{M},0} > 0$ and large, while $\alpha_{\mathrm{B},0} < 0$, again requiring $\gamma_{c,0} > 0$ to keep the growth rate consistent with ΛCDM. This is clearly visible in the $\gamma_{c,0} - \alpha_{\mathrm{M},0}$ and $\gamma_{c,0} - \alpha_{\mathrm{B},0}$ contours of figure 11.2.

The degeneracy between γ_c and α_{M} can be understood from the Einstein and Euler equations: a positive γ_c mainly enhances the growth of structure by changing the way dark matter falls in a gravitational potential, as can be seen from eq. (9.20). Indeed, the coupling of the scalar field to dark matter generates an additional force on dark matter particles. On the other hand, a positive running of the Planck mass α_{M} in the first branch implies that the mass increases with time, leading to a decrease of the effective Newton constant in the Poisson equation, see eq. (9.21). This implies that a given matter density perturbation leads to a smaller distortion of space through the Poisson equation, thus decreasing the growth of structure and counterbalancing the enhancement arising from $\gamma_c > 0$. In the second branch, a negative α_{B} counterbalances a positive γ_c. The parameter α_{B}, which encodes a mixing between the scalar and tensor kinetic terms, impacts the kinetic energy of the scalar field, which in turns affects the Poisson equation and therefore the growth of structure.

From figure 11.2, we notice that the posteriors are highly non-Gaussian, due to the strong degeneracies between the parameters. Such a behavior cannot be captured by a Fisher analysis, which assumes Gaussian posteriors. Therefore, our results show that it is essential to perform an MCMC analysis to fully understand the degeneracies in Horndeski theories and scenarios involving a breaking of the WEP, and correctly forecast the constraining power of the coming generation of surveys.

---

[7] Note that, when dark energy becomes negligible at very high redshift, $1 + \Omega_{\mathrm{r}} - 3\Omega_{\mathrm{DE}}$ changes sign. However, α_{B} and α_{M} also approach zero at that point and we recover GR.

11.2.1.2 *Including gravitational redshift by adding the dipole*

The inclusion of the dipole in the analysis (red contours in figure 11.2) has a strong impact on the constraints, favoring one of the branches over the other. This is due to the fact that the dipole is directly sensitive to the combination

$$\gamma_c \left[f - (1+z) \left(\frac{\mathcal{H}_0}{\mathcal{H}} \right)^2 \frac{3\,\Omega_{m,0}}{c_s^2 \alpha} (\alpha_B - \alpha_M + 3\gamma_c \omega_c b_c) \right] , \tag{11.12}$$

as can be seen from eq. (10.1). From this, we notice that keeping the dipole close to its ΛCDM value requires either a small γ_c or a cancellation of the two terms in the square bracket. This tightens the constraints on γ_c, as is clearly visible in figure 11.2. Moreover, the degeneracy between γ_c, α_B and α_M is broken by imposing that $(\alpha_B - \alpha_M + 3\gamma_c w_c b_c)/c_s^2\alpha$ is tuned to balance the growth rate f. From figure 11.2, we see that adding this constraint by including the dipole almost completely removes one of the branches in the parameter space and significantly tightens the other. Since w_{DE} is strongly degenerated with α_M, the tightening of the constraints on α_M from the dipole also improves the constraints on w_{DE}.

In appendix C, figure C.1, we show the constraints arising from the monopole alone and compare them to an analysis based on the combination of monopole and dipole. Also in this case, the dipole efficiently breaks the degeneracy between the parameters and removes one of the branches. The only difference with respect to the analysis with all multipoles is that the monopole is much less constraining on its own than in combination with the quadrupole and hexadecapole. This is due to the fact that the growth rate is degenerated with the galaxy bias using the monopole alone, whereas the inclusion of the other two even multipoles breaks this degeneracy and overall reduces the size of the two branches.

The improvement arising from the dipole is impressive: the constraints on the EFT parameters are tightened by up to 50%, as can be seen from table 11.1. This is especially remarkable considering that the signal-to-noise ratio (SNR) of the dipole is significantly smaller than that of the even multipoles. Indeed, for a bias difference $\Delta b = 1$ the cumulative SNR of the dipole in ΛCDM from separations $d = 20 - 160\,\mathrm{Mpc/h}$ over the redshift range $z = 0.15 - 1.55$ is 80, while that of the quadrupole is 461, i.e. almost 6 times larger.

The reason why such a small signal can significantly improve the constraints is because deviations from ΛCDM affect it differently from the even multipoles. Hence, the key element to quantify its constraining power is the amplitude of the deviations with respect to ΛCDM. For example, if we choose a point at the edge of the $2\,\sigma$ contours of figure 11.2 with $\alpha_{M,0} = 1.3$, $w_{DE} = -0.8$, $\alpha_{B,0} = -0.4$ and $\gamma_{c,0} = 0.17$, we find that the SNR of the deviation is 6.2 for the quadrupole. For the dipole, the SNR of the WEP-breaking term (first line in eq. (10.1)) is 3.6, so not even two times smaller. Since this term has a very different dependence on the EFT parameters than the quadrupole, such an SNR is sufficient to significantly tighten the constraints.

The amplitude of the WEP-breaking term in the dipole in eq. (10.1) is directly sensitive to the galaxy bias difference between the two populations of galaxies, which we assume here to be equal to 1. This is what can be typically expected if the sample of galaxies is split into two populations according to their observed flux, for a population of galaxies similar to that of BOSS [47]. The situation may be different for the galaxies detected by

	Median		Width of the 68% credible interval		
	No dipole	Dipole	No dipole	Dipole	Reduction
$\alpha_{\mathrm{M},0}$	0.02	0.00	$[-0.12, 0.47]$	$[-0.08, 0.20]$	53%
$\alpha_{\mathrm{B},0}$	-0.15	-0.12	$[-0.20, 0.12]$	$[-0.19, 0.10]$	9%
$\gamma_{\mathrm{c},0}$	0.06	0.05	$[-0.03, 0.06]$	$[-0.03, 0.06]$	0%
$\hat{w}_{\mathrm{DE}}$	-1.02	-1.01	$[-0.06, 0.02]$	$[-0.03, 0.01]$	50%

Table 11.2: Median values and 68% credible intervals for the ΛCDM fiducial model both for the standard RSD analysis (no dipole) and when adding the dipole that contains gravitational redshift, employing the alternative parametrization with the effective equation of state parameter $\hat{w}_{DE}$. For the credible interval, we also show the percent reduction obtained by the latter.

SKA2, for which the bias difference between two magnitude-limited samples may be smaller, decreasing the constraining power of the dipole. In such a case, it would be important to explore alternative ways of splitting galaxies to achieve the breaking of degeneracies we obtain in our forecasts, for example density splits where the galaxies are divided into two groups according to their environment. In this case, the bias difference between the two populations can become significantly larger [111, 234]. To mimic this, we have boosted the dipole by a factor 2, 5 and 10, see figure C.2 in appendix C. We find that the contours are significantly tightened when the dipole is boosted, completely removing the second branch. This motivates the search for estimators of the dipole that would enhance the gravitational redshift contribution.

Finally, we notice that, while the dipole tightens the constraints on the model parameters, we do not see a significant impact on the nuisance parameters X, $b_{1,\mathrm{B}}$, $b_{2,\mathrm{B}}$, $b_{1,\mathrm{F}}$ and $b_{2,\mathrm{F}}$. Concerning the four parameters specifying the biases of the two galaxy populations, this result matches our expectation that galaxy bias can be well measured from the even multipoles alone. The constraints on the relation X between the background CDM fraction and the average fraction of CDM inside a galaxy are always completely dominated by the physical prior specified below eq. (11.8), which luckily does not spoil the constraints on the model parameters. The corner plot for the full parameter space is included in appendix C, figure C.4, showing the constraints from the even multipoles alone and from all multipoles.

We could further extend our analysis by varying the cosmological parameters Ω_{m}, Ω_{b}, Ω_{r} at recombination as well as A_s and n_s in a joint analysis with CMB data. This would slightly broaden the constraints on our set of parameters. However, we do not expect this to affect the message of our work. A priori, letting the cosmological parameters vary should affect in a similar way the even multipoles and the dipole, such that the percentage improvement brought by the dipole should remain roughly the same.

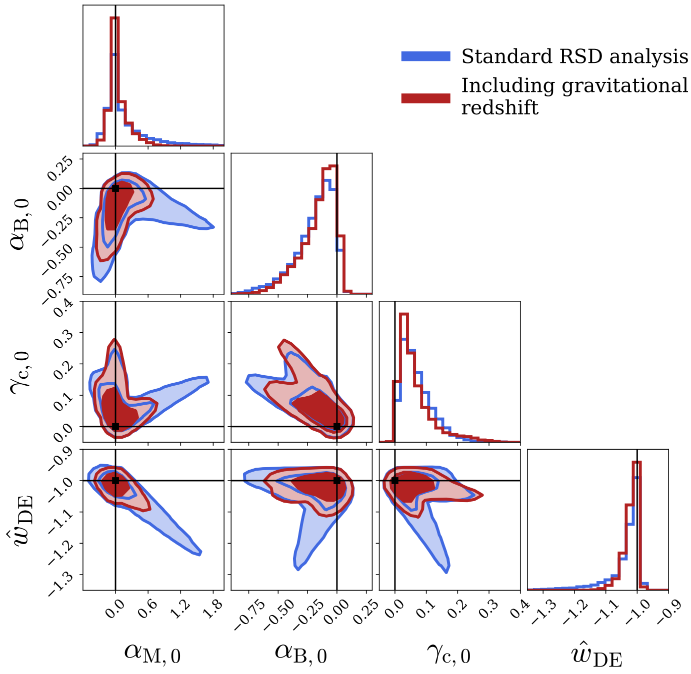

Figure 11.3: Constraints around a ΛCDM fiducial model, employing the alternative parametrization with the effective equation of state parameter $\hat{w}_{\mathrm{DE}}$.

11.2.1.3 *Changing the parametrization for the dark energy evolution*

The equation of state parameter of dark energy, w_{DE}, is defined as the ratio of the dark energy pressure and the dark energy density. From eq. (9.11), we see that the evolution of the dark energy density depends on w_{DE} and also on α_{M} and γ_c, where the latter governs the interaction of dark energy with dark matter. Alternatively, we can define an effective equation of state, $\hat{w}_{\mathrm{DE}}$, directly encoding the evolution of dark energy through

$$\bar{\rho}'_{\mathrm{DE}} = -3(1+\hat{w}_{\mathrm{DE}})\bar{\rho}_{\mathrm{DE}}\,. \tag{11.13}$$

Comparing eq. (11.13) with eq. (9.11), we see that the effective equation of state is related to the true equation of state by

$$\hat{w}_{\mathrm{DE}} = w_{\mathrm{DE}} - \frac{1}{3}\alpha_{\mathrm{M}}\frac{\bar{\rho}_{tot}}{\bar{\rho}_{\mathrm{DE}}} + \gamma_c\frac{\bar{\rho}_c}{\bar{\rho}_{\mathrm{DE}}}\,. \tag{11.14}$$

This leads to the following expression for the Hubble parameter

$$H(z) = H_0 \exp\left[\frac{3}{2}\int_{\ln(a(z))}^{0} \mathrm{d}\ln a' \left(1 + \frac{1}{3}\alpha_{\mathrm{M}} + \frac{1}{3}\Omega_{\mathrm{r}} + \hat{w}_{\mathrm{DE}}\Omega_{\mathrm{DE}} - \gamma_c\Omega_c\right)\right]\,. \tag{11.15}$$

In figure 11.3, we show the constraints on the new set of parameters $\alpha_{\mathrm{M},0}$, $\alpha_{\mathrm{B},0}$, $\gamma_{c,0}$ and $\hat{w}_{\mathrm{DE}}$. As in the previous analysis, we see that the inclusion of the dipole significantly alleviates the strong degeneracies among the parameters that would otherwise be present. The direction of the degeneracies is however different with the new parametrization, which is not surprising given that the relation between w_{DE} and $\hat{w}_{\mathrm{DE}}$ depends on γ_c and α_{M}. In particular, we notice that now an equation of state $\hat{w}_{\mathrm{DE}} < -1$ is degenerated with a positive α_{M}. This follows from the angular diameter distance constraint, which depends on the evolution of $H(z)$. In this new parametrization, the latter depends directly on α_{M}, γ_c and $\hat{w}_{DE}$, as can be seen from eq. (11.15). From this equation we notice that $\hat{w}_{\mathrm{DE}} < -1$ is counterbalanced by $\alpha_{\mathrm{M}} > 0$ and $\hat{w}_{DE} > -1$ by $\alpha_{\mathrm{M}} < 0$. As before, this leads to two branches in the parameter space when only the even multipoles are considered.

We see that the constraints are clearly asymmetric around ΛCDM. This is particularly visible in the $\alpha_{\mathrm{M},0} - \hat{w}_{DE}$ contours, which are shifted towards positive values of $\alpha_{\mathrm{M},0}$. This asymmetry is related to an interplay between the stability conditions and the constraints from the growth rate and the angular diameter distance. Indeed, linearizing the combination $c_s^2\alpha$ around ΛCDM with the new parametrization, we find

$$c_s^2\alpha = 3\alpha_{\mathrm{M}} + 3(1+\hat{w}_{\mathrm{DE}})\Omega_{\mathrm{DE}} - (2 - 3\Omega_{\mathrm{m}} - 4\Omega_{\mathrm{r}})\alpha_{\mathrm{B}} - 2\alpha_{\mathrm{B}}' - 3\gamma_c\Omega_c\,. \tag{11.16}$$

The degeneracy in the $\alpha_{\mathrm{M},0} - \hat{w}_{DE}$ plane is governed by the distance to last scattering, which is sensitive to the combination $\alpha_{\mathrm{M}} + 3(1+\hat{w}_{\mathrm{DE}})\Omega_{DE}$ through eq. (11.15). Along this degeneracy direction, when α_{M} is positive, the positivity of the combination $\alpha_{\mathrm{M}} + (1+\hat{w}_{\mathrm{DE}})\Omega_{\mathrm{DE}}$ in eq. (11.16) is automatically maintained. This leads to a positive $c_s^2\alpha$ even when $\alpha_{\mathrm{B}} = 0$, as long as γ_c is small enough. Hence, the stability condition and the requirement of having a distance and growth rate close to ΛCDM are simultaneously satisfied. On the other hand, when α_{M} is negative along the degeneracy direction, then $\alpha_{\mathrm{M}} + (1+\hat{w}_{\mathrm{DE}})\Omega_{\mathrm{DE}} < 0$. To ensure stability, it is thus necessary to have negative values of α_{B} and γ_c. This leads to stronger deviations in the growth rate, which are disfavored.

As with the other parametrization, we see that adding the dipole strongly tightens the constraints on $\alpha_{\mathrm{M},0}$ by breaking the degeneracies with $\alpha_{\mathrm{B},0}$ and $\gamma_{c,0}$, which in turns also tightens the constraints on $\hat{w}_{\mathrm{DE}}$. Quantitatively, from table 11.2, we see that the 1 σ constraints on $\alpha_{\mathrm{M},0}$ and $\hat{w}_{\mathrm{DE}}$ are improved by 53% and 50% respectively when the dipole is added. On the other hand, the constraints on $\alpha_{\mathrm{B},0}$ are only mildly improved with this parametrization, while those on $\gamma_{c,0}$ show no improvement. Nevertheless, the red 2-dimensional contours involving $\gamma_{c,0}$ in figure 11.3 show a clear preference of one branch when including gravitational redshift. Overall, comparing table 11.1 and 11.2, we see that the dipole significantly tightens the constraints in both cases, but the way the improvement is distributed among the parameters clearly depends on the parametrization.

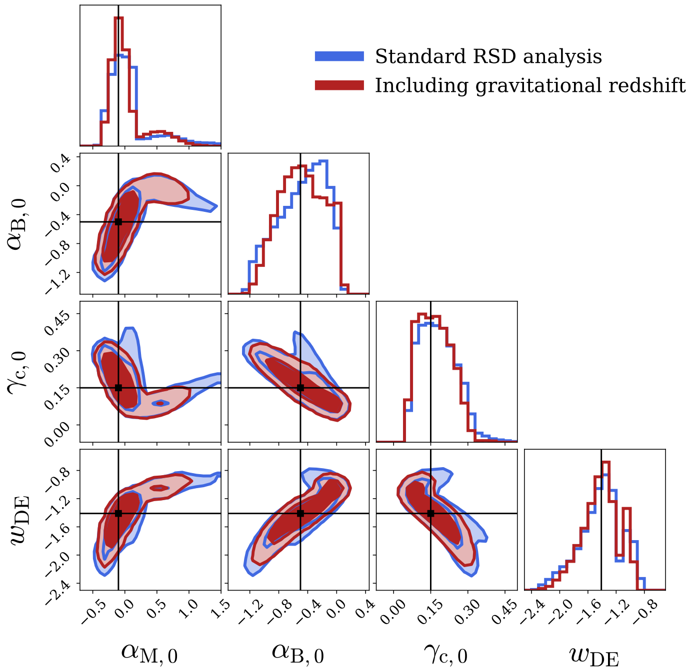

Figure 11.4: Constraints around the modified gravity fiducial MGI.

11.2.2 *Constraints around modified gravity fiducials*

As explained in section 11.1.4, we also explore constraints around two other fiducial models: one that would solve the Hubble tension (MGI) and another one that is closer to ΛCDM (MGII). The results for MGI are plotted in figure 11.4. We notice that the double branches around MGI are less pronounced in the blue contours (standard RSD analysis), than around ΛCDM (figure 11.2). This is due to the fact that the MGI fiducial model is well inside one of the branches of the ΛCDM contours. For example, we can see that the point with $\gamma_{c,0} = 0.15$ and $\alpha_{M,0} = -0.1$ are well within the vertical branch of the $\gamma_{c,0} - \alpha_{M,0}$ contour in figure 11.2. As such, when we shift the fiducial model to this region, the degeneracies are already partially broken. While of course new degeneracies can appear around this new fiducial, figure 11.4 indicates that they are much less pronounced. As a consequence, including gravitational redshift still improves the constraints, but in a less significant way than around ΛCDM. From figure 11.4, we also notice that if MGI were to be the true model in our Universe, data from SKA2 would not be able to rule out ΛCDM based on the gravity + scalar sector only, as the 2σ error bars on $\alpha_{M,0}$, $\alpha_{B,0}$ and w_{DE} encompass the corresponding ΛCDM values. However, we see that SKA2 would be able to favor MGI over ΛCDM based on the coupling to dark matter $\gamma_{c,0}$, which is incompatible with zero at more than 2σ. Note that a model different from MGI might lead to a different conclusion regarding the relation with ΛCDM.

The constraints around MGII are shown in appendix C, figure C.3. In this case, the degeneracies are still very pronounced with a standard RSD analysis. Since MGII is only mildly away from ΛCDM, the two branches around this point are quite similar to those around ΛCDM. As a consequence, we see that adding gravitational redshift significantly tightens the constraints, in a similar way as for the ΛCDM fiducial.

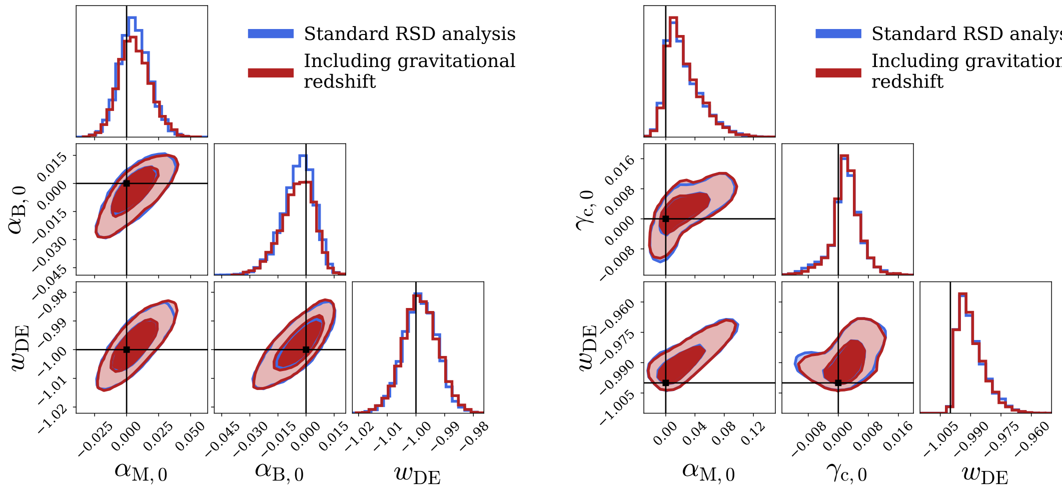

Figure 11.5: Constraints given a ΛCDM fiducial when one parameter is kept fixed. *Left panel*: γ_c is fixed to zero. *Right panel*: $\alpha_{\mathrm{B}} = \alpha_{\mathrm{M}}/2$.

11.2.3 *Constraints for specific subclasses of Horndeski theories*

As discussed above, the strength of gravitational redshift is to break the degeneracy between the parameters $\gamma_{c,0}$, $\alpha_{\mathrm{B},0}$ and $\alpha_{\mathrm{M},0}$. As a comparison, we investigate specific models where only two of the three parameters are left free. In figure 11.5 (left panel), we show the contours for the case of Horndeski theories without a breaking of the WEP, i.e. with $\gamma_c = 0$. In the right panel we show another specific case, where the parameter $\gamma_{c,0}$ is left free, but we fix $\alpha_{\mathrm{B}} = \alpha_{\mathrm{M}}/2$. This corresponds to various Horndeski theories (cf. table 1 in ref. [164]), including Brans-Dicke theories [172, 241] and some $f(R)$ models [169, 242–244]. From these figures, we see that the constraints from the RSD analysis are much tighter than before. The degeneracies in the parameter space are indeed much less severe when one parameter is removed. In particular, the strong degeneracy between $\alpha_{\mathrm{M},0}$ and w_{DE} is reduced, due to the increased constraints on $\alpha_{\mathrm{M},0}$ from the growth of structure f. In these cases, gravitational redshift does not improve the constraints further. This is consistent with the SNR comparison made above: the statistical power of the dipole term (the full expression in eq. (10.1)) is ~ 6 times smaller than that of the quadrupole. As such, when there is no strong degeneracy to break, the dipole has almost no impact on the constraints. This is also in agreement with the results of ref. [245], who showed that relativistic effects do not help to constrain Horndeski theories with no breaking of the WEP.

A word of caution is however necessary concerning these results: both the analysis of ref. [245] and our analysis assume a fixed time evolution for the parameters. Even if we have chosen this time evolution to be the same for all parameters in order to minimize its impact on the degeneracies, the simple fact that we assume a known time evolution helps breaking some of the degeneracies. For example, in eq. (11.11), the term $w_c b_c$ has a different time evolution from γ_c and α_{M} and therefore helps to break the degeneracy between these parameters in the model with $\alpha_{\mathrm{B}} = \alpha_{\mathrm{M}}/2$, when we combine multiple redshift bins. If we consider one redshift bin only, i.e. we do not exploit the fact that we have a fixed time evolution for the parameters, we find that the parameters are completely degenerated and cannot be constrained anymore.

12

SUMMARY AND CONCLUSION

In this Chapter, we show that the effect of gravitational redshift, which will be measurable with the coming generation of galaxy surveys, is crucial to efficiently test models beyond GR. To determine the constraining power of this new observable in a generic way, we have considered the Effective Theory of Interacting Dark Energy, which encompasses all scalar-tensor theories of gravity and allows for a non-minimal coupling of dark matter. We find that adding gravitational redshift to a standard RSD analysis significantly improves the constraints on the EFT parameters, by up to 50 percent. The precise results depend on the choice of parameterization within the EFT framework, on the time evolution assumed for the EFT functions and on the fiducial cosmological model, but the overall message remains unaffected by these details: gravitational redshift breaks degeneracies between parameters, leading to a significant improvement in the constraints.

To measure this novel observable, no new data are involved: one can simply fit for a dipole in the cross-correlation function between two different populations of galaxies. This requires minimal changes to the analysis pipeline, but leads to a strong impact on the constraints. The improvement is especially remarkable given that the SNR of the dipole is typically six times smaller than that of the standard quadrupole term. However, the specificity of the dipole is that it contains a particular combination of gravitational redshift and Doppler effects, which exactly vanishes if the WEP is valid. This combination is not present in the standard even multipoles of the correlation function and is able to break the degeneracies between the EFT parameters. Note that, since this combination is proportional to the bias difference between the two populations of galaxies, we expect the breaking of degeneracies to scale with the value of this difference. Here, we have assumed a bias difference equal to 1, but estimators that would boost this difference may improve the constraints further, while a lower difference may result in an overall worsening.

In this work we have focused on spectroscopic surveys, which are directly sensitive to the growth rate of structure through RSD. In a future work, we will study whether the inclusion of gravitational lensing can further improve the constraints. Since gravitational lensing is sensitive to the sum of the two gravitational potentials (the spatial and temporal perturbations in the metric), while gravitational redshift only depends on the distortion of time, combining the two may lead to more stringent constraints on the effective theory of interacting dark energy. Possible future work could also include an investigation beyond the quasi-static approximation assumed in our work and the choice of other time parametrizations for the EFT parameters.

We conclude that measuring gravitational redshift provides an efficient way of increasing the constraining power of large-scale structure surveys at minimal cost, and a combination with additional observables could further increase its remarkable constraining power. Testing the EFT of Interacting Dark Energy is a remarkable use case for the odd multipoles encoding the relativistic distortions (the dipole in this case). It is of course complementary to the model-independent test of the anisotropic stress developed in Part ii. There, we adopted and agnostic approach and constructed an estimator which does not depend on any specific model, which can tell us if gravity is genuinely modified by the presence of a gravitational slip on large scales. However, it does not help in distinguishing the model that makes the Bardeen potentials different at late times. If the observer is interested in model testing, adopting the approach of the current Part is a theoretically satisfying avenue. The EFT framework encapsulates a large class of modified gravity models, which can potentially be tested as a whole by just considering an additional observable in the analysis. The inclusion of the dipole, which is sensitive to the gravitational redshift, significantly helps in constraining the parameter space and hence in reducing the number of models allowed by the spectroscopic data.

SOFTWARE AVAILABILITY

The Python code `EF-TIGRE` (*Effective Field Theory of Interacting dark energy with Gravitational REdshift*) developed for this project is publicly available on Github at github.com/Mik3M4n/EF-TIGRE. The version used for this work is available on Zenodo at 10.5281/zenodo.10606418.

Part IV

CONSTRAINTS ON MAGNIFICATION AND EVOLUTION BIASES FROM THE ODD MULTIPOLES

13

SEARCHING FOR DEVIATIONS FROM GAUSSIANITY

This Part is based on publication 5 listed in the preamble.

As extensively discussed in the previous Parts, the coming generation of large-scale structure surveys, like DESI, Euclid, LSST and SKA will detect billions of galaxies over a large part of the history of the Universe. We have proven that these observations can be used to reconstruct the LSS at late times and to test the theory of gravity in a variety of scenarios. However, adopting a different perspective, these surveys will provide invaluable information on the properties and dynamics of galaxies as well. In particular, they will allow us to determine the luminosity and redshift distribution of galaxies, which is crucial to understand how galaxies form and evolve.

Interestingly, knowing the luminosity and redshift distribution of galaxies is necessary to perform some cosmological tests, complementary to those discussed throughout this Thesis. For example, the large-scale structure of the Universe can also be used to search for primordial non-Gaussianities (PNG) in the initial fluctuations generated during inflation [246, 247]. As we will briefly show below, this search is however contaminated by the presence of relativistic effects in the clustering of galaxies [11, 38, 137, 245, 248–257], whose amplitude directly depends on their astrophysical properties. A precise knowledge of the luminosity and redshift evolution of galaxies is therefore essential to model relativistic effects precisely and subtract the signal from the non-Gaussian one.

A second example is the test of the cosmological principle from the measurement of the kinematic dipole in the distribution of galaxies. If the cosmological principle is valid, the kinematic dipole measured from the temperature of the Cosmic Microwave Background (CMB) and the dipole in the distribution of astrophysical sources should be in agreement [258]. Current measurements show tensions between the two dipoles [259–261]. In this context, measuring the redshift evolution of the astrophysical dipole could help in assessing the origin of the tension [262, 263]. Since the amplitude of the astrophysical dipole is directly governed by the luminosity and redshift evolution of the sources [264, 265], a precise determination of these quantities is highly relevant.

The luminosity and redshift distribution of galaxies can be directly measured by binning the population of galaxies in redshift and luminosity. In this Part, we show that these measurements can be significantly improved by measuring, in addition, the 2-pt cross-correlation function between two populations of galaxies. More precisely, the luminosity and redshift distribution of galaxies can be encoded into two parameters: the magnification bias $s(z)$ which denotes the slope of the cumulative number of sources above a given luminosity threshold, and the evolution bias $f^{\mathrm{evol}}(z)$ which denotes the slope of the cumulative number sources with redshift. These two parameters directly enter the 2-pt cross-correlation function, more precisely into the dipole and octupole of these 2-pt function (see Chapters 1 and 2). By measuring these odd multipoles, one can constrain the magnification and evolution biases, and consequently improve our knowledge on the luminosity and redshift distribution of galaxies.

The rest of the current and last Part is organized as follows: in sec. 13.1 we briefly discuss the imprint of the presence of primordial non-Gaussianities in the LSS at late times. We complete this introductory part in sec. 13.2 by showing how the relativistic effects are regarded in this context as contaminants to the PNG signal. Next, we introduce a new modeling of the magnification and evolution biases in Chapter 14 for a survey like SKA, which accounts for the splitting of the background population into different sub-samples. In Chapter 15, we discuss the methodology to constrain the magnification and evolution biases, and we present our results in Chapter 16. Finally, we conclude in Chapter 17.

13.1 A BRIEF ON PRIMORDIAL NON-GAUSSIANITIES

One of the master pillars in cosmological analysis is that the primordial perturbations, i.e. the seeds of the LSS, initially obey a Gaussian distribution which then evolves due to gravitational instability. Hence, in principle, it is the non-linear gravitational evolution which makes the late-times distribution of galaxies non-Gaussian at small and intermediate scales. A signature of this non-Gaussianity is manifest in non-zero statistical higher-order moments in the galaxy distribution. The most important example is the 3-point galaxy clustering correlation function (or, in the Fourier realm, the *Bispectrum*). However, obviously, if any deviation from Gaussianity existed at early-times, it will leave an imprint in the observed higher-order moments which we might desire to disentangle from the late-times phenomenology.

Interestingly, a plethora of inflationary models actually predict small deviations from Gaussianity at early times which are compatible with CMB observations. Assuming scale-independence, these deviations can be characterized by writing the primordial potential as [137, 266, 267]

$$\Psi_{\rm in} = \psi_{\rm L} + f_{\rm NL}\left(\psi_{\rm L} - \langle\psi_{\rm L}^2\rangle\right), \tag{13.1}$$

where $\psi_{\rm L}$ is the Gaussian part of the potential and $f_{\rm NL}$ encodes the amplitude of the deviations. Note that since the primordial fluctuations are of order $\psi_{\rm L} \sim 10^{-5}$, even a value of $f_{\rm NL}$ of $\mathcal{O}(100)$ yields a non-Gaussian imprint only at the 10^{-3} level. Hence, this signal is expected to be very small. However, a detection of $f_{\rm NL} \sim 1$ or above is regarded as a major breakthrough which will require better understanding of the inflationary paradigm.

As of today, the strongest constraints on $f_{\rm NL}$ are derived from observations of the CMB by Planck, which predict $f_{\rm NL} = 0.9 \pm 5.1$ [268]. Interestingly, late-times LSS observations are expected to surpass Planck's precision. Current galaxy surveys such as eBOSS have already reached uncertainties of order $\mathcal{O}(10)$ [269]. In addition, forecasts for new generation LSS surveys such as DESI, Euclid and SKA yield constraints on $f_{\rm NL}$ of order $\mathcal{O}(1)$ [38, 105, 270].

13.2 DISENTANGLING PNG AND RELATIVISTIC EFFECTS

Besides the higher-order moments such as the bispectrum mentioned before, deviations from Gaussianity at early times leave also an imprint in the 2-pt correlation functions at linear order. A measurement of such effect is only possible by probing the ultra large-scale regime, $k \sim \mathcal{H}$, which will be accessible by the new generation of galaxy surveys. However, in this regime, the PNG signal is hidden under the late-times relativistic effects. Let us briefly see this matter following ref. [137].

13.2.1 *Imprints from early times at linear order*

In the case of a non-zero primordial $f_{\rm NL}$, the linear galaxy bias develops a scale-dependent correction which goes as

$$b(z) = b_1(z) + \Delta b(z), \qquad \Delta b(z) \sim f_{\rm NL}(b_1 - p)\,\frac{1}{k^2\,T(k)\,D(z)}, \tag{13.2}$$

where b_1 is the scale-independent part of linear bias considered in the previous analyses and p is a parameter that depends on the tracer. We have omitted some phenomenological and normalization factors, for simplicity. In the ultra-large scale limit, i.e. $k \to 0$, the transfer function $T(k) \to 1$ and hence we have $\Delta b \sim k^{-2}$. Therefore, the PNG signal is only enhanced at very large scales.

The simplest way to write down explicitly the impact of $f_{\rm NL}$ in the clustering of galaxies is to replace eq. (13.2) in the expressions for the multipoles, given in eqs.(4.4)-(4.8). Using the transfer functions of sec. 2.1 in the single-tracer case ($b_{\rm L} = b_{\rm M} = b$), one can find that in GR the even multipoles receive corrections of the form

$$\Delta P^{(0)}(k,z) = \left[\left(2\,b_1(z) + \frac{2}{3}\,f(z)\right)\Delta b(k,z) + \Delta b^2(k,z)\right] P_{\delta\delta}(k,z) \tag{13.3}$$

$$\Delta P^{(2)}(k,z) = \frac{4}{3}\Delta b(k,z)\,f(z)\,P_{\delta\delta}(k,z). \tag{13.4}$$

Therefore, we conclude that, in the presence of deviations from Gaussianity at early times, i.e. $f_{\rm NL} \neq 0$, the monopole develops two corrections scaling with k^{-2} and k^{-4}. On the other hand, the quadrupole only develops a correction which grows as k^{-2}. This is the galaxy clustering PNG signal that we could extract, in principle, from the two point statistics. Note that the hexadecapole is not affected by PNG as it is independent on the galaxy bias. We do not discuss the $f_{\rm NL}$ corrections in the odd multipoles since their signal is subdominant with respect to the even multipoles and strongly suppressed at very large scales, where cosmic variance is expected to dominate. However, this last statement does not mean that the relativistic effects are irrelevant in this context.

13.2.2 *Relativistic effects at very large scales*

Let us briefly remind about our result for the galaxy number counts at linear order in perturbation theory. We split the expression into four contributions according to eq. (1.57). So far, we have just considered the standard and dipolar contributions of eqs. (1.42) and eqs. (1.58) (or (1.59) if Euler equation is valid.), which are the dominant contributions at sub-horizon scales $k \gg \mathcal{H}$ and low redshift. The lensing contribution is negligible at least below $z = 1.5$, but is not for deeper surveys [27, 136, 271]. However, the last contribution Δ_{CORR} given (1.61) is suppressed by two powers $(\mathcal{H}/k)^2$ compared to the standard contribution. It contains Sachs-Wolfe effects, integrated Sachs-Wolfe and time delay. These terms are currently negligible compared to the standard contributions for analyses at scales $k \gg \mathcal{H}$.

Importantly, the coming generation of surveys will observe very large parts of the sky, allowing us to measure the galaxy power spectrum at very large scales (i.e. very low k). In this regime, $\mathcal{H}/k \sim 1$ and Δ_{CORR} becomes relevant. As discussed above, another goal of the coming generation of surveys is to measure PNG, by looking at their effect on the galaxy power spectrum at small k, it is necessary to have a precise modelling of Δ_{CORR}, which directly contaminates the non-Gaussian signal. The integrated terms are expected to be negligible at low redshift, similarly as for Δ_{LENS}. Hence, the relevant additional relativistic corrections are

$$\Delta_{\text{CORR}} = \left(3 - f^{\text{evol}}\right) \mathcal{H}\nabla^{-2}(\nabla \mathbf{V}) + (5s-2)\Phi + \frac{1}{\mathcal{H}}\dot{\Phi} + \left(1 + \frac{\dot{\mathcal{H}}}{\mathcal{H}^2} + \frac{2-5s}{r\mathcal{H}} + 5s - f^{\text{evol}}\right)\Psi + \dots, \tag{13.5}$$

where we explicitly see that this contribution depends on the magnification bias $s(z)$ and the evolution bias $f^{\text{evol}}(z)$ of the galaxy population. To properly model the contamination from Δ_{CORR} to primordial non-Gaussianities, it is therefore necessary to have a precise determination of s and f^{evol}.

Let us first justify what we mean about model the contamination. It is simpler to see explain it in Fourier space, where the galaxy number counts of eq. (2.17) picks up a correction going as $(\mathcal{H}/k)^2$. In GR, we can use the transfer functions to write down the expression in terms of the matter perturbations. In the case of one population of tracers, we have

$$\Delta(\mathbf{k}, z) = \left[b_1 + f\,(\mathbf{k}\cdot\mathbf{n})^2 + i\frac{\mathcal{H}}{k}\alpha_1(z)\, f\,(\mathbf{k}\cdot\mathbf{n}) + \left(\frac{\mathcal{H}}{k}\right)^2 \alpha_2(z)\right] \delta(\mathbf{k}, z), \tag{13.6}$$

where $\alpha_1 = 1 - \alpha_{\text{L}}$ with α_{L} given in eq. (2.18). [1] We have also the factor [137]

$$\alpha_2(z) \equiv \left(3 - f^{\text{evol}}(z)\right) f + \left(\frac{\dot{\mathcal{H}}(z)}{\mathcal{H}^2(z)} - 1\right)\left(\alpha_1(z) + f(z) - (2 - 5s(z))\right). \tag{13.7}$$

By computing the power spectrum from this eq. (13.6), one finds that the relativistic corrections only modify the monopole and the quadrupole by

$$\Delta P^{(0)}(k,z) = \left[\left(\frac{\mathcal{H}}{k}\right)^2 \left(2\,b_1\alpha_2 + \frac{2}{3}\alpha_2 f + \frac{1}{3}\alpha_1^2 f^2\right) + \left(\frac{\mathcal{H}}{k}\right)^4 \alpha_2^2\right] P_{\delta\delta}(k,z), \tag{13.8}$$

$$\Delta P^{(2)}(k,z) = \frac{2}{3}\left(\frac{\mathcal{H}}{k}\right)^2 \left[2\,\alpha_2 f + \alpha_1^2 f^2\right] P_{\delta\delta}(k,z). \tag{13.9}$$

When comparing these results with eqs. (13.3) and (13.4) it is manifest that the relativistic corrections can mimic the effect of a non-zero value of f_{NL}. Both the monopole and the quadrupole develop corrections scaling with k^{-2}, k^{-4} and k^{-2}, respectively, which might

---

[1] We omitted the L luminosity label, not needed in the single tracer case

hide the true PNG signal. In particular, the extent to which the relativistic corrections can wash out the f_{NL} signal is explicitly dependent on the precise amplitudes of $\alpha_1(z)$ and $\alpha_2(z)$, which in turn depend on the magnification and evolution biases. Hence, a precise modeling of these systematic effects is crucial to disentangle the PNG signal from the relativistic corrections appearing in the $k \sim \mathcal{H}$ regime.

13.3 MEASURING $s(z)$ AND $f^{\mathrm{evol}}(z)$ AT SUB-HORIZON SCALES

In the following, we will show that we can use the odd multipoles of the 2-pt correlation function, generated by the Δ_{REL} contributions in (1.59), to precisely determine s and f^{evol}. In other words, we measure the multipoles in sub-horizon scales and combine them to constrain s and f^{evol}. These constraints would later be used in the modeling of ultra-large scales to separate the PNG and relativistic signals.

For this purpose, we recover the GR parametrization of the galaxy clustering multipoles. As briefly reminder, the standard contributions generate the three even multipoles: a monopole, a quadrupole and a hexadecapole ($\ell = 0, 2, 4$, respectively). Separating the populations into two sub-samples provides 7 independently measurable signals, which are given by eqs. (2.52)-(2.54). There we compute the GR matter power spectrum at $z_* = 0$, which is computed for any theory of gravity by solving the correspondent second order evolution equations for the matter density perturbations. In this analysis, we fix the cosmology to be ΛCDM and compute the power spectrum using CAMB [153, 154]. In addition to their dependence on cosmological parameters, the multipoles depend on the galaxy biases $b_{\mathrm{L,M}}(z)$. Those can be modelled for each population of galaxies, with a number of free parameters that are determined from the data, as we will describe in detail in sec. 14.5.

The next-to-leading order contribution originates from the cross-correlation of Δ_{ST} and Δ_{REL}, which induces a breaking of the symmetry in the correlation function generating odd multipoles: a dipole and an octupole ($\ell = 1$, 3, respectively). These odd multipoles are non-zero only for the cross-correlation of two different populations, setting $\mathrm{L} = \mathrm{B}$ and $\mathrm{M} = \mathrm{F}$ [47, 48] in eqs. (2.58) and (2.56). In this work, we assume that the wide-angle effects are removed by an appropriate definition of the odd multipoles estimators, and are thus not taken into account. By inspection of eqs. (2.58) and (2.56), we can consider them as a contamination that mitigates the dipole signal, while artificially enhances the octupole signal (see also the discussion regarding the wide-angle effects in sec. 2.2).

In summary, the cosmological and astrophysical parameters can be constrained using galaxy clustering information. In particular, measurements of the even multipoles put constraints on the galaxy bias $b_{\mathrm{L}}(z)$ of each population and on the growth rate $f(z)$, which is particularly sensitive to modifications of gravity [99]. The relativistic effects carry additional information through the gravitational redshift contribution that can be exploited for various applications, such as measuring the gravitational potential [122, 123], constraining modified gravity models and testing for additional interactions in the dark sector [77, 103, 218]. Here we adopt a different perspective: we assume that the ΛCDM model is valid, and we use the even and odd multipoles to determine the cosmological parameters, the galaxy biases $b_{\mathrm{L}}(z)$, the evolution biases $f_{\mathrm{L}}^{\mathrm{evol}}$ and the magnification biases s_{L}.

14

REVISITING THE MODELING OF THE GALAXY, EVOLUTION AND MAGNIFICATION BIASES

The galaxy, magnification and evolution biases depend on the population of galaxies as well as on the characteristics of the survey. In this work we consider the futuristic Square Kilometre Array Phase 2 (SKA2) HI galaxy survey. We first review the modelling of the number of galaxies and biases derived in [35] for this survey, and then extend it to the case of two populations. This modelling is used to determine the fiducial values of the biases, which control the amplitude of the signal. We then derive fitting functions for the different biases, and we forecast how well the parameters of the fitting functions can be determined with a survey like SKA2.

SKA2 is expected to detect around 1 billion HI galaxies over $30,000$ square degrees in the redshift range $z \in [0.1, 2.0]$. Following [35] we parametrise the background (physical) number of sources per redshift z and per solid angle, detected above flux threshold $\mathcal{F}_\star$ as

$$\bar{N}_g(z, \mathcal{F}_\star) = 10^{c_1}\, z^{c_2}\, e^{-c_3 z}\,, \tag{14.1}$$

where the parameters c_i depend on $\mathcal{F}_\star$ [35, 272]. For SKA2, the expected flux threshold will depend on redshift, as shown in [35], Table 2. In order to express $\bar{N}_g$ as a function of redshift alone, we first compute the $c_i(\mathcal{F}_\star)$ using Table 3 of [272]. Secondly, we reconstruct $\mathcal{F}_\star(z)$ from Table 2 in [35]. This allows us to compute $\bar{N}_g(z)$ by replacing this $\mathcal{F}_\star(z)$ into the interpolated $c_i(\mathcal{F}_\star)$. We do this for the redshift interval of $z \in [0.1, 2]$ using bins of size $\delta z = 0.1$. The resulting number of galaxies as a function of redshift is plotted in fig. 14.1.

14.1 THE MAGNIFICATION AND EVOLUTION BIASES FOR A SINGLE POPULATION OF GALAXIES

The magnification bias s is defined as the logarithmic slope of the cumulative number of sources above a given luminosity threshold. Since the luminosity threshold is related to the flux threshold by the luminosity distance d_L (which does not depend on luminosity)

$$L_\star(z) = 4\pi\, \mathcal{F}_\star(z)\, d_L(z)\,, \tag{14.2}$$

s can equally be expressed as a derivative of $\bar{N}_g(z, \mathcal{F}_\star)$ with respect to $\mathcal{F}_\star$

$$s(z, L_\star) = -\frac{2}{5}\frac{\partial \log \bar{N}_g(z, L_\star)}{\partial \log L_\star}\bigg|_z = -\frac{2}{5}\frac{\partial \log \bar{N}_g(z, \mathcal{F}_\star)}{\partial \log \mathcal{F}_\star}\bigg|_z = s(z, \mathcal{F}_\star)\,. \tag{14.3}$$

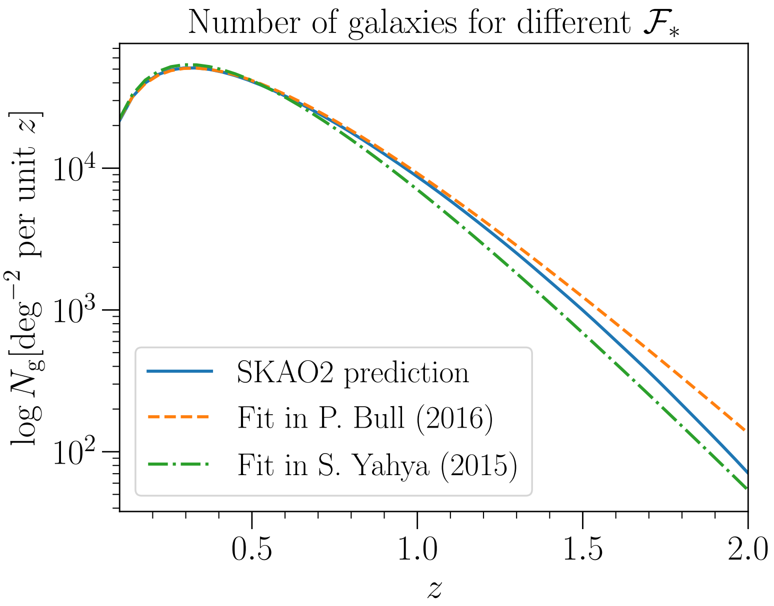

Figure 14.1: Logarithm of the number of galaxies per unit of solid angle and redshift for different choices of the flux limit. The solid blue line is obtained by using the z-dependent $\mathcal{F}_*$ from [35]. The dashed orange line is obtained by using the fit in [147]. Finally, the dashdot green line corresponds to the fit from [272] with redshift-independent flux limit $\mathcal{F}_* = 5.0\,\mu$Jy.

The magnification bias is therefore an observable quantity: it can be measured by binning $\bar{N}_g(z, \mathcal{F}_\star)$ in $\mathcal{F}_\star$ and computing the derivative at the chosen flux threshold. Note that since the cumulative number of sources can only increase when decreasing $\mathcal{F}_\star$, $s(z, \mathcal{F}_\star)$ is always positive.

The evolution bias f^{evol} is defined as the partial redshift derivative of the cumulative comoving number density of galaxies above $L_\star$, $\bar{n}_g(z, L_\star)$, taken at fixed value of the luminosity threshold

$$f^{\mathrm{evol}}(z, L_\star) = -\frac{\partial \ln \bar{n}_g(z, L_\star)}{\partial \ln(1+z)}\bigg|_{L_\star} = -\frac{d \ln \bar{n}_g(z, L_\star(z))}{d \ln(1+z)} + \frac{\partial \ln \bar{n}_g(z, L_\star)}{\partial \ln L_\star}\frac{d \ln L_\star(z)}{d \ln(1+z)}\,. \tag{14.4}$$

The comoving number density $\bar{n}_g(z, L_\star)$ is not directly observable. It can however be related to $\bar{N}_g(z, \mathcal{F}_\star)$ through

$$\bar{N}_g(z, \mathcal{F}_\star) = \frac{r^2(z)}{H(z)}\,\bar{n}_g(z, L_\star)\,, \tag{14.5}$$

where H is the Hubble parameter (in physical time). Following [35], the partial derivative with respect to z can be related to a total derivative with respect to z accounting for the fact that when varying the redshift, the luminosity threshold also varies. In addition, one needs to take into account the evolution with redshift of the volume factor, $r^2(z)/H(z)$ in (14.5), as well as the fact that the flux threshold can also vary with redshift. Putting everything together we obtain

$$\begin{aligned} f^{\mathrm{evol}}(z,\mathcal{F}_\star) = &- \frac{d\ln \bar{N}_g(z,\mathcal{F}_\star)}{d\ln(1+z)} - \frac{d\ln H(z)}{d\ln(1+z)} + \frac{2(1+z)}{r(z)H(z)} \\ &- 5\,s(z,\mathcal{F}_\star)\left[1+\frac{(1+z)}{r(z)H(z)}\right] - \frac{5}{2}s(z,\mathcal{F}_\star)\,\frac{d\ln\mathcal{F}_\star(z)}{d\ln(1+z)}\,. \end{aligned} \tag{14.6}$$

Written in this way, the evolution bias is an observable quantity: $\bar{N}_g$ can indeed be split in bins of redshift and the total derivative (first term) can be measured. In the following we shall refer to this quantity as $n^{evol}(z)$

$$n^{evol}(z) \equiv \frac{d\log \bar{N}_g(z,\mathcal{F}_\star)}{d\log(1+z)}\,. \tag{14.7}$$

The second and third term in (14.6) can either be obtained from measurements of $H(z)$ and $d_L(z) = (1+z)r(z)$ or from measurements of cosmological parameters in a given model. Finally, the last term in the second line is a (known) survey-dependent quantity. For surveys with a fixed flux threshold over the whole redshift range, this last term vanishes.

These results apply for the single-tracer case. Let us now extend them to the case of multiple populations of galaxies.

14.2 DIVIDING GALAXIES INTO BRIGHT AND FAINT POPULATIONS

We now split galaxies into two different populations by introducing an appropriate flux cut $\mathcal{F}_c$. We denote galaxies with fluxes $\mathcal{F} > \mathcal{F}_c$ as *bright* galaxies, and galaxies with fluxes $\mathcal{F}_c > \mathcal{F} > \mathcal{F}_\star$ as *faint* galaxies

$$\bar{N}_{\mathrm{B}}(z,\mathcal{F}_c) \equiv \bar{N}_g(z,\mathcal{F} > \mathcal{F}_c)\,, \tag{14.8}$$

$$\bar{N}_{\mathrm{F}}(z,\mathcal{F}_c) \equiv \bar{N}_g(z,\mathcal{F}_c > \mathcal{F} > \mathcal{F}_\star)\,. \tag{14.9}$$

We introduce the parameter $m = \bar{N}_g(z,\mathcal{F}_\star)/N_{\mathrm{B}}(z,\mathcal{F}_c)$, from which we can obtain the fraction of bright galaxies as m^{-1}. For a given value of m we can find the corresponding $\mathcal{F}_c$ in each of the redshift bin using the fit (14.1) to calculate both $\bar{N}_g(z,\mathcal{F}_\star)$ and $\bar{N}_{\mathrm{B}}(z,\mathcal{F}_c)$ and solving numerically the equation

$$\log \bar{N}_{\mathrm{B}}(z,\mathcal{F}_c) - \log \bar{N}_g(z,\mathcal{F}_\star) + \log m = 0\,. \tag{14.10}$$

This gives $\mathcal{F}_c(z)$ as a function of redshift, which is generally different from $\mathcal{F}_\star(z)$. The number of faint galaxies, $\bar{N}_{\mathrm{F}}(z,\mathcal{F}_c)$, is then simply obtained by subtracting the number of bright galaxies from the total. Note that the logarithmic evolution of the galaxies, n^{evol} given in (14.7) is the same for the total population, and for the bright and faint galaxies, since m is kept fixed over the redshift bins.

14.3 MAGNIFICATION BIAS

The dipole (2.58) and octupole (2.56) depend on the magnification bias of the bright and of the faint populations. These biases multiply the Doppler contribution. They account for the fact that galaxies that are moving with respect to the observer do not

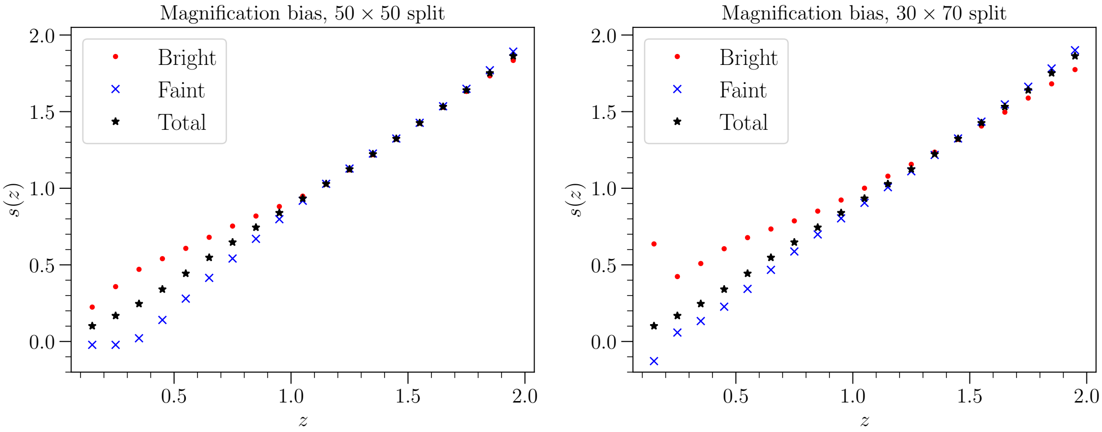

Figure 14.2: Predicted values of the magnification biases for the bright population s_B, the faint population s_F, and the total population s_M. The left panel shows the magnification biases for $m = 2$ (50% of bright galaxies), and the right panel for $m = 10/3$ (30% of bright galaxies).

have the same luminosity distance as galaxies at the same redshift with no peculiar velocities, as shown in [37]. As a consequence their flux is magnified or de-magnified by the peculiar velocity (depending on its direction). This can change the number of bright and faint galaxies that are observed and consequently impact the correlation function.

For the bright population, galaxies can cross the flux limit $\mathcal{F}_c$, enhancing or decreasing the number of bright galaxies. The magnification bias of this population is therefore similar to that of the total population, simply replacing $\mathcal{F}_\star$ by $\mathcal{F}_c$ in eq. (14.3)

$$s_B(z) = s(z, \mathcal{F}_c) = -\frac{2}{5}\frac{\partial \log \bar{N}_g(z, \mathcal{F} > \mathcal{F}_c)}{\partial \log \mathcal{F}_c}\bigg|_z . \tag{14.11}$$

The magnification bias for the faint galaxies is however more subtle: the faint galaxies can indeed either cross the $\mathcal{F}_c$ threshold, or the $\mathcal{F}_\star$ threshold. Following [39], we obtain the following relation for the magnification biases

$$\bar{N}_g(z, \mathcal{F}_\star)\, s_M(z) = \bar{N}_B(z, \mathcal{F}_c)\, s_B(z) + \bar{N}_F(z, \mathcal{F}_c)\, s_F(z)\,, \tag{14.12}$$

where we have defined $s_M(z) \equiv s(z, \mathcal{F}_\star)$ as the magnification bias of the whole population (bright plus faint). Using that $\bar{N}_B = \bar{N}_g/m$, we can rewrite the above equation as

$$s_F(z) = \frac{m}{m-1}\, s_M(z) - \frac{1}{m-1}\, s_B(z)\,. \tag{14.13}$$

Note that since by construction $\bar{N}_B < \bar{N}_g$ we have $m > 1$.

Contrary to s_M and s_B that are always positive, since they represent the slopes of a cumulative number of galaxies, s_F can be negative if the second term in eq. (14.13) dominates over the first one. This can happen if the slope at the flux cut, s_B, is steeper than the slope at the flux threshold of the survey s_M. In this case, when the fluxes are magnified by Doppler effects, more galaxies will cross the flux cut $\mathcal{F}_c$ (thus leaving the faint sample to become bright) than galaxies which will cross the flux threshold of the survey $\mathcal{F}_\star$ to become detectable. In this case, a magnification of the fluxes leads to decrease in the number of faint galaxies (and vice-versa for a de-magnification).

From eq. (14.13) we see that s_F can be directly reconstructed from s_M and s_B. In our forecasts we will therefore treat s_M and s_B as free parameters, and compute s_F from these two quantities. In fig. 14.2 we show the magnification bias of the total population, and of the bright and faint populations, for two different splits: 50% of bright galaxies (left panel) and 30% of bright galaxies (right panel).

14.4 EVOLUTION BIAS

In addition to the dependence on magnification biases, the dipole (2.58) and octupole (2.56) depend also on the evolution bias of the bright and faint populations. The evolution bias encodes the fact that the number of galaxies is evolving with redshift, due to the formation and merging of galaxies. In a homogeneous Universe, all galaxies observed at fixed redshift z are at the same distance from the observer and they share therefore the same history. However, in a inhomogeneous Universe, galaxies that are moving for example towards the observer, are at a larger distance from the observer than galaxies at the same redshift with no peculiar velocities. As a consequence, such moving galaxies live at an earlier time than the ones at rest with the Hubble flow. If the number of galaxies is evolving with time (for example decreasing due to mergers) we will see less galaxies at earlier time than closer to us, which creates fluctuations in the galaxy number density.

In the case of two populations, the evolution bias of each population encodes how each of the population evolves and it is therefore simply given by [35, 39]

$$f^{\mathrm{evol}}\mathrm{B}(z) = -\left.\frac{\partial \log \bar{n}_\mathrm{B}(z, L_c)}{\partial \log(1+z)}\right|_{L_c}, \tag{14.14}$$

$$f^{\mathrm{evol}}\mathrm{F}(z) = -\left.\frac{\partial \log \bar{n}_\mathrm{F}(z, L_\star, L_c)}{\partial \log(1+z)}\right|_{L_\star, L_c}. \tag{14.15}$$

Following the same steps as in the case of one population of galaxies, we can rewrite Eqs. (14.14) and (14.15) in terms of observable quantities

$$\begin{aligned} f^{\mathrm{evol}}\mathrm{B}(z) = &-n^{evol}(z) - \frac{d\log H(z)}{d\log(1+z)} + \frac{2(1+z)}{r(z)H(z)} - 5\, s_\mathrm{B}(z)\left[1 + \frac{(1+z)}{r(z)H(z)}\right] \\ &- \frac{5}{2} s_\mathrm{B}(z)\, \frac{d\log \mathcal{F}_c}{d\log(1+z)}, \end{aligned} \tag{14.16}$$

$$\begin{aligned} f^{\mathrm{evol}}\mathrm{F}(z) = &-n^{evol}(z) - \frac{d\log H(z)}{d\log(1+z)} + \frac{2(1+z)}{r(z)H(z)} - 5\, s_\mathrm{F}(z)\left[1 + \frac{(1+z)}{r(z)H(z)}\right] \\ &- \frac{5}{2}\left[\frac{\bar{N}_g}{\bar{N}_\mathrm{F}} s_\mathrm{M}(z) \frac{d\log \mathcal{F}_\star}{d\log(1+z)} - \frac{\bar{N}_\mathrm{B}}{\bar{N}_\mathrm{F}} s_\mathrm{B}(z) \frac{d\log \mathcal{F}_c}{d\log(1+z)}\right], \end{aligned} \tag{14.17}$$

where $n^{evol}(z)$ is given by eq. (14.7). These results are consistent with eq. (17) of [39] when both $\mathcal{F}_\star$ and $\mathcal{F}_c$ are constant. Note that the ratios in the second line of eq. (14.17) are the same as those appearing in eq. (14.13). They are constant by construction and only depend on the fraction of bright and faint populations, encoded in m:

$$\frac{\bar{N}_g}{\bar{N}_\mathrm{F}} = \frac{m}{m-1}, \qquad \frac{\bar{N}_\mathrm{B}}{\bar{N}_\mathrm{F}} = \frac{1}{m-1}. \tag{14.18}$$

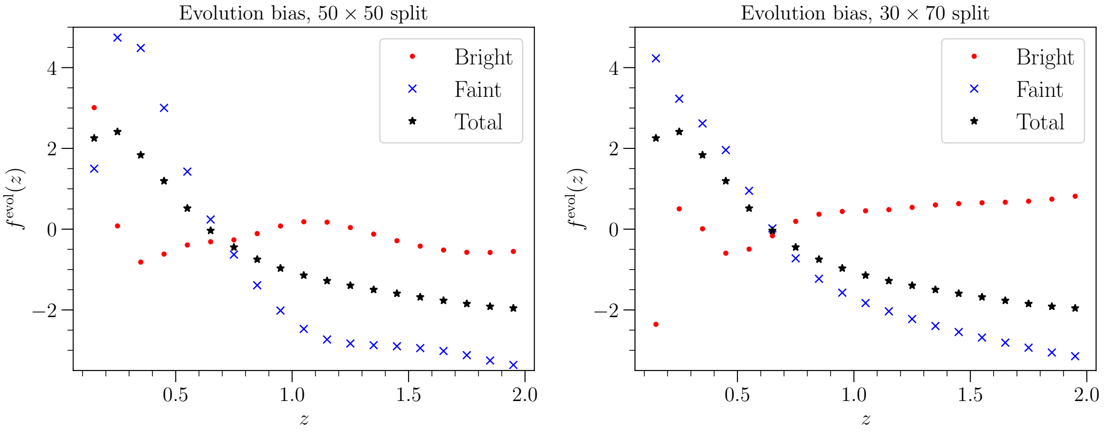

Figure 14.3: Predicted values of the evolution biases for the bright population $f^{\rm evol}$B, the faint population $f^{\rm evol}$F, and the total population $f^{\rm evol}$. The left panel shows the evolution biases for $m = 2$ (50% of bright galaxies), and the right panel for $m = 10/3$ (30% of bright galaxies).

We have now all the ingredients to compute the evolution bias numerically. As shown in sec. 14.2, the first term, n^{evol}, in Eqs. (14.16) and (14.17) is the same for both populations, and equal to that of the total population. In practice, n^{evol} can be measured directly from the data, by binning the galaxies in redshift, and computing the total derivative. Here we perform this derivative numerically (using 5-point stencil) from the number of galaxies obtained through eq. (14.1). Similarly, we compute numerically the redshift derivatives of the flux cuts. The results for the evolution bias of the whole population, and that of the bright and faint populations are shown in fig. 14.3 for two choices of splitting. We see that the amplitude of the evolution bias of the faint sample is always larger than that of the bright sample: faint galaxies therefore evolve faster than bright ones in our modelling. Note that at low redshift, the evolution biases of the two populations are quite sensitive to the choice of m, providing significantly different predictions.

From Eqs. (14.11), (14.12), (14.16) and (14.17) we see that the magnification biases and evolution biases of the bright and faint populations depend only on three quantities: $s_{\rm B}, s_{\rm M}$ and n^{evol}. Interestingly, two of these quantities, $s_{\rm M}$ and n^{evol}, are the same for all splits, since they do not depend on $\mathcal{F}_c$. It is therefore possible to combine different splits (with different values of m) to improve the measurements of $s_{\rm M}$ and n^{evol}. These two quantities fully determine the magnification bias and evolution bias of the whole population. Hence even though measuring relativistic effects requires two populations of galaxies, the quantities that can be extracted from this signal are useful to characterise the whole population. This is particularly interesting to model the amplitude of the relativistic contaminations to local primordial non-Gaussianities, as well as the amplitude of the kinematic dipole, which do not require the use of two populations.

14.5 GALAXY BIAS

Finally, the dipole and octupole depend also on the galaxy biases of the bright and faint populations. The bias of each population depends directly on the splitting parameter m, i.e. on the fraction of bright and faint galaxies. Typically, a larger value of m (small fraction of bright galaxies) implies a larger $\mathcal{F}_c$, which leads to a larger bias for the bright population and therefore a larger bias difference Δb between bright and faint sources. On the contrary a smaller value of m decreases the bias difference (see e.g. [39] for an example in the case of the survey DESI).

In the following we model the biases of the two populations in terms of the bias of the total population b_T, the bias difference Δb and the parameter m. The bright and faint biases obey the system of equations

$$\frac{\bar{N}_\mathrm{B}}{\bar{N}_g}\, b_\mathrm{B} + \frac{\bar{N}_\mathrm{F}}{\bar{N}_g}\, b_\mathrm{F} = b_\mathrm{T}\,, \tag{14.19}$$

$$b_\mathrm{B} - b_\mathrm{F} = \Delta b\,. \tag{14.20}$$

Using $\bar{N}_\mathrm{B}/\bar{N}_g = 1/m$ and $\bar{N}_\mathrm{F}/\bar{N}_g = (m-1)/m$ we obtain

$$b_\mathrm{B} = b_\mathrm{T} + \frac{m-1}{m}\,\Delta b\,, \tag{14.21}$$

$$b_\mathrm{F} = b_\mathrm{T} - \frac{1}{m}\,\Delta b\,. \tag{14.22}$$

Note that this is consistent with eqs. (6.2) and (6.3) for $m = 2$, which is the value defining an even split with 50% of B and 50% of F galaxies. We will denote such a split as 50×50. Similarly as in sec. 6.1.1, we model the galaxy bias of the total population following [147] as

$$b_\mathrm{T} = c\, e^{\,d\, z}\,, \tag{14.23}$$

where $[c, d] = [0.554, 0.783]$. Importantly, however, without precise knowledge of the luminosity function of the population of galaxies, we do not know the bias difference Δb for a given splitting parameter m. In our forecast, we assume that for $m = 2$, $\Delta b = 1$, in agreement with the measurements done in the BOSS survey [47]. We then choose a smaller value of $\Delta b = 0.8$ in the case where we have 70% percent of bright galaxies and a larger value of $\Delta b = 1.2$ when we have 30% of bright galaxies. These choices are somewhat arbitrary, but they are only necessary because we are doing a forecast. Once we perform such an analysis on real data, the bright and faint biases will be considered as free parameters, directly measured from the even multipoles of the correlation function.

15

METHODOLOGY

We forecast the capacity of a spectroscopic survey like the SKA2 HI galaxy survey to measure the magnification and evolution biases using galaxy clustering information. To this end we first parameterise the different biases with a set of free parameters, that we then constrain with the dipole and the octupole.

We use the Fisher formalism and compute the Fisher matrix by performing the second derivative of the natural logarithm of the likelihood with respect to the parameters of the model. Assuming Gaussianity and neglecting the dependence of the covariance on the model parameters, the Fisher matrix can be expressed as described in sec. 6.1.4. We describe below how we build the data vector and the relevant covariant matrix entering in eq. (2.107) for the specific analysis under consideration for this work. Once the Fisher matrix is computed, we estimate the covariance matrix of the parameters as the inverse of the Fisher matrix (see eq. (2.108)). The parameters uncertainties are encoded in the diagonal of the latter, while the off-diagonal terms encode the cross-correlations between the parameters.

15.1 SURVEY SPECIFICATIONS

We consider a futuristic survey akin to the HI galaxy survey in Phase 2 of the Square Kilometer Array, as described in [35, 147]. Such a survey is proposed to span $30,000$ square degrees ranging from $z = 0.1$ to $z = 2$, and observing close to a billion galaxies. In practice, we divide this redshift range into 19 bins of size $\Delta z = 0.1$ and evaluate all the quantities at the centre of each z-bin. We split the full population of galaxies provided by the survey into two samples following the prescription described in sec. 14.2 in order to have a constant ratio of bright versus faint galaxies in every z-bin. Then, we compute the signal dataset and the covariance matrices at each z-bin in the linear regime, including separations spanning from $d_{\rm min} = 20\,{\rm Mpc}/h$ to $d_{max} = 160\,{\rm Mpc}/h$. We use fiducial cosmological parameters from Planck [6] (see also Table D.3 in Appendix D.3). The fiducial values for the biases described in Chapter 14.

In fig. 15.1, as illustration, we show the cross-correlation monopole, dipole, quadrupole and octupole at $z = 0.25$ (second redshift bin) for two different splits: 50% bright and 50% faint galaxies (blue, solid curves); 30% bright and 70% faint galaxies (red, dashed-dot curves). We see that the monopole and the quadrupole are significantly larger than the dipole and octupole. The cumulative SNR over all redshifts and separations for the $50\% - 50\%$ split is: 624 and 601 respectively for the bright-faint cross-correlation monopole and quadrupole; 57 and 5 respectively for the dipole and octupole. Table D.1 in Appendix D.3 reports the SNR for all multipoles in the different splits. Note that the

SNR of the dipole and octupole are without wide-angle effects, since as explained before in sec. 2.2, one can choose an estimator to remove them.

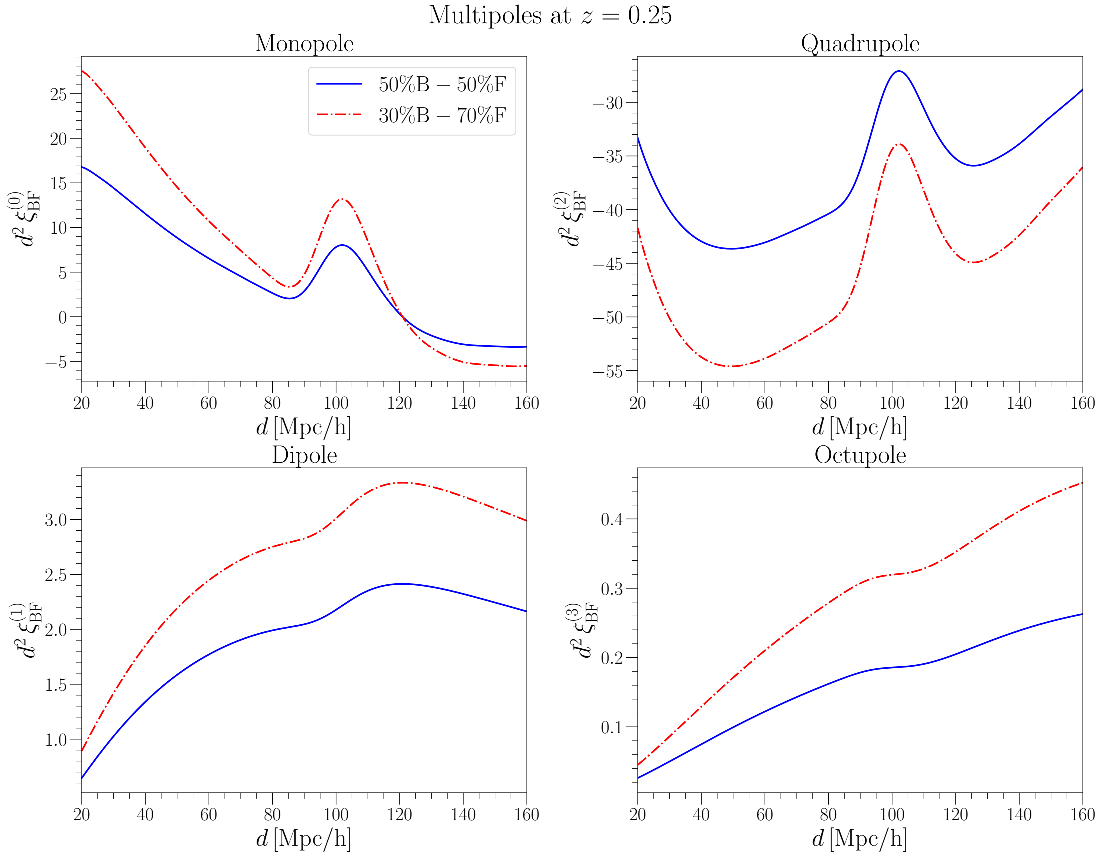

Figure 15.1: Multipoles of the cross-correlation between B and F populations at redshift $z = 0.25$.

15.2 FITTING MODELS FOR THE GALAXY BIASES, MAGNIFICATION BIASES AND EVOLUTION BIASES

Our goal is to constrain the various biases from the data. As shown in Chapter 14, the magnification and evolution biases can be written in terms of three observable quantities: $s_{\rm M}, s_{\rm B}$ and n^{evol}, that can be directly measured from the number of galaxies. Our strategy is therefore the following: we use our modelling to compute these three quantities. We then parametrise them with a set of free parameters, with fiducial values given by our model and with uncertainties expected from future surveys. Typically, we choose two different values for the uncertainties: 50% uncertainties and 20% uncertainties. Those are quite large and future surveys may very well provide tighter constraints, but we prefer to remain conservative here. We then perform a Fisher forecast to determine the capability of the dipole and the octupole to improve the precision on these parameters. From this we then reconstruct $s_{\rm B}(z), s_{\rm F}(z)$, $f^{\rm evol}{\rm B}(z)$ and $f^{\rm evol}{\rm F}(z)$.

15.2.1 *Parametrization of* $s_{\rm M}(z)$ *and* $s_{\rm B}(z)$

We parametrise the redshift evolution of $s_{\rm M}(z)$ and $s_{\rm B}(z)$ with 4 parameters each:

$$s_{\rm L}(z) = s_{{\rm L},0} + s_{{\rm L},1}\, z + s_{{\rm L},2}\, \log z + s_{{\rm L},3}\, (\log z)^2 \,, \tag{15.1}$$

where L = B, M. This expansion recovers well the redshift evolution plotted in fig. 14.2. Thus, we include 8 parameters in the analysis: $\{s_{{\rm L},0},\, s_{{\rm L},1},\, s_{{\rm L},2},\, s_{{\rm L},3}\}$. The magnification bias of the bright population is sensitive to the choice of splitting, and we have therefore different fiducial values for the parameters for different splitting parameter m. On the other hand, $s_{\rm M}$ does not depend on m. The fiducial values can be found in Tables D.2 and D.3 in Appendix D.3. As explained above we introduce Gaussian priors of 50% and 20% around the fiducial values on both set of parameters for each choice of m, to account for our prior knowledge on $s_{\rm B}$ and $s_{\rm M}$ from direct measurements.

15.2.1.1 *Parametrization of* $n^{\rm evol}(z)$

Since by construction, we split the two populations keeping constant the ratio of bright and faint galaxies in all redshift bins, the function $n^{\rm evol}$ defined in (14.7) is the same for both populations and for the total population. We parametrise the redshift evolution of this function with 4 parameters as

$$n^{\rm evol}(z) = n^{\rm evol}_0 + n^{\rm evol}_1\, z + n^{\rm evol}_2\, \frac{1}{z} + n^{\rm evol}_3\, e^{-z}\,. \tag{15.2}$$

We have therefore 4 additional free parameters in our analysis $\{n^{\rm evol}_0, n^{\rm evol}_1, n^{\rm evol}_2, n^{\rm evol}_3\}$. The fiducial values are independent of the value of m and can be found in Table D.3 in Appendix D.3. Similarly to the magnification bias, we consider Gaussian priors of 50% and 20% around the fiducial values.

15.2.1.2 *Parametrization of the galaxy biases*

We parametrise the evolution of the biases with redshift using (14.21)–(14.23). For a given splitting we fix the bias difference Δb in Eqs. (14.21) and (14.22). The fiducial values for c and d are independent of the splitting since they encode the evolution of the total population. In our forecast we vary however these parameters separately when they enter into the bright or faint biases, since these two quantities can in principle vary independently. Hence we have 4 additional parameters $\{c_{\rm B}, d_{\rm B}, c_{\rm F}, d_{\rm F}\}$, with fiducial values given in Table D.3 in Appendix D.3. Note that we could have alternatively used as free parameters $\{c, d, \Delta b\}$.

15.3 GALAXY SAMPLES AND DATA VECTORS

Since the magnification bias of the total population, $s_{\rm M}$, and the quantity $n^{\rm evol}(z)$ are independent of the way galaxies are split, we explore different cases and compare the constraints. We first perform Fisher analyses using two populations of galaxies, and then we consider a case where we have four different populations.

15.3.1 *Two galaxy populations*

We consider three different samples of bright (B) and faint (F) galaxies:

- Analysis with 50% of B and 50% of F galaxies (50×50): we set $m = 2.0$ and $\Delta b = 1.0$. This is the standard approach used in previous works, e.g. refs. [103, 122, 123].
- Analysis with 30% of B and 70% of F galaxies (30×70): we set $m = 10/3$ and $\Delta b = 1.2$.
- Analysis with 70% of B and 30% of F galaxies (70×30): we set $m = 10/7$ and $\Delta b = 0.8$.

As observables we consider the multipoles of the correlation function described in secs. 2.2.3 and 2.2.4. For any value of m, we have 7 even multipoles: the monopoles and quadrupoles of the BB, BF and FF correlations, plus the hexadecapole of the full population. Additionally, we have 2 odd multipoles arising from BF cross-correlations, namely a dipole and an octupole. The data vector at each z-bin takes the form

$$\vec{\Xi}(z,d) = \left(\xi_{\mathrm{BB}}^{(0)}, \xi_{\mathrm{BF}}^{(0)}, \xi_{\mathrm{FF}}^{(0)}, \xi_{\mathrm{BF}}^{(1)}, \xi_{\mathrm{BB}}^{(2)}, \xi_{\mathrm{BF}}^{(2)}, \xi_{\mathrm{FF}}^{(2)}, \xi_{\mathrm{BF}}^{(3)}, \xi_{\mathrm{T}}^{(4)}\right)\Big|_{(z,d)} . \tag{15.3}$$

We compute the Gaussian covariance matrix of $\vec{\Xi}(z,d)$ including all the possible cross-correlations between the multipoles, and accounting for both cosmic variance and shot-noise. We also include the shot-noise contributions associated to the cross-correlations between the hexadecapole and the monopoles and quadrupoles, arising from the fact that the B and F populations overlap with the full population. This contribution is usually neglected (see e.g. [103, 122, 123]), since cosmic variance dominates the error budget of the even multipoles for a survey like the one with SKA2. In this work, we develop a shot-noise model accounting for overlapping populations (see Appendices D.1 and D.2) and we find that indeed the resulting contribution is negligible and has only a small impact on the constraints.

In total we have 21 free parameters: 16 parameters describing the various biases plus 5 cosmological parameters $h, A_{\mathrm{s}}, n_{\mathrm{s}}, \Omega_{\mathrm{b}}, \Omega_{\mathrm{m}}$, whose fiducial values are also listed in Table D.3 in Appendix D.3. The derivatives of the multipoles with respect to the cosmological parameters are computed numerically from CAMB [10, 154] and the FFTLOG algorithm [273] using the 5-point stencil method.[1] The derivatives with respect to the other parameters can be computed analytically.

15.3.2 *Four galaxy populations: combining the information of two sample separations*

We explore the possibility of further improving the constraints on the magnification and evolution biases by performing an additional Fisher analysis in which we combine two different splits. In this case, we have four populations of galaxies: two different bright populations (B and b) and two different faint populations (F and f). These four populations are clearly not independent, since they are drawn from the same initial population of galaxies. In the signal, in addition to auto-correlations of each population

---

[1] We used the Python implementation available in GitHub: 1D FFTlog in Python.

with itself, we only consider the cross-correlations of B with F and b with f (since parts of the galaxies in B are also in b and similarly for the faint). The data vector is therefore $\vec{\Xi}_{\rm J} = \left(\vec{\Xi}_m, \vec{\Xi}_{m'}\right)$ with $m = 2$ and $m' = 10/3$.

In the covariance matrix we include all the cross-correlations between the multipoles of the different splits. In particular, we take into account the shot-noise contributions due to the fact that we are using the same underlying population, split in different fractions of B and F galaxies, meaning that there is certain overlap between the B and F populations of each m, m' sub-samples. These contributions are computed in Appendix D.1. Note that neglecting the shot-noise contributions between the two different splits would lead to an overestimation of the parameter constraints.

In this case we have 29 parameters: 5 cosmological parameters, 8 parameters common to the two different splits (parametrising $n^{\rm evol}$ and $s_{\rm M}$) and 16 parameters for $s_{\rm B}, s_{\rm b}, b_{\rm B}, b_{\rm b}, b_{\rm F}$ and $b_{\rm f}$.

16

RESULTS

We first consider the cases with two populations of galaxies, and then show the constraints when combining four populations. We compare the relative reduction of uncertainties with respect to the priors on the parameters of the model when including the dipole only versus when adding the octupole, showing that in this context the octupole contains valuable information and needs to be included. We also reconstruct the 68% confidence regions for the magnification and evolution biases as a function of redshift.

16.1 CONSTRAINTS FROM TWO GALAXY POPULATIONS

	50 × 50 split		30 × 70 split		70 × 30 split	
	$\xi^{(1)}_{\mathrm{BF}}$	$\xi^{(1)}_{\mathrm{BF}} + \xi^{(3)}_{\mathrm{BF}}$	$\xi^{(1)}_{\mathrm{BF}}$	$\xi^{(1)}_{\mathrm{BF}} + \xi^{(3)}_{\mathrm{BF}}$	$\xi^{(1)}_{\mathrm{BF}}$	$\xi^{(1)}_{\mathrm{BF}} + \xi^{(3)}_{\mathrm{BF}}$
$s_{\mathrm{B},0}$	36.81	30.02	41.58	32.77	26.65	23.28
$s_{\mathrm{B},1}$	20.01	18.47	39.44	36.00	17.44	16.73
$s_{\mathrm{B},2}$	26.36	25.03	44.66	43.48	24.12	22.87
$s_{\mathrm{B},3}$	26.18	23.81	24.08	21.43	28.86	26.80
$s_{\mathrm{M},0}$	47.70	39.29	47.97	37.71	46.19	37.30
$s_{\mathrm{M},1}$	31.80	27.83	20.88	18.49	28.56	26.66
$s_{\mathrm{M},2}$	49.26	45.07	49.53	46.46	48.01	41.23
$s_{\mathrm{M},3}$	49.99	49.94	49.98	49.96	49.94	49.84
n_0^{evol}	44.85	41.31	41.32	40.50	46.17	41.65
n_1^{evol}	43.74	31.04	37.21	28.01	47.18	32.74
n_2^{evol}	40.39	25.55	33.77	24.09	32.34	26.57
n_3^{evol}	33.16	30.71	31.39	29.61	35.96	31.62

Table 16.1: Relative 1σ uncertainties for the magnification biases and number evolution parameters, assuming 50% Gaussian priors. We show the results for 3 different splits, including only the dipole ($\xi^{(1)}_{\mathrm{BF}}$) and including both the dipole and octupole ($\xi^{(1)}_{\mathrm{BF}} + \xi^{(3)}_{\mathrm{BF}}$). In all cases the even multipoles (monopole, quadrupole and hexadecapole) are included.

We show the relative uncertainty when only the dipole is included, and when both the dipole and the octupole are used. We see that even though the SNR of the octupole is 10 times smaller than that of the dipole, adding the octupole in the analysis has a significant impact on some of the parameters. For example, adding the octupole improves the constraints on n_1^{evol} and n_2^{evol} by 20-30% with respect to the constraints from the dipole only, for all the splits. From Eqs. (2.58) and (2.56), combined with the expressions for the evolution biases (14.16) and (14.17), we see that the dipole depends on the magnification bias difference $s_{\rm B} - s_{\rm F}$, on the combination $b_{\rm F}s_{\rm B} - b_{\rm B}s_{\rm F}$, as well as on the product $(b_{\rm B} - b_{\rm F})n^{evol}$. On the contrary, the octupole depends only on the magnification bias difference $s_{\rm B} - s_{\rm F}$. As a consequence, there is a strong degeneracy between n^{evol}, $s_{\rm B}$ and $s_{\rm M}$ when only the dipole is included. Adding the octupole, which does not depend on n^{evol} partially lifts this degeneracy, improving the constraints on the parameters. Moreover, the redshift evolution of the dipole and the octupole differ. The octupole is proportional to $f^2(z)(1 - 1/r(z)\mathcal{H}(z))$, whereas the dipole contains also other terms that scale with $f(z)$ and with the biases $b_{\rm B}(z)$ and $b_{\rm F}(z)$. As a consequence, adding the octupole breaks degeneracies between the different parameters governing the redshift evolution of $s_{\rm B}, s_{\rm M}$ and n^{evol}. Hence even though we find that the diagonal Fisher elements for the dipole are always significantly larger than for the octupole (by a factor 25-80 depending on the parameters), the octupole significantly helps to constrain the parameters by breaking degeneracies.

We find similar results when the priors are reduced to 20% (see Table D.4 in Appendix D.3). In this case the uncertainty on $s_{\rm B,1}, s_{\rm B,2}, s_{\rm B,3}$ are reduced by a factor ~ 2, for the 50×50 and 70×30 splits. Generally, we see that the improvement with respect to the priors are similar for the 3 splits we have chosen. Some parameters are better constrained in one split than in another, but there is no systematic trend that would single out one of the splits.

In fig. 16.1, we show the constraints on the redshift evolution of the various functions for the 50×50 split: the functions entering our forecasts ($n^{evol}, s_{\rm M}$ and $s_{\rm B}$ in red), and the derived ones ($s_{\rm F}$, $f^{\rm evol}$B and $f^{\rm evol}$F in blue). We show the prior in grey (50% in this case), as well as the uncertainty when only the dipole is included, and when both the dipole and octupole are included. We see that the improvement on the redshift evolution is significant for all functions. Adding the octupole helps constraining all parameters, and the improvement is especially relevant for n^{evol} and the two evolution biases. Similar results are found using a 20% prior instead of a 50% prior (see fig. D.2 in Appendix D.3) and for the other splits (see fig. D.3 in Appendix D.3).

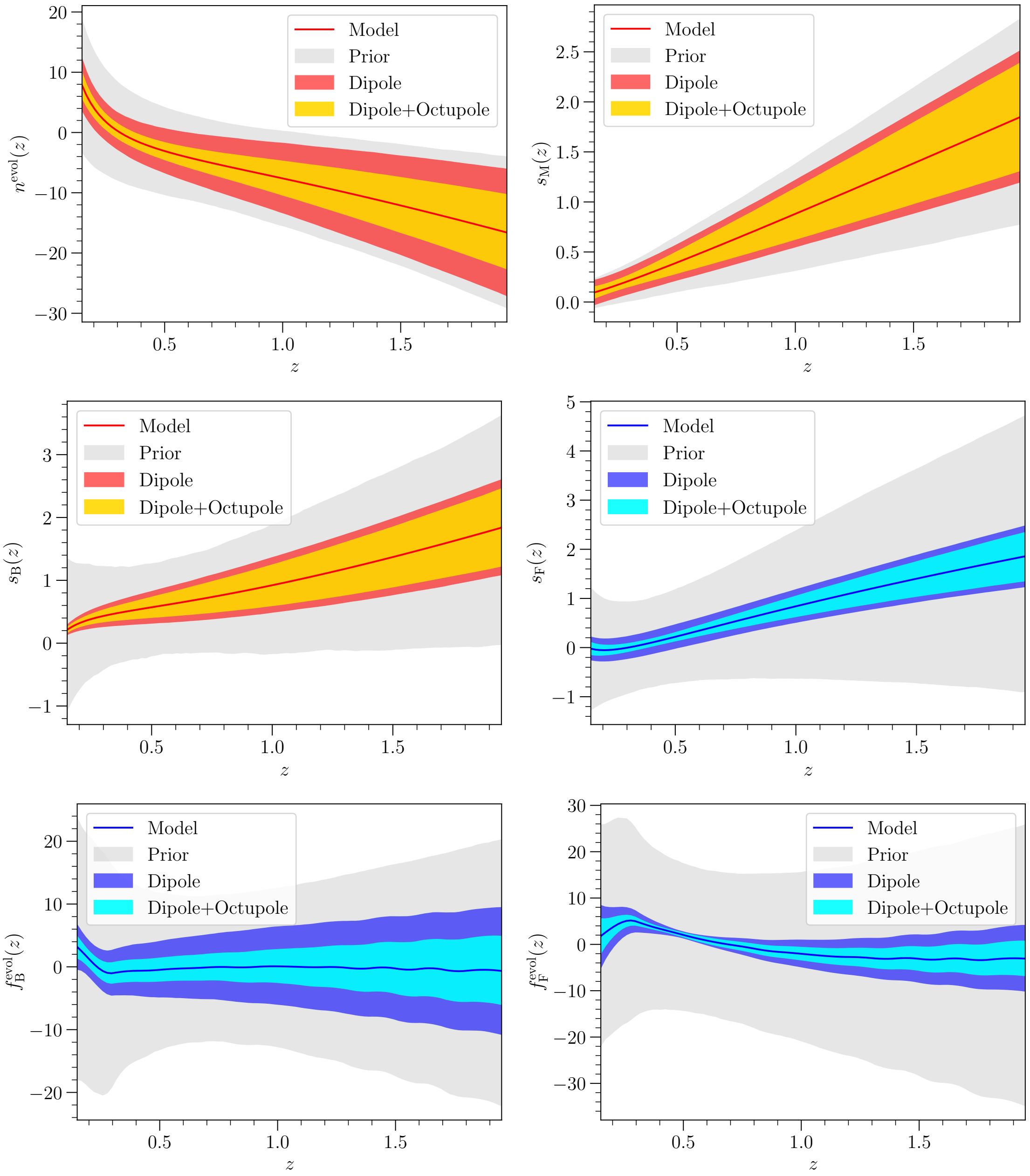

Figure 16.1: Constraints on the redshift evolution of the various functions for the 50×50 split, starting with a 50% prior on the parameters (grey region). We show the results when only the dipole is used and when both the dipole and octupole are included. In all cases the even multipoles (monopole, quadrupole and hexadecapole) are included. The red functions are those entering the forecasts, while the blue ones are derived from the red.

16.2 CONSTRAINTS FROM THE COMBINED ANALYSIS

	50×50	Joint	$\Delta_{m=2}(\%)$	30×70	Joint	$\Delta_{m=10/3}(\%)$
$s_{\mathrm{B},0}$	30.02	23.72	**20.96**	32.77	30.89	**5.74**
$s_{\mathrm{B},1}$	18.47	13.35	**27.73**	36.00	33.36	**7.33**
$s_{\mathrm{B},2}$	25.03	19.53	**21.97**	43.48	42.91	**1.33**
$s_{\mathrm{B},3}$	23.81	18.75	**21.22**	21.43	21.18	**1.19**
$s_{\mathrm{M},0}$	39.29	33.61	**14.45**	37.71	33.61	**10.87**
$s_{\mathrm{M},1}$	27.83	16.42	**40.99**	18.49	16.42	**11.20**
$s_{\mathrm{M},2}$	45.07	40.30	**10.58**	46.46	40.30	**13.25**
$s_{\mathrm{M},3}$	49.94	49.82	**0.26**	49.96	49.82	**0.28**
n_0^{evol}	41.31	39.95	**3.29**	40.50	39.95	**1.36**
n_1^{evol}	31.04	26.66	**14.13**	28.01	26.66	**4.82**
n_2^{evol}	25.55	19.57	**23.40**	24.09	19.57	**18.76**
n_3^{evol}	30.71	27.32	**11.03**	29.61	27.32	**7.73**

Table 16.2: Relative 1σ uncertainties for the magnification biases and the number evolution, assuming 50% Gaussian priors and including all multipoles. We show the results for a single split and for the joint analysis. The bold numbers are the relative improvement with respect to the results from a single split. Note that since the $s_{\mathrm{B},i}$ parameters differ for the two splits, we have two sets of parameters in the joint analysis. Hence we show the constraints for the 50×50 $s_{\mathrm{B},i}$ parameters in column 2 and 3, and the constraints for the 30×70 $s_{\mathrm{B},i}$ parameters in column 5 and 6.

In Table 16.2 we show the constraints obtained when combining the 50×50 split with the 30×70 split and we compare them with the constraints from a single split. The improvement is non-negligible for most parameters, and can even reach $20 - 40\%$. Hence even if adding a new split adds 4 new parameters to the Fisher (due to the magnification bias, which differs in different splits), the common parameters $s_{\mathrm{M},i}$ and n_i^{evol} are improved by the additional signals. Interestingly, this improvement in the common parameters also impacts the individual $s_{\mathrm{B},i}$ that are better measured due to the breaking of degeneracies brought by the additional split.

In fig. 16.2 we show the constraints on the redshift evolution of the functions entering the forecasts and in fig. 16.3 on the derived functions. In general, we see that the improvement is less significant in the case of the 30×70 split, but they are still non-negligible, especially for the evolution biases. Note that the wiggles in the redshift evolution of the evolution biases are due to the reconstruction of these functions from n^{evol}, s_{B} and s_{F}.

Finally, in Table D.5 we show the constraints on the cosmological parameters. We find that these parameters are almost purely constrained by the even multipoles. Adding the odd multipoles only improves the constraints by 0.1% at most. This is also the case for the galaxy bias parameters (see Table D.6). Note that this is consistent with the results of [245], who showed that relativistic effects are not useful to constrain cosmological parameters. Both the cosmological and galaxy bias parameters are already very well constrained by the even multipoles, and hence the odd multipoles add no new information on them. As we have extensively demonstrated in the previous parts of this Thesis, their capacity lies instead in constraining theories beyond ΛCDM [54, 77, 103, 104, 123, 218, 274], or magnification biases and evolution biases, as we show here.

We compare the constraints on cosmological parameters using a single split and using the joint analysis. First we see that the constraints from the 30×70 split are always tighter than those from the 50×50 split. This suggests that multi-tracer analyses should carefully explore various splits and determine the optimal one. The 50×50 split is clearly the one which minimises shot noise in the cross-correlation signals (since one can form more pairs in this case), but since shot noise will be small in future surveys due to the very high number density of detected galaxies, this is not necessarily the optimal choice. The signal may indeed increase in other choices of splits, improving cosmological constraints. Note that these conclusions rely on our modelling of the galaxy biases, and may differ for a different modelling. Finally, we see that the joint analysis provides tighter constraints than the two single splits. The improvement with respect to the 30×70 split lies between 1.5% and 3% (see Table D.5). In the case of the galaxy bias parameters, we find slightly larger improvements, between 1.7% to 5% (see Table D.6). This is a somewhat limited improvement, but it comes at almost no cost. It does not require new data or different analysis techniques, but simply relies on doubling the size of the data vector by considering two types of cross-correlations.

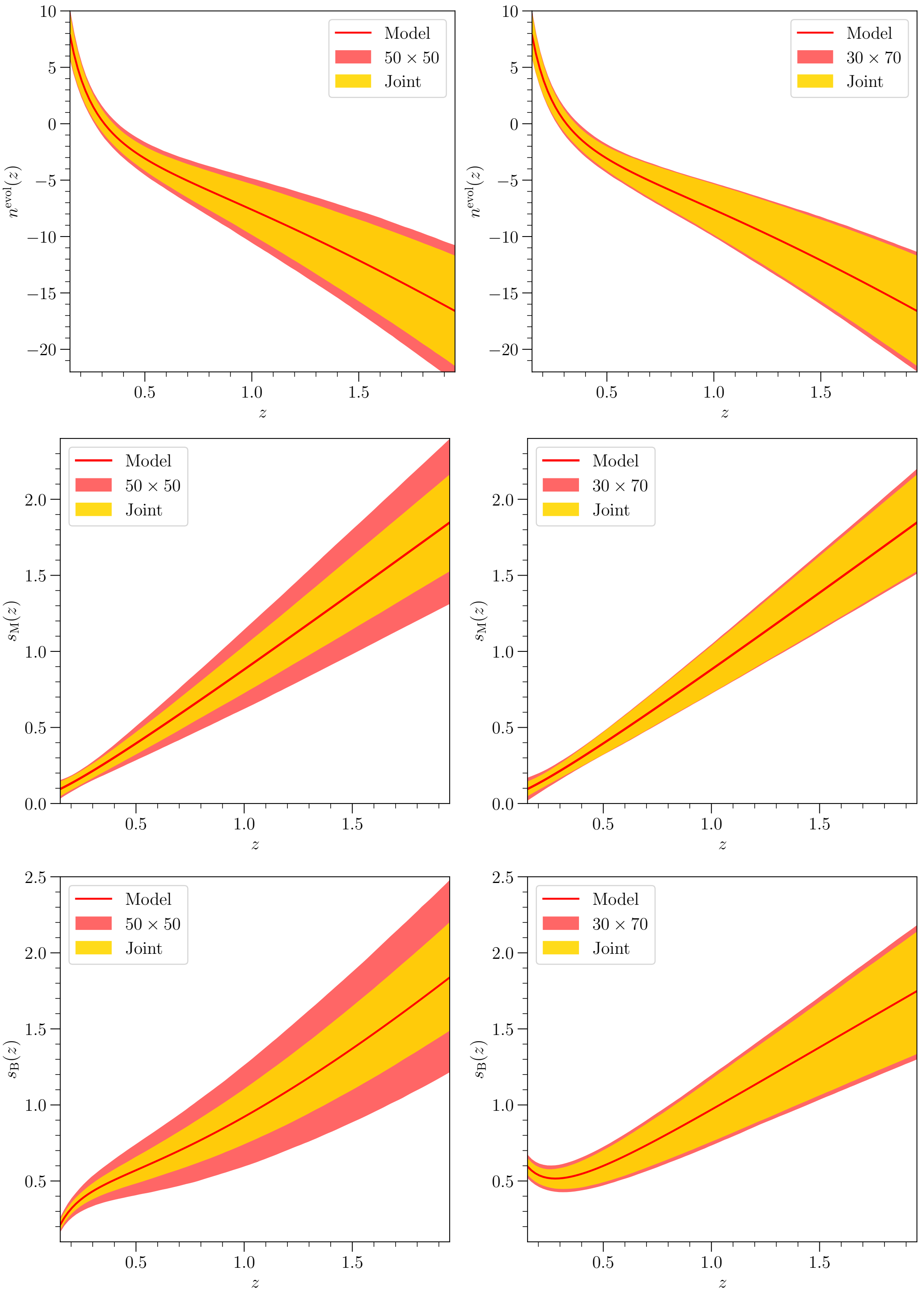

Figure 16.2: Constraints on the redshift evolution of the functions entering the forecasts, assuming a 50% prior on the parameters. We show the results for a single split (50 × 50 on the left, 30 × 70 on the right) and for the joint analysis. Note that s_{B} is different in the two splits. In all cases all multipoles are included.

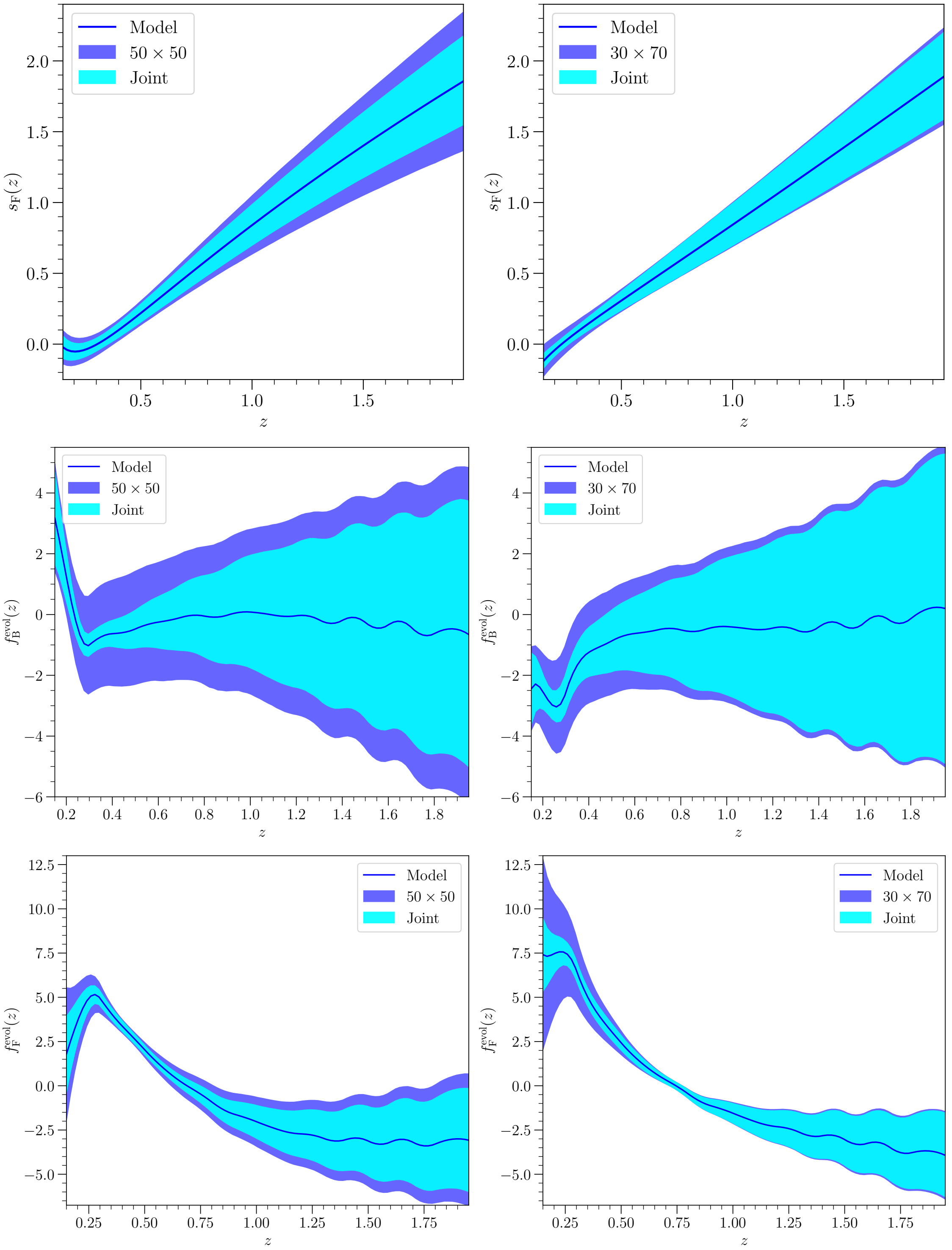

Figure 16.3: Constraints on the redshift evolution of the derived functions, assuming a 50% prior on the parameters. We show the results for a single split (50 × 50 on the left, 30 × 70 on the right) and for the joint analysis. Note that the three functions are different in the two splits. In all cases all multipoles are included.

17

SUMMARY AND CONCLUSION

In this work, we showed that exploiting the information carried by the odd multipoles of the 2-point correlation function can significantly improve our knowledge of the astrophysical properties of galaxies. We developed a physically motivated model for the magnification biases and evolution biases that govern the amplitude of the odd multipoles. These biases are directly related to the distribution in luminosity and the redshift evolution of galaxies. We found that:

- The magnification biases and evolution biases of the various samples can all be related to three observable quantities: the magnification bias of the whole (un-split) population s_{M}, the magnification bias of the bright sample s_{B}, and the redshift evolution of the number of galaxies n^{evol}.
- These three quantities cannot be measured from the odd multipoles if we have no prior knowledge about them, since they are fully degenerate with each other. However, parametrising their redshift evolution and assuming a prior of 50% on the parameters, the odd multipoles provide constraints that are tighter than the prior by a factor of up to $2-3$.
- Combining the dipole and the octupole is crucial to obtain tight constraints, since they do not suffer from the same degeneracies between parameters.
- Splitting the galaxies in different ways provides different constraints, but there is no significant trend that would single out one split as optimal.
- Combining two different splits further improves the constraints by up to 20% on the biases and by $\sim 3\%$ on the cosmological parameters n_{s} and Ω_{m}.

Knowing the astrophysical properties of galaxies is necessary to robustly constrain local primordial non-Gaussianities from large-scale structure, since these are contaminated by relativistic effects at very large scales. Since these effects directly depend on the magnification and evolution biases, having precise measurements of these quantities is essential. Interestingly, one can use the odd multipoles to constrain these quantities at intermediate scales, where local primordial non-Gaussianities are irrelevant, and from this one can predict the contamination from relativistic effects to the even multipoles at very large scales, where primordial non-Gaussianities are measured.

Finally, a good knowledge of the magnification and evolution biases is also essential to infer the observer velocity from the kinematic dipole, since they enter as a pre-factor in front of the observer velocity and are therefore fully degenerate with it. An accurate theoretical model of the kinematic dipole is critical for robust tests of the Cosmological Principle.

Part V

SUMMARY OF CONCLUSIONS AND OUTLOOK

18

If I were asked to summarize the present Thesis into a single sentence or paragraph, I would choose the following: the relativistic effects in the LSS cannot be swept under the carpet in the analysis of the data to be provided by the Stage IV galaxy surveys. They contain valuable and unique information that allows us to test gravity in a variety of ways. In this Thesis, we have demonstrated two use cases for measurements of the gravitational redshift at cosmological scales. In addition, we have proven that the relativistic effects contributing to the dipole of the 2-pt correlation function are crucially useful for constraining systematic biases such as the magnification and evolution bias at sub-horizon scales, whose modeling is crucial in the search for primordial non-Gaussianities on the largest scales. Furthermore, it is important to emphasize that measuring the relativistic effects is an efficient way to increase the constraining power of LSS surveys at a minimal cost, in the sense that it does not involve the addition of any new data.

In Part ii we constructed a model-independent test of gravity targeting the anisotropic stress, also known as the gravitational slip, which we defined as $\eta = \Phi/\Psi$. This new test combines measurements of the gravitational redshift from spectroscopic galaxy clustering and the evolution of the Weyl potential from photometric surveys. In the first case, we combine the multipoles of the 2-pt correlation functions for two populations of galaxies to isolate the gravitational redshift contribution, manifest as the correlations between density and Ψ perturbations. We introduce an appropriate parametrization for measuring the evolution of Ψ, the function $\hat{I}(z)$, for which we find a precision of $\sim 20\%$ at low redshift. If we assume a specific time evolution we can simplify the analysis to a single parameter I_0, reaching the 10% level. In addition, we introduce a new parametrization for measuring the evolution of the Weyl potential, the function $\hat{J}(z)$, for which we find sub-percent level precision. Then, we construct an estimator based on the ratio between these two functions, which represents a direct measurement of the ratio between Ψ and the Weyl potential. Hence, it is a proxy for a direct measurement of η through the quantity $2/(1+\eta)$. The precision on this estimator is fully determined by the precision of $\hat{I}$, ranging from $20\% - 40\%$ at low redshifts. However, due to systematic limitations, we observe that the test is not meaningful for redshifts above $z = 1.0$. In any case, we argue that, in comparison with current tests of gravity, the future constraints on Ψ are roughly of the same order of magnitudes than current constraints on the peculiar velocities, and they will be only two orders of magnitude worse than future constraints on V, when using spectroscopic information alone. In addition, we emphasize that neither the Ψ nor the η estimators proposed here rely on intermediate assumptions about the theory of gravity or about the properties of dark matter, such as the validity of the continuity and Euler equations. Remarkably, our test is able to reach a precision comparable to those of the expected for the $\mu - \Sigma$ parametrization when relaxing the assumption about the validity of the weak equivalence principle for dark matter. Therefore, this seems to be the level at which the theory of gravity can be tested in a model-independent way even with futuristic surveys. Importantly, however, the analyses hereby described are conducted in the quasi-static approximation, where we can neglect scale dependency. The natural extension of these works will be to include scale-dependency, which in principle should not change the conclusions we brought here. Additionally, another avenue to follow would be to include into the modeling information of the non-linear scales and evaluate the impact on the constraints.

In Part iii we delve into the Effective Field Theory of Dark Energy framework and study the capability of the gravitational redshift in breaking degeneracies among the fundamental parameters. This framework represents a theoretically satisfactory scenario which encompasses a large plethora of modified gravity models, including those in which interactions in the dark sector are allowed. Generally speaking, these interactions induce a breaking in the weak equivalence principle for dark matter. It is in this context when the gravitational redshift is particularly crucial. We have shown that the dipole contains a combination of the Doppler effects and the gravitational redshift which exactly vanishes when the Euler equation is valid. It is thus specifically remarkable in theories with this feature, for which we are able to find improvements on the EFT parameters by up to $\sim 50\%$. This is particularly outstanding, provided that the SNR of the dipole is about six times smaller than that of the quadrupole contribution. In a future work, we could study whether the addition of gravitational lensing information into the game further helps in breaking degeneracies, and hence provide even better constraints on the parameters. This is expected as the gravitational lensing is sensitive to the Weyl potential, and hence carries a different combination of the EFT parameters compared to that of the gravitational redshift. Additionally, natural extensions of this piece of work will simply be to explore other time parametrizations for the EFT parameters or study the physics beyond the quasi-static approximation.

Finally, in Part iv we depart from testing gravity theories and focus on other aspects of the relativistic effects. We demonstrate we can use the odd multipoles of the 2-pt correlation function to significantly improve our knowledge about s and $f^{\rm evol}$. We identified the three quantities that can be directly measurable from the data: the magnification bias of the bright population, s_B, the magnification bias of the total population s_M, and the logarithmic evolution of the full sample, $n^{\rm evol}$. Then, the $f^{\rm evol}$ of each population can be reconstructed from these measurements. We demonstrate that including the octupole is necessary in this context and is crucial to fully optimize the measurements. In particular, assuming ΛCDM, we forecast that we can reduce the uncertainties in most of the parameters involved, but that the amount of improvement obtained in each case is sensitive to the way we split the populations and to the priors. For instance, for a prior of 50% we find improvements of a factor $2-3$ for s_B parameters in the 50×50 and 70×30 splits. We support these findings by reconstructing the predicted 68% confidence regions as a function of redshift for various sample separations (see figs. 16.1, D.3). We observe a systematic reduction of the shaded regions, specially when the octupole is included. We complete the study by analyzing the case of having four populations of galaxies, for which we combine the information of two different splits that are assumed to be independent 'experiments'. The relative gain with respect to the single split cases depends on the split we compare the results with, but overall, the 68% constraints are improved for most of the parameters and inferred quantities (see figs. 16.2 and 16.3). Naturally, following the introductory Chapter 13, the continuation of this work is to transfer the improvements on the constraints to the modeling of the relativistic effects on ultra-large scales, and assess the impact that the predicted variability on s and $f^{\rm evol}$ has in the predicted uncertainty for $f_{\rm NL}$. In addition, we could evaluate the necessity of considering 4 populations of galaxies to constrain the galaxy biases and the cosmic parameters, optimizing the choices for separating the sample and trying to find an optimal configuration for fully exploiting the information contained in the 2-pt correlation function.

On the whole, this Thesis is essentially a compilation of reasons for measuring the relativistic effects in the LSS. The expectation on the upcoming generation of surveys considered in these investigations is that they will serve as a window to a completely new and largely unexplored source of information. This will allow us to probe new sectors of gravitational theories in innovative ways and with unprecedented precision. It is therefore a truly exciting time to work on Cosmology in general, and particularly on this topic. The study of the relativistic effects in the LSS is key to further improving our knowledge about the Universe we happen to live in, marking a new milestone in the ongoing development of the *study of the Heavens*.

Part VI

APPENDIX

A

SOME USEFUL FORMULAE

The sections below provide a brief introduction to a few mathematical concepts that have been used in the Thesis. We also include some useful formulae derived from those concepts. They can be studied in more detail in e.g. [275].

A.1 FOURIER TRANSFORMS

The Fourier transform of any function $f(x)$ is a mathematical operation that converts the function from its original domain, usually named the *configuration space* (time or space) to the frequency domain, also known as the *Fourier space*. According to the convention we use in this Thesis, the Fourier transform of a spatial 3-vector can be give as:

$$f(\mathbf{k}) = \int d^3x f(\mathbf{x}) e^{i\mathbf{k}\cdot\mathbf{x}} \tag{A.1}$$

so that the inverse Fourier transform is

$$f(\mathbf{x}) = \frac{1}{(2\pi)^3} \int d^3k f(\mathbf{k}) e^{-i\mathbf{k}\cdot\mathbf{x}} \tag{A.2}$$

A.2 LEGENDRE POLYNOMIALS

The Legendre polynomials are defined in the interval [-1, 1] and form an orthonormal set. The normalization condition is the following:

$$\int_{-1}^{1} dx \mathcal{P}_\ell(x) \mathcal{P}'_\ell(x) = \frac{2}{2\ell+1} \delta_{\ell\ell'} \tag{A.3}$$

The Legendre polynomials obey the following differential equation:

$$(1-x^2)\mathcal{P}''_\ell - 2x\mathcal{P}'_\ell + \ell(\ell+1)\mathcal{P}_\ell = 0 \tag{A.4}$$

We can obtain them via the recursion relation:

$$(\ell+1)\mathcal{P}_{\ell+1}(x) = (2\ell+1)x\mathcal{P}_\ell(x) - \ell\mathcal{P}_{\ell-1}(x) \tag{A.5}$$

The Rodrigues' formula is:

$$\mathcal{P}_\ell(x) = \frac{1}{2^\ell \ell!} \frac{d^\ell}{dx^\ell} (x^2-1)^\ell \tag{A.6}$$

Some lowest-order Legendre polynomials are as follows:

$$\mathcal{P}_0 = 1, \tag{A.7}$$

$$\mathcal{P}_1 = x, \tag{A.8}$$

$$\mathcal{P}_2 = \frac{1}{2}(3x^2 - 1), \tag{A.9}$$

$$\mathcal{P}_3 = \frac{1}{2}(5x^3 - 3x), \tag{A.10}$$

$$\mathcal{P}_4 = \frac{1}{8}(35x^4 - 30x^2 + 3) \tag{A.11}$$

We also find that $\mathcal{P}_\ell(-x) = (-1)^\ell \mathcal{P}_\ell(x)$ and $\mathcal{P}_\ell(1) = 1$. We can also invert these relations to find

$$x^2 = \frac{2}{3}\mathcal{P}_2 + 1/3, \tag{A.12}$$

$$x^3 = \frac{2}{5}\mathcal{P}_3 + \frac{3}{5}\mathcal{P}_1, \tag{A.13}$$

$$x^4 = \frac{8}{35}\mathcal{P}_4 + \frac{4}{7}\mathcal{P}_2 + 1/5. \tag{A.14}$$

Finally, we can define the associate Legendre functions by:

$$\mathcal{P}_{\ell m}(x) = (1-x^2)^{m/2}\frac{d^m \mathcal{P}_\ell(x)}{dx^m} = (1-x^2)^{m/2}\frac{1}{2^\ell \ell!}\frac{d^{\ell+m}}{dx^{\ell+m}}(x^2-1)^\ell \tag{A.15}$$

for $0 \leq m \leq \ell$. These Legendre functions are solutions of the following differential equation:

$$(1-x^2)\mathcal{P}''_{\ell m} - 2x\mathcal{P}'_{\ell m} + \left[\ell(\ell+1) - \frac{m^2}{1-x^2}\right]\mathcal{P}_{\ell m} = 0 \tag{A.16}$$

The orthogonality relation holds as follows:

$$\int_{-1}^{1} \mathcal{P}_{\ell m}(x)\mathcal{P}_{\ell' m}(x)dx \tag{A.17}$$

$$= \int_0^\pi \mathcal{P}_{\ell m}(\cos\vartheta)\mathcal{P}_{\ell' m}(\cos\vartheta \sin\vartheta)d\vartheta = \frac{2}{2\ell+1}\frac{(\ell+m)!}{(\ell-m)!}\delta_{\ell\ell'} \tag{A.18}$$

A.3 SPHERICAL HARMONICS

Spherical harmonics are special functions defined on the surface of a sphere. They are found by solving the Laplace's equation. Being $f : \mathcal{R}^3 \longrightarrow \mathbb{C}$ a smooth, scalar function, one solves, in spherical coordinates, the equation $\nabla^2 f(r,\vartheta,\varphi) = 0$. By separation of variables, we can always find solutions of the form $f(r,\vartheta,\varphi) = R(r)\,Y(\vartheta,\varphi)$. Leaving aside the radial part, we find the angular to be of the form

$$Y_{\ell m}(\vartheta,\varphi) = N\,e^{im\varphi}\,\mathcal{P}_{\ell m}(\cos\vartheta), \tag{A.19}$$

i.e. multiples of the associated Legendre functions defined in the previous section, up to a normalization factor N and a phase. Here $Y : S^2 \longrightarrow \mathbb{C}$ are the *Spherical Harmonics*. For a fixed integer ℓ, we can rewrite the above as an eigenvalue problem

$$\nabla^2\,Y_{\ell m}(\vartheta,\varphi) = -\frac{1}{r^2}\,\ell(\ell+1)\,Y_{\ell m}(\vartheta,\varphi). \tag{A.20}$$

For our purposes, it is sufficient to be familiar with spherical harmonics of spin-0. If we have a unit vector **n** defined by its polar angles (ϑ, φ), we can write the spherical harmonics as:

$$Y_{\ell m} = (-1)^m \sqrt{\frac{2\ell+1}{4\pi}\frac{(\ell-m)!}{(\ell+m)!}}\, e^{im\varphi}\, \mathcal{P}_{\ell m}(\mu), \quad \mu = \cos\vartheta \tag{A.21}$$

We can also prove that $Y_{\ell -m} = (-1)^m Y^*_{\ell m}$. From this expression, we can see that in a coordinate system in which $m = 0$, i.e. the direction vector is aligned to the z-axis, the above reduces to the standard Legendre polynomial

$$Y_{\ell 0} = \sqrt{\frac{4\pi}{2\ell+1}} P_\ell(\cos\vartheta). \tag{A.22}$$

Hence, in combination with eq. (A.21), this gives the action of the Laplace operator on Legendre polynomials to be

$$r^2\nabla^2\, \mathcal{P}_\ell(\cos\vartheta) = -\ell(\ell+1)\, \mathcal{P}_\ell(\cos\vartheta). \tag{A.23}$$

The derivative operator here often receives the name of *transverse* Laplacian, and is denoted by $\Delta_\Omega \equiv r^2\,\nabla^2$. The addition theorem for spherical harmonics is given by:

$$P_\ell(\mathbf{n}_1\cdot\mathbf{n}_2) = \frac{4\pi}{2\ell+1}\sum_{m=-\ell}^{\ell} Y^*_{\ell m}(\mathbf{n}_1) Y_{\ell m}(\mathbf{n}_2) \tag{A.24}$$

Integrals over a direction **n** involving only one spherical harmonic enforce ℓ and m to be zero

$$\int d\Omega_{\mathbf{n}}\, Y^*_{\ell m}(\mathbf{n}) = \sqrt{4\pi}\,\delta_{\ell 0}\delta_{m0} \tag{A.25}$$

Terms with two spherical harmonics provide the orthogonality relation

$$\int d\Omega_{\mathbf{n}}\, Y_{\ell m}(\mathbf{n})\hat{Y}_{\ell' m'}(\mathbf{n}) = \delta_{\ell\ell'}\delta_{mm'}. \tag{A.26}$$

If we integrate three spherical harmonics, we obtain $3J$ Wigner symbols

$$\int d\Omega_{\mathbf{n}}\, Y^*_{LM}(\mathbf{n})Y^*_{\ell m}(\mathbf{n})Y^*_{\ell' m'}(\mathbf{n}) = \sqrt{\frac{(2L+1)(2\ell+1)(2\ell'+1)}{4\pi}} \tag{A.27}$$

$$\times \begin{pmatrix} L & \ell & \ell' \\ -M & -m & -m' \end{pmatrix} \begin{pmatrix} L & \ell & \ell' \\ 0 & 0 & 0 \end{pmatrix} \tag{A.28}$$

Some low order spherical harmonics are given by:

$$\ell = 0 \quad Y_{00} = \frac{1}{\sqrt{4\pi}}, \tag{A.29}$$

$$\ell = 1 \quad \begin{cases} Y_{11} & = -\sqrt{\frac{3}{8\pi}}\sin\vartheta e^{i\varphi}, \\ Y_{10} & = \sqrt{\frac{3}{4\pi}}\cos\vartheta, \end{cases}, \tag{A.30}$$

$$\ell = 2 \quad \begin{cases} Y_{22} &= \sqrt{\frac{15}{32\pi}} \sin^2 \vartheta e^{2i\varphi}, \\ Y_{21} &= -\sqrt{\frac{15}{8\pi}} \sin \vartheta \cos \vartheta e^{i\varphi}, \\ Y_{20} &= \sqrt{\frac{5}{4\pi}} \left(\frac{3}{2} \cos^2 \vartheta - \frac{1}{2}\right), \end{cases} \tag{A.31}$$

$$\ell = 3 \quad \begin{cases} Y_{33} &= -\sqrt{\frac{35}{64\pi}} \sin^3 \vartheta e^{3i\varphi}, \\ Y_{32} &= \sqrt{\frac{105}{32\pi}} \sin^2 \vartheta \cos \vartheta e^{2i\varphi}, \\ Y_{31} &= -\sqrt{\frac{21}{16\pi}} \sin \vartheta \left(\frac{5}{2} \cos^2 \vartheta - \frac{1}{2}\right) e^{i\varphi}, \\ Y_{30} &= \sqrt{\frac{7}{4\pi}} \cos \vartheta \left(\frac{5}{2} \cos^2 \vartheta - \frac{3}{2}\right) \end{cases} \tag{A.32}$$

$$Y_{\ell -m} = (-1)^m Y^*_{\ell m} \tag{A.33}$$

A.4 BESSEL FUNCTIONS AND SPHERICAL BESSEL FUNCTIONS

The two kinds of Bessel functions $J_\nu(x)$ and $Y_\nu(x)$ are real solutions to the following differential equation:

$$x^2 \frac{df}{dx^2} + x\frac{df}{dx} + (x^2 - \nu^2) f = 0 \tag{A.34}$$

The Hankel functions can be defined as:

$$H_\nu^{(1)} = J_\nu + iY_\nu, \quad H_\nu^{(2)} = J_\nu - iY_\nu \tag{A.35}$$

These functions satisfy the recurrence relations:

$$F_{\nu-1} + F_{\nu+1} = \frac{2\nu}{x} F_\nu, \tag{A.36}$$

$$F_{\nu-1} - F_{\nu+1} = 2F'_\nu, \tag{A.37}$$

$$F_{\nu-1} - \frac{\nu}{x} F_\nu = F'_\nu, \tag{A.38}$$

$$- F_{\nu+1} + \frac{\nu}{x} F_\nu = F'_\nu \tag{A.39}$$

We can represent the Bessel functions J_n, $n \in \mathbb{N}$ as the integral:

$$J_n(x) = \frac{(-i)^n}{\pi} \int_0^\pi e^{ix\cos\theta} \cos(n\theta) d\theta \tag{A.40}$$

from which we obtain the expansion:

$$e^{iy\cos\phi} = J_0(y) + 2\sum_{n=1}^{\infty} i^n J_n(y) \cos(n\phi) = \sum_{n=-\infty}^{\infty} i^n J_n(y) e^{in\phi} \tag{A.41}$$

The spherical Bessel and Hankel functions can be derived from the normal Bessel and Hankel functions as follows:

$$j_n(x) = \sqrt{\frac{\pi}{2x}} J_{n+1/2}(x), \tag{A.42}$$

$$y_n(x) = \sqrt{\frac{\pi}{2x}} Y_{n+1/2}(x), \tag{A.43}$$

$$h_n^{(1)} = j_n + iy_n, \tag{A.44}$$

$$h_n^{(2)} = j_n - iy_n. \tag{A.45}$$

They are solutions of the differential equation:

$$x^2 \frac{df}{dx^2} + 2x\frac{df}{dx} + (x^2 - n(n+1))f = 0 \tag{A.46}$$

and they satisfy the following recurrence relations:

$$\frac{f_n}{x} = \frac{1}{2n+1}(f_{n-1} + f_{n+1}), \tag{A.47}$$

$$f_n' = \frac{1}{2n+1}(nf_{n-1} - (n+1)f_{n+1}), \tag{A.48}$$

The following expansion holds for an exponential function in terms of spherical Bessel functions and spherical harmonics:

$$e^{i\mathbf{x}\cdot\mathbf{k}} = e^{i(kr)\hat{\mathbf{x}}\cdot\hat{\mathbf{k}}} = 4\pi \sum_{\ell m} i^\ell j_\ell(kr) Y^*_{\ell m}(\hat{\mathbf{k}}) Y_{\ell m}(\hat{\mathbf{x}}) \tag{A.49}$$

A similar relation but in terms of the Legendre polynomials can be found

$$e^{i\mathbf{k}\cdot\mathbf{n}r} = \sum_{\ell=0}^{\infty} (2\ell+1) i^\ell j_\ell(kr) P_\ell(\mu) \tag{A.50}$$

where $P_\ell(\mu)$ are Legendre polynomials defined in the previous section. In addition, the closure relation of spherical Bessel functions holds

$$\frac{2}{\pi}\int_0^\infty dr\, r^2\, j_\ell(kr) j_\ell(k'r) = \delta(k-k')\, k^{-2}. \tag{A.51}$$

A.5 COEFFICIENTS OF THE 2-PT CORRELATION FUNCTION

From the previous definitions and recurrence relations for $j_\ell(k)$ we can construct useful combinations. We use $d = \sqrt{r_1^2 + r_2^2 - r_1 r_2 \cos\theta}$ as defined in the main text of Chapter 2. For a given k mode, we have

$$\sum_\ell (2\ell+1)\mathcal{P}_\ell(\cos\theta)\, j_\ell(kr_1)\, j_\ell(kr_2) = j_0(kd). \tag{A.52}$$

Note that $j_0(kd) = \sin(kd)/kd$. We define $x_i \equiv kr_i$. More generally, we define the combinations

$$\zeta^{ij} \equiv \sum_\ell (2\ell+1)\mathcal{P}_\ell(\cos\theta)\, j_\ell^{(i)}(x_1)\, j_\ell^{(j)}(x_2), \tag{A.53}$$

where

$$j_\ell^{(i)}(x) = \frac{\partial}{\partial x_i} j_\ell(x), \tag{A.54}$$

which are computed using the recurrence relations. We also have symmetry $\zeta^{ij}(x_1, x_2) = \zeta^{ji} x_2, x_1$. More generally, we can use

$$\frac{\partial}{\partial x_1^n\, \partial x_2^m}\, \zeta^{ij} = \zeta^{i+m,j+n}. \tag{A.55}$$

All together permits the computation of the explicit expressions of the relevant ζ^{ij}. Let us include a summary of the relevant quantities used in the text

$$\begin{aligned}
\zeta^{00} &= j_0(kd) && \text{(A.56)}\\
\zeta^{01} &= \frac{r_1\cos\theta - r_2}{d}\, j_1(kd) && \text{(A.57)}\\
\zeta^{02} &= \left(\frac{2}{3} - (1-\cos^2\theta)\frac{r_1^2}{d^2}\right) j_2(kd) - \frac{1}{3} j_0(kd) && \text{(A.58)}\\
\zeta^{12} &= \frac{(1+2\cos^2\theta)r_1 - 3r_2\cos\theta}{5d}\, j_1(kd) && \text{(A.59)}\\
&\quad + \frac{(1-3\cos^2\theta)r_1^3 + \cos\theta(5+\cos^2\theta)r_1^2 r_2 - 2(2+\cos^2\theta)r_1 r_2^2 + 2r_2^2\cos\theta}{5d^3}\, j_3(kd)\\
\zeta^{22} &= \frac{1+2\cos^2\theta}{15} j_0(kd) - \frac{18}{21}\left[\frac{1}{18} + \frac{11\cos^2\theta}{18} + \frac{\cos\theta(\cos^2\theta - 1)r_1 r_2}{d^2}\right] j_2(kd)\\
&\quad + \left[\frac{4(3\cos^2\theta - 1)(r_1^4 + r_2^4)}{35d^4}\right. && \text{(A.60)}\\
&\quad \left. + r_1 r_2(3+\cos^2\theta)\frac{3(3+\cos^2\theta)r_1 r_2 - 8(r_1^2 + r_2^2)\cos\theta}{35d^4}\right] j_4(kd)
\end{aligned}$$

In the distant-observer approximation $d \ll r$ the angles are small and the above can be written in terms of a power series in (d/r) containing Legendre polynomials. In the main text, we performed this approximation and rewrote the expressions in the coordinates (d, μ, z), being $\mu = \cos\beta$, according to fig. 2.1. The ζ^{ij} factors are reduced to the following

$$\begin{aligned}
\zeta^{00} &= j_0(kd) && \text{(A.61)}\\
\zeta^{01} &= \mathcal{P}_1(\mu)\, j_1(kd), \qquad \zeta^{10} = -\zeta^{01}, && \text{(A.62)}\\
\zeta^{02} &= -\frac{1}{3} j_0(kd) + \frac{2}{3}\mathcal{P}_2(\mu)\, j_2(kd) + \frac{2}{5}\frac{d}{r}(\mathcal{P}_1(\mu) - \mathcal{P}_3(\mu))\, j_2(kd), && \text{(A.63)}\\
\zeta^{20} &= -\frac{1}{3} j_0(kd) + \frac{2}{3}\mathcal{P}_2(\mu)\, j_2(kd) - \frac{2}{5}\frac{d}{r}(\mathcal{P}_1(\mu) - \mathcal{P}_3(\mu))\, j_2(kd), && \text{(A.64)}\\
\zeta^{12} &= -\frac{3}{5}\mathcal{P}_1(\mu)\, j_1(kd) + \frac{2}{5}\mathcal{P}_3(\mu)\, j_3(kd), \qquad \zeta^{21} = -\zeta^{12}, && \text{(A.65)}\\
\zeta^{22} &= \frac{1}{5} j_0(kd) - \frac{4}{7}\mathcal{P}_2(\mu)\, j_2(kd) + \frac{8}{35}\mathcal{P}_4(\mu)\, j_4(kd). && \text{(A.66)}
\end{aligned}$$

The change of sign in the terms entering into the relativistic effects contribution make manifest the breaking of symmetry induced by them to the correlation function. This asymmetric contributions are all contained in odd multipoles (associated to the $\mathcal{P}_\ell$'s with $\ell = 1, 3$) for the choice of coordinates (d, μ, z).

We include here the contributions to the galaxy 2-pt correlation function as computed in sec. 2.2, expressed in terms of the $\zeta^{ij}(kd)$ functions above. First, we define the terms relevant to the auto-correlations of the standard terms

$$\begin{aligned}
Q^{\delta\delta}_{\mathrm{LM}}(\theta, z_1, z_2) &= b_{\mathrm{L}}(z_1)\, b_{\mathrm{M}}(z_2)\, T_\delta(k, z_1) T_\delta(k, z_2)\, \zeta^{00}(kr_1, kr_2) && \text{(A.67)}\\
Q^{\delta\,\mathrm{RSD}}_{\mathrm{LM}}(\theta, z_1, z_2) &= -\frac{k}{\mathcal{H}(z_2)}\, b_{\mathrm{L}}(z_1)\, T_\delta(k, z_1) T_V(k, z_2)\, \zeta^{02}(kr_1, kr_2) && \text{(A.68)}
\end{aligned}$$

$$Q_{\rm LM}^{{\rm RSD}\,\delta}(\theta, z_1, z_2) = -\frac{k}{\mathcal{H}(z_1)}\, b_{\rm M}(z_2)\, T_\delta(k, z_2) T_V(k, z_1)\, \zeta^{02}(kr_2, kr_1) \tag{A.69}$$

$$Q_k^{\rm RSD}(\theta, z_1, z_2) = \frac{k^2}{\mathcal{H}(z_1)\mathcal{H}(z_2)}\, T_V(k, z_1) T_V(k, z_2)\, \zeta^{22}(kr_1, kr_2), \tag{A.70}$$

These contributions are completely symmetric under the exchange $z_1 \to z_2$. Similarly, the terms relevant to the cross-correlation between standard and relativistic contributions are defined to be

$$Q_{\rm LM}^{\delta\,V}(\theta, z_1, z_2) = b_{\rm L}(z_1)\alpha_{\rm M}(z_2)\, T_\delta(k, z_1) T_V(k, z_2) \zeta^{01}(kr_1, kr_2) + b_{\rm M}(z_2)\alpha_{\rm L}(z_1)\, T_\delta(k, z_2) T_V(k, z_1) \zeta^{01}(kr_2, kr_1), \tag{A.71}$$

$$Q_{\rm LM}^{\delta\,\dot{V}}(\theta, z_1, z_2) = \frac{b_{\rm L}(z_1)}{\mathcal{H}(z_2)}\, T_\delta(k, z_1) T_{\dot{V}}(k, z_2) \zeta^{01}(kr_1, kr_2) + \frac{b_{\rm M}(z_2)}{\mathcal{H}(z_1)}\, T_\delta(k, z_2) T_{\dot{V}}(k, z_1) \zeta^{01}(kr_2, kr_1), \tag{A.72}$$

$$Q_{\rm LM}^{{\rm RSD}\,V}(\theta, z_1, z_2) = -k \left[\frac{\alpha_{\rm M}(z_2)}{\mathcal{H}(z_1)}\, T_V(k, z_1) T_V(k, z_2)\, \zeta^{21}(kr_1, kr_2) + \frac{\alpha_{\rm L}(z_1)}{\mathcal{H}(z_2)}\, T_V(k, z_1) T_V(k, z_2)\, \zeta^{21}(kr_2, kr_1) \right] \tag{A.73}$$

$$Q_{\rm LM}^{{\rm RSD}\,\dot{V}}(\theta, z_1, z_2) = -\frac{k}{\mathcal{H}(z_1)\mathcal{H}(z_2)} \left[T_V(k, z_1) T_{\dot{V}}(k, z_2)\, \zeta^{21}(kr_1, kr_2) + T_V(k, z_2) T_{\dot{V}}(k, z_1)\, \zeta^{21}(kr_2, kr_1) \right] \tag{A.74}$$

$$Q_{\rm LM}^{\delta\,\Psi}(\theta, z_1, z_2) = -k \left[\frac{b_{\rm L}(z_1)}{\mathcal{H}(z_2)}\, T_\delta(k, z_1) T_\Psi(k, z_2)\, \zeta^{01}(kr_1, kr_2) + \frac{b_{\rm M}(z_2)}{\mathcal{H}(z_1)}\, T_\delta(k, z_2) T_\Psi(k, z_1)\, \zeta^{01}(kr_2, kr_1) \right] \tag{A.75}$$

$$Q_{\rm LM}^{{\rm RSD}\,\Psi}(\theta, z_1, z_2) = -\frac{k^2}{\mathcal{H}(z_1)\mathcal{H}(z_2)} \left[T_V(k, z_1) T_\Psi(k, z_2)\, \zeta^{21}(kr_1, kr_2) + T_V(k, z_2) T_\Psi(k, z_1)\, \zeta^{21}(kr_2, kr_1) \right]. \tag{A.76}$$

Let us stress that these are not the complete set of contributions to the 2-pt correlation functions, but only those arising from $\Delta_{\rm ST}$ and $\Delta_{\rm REL}$ as given by eqs. (1.42) and (1.58). The lensing convergence and other integrated terms involving the gravitational potentials where neglected. A more complete list of Q functions is given in e.g. [42, 46], from where we borrow some formulae and computational techniques. In any case, these are *exact* expressions in the full-sky, on which we shall perform the distant-observer or flat-sky approximation as described above.

B

MEASURING THE ANISOTROPIC STRESS WITH RELATIVISTIC EFFECTS

In this appendix we provide the fiducial values for all the parameters considered for the analysis discussed in Chapter 6, including those that have been fixed. The latter are presented in table B.1, while the former are shown in table B.2. In particular, the values correspond to those used in secs. 6.1.2 and 6.1.3, where we adapted the z bins of the SKA analysis to match with the binning for the LSST lenses. For the original $\hat{I}$ measurements, described in secs. 6.1.1 and 6.2.1.1, we considered 12 bins of size $\Delta z = 0.1$ evaluating the quantities at the center of each bin. The fiducial is however always fixed to GR.

Parameter	Fiducial value
$\Omega_{\mathrm{m},0}$	0.3111
$\Omega_{\mathrm{b},0}$	0.0490
h	0.677
n_s	0.9665
A_s	2.105×10^{-9}
$s_{\mathrm{B},1}$	$s_\mathrm{B}(z = 0.25) = 0.3706$
$s_{\mathrm{B},2}$	$s_\mathrm{B}(z = 0.38) = 0.4665$
$s_{\mathrm{B},3}$	$s_\mathrm{B}(z = 0.51) = 0.5757$
$s_{\mathrm{B},4}$	$s_\mathrm{B}(z = 0.65) = 0.6817$
$s_{\mathrm{B},5}$	$s_\mathrm{B}(z = 0.79) = 0.7839$
$s_{\mathrm{B},6}$	$s_\mathrm{B}(z = 0.95) = 0.8974$
$s_{\mathrm{B},7}$	$s_\mathrm{B}(z = 1.13) = 1.0224$
$s_{\mathrm{F},1}$	$s_\mathrm{F}(z = 0.25) = -0.1618$
$s_{\mathrm{F},2}$	$s_\mathrm{F}(z = 0.38) = -0.1279$
$s_{\mathrm{F},3}$	$s_\mathrm{F}(z = 0.51) = -0.1269$
$s_{\mathrm{F},4}$	$s_\mathrm{F}(z = 0.65) = -0.1209$
$s_{\mathrm{F},5}$	$s_\mathrm{F}(z = 0.79) = -0.1164$
$s_{\mathrm{F},6}$	$s_\mathrm{F}(z = 0.95) = -0.1120$
$s_{\mathrm{F},7}$	$s_\mathrm{F}(z = 1.13) = -0.1080$

Table B.1: List of fixed parameters considered in the Fisher analysis, together with their fiducial values in the ΛCDM model.

Parameter	Fiducial value
$\hat{J}_1$	$\hat{J}(z=0.25)=\Omega_\mathrm{m}\cdot\sigma_8(z=0.25)=0.3388$
$\hat{J}_2$	$\hat{J}(z=0.38)=\Omega_\mathrm{m}\cdot\sigma_8(z=0.38)=0.3666$
$\hat{J}_3$	$\hat{J}(z=0.51)=\Omega_\mathrm{m}\cdot\sigma_8(z=0.51)=0.3846$
$\hat{J}_4$	$\hat{J}(z=0.65)=\Omega_\mathrm{m}\cdot\sigma_8(z=0.65)=0.3949$
$\hat{J}_5$	$\hat{J}(z=0.79)=\Omega_\mathrm{m}\cdot\sigma_8(z=0.79)=0.3979$
$\hat{J}_6$	$\hat{J}(z=0.95)=\Omega_\mathrm{m}\cdot\sigma_8(z=0.95)=0.3948$
$\hat{J}_7$	$\hat{J}(z=1.13)=\Omega_\mathrm{m}\cdot\sigma_8(z=1.13)=0.3859$
$\hat{J}_8$	$\hat{J}(z=1.35)=\Omega_\mathrm{m}\cdot\sigma_8(z=1.35)=0.3707$
$\hat{J}_9$	$\hat{J}(z=1.7)=\Omega_\mathrm{m}\cdot\sigma_8(z=1.7)=0.3427$
$\hat{J}_{10}$	$\hat{J}(z=2.1)=\Omega_\mathrm{m}\cdot\sigma_8(z=2.1)=0.3111$
$\hat{b}_1$	$\hat{b}(z=0.25)=b\cdot\sigma_8(z=0.25)=1.4462$
$\hat{b}_2$	$\hat{b}(z=0.38)=b\cdot\sigma_8(z=0.38)=1.3512$
$\hat{b}_3$	$\hat{b}(z=0.51)=b\cdot\sigma_8(z=0.51)=1.2644$
$\hat{b}_4$	$\hat{b}(z=0.65)=b\cdot\sigma_8(z=0.65)=1.1796$
$\hat{b}_5$	$\hat{b}(z=0.79)=b\cdot\sigma_8(z=0.79)=1.1035$
$\hat{b}_6$	$\hat{b}(z=0.95)=b\cdot\sigma_8(z=0.95)=1.0259$
$\hat{b}_7$	$\hat{b}(z=1.13)=b\cdot\sigma_8(z=1.13)=0.9492$
$\hat{b}_8$	$\hat{b}(z=1.35)=b\cdot\sigma_8(z=1.35)=0.8683$
$\hat{b}_9$	$\hat{b}(z=1.7)=b\cdot\sigma_8(z=1.7)=0.7631$
$\hat{b}_{10}$	$\hat{b}(z=2.1)=b\cdot\sigma_8(z=2.1)=0.6690$
A_IA	1.0
$\hat{I}_1$	$\hat{I}(z=0.25)=\Omega_\mathrm{m}\cdot\sigma_8(z=0.25)=0.3388$
$\hat{I}_2$	$\hat{I}(z=0.38)=\Omega_\mathrm{m}\cdot\sigma_8(z=0.38)=0.3666$
$\hat{I}_3$	$\hat{I}(z=0.51)=\Omega_\mathrm{m}\cdot\sigma_8(z=0.51)=0.3846$
$\hat{I}_4$	$\hat{I}(z=0.65)=\Omega_\mathrm{m}\cdot\sigma_8(z=0.65)=0.3949$
$\hat{I}_5$	$\hat{I}(z=0.79)=\Omega_\mathrm{m}\cdot\sigma_8(z=0.79)=0.3979$
$\hat{I}_6$	$\hat{I}(z=0.95)=\Omega_\mathrm{m}\cdot\sigma_8(z=0.95)=0.3948$
$\hat{I}_7$	$\hat{I}(z=1.13)=\Omega_\mathrm{m}\cdot\sigma_8(z=1.13)=0.3859$
$\hat{f}_1$	$\hat{f}(z=0.25)=f\cdot\sigma_8(z=0.25)=0.4761$
$\hat{f}_2$	$\hat{f}(z=0.38)=f\cdot\sigma_8(z=0.38)=0.4826$
$\hat{f}_3$	$\hat{f}(z=0.51)=f\cdot\sigma_8(z=0.51)=0.4811$
$\hat{f}_4$	$\hat{f}(z=0.65)=f\cdot\sigma_8(z=0.65)=0.4733$
$\hat{f}_5$	$\hat{f}(z=0.79)=f\cdot\sigma_8(z=0.79)=0.4612$
$\hat{f}_6$	$\hat{f}(z=0.95)=f\cdot\sigma_8(z=0.95)=0.4444$
$\hat{f}_7$	$\hat{f}(z=1.13)=f\cdot\sigma_8(z=1.13)=0.4238$

$\hat{b}_{\mathrm{B},1}$	$\hat{b}_{\mathrm{B}}(z=0.25) = b_{\mathrm{B}} \cdot \sigma_8(z=0.25) = 0.8486$
$\hat{b}_{\mathrm{B},2}$	$\hat{b}_{\mathrm{B}}(z=0.38) = b_{\mathrm{B}} \cdot \sigma_8(z=0.38) = 0.8416$
$\hat{b}_{\mathrm{B},3}$	$\hat{b}_{\mathrm{B}}(z=0.51) = b_{\mathrm{B}} \cdot \sigma_8(z=0.51) = 0.8380$
$\hat{b}_{\mathrm{B},4}$	$\hat{b}_{\mathrm{B}}(z=0.65) = b_{\mathrm{B}} \cdot \sigma_8(z=0.65) = 0.8382$
$\hat{b}_{\mathrm{B},5}$	$\hat{b}_{\mathrm{B}}(z=0.79) = b_{\mathrm{B}} \cdot \sigma_8(z=0.79) = 0.8430$
$\hat{b}_{\mathrm{B},6}$	$\hat{b}_{\mathrm{B}}(z=0.95) = b_{\mathrm{B}} \cdot \sigma_8(z=0.95) = 0.8541$
$\hat{b}_{\mathrm{B},7}$	$\hat{b}_{\mathrm{B}}(z=1.13) = b_{\mathrm{B}} \cdot \sigma_8(z=1.13) = 0.8739$
$\hat{b}_{\mathrm{F},1}$	$\hat{b}_{\mathrm{F}}(z=0.25) = b_{\mathrm{F}} \cdot \sigma_8(z=0.25) = 0.1256$
$\hat{b}_{\mathrm{F},2}$	$\hat{b}_{\mathrm{F}}(z=0.38) = b_{\mathrm{F}} \cdot \sigma_8(z=0.38) = 0.1661$
$\hat{b}_{\mathrm{F},3}$	$\hat{b}_{\mathrm{F}}(z=0.51) = b_{\mathrm{F}} \cdot \sigma_8(z=0.51) = 0.2059$
$\hat{b}_{\mathrm{F},4}$	$\hat{b}_{\mathrm{F}}(z=0.65) = b_{\mathrm{F}} \cdot \sigma_8(z=0.65) = 0.2486$
$\hat{b}_{\mathrm{F},5}$	$\hat{b}_{\mathrm{F}}(z=0.79) = b_{\mathrm{F}} \cdot \sigma_8(z=0.79) = 0.2914$
$\hat{b}_{\mathrm{F},6}$	$\hat{b}_{\mathrm{F}}(z=0.95) = b_{\mathrm{F}} \cdot \sigma_8(z=0.95) = 0.3413$
$\hat{b}_{\mathrm{F},7}$	$\hat{b}_{\mathrm{F}}(z=1.13) = b_{\mathrm{F}} \cdot \sigma_8(z=1.13) = 0.3995$

Table B.2: List of free parameters considered with their fiducial values in the ΛCDM model. All the parameters were varied in the Fisher analysis.

C

CONSTRAINTS ON THE EFFECTIVE THEORY OF INTERACTING DARK ENERGY

Here, we present additional plots, supplementing those presented in section 6.2. All results in this appendix, except figure C.3, are obtained using the ΛCDM fiducial model. First, the corner plot in figure C.1 shows the constraints obtained on the parameters $\alpha_{\mathrm{M},0}$, $\alpha_{\mathrm{B},0}$, $\gamma_{c,0}$ and w_{DE} when including only the monopole of the galaxy correlation function (yellow contours), compared to the combination with the dipole term, which contains gravitational redshift (green contours). In figure C.2, we further illustrate the impact of a dipole boosted by factors 2, 5, and 10 (beige–brown shaded contours), compared to the base case (red contours) without a boost. In figure C.4 we show the full corner plot, including all parameters specified in eq. (11.9), for the standard RSD analysis (blue contours) and also including gravitational redshift (red contours). Finally, in figure C.3 we show the constraints around the modified gravity fiducial model MGII. The contours are very similar to those obtained around ΛCDM, see figure 11.2.

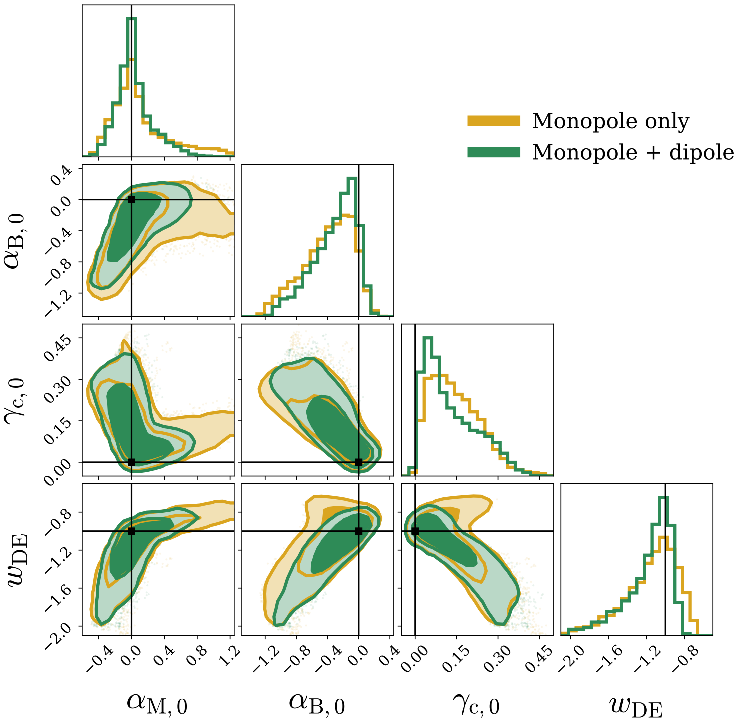

Figure C.1: Constraints around the ΛCDM fiducial when including only the monopole, and combining monopole and dipole.

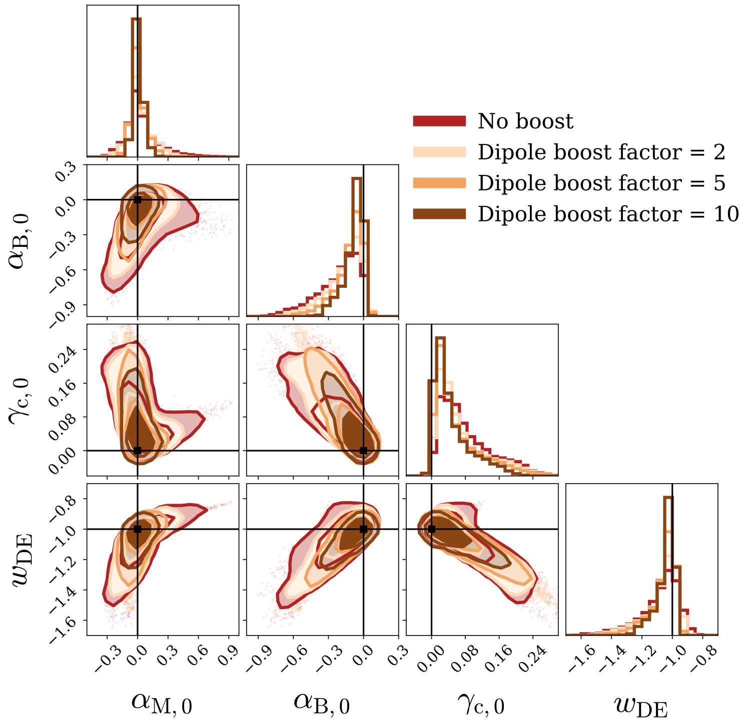

Figure C.2: Constraints around the ΛCDM fiducial when including all multipoles and applying various boost factors to the dipole.

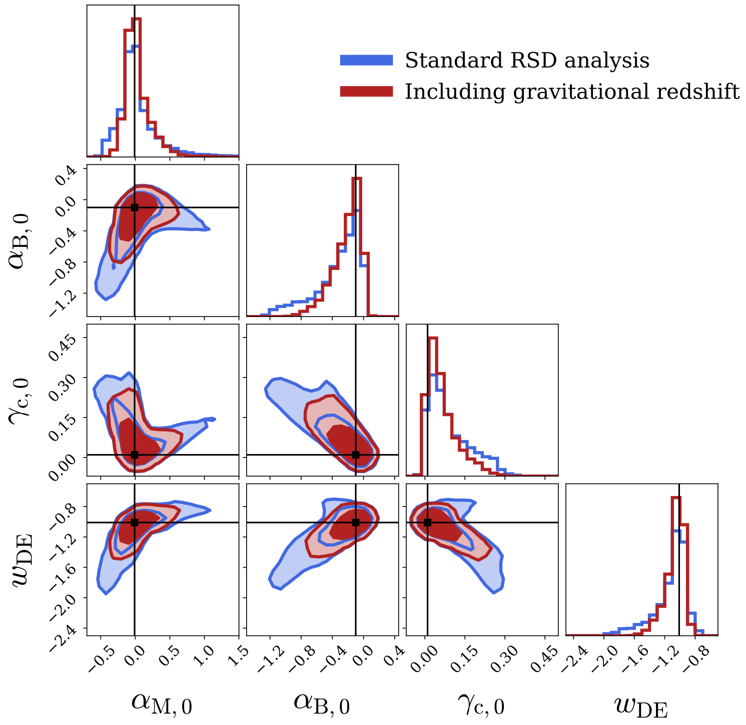

Figure C.3: Constraints around the modified gravity fiducial MGII. The constraints are very similar to those around ΛCDM, see figure 11.2

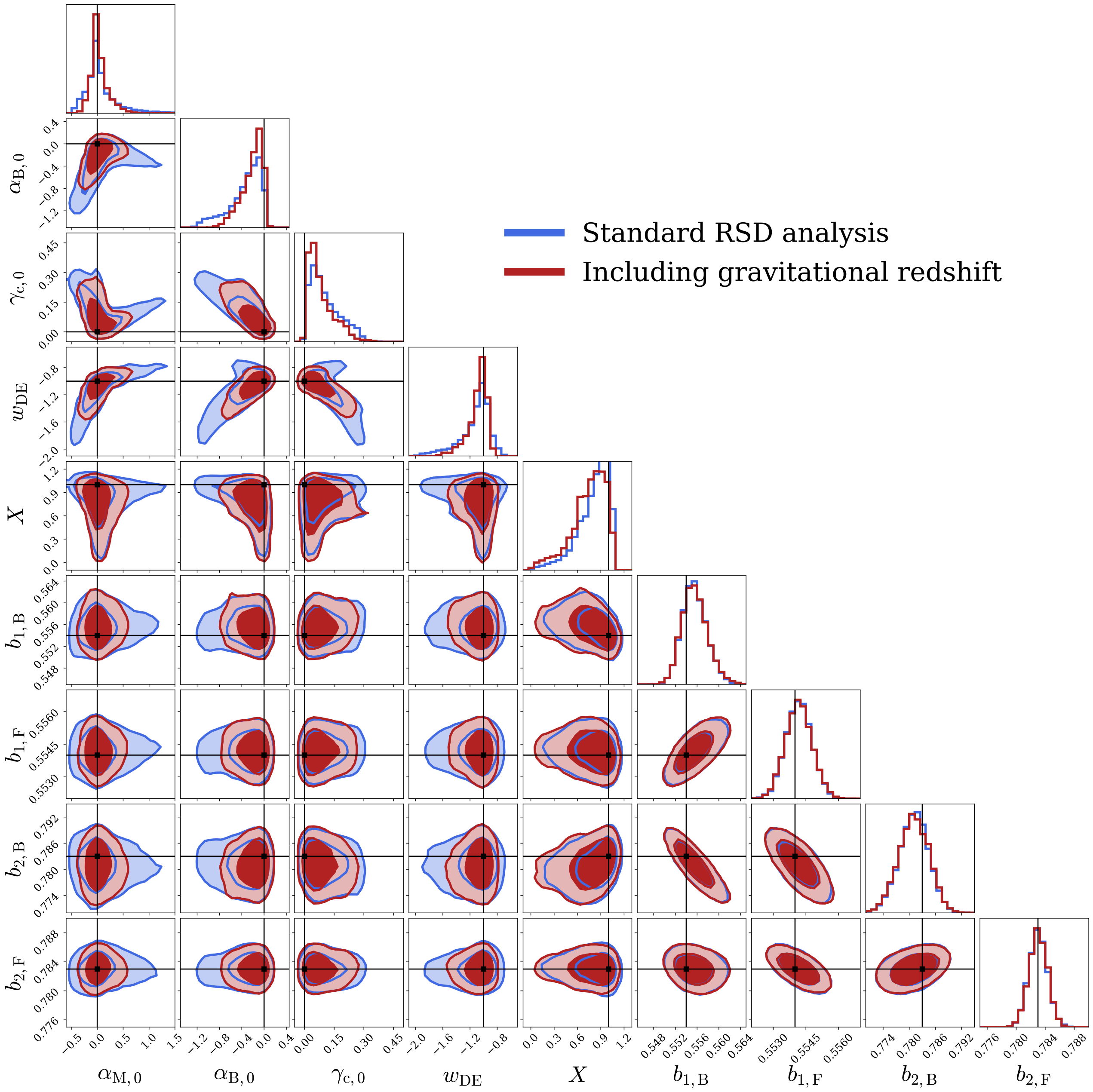

Figure C.4: Constraints around a ΛCDM fiducial for the full parameter space.

D

CONSTRAINING THE EVOLUTION AND MAGNIFICATION BIASES

D.1 MODELING THE SHOT-NOISE FOR OVERLAPPING POPULATIONS

In this Appendix, we introduce a model describing the shot-noise contributions due to the overlap between two populations of galaxies. One usually assumes that, once the population is split into B and F galaxies, the populations are independent and therefore there is no shot noise contribution in the cross-correlation. This is appropriate for a single split, but it is inconsistent when combining two splits with two different values m and m' into the same analysis pipeline. In this case, there is automatically an overlap between the populations of the two different splits, as depicted in fig. D.1. This leads to a non-zero shot noise contribution between the splits.

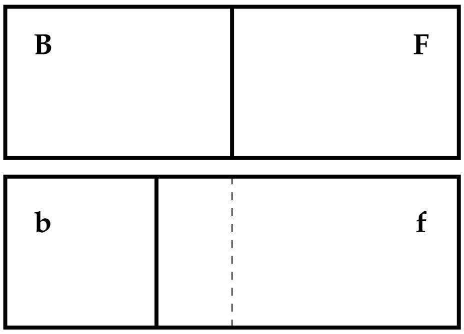

Figure D.1: Schematic representation of the overlap between two different splits. In the m split we have more bright galaxies than in the m' split, implying that some of the bright galaxies in the former are actually faint galaxies in the second case.

Let us denote by B and F the bright and faint samples of the first split m, and by b and f those of the second split m'. From fig. D.1 we see that some of the B galaxies are the same as some of the f galaxies. Moreover, all b galaxies are included in the B sample and all F galaxies are included in the f sample. Mathematically speaking, we can generally define the number density of each population of the m' split as

$$\bar{n}_\mathrm{b} = \theta_\mathrm{Bb}\, \bar{n}_\mathrm{B} + \theta_\mathrm{Fb}\, \bar{n}_\mathrm{F}, \tag{D.1}$$

$$\bar{n}_\mathrm{f} = \theta_\mathrm{Bf}\, \bar{n}_\mathrm{B} + \theta_\mathrm{Ff}\, \bar{n}_\mathrm{F}, \tag{D.2}$$

where the θ parameters are numbers between 0 and 1 quantifying the overlap between the populations of each split. We need to find the specific values for each m and m' sub-samples combinations. In particular, for the case of a joint analysis combining the 50×50 split with the 30×70 split, we find:

$$\theta_\mathrm{Bb} = \frac{3}{5}, \quad \theta_\mathrm{Fb} = 0, \quad \theta_\mathrm{Bf} = \frac{2}{5}, \quad \theta_\mathrm{Ff} = 1. \tag{D.3}$$

We immediately note that there is no overlap between the b and the F populations.

In general, the fluctuations in the galaxy number count cross-correlations between the populations of each split have the form

$$\langle \Delta_{\mathrm{L}}(x_i)\, \Delta_\lambda(x_j) \rangle = C_{ij}^{\mathrm{L}\lambda} + \frac{\theta_{\mathrm{L}\lambda}}{\bar{n}_\lambda}\, \delta_{ij}, \tag{D.4}$$

where L, λ label the galaxies luminosities in each split and i, j label the pixel sky positions. We have denoted by $\bar{n}_\lambda$ the background number density. The first term represents the cosmic variance contribution, which is non-zero even if the populations do not overlap, since they trace the same underlying matter density field. The second term encodes the shot-noise contribution, which depends directly on the overlapping faction $\theta_{\mathrm{L}\lambda}$: the less the populations overlap with each other, the smaller the shot-noise contribution is.

Considering two multipoles of orders ℓ and ℓ', the $m \times m'$ cross-variances will have the form

$$\mathrm{COV}\left(\xi_{\mathrm{LK}}^{(\ell)}(z,d),\, \xi_{\lambda\kappa}^{(\ell')}(z,d')\right) = \mathrm{COV}_{\mathrm{CC}} + \mathrm{COV}_{\mathrm{CP}} + \mathrm{COV}_{\mathrm{P}}\,, \tag{D.5}$$

where L,K $\in \{\mathrm{B},\mathrm{F}\}$ and $\lambda, \kappa \in \{\mathrm{b},\mathrm{f}\}$. The last term contains the pure shot-noise contributions. For the dipole and octupole, the only non-vanishing contribution is when $\mathrm{L}, K = \mathrm{B}, \mathrm{F}$ and $\lambda, \kappa = \mathrm{b}, f$ (in all other cases, the signal itself vanishes) and it reads

$$\mathrm{COV}_{\mathrm{P}}\left(\xi_{\mathrm{BF}}^{(\ell)}(z,d),\, \xi_{\mathrm{bf}}^{(\ell')}(z,d')\right) = \frac{2\ell+1}{4\pi\, V \bar{N}_{tot}^2 l_{\mathrm{p}}} \frac{\delta_{d\,d'}\, \delta_{\ell\ell'}}{d^2} \frac{\theta_{\mathrm{Bb}}\, \theta_{\mathrm{Ff}}}{q_{\mathrm{b}}\, q_{\mathrm{f}}} \quad \text{for} \quad \ell, \ell' = 1, 3\,. \tag{D.6}$$

For the even multipoles however, there are also other non-vanishing correlations and one obtains

$$\mathrm{COV}_{\mathrm{P}}\left(\xi_{\mathrm{LK}}^{(\ell)}(z,d),\, \xi_{\lambda\kappa}^{(\ell')}(z,d')\right) = \frac{2\ell+1}{4\pi\, V \bar{N}_{tot}^2 l_{\mathrm{p}}} \frac{\delta_{d\,d'}\, \delta_{\ell\ell'}}{d^2} \frac{1}{q_\lambda\, q_\kappa} \left(\theta_{\mathrm{L}\lambda}\, \theta_{\mathrm{K}\kappa} + \theta_{\mathrm{L}\kappa}\, \theta_{\mathrm{K}\lambda}\right) \tag{D.7}$$
$$\text{for} \quad \ell, \ell' = 0, 2, 4 \quad \text{and} \quad \mathrm{L}, \mathrm{K} \in \{\mathrm{B}, \mathrm{F}\}, \lambda, \kappa \in \{\mathrm{b}, \mathrm{f}\}\,.$$

Here V is the total volume of the survey, $\bar{N}_{tot}$ is the background total number density of galaxies, l_{p} is the pixel size and $q_\lambda = \bar{N}_\lambda / \bar{N}_g$ the fraction of galaxies of each type. In addition, there are also non-zero mixed (CP) contributions:

$$\begin{aligned}
\mathrm{COV}_{\mathrm{CP}}(\xi_{\mathrm{LK}}^{(\ell)}(z,d),\, \xi_{\lambda\kappa}^{(\ell')}(z,d')) &= \left(\frac{D_1(z)}{D_1(0)}\right)^2 \frac{1}{V \bar{N}_{tot}} (-1)^{\frac{\ell-\ell'}{2}} (-1)^{\ell+\ell'} \\
&\times \frac{1}{8} \sum_a \left[\frac{\theta_{\mathrm{K}\kappa}}{q_\kappa}\, \mathcal{C}_a^{\mathrm{ST}}(\mathrm{L}, \lambda) + (-1)^{\ell+\ell'} \frac{\theta_{\mathrm{L}\lambda}}{q_\lambda}\, \mathcal{C}_a^{\mathrm{ST}}(\mathrm{K}, \kappa) \right. \\
&\qquad \left. + (-1)^{\ell'} \left(\frac{\theta_{\mathrm{K}\lambda}}{q_\lambda}\, \mathcal{C}_a^{\mathrm{ST}}(\mathrm{L}, \kappa) + (-1)^{\ell+\ell'} \frac{\theta_{\mathrm{L}\kappa}}{q_\kappa}\, \mathcal{C}_a^{\mathrm{ST}}(\mathrm{K}, \lambda) \right) \right] \\
&\times \mathcal{G}(\ell, \ell', a)\, \mathcal{I}(\ell, \ell', d, d')\,,
\end{aligned} \tag{D.8}$$

where $D_1(z)$ is the growth function at redshift z and the index a runs over the values 0, 2, 4. We have previously defined the set of $\mathcal{C}_a^{\mathrm{ST}}(\mathrm{L}, \mathrm{M})$ functions of the growth rate and the galaxy biases in eqs.(2.89)-(2.91). In addition, we also have

$$\mathcal{G}(\ell, \ell', a) = \int_{-1}^{1} d\mu\, P_\ell(\mu)\, P_{\ell'}(\mu)\, P_a(\mu)\,, \tag{D.9}$$

where $\mu = \mathbf{k} \cdot \mathbf{n} = \cos\beta$ is the angle formed by the direction of the incoming photons and the orientation of a pair of galaxies. Finally, we have the Fourier-Bessel transformations of the power spectrum at $z = 0$

$$\mathcal{I}(\ell, \ell', d, d') = \frac{2(2\ell+1)(2\ell'+1)}{\pi^2} \int dk\, k^2\, P_{\delta\delta}(k, z=0)\, j_\ell(kd)\, j_{\ell'}(kd')\,. \tag{D.10}$$

Finally, in order to compute the CC contributions, we can use the usual expressions, replacing the corresponding values for the galaxy biases of each m, m' sample [48, 69]. The pure relativistic contributions to the cosmic variance relevant to the dipole and octupole covariances have been computed in [39] and are also taken into account in this work.

D.2 COVARIANCES INVOLVING THE HEXADECAPOLE OF THE FULL POPULATION

The hexadecapole of the 2-point correlation function is independent of the galaxy bias (see eq. (5.8)) and it is therefore the same for each of the populations. As a consequence we only consider the hexadecapole of the whole population in our analysis. Since the whole population overlaps with the B and F populations, there is a non-zero shot noise contribution in the covariance of the hexadecapole with the monopole and quadrupole of the B and F populations. This can be computed using the formalism described in Appendix D.2, where we cross-correlate three populations instead of four (as in fig. D.1). In this case, we have

$$\bar{n}_{\mathrm{T}} = \theta_{\mathrm{TB}}\, \bar{n}_{\mathrm{B}} + \theta_{\mathrm{TF}}\, \bar{n}_{\mathrm{F}}, \tag{D.11}$$

where $\theta_{\mathrm{TB}} = \theta_{\mathrm{TF}} = 1$. The expressions are formally the same as Eqs. (D.7)–(D.8). We use b_{B}, b_{F} for the monopoles and quadrupoles ($\ell = 0$, 2) and b_{T} for the hexadecapole ($\ell' = 4$). In this case the P and CP contributions are only sensitive to the total number density of galaxies, since the overlap of the B and F populations with the full population is total.

D.3 ADDITIONAL PLOTS AND TABLES

In this Appendix, we provide additional figures and tables associated with the discussion and results developed in this work.

In Table D.1 we show the cumulative SNR over all redshifts and separations for each of the multipoles and three different values of the sample separation parameter, $m = 10/3$, 2.0, $10/7$.

Tables D.2 and D.3 contain the fiducial values for all free parameters considered in the analyses. In Table D.2 we show the parameters that differ for each splits, whereas in Table D.3 we show the parameters that do not depend on the split.

In Table D.4 we show the constraints on the various parameters starting with a 20% prior, for three different splits.

In Table D.5 we show the constraints on the cosmic parameters. In Table D.6 we show the constraints on galaxy bias parameteres and evaluate the impact of the odd multipoles on the resulting constraints. We compare two splits with the joint analysis in both cases.

Finally, we include additional plots showing the redshift evolution of the parameters (s_B, s_M, n^evol) and the inferred quantities (s_F, $f_\mathrm{B}^\mathrm{evol}$, $f_\mathrm{F}^\mathrm{evol}$), together with the predicted 68% confidence regions. In fig. D.2 we show the results for the 50×50 split when assuming a 20% prior. In fig. D.3 we show the predictions for the 30×70 split when assuming a 50% prior.

	$\xi_\mathrm{BB}^{(0)}$	$\xi_\mathrm{BF}^{(0)}$	$\xi_\mathrm{FF}^{(0)}$	$\xi_\mathrm{BF}^{(1)}$	$\xi_\mathrm{BB}^{(2)}$	$\xi_\mathrm{BF}^{(2)}$	$\xi_\mathrm{FF}^{(2)}$	$\xi_\mathrm{BF}^{(3)}$	$\xi_\mathrm{T}^{(4)}$
30×70	457.07	474.80	422.31	62.32	313.42	479.35	546.15	7.33	
50×50	521.12	426.13	301.99	55.47	391.46	522.47	489.21	4.78	74.50
70×30	671.17	571.24	395.93	51.87	497.11	601.89	543.65	6.45	

Table D.1: Cumulative SNR over all redshifts and separations for the multipoles considered in the analysis. We show the SNR for three different splits. For the hexadecapole we show only one value corresponding to the whole population.

	30×70	50×50	70×30
$s_{0,\mathrm{B}}$	0.3252	-0.9011	-0.9337
$s_{1,\mathrm{B}}$	0.6442	1.8230	1.8243
$s_{2,\mathrm{B}}$	0.1614	-1.0188	-0.9284
$s_{3,\mathrm{B}}$	0.1333	-0.3034	-0.2410

Table D.2: Summary of the fiducial values of the $s_B(z)$ fitting parameters. These are generally different for different population splittings.

$s_{0,\mathrm{M}}$	-0.1938
$s_{1,\mathrm{M}}$	1.0747
$s_{2,\mathrm{M}}$	-0.0781
$s_{3,\mathrm{M}}$	-0.0056
n_0^{evol}	7.9460
n_1^{evol}	-12.0375
n_2^{evol}	2.2993
n_3^{evol}	-15.8389
c_{B}	0.5540
d_{B}	0.7830
c_{F}	0.5540
d_{F}	0.7830
h	0.6766
$\tilde{A}_s$	3.0204
n_s	0.9665
Ω_{b}	0.0490
Ω_{m}	0.3111

Table D.3: Summary of the fiducial values for the parameters varied in the analyses that are common to any splitting. We have defined $\tilde{A}_s = \ln\left(10^{10} As\right)$ for simplicity.

	50 × 50 split		30 × 70 split		70 × 30 split	
	$\xi_{\rm BF}^{(1)}$	$\xi_{\rm BF}^{(1)} + \xi_{\rm BF}^{(3)}$	$\xi_{\rm BF}^{(1)}$	$\xi_{\rm BF}^{(1)} + \xi_{\rm BF}^{(3)}$	$\xi_{\rm BF}^{(1)}$	$\xi_{\rm BF}^{(1)} + \xi_{\rm BF}^{(3)}$
$s_{\rm B,0}$	15.03	13.83	17.45	16.25	12.50	11.71
$s_{\rm B,1}$	10.36	9.69	17.60	16.93	9.28	8.95
$s_{\rm B,2}$	10.72	10.60	17.93	17.73	10.49	10.33
$s_{\rm B,3}$	11.98	11.20	12.36	11.75	13.11	12.60
$s_{\rm M,0}$	19.18	17.16	19.31	17.47	18.51	16.29
$s_{\rm M,1}$	14.39	13.16	8.86	8.37	14.73	13.89
$s_{\rm M,2}$	19.73	18.81	19.83	19.29	19.28	17.76
$s_{\rm M,3}$	19.99	19.99	19.99	19.99	19.98	19.96
$n_0^{\rm evol}$	18.03	17.17	16.85	16.65	18.63	17.35
$n_1^{\rm evol}$	18.42	15.00	16.62	14.49	19.36	16.14
$n_2^{\rm evol}$	16.48	14.42	14.73	13.45	15.49	14.45
$n_3^{\rm evol}$	14.31	13.92	13.44	13.29	15.52	14.55

Table D.4: Relative 1σ uncertainties for the magnification biases and number evolution parameters, assuming 20% Gaussian priors. We show the results for 3 different splits, including only the dipole (ξ_1) and including both the dipole and octupole ($\xi_1 + \xi_3$). In all cases the even multipoles (monopole, quadrupole and hexadecapole) are included.

	50×50	30×70	Joint	$\Delta_{m=2}(\%)$	$\Delta_{m=10/3}(\%)$
h	1.1045	1.0767	1.0536	**4.61**	**2.15**
$\ln\left(10^{10} A_{\mathrm{s}}\right)$	0.7080	0.6890	0.6710	**5.23**	**2.61**
n_{s}	0.9005	0.8715	0.8449	**6.18**	**3.05**
Ω_{b}	1.1296	1.1103	1.0928	**3.26**	**1.58**
Ω_{m}	0.4963	0.4793	0.4662	**6.05**	**2.74**

Table D.5: Relative 1σ uncertainties for the cosmic parameters. We show the results for two individual splits and for the joint analysis. The bold numbers show the relative improvement with respect to a single split.

Using all the multipoles

	50×50	Joint	$\Delta_{m=2}(\%)$	30×70	Joint	$\Delta_{m=10/3}(\%)$
c_{B}	0.4275	0.3929	**8.08**	0.5197	0.5011	**3.58**
d_{B}	0.3683	0.3551	**3.60**	0.4353	0.4277	**1.76**
c_{F}	0.1415	0.1280	**9.50**	0.1566	0.1490	**4.83**
d_{F}	0.2789	0.2671	**4.22**	0.2655	0.2608	**1.78**

Using only even multipoles

	50×50	Joint	$\Delta_{m=2}(\%)$	30×70	Joint	$\Delta_{m=10/3}(\%)$
c_{B}	0.4279	0.3934	**8.06**	0.5204	0.5018	**3.58**
d_{B}	0.3685	0.3553	**3.57**	0.4355	0.4278	**1.75**
c_{F}	0.1415	0.1281	**9.50**	0.1566	0.1491	**4.82**
d_{F}	0.2793	0.2677	**4.16**	0.2661	0.2614	**1.79**

Table D.6: Relative 1σ constraints on the galaxy bias parameters of each population. We show the results of the analysis using the full set of multipoles (above) and the analysis using only the even multipoles (below) for each of the splits and the joint analysis. Bold numbers represent the relative improvement found by the joint analysis with respect to the independent splits cases.

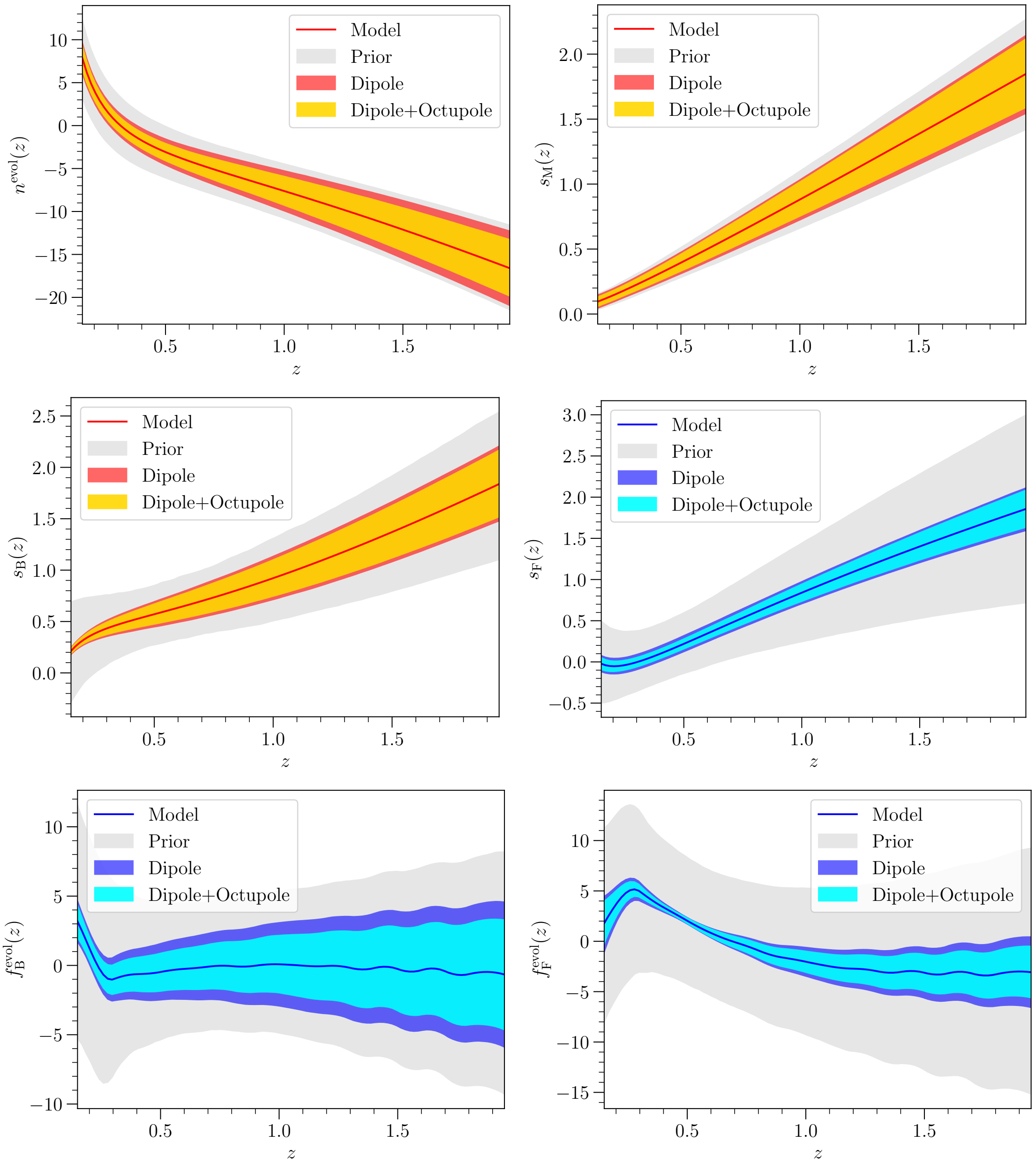

Figure D.2: Constraints on the redshift evolution of the various functions for the 50 × 50 split, starting with a 20% priors on the parameters. We show the results when only the dipole is used and when both the dipole and octupole are included.

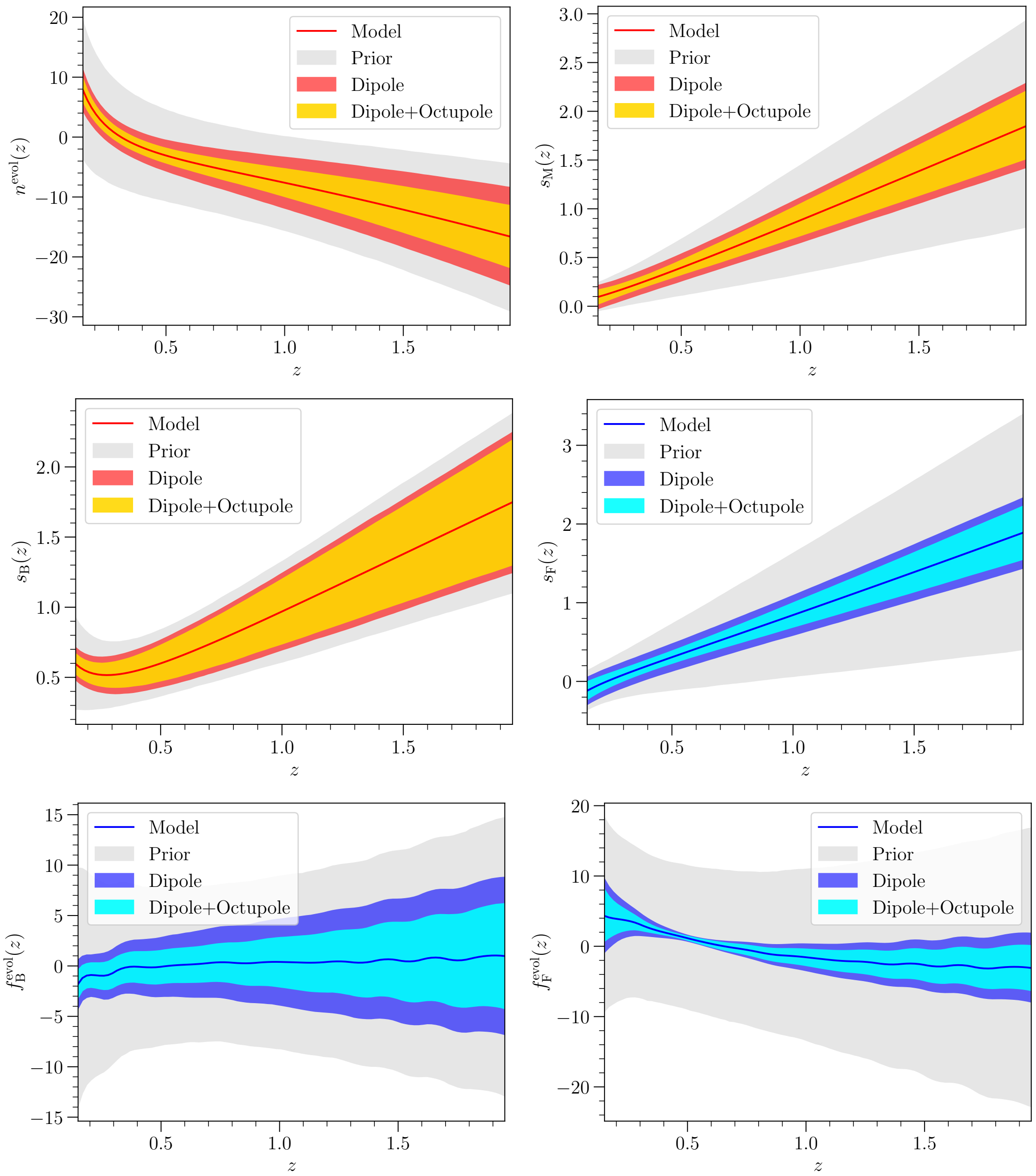

Figure D.3: Constraints on the redshift evolution of the various functions for the 30 × 70 split, starting with a 50% priors on the parameters. We show the results when only the dipole is used and when both the dipole and octupole are included.

BIBLIOGRAPHY

[1] Scott Dodelson. *Modern Cosmology*. Amsterdam: Academic Press, 2003. ISBN: 978-0-12-219141-1.

[2] Ruth Durrer. *The Cosmic Microwave Background*. Cambridge University Press, Dec. 2020. ISBN: 978-1-316-47152-4, 978-1-107-13522-2. DOI: 10.1017/9781316471524.

[3] Ruth Durrer. «Gauge invariant cosmological perturbation theory: A General study and its application to the texture scenario of structure formation.» In: *Fund. Cosmic Phys.* 15 (1994), pp. 209–339. arXiv: astro-ph/9311041.

[4] James M. Bardeen. «Gauge Invariant Cosmological Perturbations.» In: *Phys. Rev. D* 22 (1980), pp. 1882–1905. DOI: 10.1103/PhysRevD.22.1882.

[5] Camille Bonvin and Ruth Durrer. «What galaxy surveys really measure.» In: *Phys. Rev.* D84 (2011), p. 063505. DOI: 10.1103/PhysRevD.84.063505. arXiv: 1105.5280 [astro-ph.CO].

[6] N. Aghanim et al. «Planck 2018 results. VI. Cosmological parameters.» In: *Astron. Astrophys.* 641 (2020). [Erratum: Astron.Astrophys. 652, C4 (2021)], A6. DOI: 10.1051/0004-6361/201833910. arXiv: 1807.06209 [astro-ph.CO].

[7] Camille Bonvin. «Isolating relativistic effects in large-scale structure.» In: *Class. Quant. Grav.* 31.23 (2014), p. 234002. DOI: 10.1088/0264-9381/31/23/234002. arXiv: 1409.2224 [astro-ph.CO].

[8] Jaiyul Yoo, A. Liam Fitzpatrick, and Matias Zaldarriaga. «A New Perspective on Galaxy Clustering as a Cosmological Probe: General Relativistic Effects.» In: *Phys. Rev.* D80 (2009), p. 083514. DOI: 10.1103/PhysRevD.80.083514. arXiv: 0907.0707 [astro-ph.CO].

[9] Jaiyul Yoo. «General Relativistic Description of the Observed Galaxy Power Spectrum: Do We Understand What We Measure?» In: *Phys. Rev. D* 82 (2010), p. 083508. DOI: 10.1103/PhysRevD.82.083508. arXiv: 1009.3021 [astro-ph.CO].

[10] Anthony Challinor and Antony Lewis. «The linear power spectrum of observed source number counts.» In: *Phys. Rev.* D84 (2011), p. 043516. DOI: 10.1103/PhysRevD.84.043516. arXiv: 1105.5292 [astro-ph.CO].

[11] Donghui Jeong, Fabian Schmidt, and Christopher M. Hirata. «Large-scale clustering of galaxies in general relativity.» In: *Phys. Rev. D* 85 (2012), p. 023504. DOI: 10.1103/PhysRevD.85.023504. arXiv: 1107.5427 [astro-ph.CO].

[12] Jaiyul Yoo, Nico Hamaus, Uros Seljak, and Matias Zaldarriaga. «Going beyond the Kaiser redshift-space distortion formula: a full general relativistic account of the effects and their detectability in galaxy clustering.» In: *Phys. Rev.* D86 (2012), p. 063514. DOI: 10.1103/PhysRevD.86.063514. arXiv: 1206.5809 [astro-ph.CO].

[13] Jaiyul Yoo. «Relativistic effect in galaxy clustering.» In: *Classical and Quantum Gravity* 31.23, 234001 (Dec. 2014), p. 234001. DOI: 10.1088/0264-9381/31/23/234001. arXiv: 1409.3223 [astro-ph.CO].

[14] N. Kaiser. «Clustering in real space and in redshift space.» In: *Mon. Not. Roy. Astron. Soc.* 227 (1987), pp. 1–27.

[15] A. J. S. Hamilton. «Linear redshift distortions: A Review.» In: *Ringberg Workshop on Large Scale Structure Ringberg, Germany, September 23-28, 1996*. 1997. DOI: 10.1007/978-94-011-4960-0_17. arXiv: astro-ph/9708102 [astro-ph].

[16] P. J. E. Peebles and J. T. Yu. «Primeval adiabatic perturbation in an expanding universe.» In: *Astrophys. J.* 162 (1970), pp. 815–836. DOI: 10.1086/150713.

[17] Wayne Hu and Naoshi Sugiyama. «Small scale cosmological perturbations: An Analytic approach.» In: *Astrophys. J.* 471 (1996), pp. 542–570. DOI: 10.1086/177989. arXiv: astro-ph/9510117.

[18] Kyle S. Dawson et al. «The Baryon Oscillation Spectroscopic Survey of SDSS-III.» In: *Astron. J.* 145 (2013), p. 10. DOI: 10.1088/0004-6256/145/1/10. arXiv: 1208.0022 [astro-ph.CO].

[19] Shadab Alam et al. «The clustering of galaxies in the completed SDSS-III Baryon Oscillation Spectroscopic Survey. Cosmological analysis of the DR12 galaxy sample.» In: *Mon. Not. Roy. Astron. Soc.* 470.3 (2017), pp. 2617–2652. DOI: 10.1093/mnras/stx721. arXiv: 1607.03155 [astro-ph.CO].

[20] M. T. Soumagnac, R. Barkana, C. G. Sabiu, A. Loeb, A. J. Ross, F. B. Abdalla, S. T. Balan, and O. Lahav. «Large-Scale Distribution of Total Mass versus Luminous Matter from Baryon Acoustic Oscillations: First Search in the Sloan Digital Sky Survey III Baryon Oscillation Spectroscopic Survey Data Release 10.» In: *Phys. Rev. Lett.* 116.20 (2016), p. 201302. DOI: 10.1103/PhysRevLett.116.201302. arXiv: 1602.01839 [astro-ph.CO].

[21] T. M. C. Abbott et al. «Dark Energy Survey Year 1 Results: Measurement of the Baryon Acoustic Oscillation scale in the distribution of galaxies to redshift 1.» In: *Mon. Not. Roy. Astron. Soc.* 483.4 (2019), pp. 4866–4883. DOI: 10.1093/mnras/sty3351. arXiv: 1712.06209 [astro-ph.CO].

[22] T. M. C. Abbott et al. «Dark Energy Survey: A 2.1% measurement of the angular Baryonic Acoustic Oscillation scale at redshift z_{eff}=0.85 from the final dataset.» In: (Feb. 2024). arXiv: 2402.10696 [astro-ph.CO].

[23] Cullan Howlett, Ashley Ross, Lado Samushia, Will Percival, and Marc Manera. «The clustering of the SDSS main galaxy sample – II. Mock galaxy catalogues and a measurement of the growth of structure from redshift space distortions at $z = 0.15$.» In: *MNRAS* 449.1 (2015), pp. 848–866. DOI: 10.1093/mnras/stu2693. arXiv: 1409.3238 [astro-ph.CO].

[24] Camille Bonvin, Lam Hui, and Enrique Gaztanaga. «Asymmetric galaxy correlation functions.» In: *Phys. Rev. D* 89.8 (2014), p. 083535. DOI: 10.1103/PhysRevD.89.083535. arXiv: 1309.1321 [astro-ph.CO].

[25] Ryan Scranton et al. «Detection of cosmic magnification with the Sloan Digital Sky Survey.» In: *Astrophys. J.* 633 (2005), pp. 589–602. DOI: 10.1086/431358. arXiv: astro-ph/0504510.

[26] M. Garcia-Fernandez et al. «Weak lensing magnification in the Dark Energy Survey Science Verification Data.» In: *Mon. Not. Roy. Astron. Soc.* 476.1 (2018), pp. 1071–1085. DOI: 10.1093/mnras/sty282. arXiv: 1611.10326 [astro-ph.CO].

[27] Goran Jelic-Cizmek, Francesca Lepori, Camille Bonvin, and Ruth Durrer. «On the importance of lensing for galaxy clustering in photometric and spectroscopic surveys.» In: (2020). arXiv: 2004.12981 [astro-ph.CO].

[28] Antony Lewis and Anthony Challinor. «Weak gravitational lensing of the CMB.» In: *Phys. Rept.* 429 (2006), pp. 1–65. DOI: 10.1016/j.physrep.2006.03.002. arXiv: astro-ph/0601594.

[29] N. Aghanim et al. «Planck 2018 results. VIII. Gravitational lensing.» In: *Astron. Astrophys.* 641 (2020), A8. DOI: 10.1051/0004-6361/201833886. arXiv: 1807.06210 [astro-ph.CO].

[30] Camille Bonvin. «Effect of Peculiar Motion in Weak Lensing.» In: *Phys. Rev. D* 78 (2008), p. 123530. DOI: 10.1103/PhysRevD.78.123530. arXiv: 0810.0180 [astro-ph].

[31] David J. Bacon, Sambatra Andrianomena, Chris Clarkson, Krzysztof Bolejko, and Roy Maartens. «Cosmology with Doppler Lensing.» In: *Mon. Not. Roy. Astron. Soc.* 443.3 (2014), pp. 1900–1915. DOI: 10.1093/mnras/stu1270. arXiv: 1401.3694 [astro-ph.CO].

[32] Jaiyul Yoo, Nastassia Grimm, Ermis Mitsou, Adam Amara, and Alexandre Refregier. «Gauge-Invariant Formalism of Cosmological Weak Lensing.» In: *JCAP* 04 (2018), p. 029. DOI: 10.1088/1475-7516/2018/04/029. arXiv: 1802.03403 [astro-ph.CO].

[33] Sambatra Andrianomena, Camille Bonvin, David Bacon, Philip Bull, Chris Clarkson, Roy Maartens, and Teboho Moloi. «Testing General Relativity with the Doppler magnification effect.» In: *Mon. Not. Roy. Astron. Soc.* 488.3 (2019), pp. 3759–3771. DOI: 10.1093/mnras/stz1905. arXiv: 1810.12793 [astro-ph.CO].

[34] Nastassia Grimm and Jaiyul Yoo. «General relativistic effects in weak lensing angular power spectra.» In: *Phys. Rev. D* 104.8 (2021), p. 083548. DOI: 10.1103/PhysRevD.104.083548. arXiv: 2012.06368 [astro-ph.CO].

[35] Roy Maartens, José Fonseca, Stefano Camera, Sheean Jolicoeur, Jan-Albert Viljoen, and Chris Clarkson. «Magnification and evolution biases in large-scale structure surveys.» In: *JCAP* 12.12 (2021), p. 009. DOI: 10.1088/1475-7516/2021/12/009. arXiv: 2107.13401 [astro-ph.CO].

[36] R. Moessner, B. Jain, and J. V. Villumsen. «The effect of weak lensing on the angular correlation function of faint galaxies.» In: *Mon. Not. Roy. Astron. Soc.* 294 (1998), p. 291. DOI: 10.1046/j.1365-8711.1998.01225.x. arXiv: astro-ph/9708271.

[37] Camille Bonvin, Ruth Durrer, and M. Alice Gasparini. «Fluctuations of the luminosity distance.» In: *Phys. Rev. D* 73 (2006). [Erratum: Phys.Rev.D 85, 029901 (2012)], p. 023523. DOI: 10.1103/PhysRevD.85.029901. arXiv: astro-ph/0511183.

[38] Stefano Camera, Mario G. Santos, and Roy Maartens. «Probing primordial non-Gaussianity with SKA galaxy redshift surveys: a fully relativistic analysis.» In: *Mon. Not. Roy. Astron. Soc.* 448.2 (2015). [Erratum: Mon. Not. Roy. Astron. Soc.467,no.2,1505(2017)], pp. 1035–1043. DOI: 10.1093/mnras/stv040,10.1093/mnras/stx159. arXiv: 1409.8286 [astro-ph.CO].

[39] Camille Bonvin, Francesca Lepori, Sebastian Schulz, Isaac Tutusaus, Julian Adamek, and Pablo Fosalba. «A case study for measuring the relativistic dipole of a galaxy cross-correlation with the Dark Energy Spectroscopic Instrument.» In: *Mon. Not. Roy. Astron. Soc.* 525.3 (2023), pp. 4611–4627. DOI: `10.1093/mnras/stad2567`. arXiv: `2306.04213 [astro-ph.CO]`.

[40] Stefano Zazzera, José Fonseca, Tessa Baker, and Chris Clarkson. «Magnification and evolution bias of transient sources: GWs and SNIa.» In: (Sept. 2023). arXiv: `2309.04391 [astro-ph.CO]`.

[41] Roman Scoccimarro, H. M. P. Couchman, and Joshua A. Frieman. «The Bispectrum as a Signature of Gravitational Instability in Redshift-Space.» In: *Astrophys. J.* 517 (1999), pp. 531–540. DOI: `10.1086/307220`. arXiv: `astro-ph/9808305`.

[42] Vittorio Tansella, Camille Bonvin, Ruth Durrer, Basundhara Ghosh, and Elena Sellentin. «The full-sky relativistic correlation function and power spectrum of galaxy number counts: I. Theoretical aspects.» In: (2017). arXiv: `1708.00492 [astro-ph.CO]`.

[43] Alexander S. Szalay, Takahiko Matsubara, and Stephen D. Landy. «Redshift space distortions of the correlation function in wide angle galaxy surveys.» In: *Astrophys. J. Lett.* 498 (1998), p. L1. DOI: `10.1086/311293`. arXiv: `astro-ph/9712007`.

[44] Daniele Bertacca, Roy Maartens, Alvise Raccanelli, and Chris Clarkson. «Beyond the plane-parallel and Newtonian approach: Wide-angle redshift distortions and convergence in general relativity.» In: *JCAP* 10 (2012), p. 025. DOI: `10.1088/1475-7516/2012/10/025`. arXiv: `1205.5221 [astro-ph.CO]`.

[45] J. E. Campagne, S. Plaszczynski, and J. Neveu. «The Galaxy Count Correlation Function in Redshift Space Revisited.» In: *Astrophys. J.* 845.1 (2017), p. 28. DOI: `10.3847/1538-4357/aa7cf8`. arXiv: `1703.02818 [astro-ph.CO]`.

[46] Vittorio Tansella, Goran Jelic-Cizmek, Camille Bonvin, and Ruth Durrer. «COFFE: a code for the full-sky relativistic galaxy correlation function.» In: *JCAP* 10 (2018), p. 032. DOI: `10.1088/1475-7516/2018/10/032`. arXiv: `1806.11090 [astro-ph.CO]`.

[47] Enrique Gaztanaga, Camille Bonvin, and Lam Hui. «Measurement of the dipole in the cross-correlation function of galaxies.» In: *JCAP* 01 (2017), p. 032. DOI: `10.1088/1475-7516/2017/01/032`. arXiv: `1512.03918 [astro-ph.CO]`.

[48] Camille Bonvin, Lam Hui, and Enrique Gaztanaga. «Optimising the measurement of relativistic distortions in large-scale structure.» In: *JCAP* 08 (2016), p. 021. DOI: `10.1088/1475-7516/2016/08/021`. arXiv: `1512.03566 [astro-ph.CO]`.

[49] Patrick McDonald. «Gravitational redshift and other redshift-space distortions of the imaginary part of the power spectrum.» In: *JCAP* 0911 (2009), p. 026. DOI: `10.1088/1475-7516/2009/11/026`. arXiv: `0907.5220 [astro-ph.CO]`.

[50] Rupert A. C. Croft. «Gravitational redshifts from large-scale structure.» In: *Mon. Not. Roy. Astron. Soc.* 434 (2013), pp. 3008–3017. DOI: `10.1093/mnras/stt1223`. arXiv: `1304.4124 [astro-ph.CO]`.

[51] Florian Beutler, Emanuele Castorina, and Pierre Zhang. «Interpreting measurements of the anisotropic galaxy power spectrum.» In: *JCAP* 03 (2019), p. 040. DOI: `10.1088/1475-7516/2019/03/040`. arXiv: `1810.05051 [astro-ph.CO]`.

[52] Paulo H. F. Reimberg, Francis Bernardeau, and Cyril Pitrou. «Redshift-space distortions with wide angular separations.» In: *JCAP* 01 (2016), p. 048. DOI: `10.1088/1475-7516/2016/01/048`. arXiv: `1506.06596 [astro-ph.CO]`.

[53] Basundhara Ghosh and Ruth Durrer. «The observable E_g statistics.» In: *JCAP* 06 (2019), p. 010. DOI: `10.1088/1475-7516/2019/06/010`. arXiv: `1812.09546 [astro-ph.CO]`.

[54] Camille Bonvin and Pierre Fleury. «Testing the equivalence principle on cosmological scales.» In: *JCAP* 1805.05 (2018), p. 061. DOI: `10.1088/1475-7516/2018/05/061`. arXiv: `1803.02771 [astro-ph.CO]`.

[55] D. Nelson Limber. «The Analysis of Counts of the Extragalactic Nebulae in Terms of a Fluctuating Density Field.» In: *APJ* 117 (1953), p. 134. DOI: `10.1086/145672`.

[56] Nick Kaiser. «Weak gravitational lensing of distant galaxies.» In: *Astrophys. J.* 388 (1992), p. 272. DOI: `10.1086/171151`.

[57] Nick Kaiser. «Weak lensing and cosmology.» In: *Astrophys. J.* 498 (1998), p. 26. DOI: `10.1086/305515`. arXiv: `astro-ph/9610120`.

[58] Marilena LoVerde and Niayesh Afshordi. «Extended Limber Approximation.» In: *Phys. Rev. D* 78 (2008), p. 123506. DOI: `10.1103/PhysRevD.78.123506`. arXiv: `0809.5112 [astro-ph]`.

[59] A. Blanchard et al. «Euclid preparation: VII. Forecast validation for Euclid cosmological probes.» In: *Astron. Astrophys.* 642 (2020), A191. DOI: `10.1051/0004-6361/202038071`. arXiv: `1910.09273 [astro-ph.CO]`.

[60] T. M. C. Abbott et al. «Dark Energy Survey year 1 results: Cosmological constraints from galaxy clustering and weak lensing.» In: *Phys. Rev. D* 98.4 (2018), p. 043526. DOI: `10.1103/PhysRevD.98.043526`. arXiv: `1708.01530 [astro-ph.CO]`.

[61] T. M. C. Abbott et al. «Dark Energy Survey Year 3 results: Cosmological constraints from galaxy clustering and weak lensing.» In: *Phys. Rev. D* 105.2 (2022), p. 023520. DOI: `10.1103/PhysRevD.105.023520`. arXiv: `2105.13549 [astro-ph.CO]`.

[62] K. Tanidis et al. «Euclid preparation - XXXIV. The effect of linear redshift-space distortions in photometric galaxy clustering and its cross-correlation with cosmic shear.» In: *Astron. Astrophys.* 683 (2024), A17. DOI: `10.1051/0004-6361/202347870`. arXiv: `2309.00052 [astro-ph.CO]`.

[63] T. M. C. Abbott et al. «Dark Energy Survey Year 3 results: Constraints on extensions to ΛCDM with weak lensing and galaxy clustering.» In: *Phys. Rev. D* 107.8 (2023), p. 083504. DOI: `10.1103/PhysRevD.107.083504`. arXiv: `2207.05766 [astro-ph.CO]`.

[64] J. Prat et al. «Dark Energy Survey year 1 results: Galaxy-galaxy lensing.» In: *Phys. Rev. D* 98.4 (2018), p. 042005. DOI: `10.1103/PhysRevD.98.042005`. arXiv: `1708.01537 [astro-ph.CO]`.

[65] Sarah Bridle and Lindsay King. «Dark energy constraints from cosmic shear power spectra: impact of intrinsic alignments on photometric redshift requirements.» In: *New J. Phys.* 9 (2007), p. 444. DOI: `10.1088/1367-2630/9/12/444`. arXiv: `0705.0166 [astro-ph]`.

[66] Donnacha Kirk, Anais Rassat, Ole Host, and Sarah Bridle. «The cosmological impact of intrinsic alignment model choice for cosmic shear.» In: *MNRAS* 424.3 (Aug. 2012), pp. 1647–1657. DOI: `10.1111/j.1365-2966.2012.21099.x`. arXiv: `1112.4752 [astro-ph.CO]`.

[67] Claire Lamman, Eleni Tsaprazi, Jingjing Shi, Nikolina Niko Šarčević, Susan Pyne, Elisa Legnani, and Tassia Ferreira. «The IA Guide: A Breakdown of Intrinsic Alignment Formalisms.» In: (Sept. 2023). DOI: `10.21105/astro.2309.08605`. arXiv: `2309.08605 [astro-ph.CO]`.

[68] Camille Bonvin, Sambatra Andrianomena, David Bacon, Chris Clarkson, Roy Maartens, Teboho Moloi, and Philip Bull. «Dipolar modulation in the size of galaxies: The effect of Doppler magnification.» In: *Mon. Not. Roy. Astron. Soc.* 472.4 (2017), pp. 3936–3951. DOI: `10.1093/mnras/stx2049`. arXiv: `1610.05946 [astro-ph.CO]`.

[69] Alex Hall and Camille Bonvin. «Measuring cosmic velocities with 21 cm intensity mapping and galaxy redshift survey cross-correlation dipoles.» In: *Phys. Rev.* D95.4 (2017), p. 043530. DOI: `10.1103/PhysRevD.95.043530`. arXiv: `1609.09252 [astro-ph.CO]`.

[70] Gregory Walter Horndeski. «Second-order scalar-tensor field equations in a four-dimensional space.» In: *Int. J. Theor. Phys.* 10 (1974), pp. 363–384. DOI: `10.1007/BF01807638`.

[71] Pengjie Zhang, Michele Liguori, Rachel Bean, and Scott Dodelson. «Probing Gravity at Cosmological Scales by Measurements which Test the Relationship between Gravitational Lensing and Matter Overdensity.» In: *Phys. Rev. Lett.* 99 (2007), p. 141302. DOI: `10.1103/PhysRevLett.99.141302`. arXiv: `0704.1932 [astro-ph]`.

[72] Luca Amendola, Martin Kunz, Mariele Motta, Ippocratis D. Saltas, and Ignacy Sawicki. «Observables and unobservables in dark energy cosmologies.» In: *Phys. Rev. D* 87.2 (2013), p. 023501. DOI: `10.1103/PhysRevD.87.023501`. arXiv: `1210.0439 [astro-ph.CO]`.

[73] Paolo Creminelli, Jérôme Gleyzes, Lam Hui, Marko Simonović, and Filippo Vernizzi. «Single-Field Consistency Relations of Large Scale Structure. Part III: Test of the Equivalence Principle.» In: *JCAP* 1406 (2014), p. 009. DOI: `10.1088/1475-7516/2014/06/009`. arXiv: `1312.6074 [astro-ph.CO]`.

[74] Alexandros Kehagias, Jorge Noreña, Hideki Perrier, and Antonio Riotto. «Consequences of Symmetries and Consistency Relations in the Large-Scale Structure of the Universe for Non-local bias and Modified Gravity.» In: *Nucl. Phys. B* 883 (2014), pp. 83–106. DOI: `10.1016/j.nuclphysb.2014.03.020`. arXiv: `1311.0786 [astro-ph.CO]`.

[75] Mariele Motta, Ignacy Sawicki, Ippocratis D. Saltas, Luca Amendola, and Martin Kunz. «Probing Dark Energy through Scale Dependence.» In: *Phys. Rev. D* 88.12 (2013), p. 124035. DOI: `10.1103/PhysRevD.88.124035`. arXiv: `1305.0008 [astro-ph.CO]`.

[76] Felipe Oliveira Franco, Camille Bonvin, and Chris Clarkson. «A null test to probe the scale-dependence of the growth of structure as a test of General Relativity.» In: (2019). arXiv: `1906.02217 [astro-ph.CO]`.

[77] Camille Bonvin, Felipe Oliveira Franco, and Pierre Fleury. «A null test of the equivalence principle using relativistic effects in galaxy surveys.» In: *JCAP* 08 (2020), p. 004. DOI: 10.1088/1475-7516/2020/08/004. arXiv: 2004.06457 [astro-ph.CO].

[78] David Parkinson et al. «The WiggleZ Dark Energy Survey: Final data release and cosmological results.» In: *Phys. Rev. D* 86 (2012), p. 103518. DOI: 10.1103/PhysRevD.86.103518. arXiv: 1210.2130 [astro-ph.CO].

[79] Marika Asgari et al. «KiDS-1000 Cosmology: Cosmic shear constraints and comparison between two point statistics.» In: *Astron. Astrophys.* 645 (2021), A104. DOI: 10.1051/0004-6361/202039070. arXiv: 2007.15633 [astro-ph.CO].

[80] M. Gatti et al. «Dark Energy Survey Year 3 Results: Weak Lensing Shape Catalogue.» In: (2020). arXiv: 2011.03408 [astro-ph.CO].

[81] Blake D. Sherwin et al. «Two-season Atacama Cosmology Telescope polarimeter lensing power spectrum.» In: *Phys. Rev. D* 95.12 (2017), p. 123529. DOI: 10.1103/PhysRevD.95.123529. arXiv: 1611.09753 [astro-ph.CO].

[82] W. L. K. Wu et al. «A Measurement of the Cosmic Microwave Background Lensing Potential and Power Spectrum from 500 deg^2 of SPTpol Temperature and Polarization Data.» In: *Astrophys. J.* 884 (2019), p. 70. DOI: 10.3847/1538-4357/ab4186. arXiv: 1905.05777 [astro-ph.CO].

[83] M. A. O. Aguilar Faúndez et al. «Measurement of the Cosmic Microwave Background Polarization Lensing Power Spectrum from Two Years of POLARBEAR Data.» In: *Astrophys. J.* 893 (2020), p. 85. DOI: 10.3847/1538-4357/ab7e29. arXiv: 1911.10980 [astro-ph.CO].

[84] P. A. R. Ade et al. «Planck 2015 results. XXI. The integrated Sachs-Wolfe effect.» In: *Astron. Astrophys.* 594 (2016), A21. DOI: 10.1051/0004-6361/201525831. arXiv: 1502.01595 [astro-ph.CO].

[85] Luca Amendola, Simone Fogli, Alejandro Guarnizo, Martin Kunz, and Adrian Vollmer. «Model-independent constraints on the cosmological anisotropic stress.» In: *Phys. Rev. D* 89.6 (2014), p. 063538. DOI: 10.1103/PhysRevD.89.063538. arXiv: 1311.4765 [astro-ph.CO].

[86] Ana Marta Pinho, Santiago Casas, and Luca Amendola. «Model-independent reconstruction of the linear anisotropic stress η.» In: *JCAP* 11 (2018), p. 027. DOI: 10.1088/1475-7516/2018/11/027. arXiv: 1805.00027 [astro-ph.CO].

[87] Rubén Arjona and Savvas Nesseris. «Hints of dark energy anisotropic stress using Machine Learning.» In: *JCAP* 11 (2020), p. 042. DOI: 10.1088/1475-7516/2020/11/042. arXiv: 2001.11420 [astro-ph.CO].

[88] Julian Adamek, David Daverio, Ruth Durrer, and Martin Kunz. «gevolution: a cosmological N-body code based on General Relativity.» In: *JCAP* 07 (2016), p. 053. DOI: 10.1088/1475-7516/2016/07/053. arXiv: 1604.06065 [astro-ph.CO].

[89] Julian Adamek, Ruth Durrer, and Martin Kunz. «Relativistic N-body simulations with massive neutrinos.» In: *JCAP* 11 (2017), p. 004. DOI: 10.1088/1475-7516/2017/11/004. arXiv: 1707.06938 [astro-ph.CO].

[90] Ippocratis D. Saltas, Ignacy Sawicki, Luca Amendola, and Martin Kunz. «Anisotropic Stress as a Signature of Nonstandard Propagation of Gravitational Waves.» In: *Phys. Rev. Lett.* 113.19 (2014), p. 191101. DOI: `10.1103/PhysRevLett.113.191101`. arXiv: `1406.7139 [astro-ph.CO]`.

[91] Kazuya Koyama. «Cosmological Tests of Modified Gravity.» In: *Rept. Prog. Phys.* 79.4 (2016), p. 046902. DOI: `10.1088/0034-4885/79/4/046902`. arXiv: `1504.04623 [astro-ph.CO]`.

[92] Austin Joyce, Lucas Lombriser, and Fabian Schmidt. «Dark Energy Versus Modified Gravity.» In: *Ann. Rev. Nucl. Part. Sci.* 66 (2016), pp. 95–122. DOI: `10.1146/annurev-nucl-102115-044553`. arXiv: `1601.06133 [astro-ph.CO]`.

[93] Joshua A. Frieman and Ben-Ami Gradwohl. «Dark matter and the equivalence principle.» In: *Phys. Rev. Lett.* 67 (21 Nov. 1991), pp. 2926–2929. DOI: `10.1103/PhysRevLett.67.2926`. URL: `https://link.aps.org/doi/10.1103/PhysRevLett.67.2926`.

[94] Ben-Ami Gradwohl and Joshua A. Frieman. «Dark Matter, Long-Range Forces, and Large-Scale Structure.» In: *APJ* 398 (Oct. 1992), p. 407. DOI: `10.1086/171865`.

[95] Bruno J. Barros, Luca Amendola, Tiago Barreiro, and Nelson J. Nunes. «Coupled quintessence with a ΛCDM background: removing the σ_8 tension.» In: *JCAP* 01 (2019), p. 007. DOI: `10.1088/1475-7516/2019/01/007`. arXiv: `1802.09216 [astro-ph.CO]`.

[96] Mahnaz Asghari, Jose Beltrán Jiménez, Shahram Khosravi, and David F. Mota. «On structure formation from a small-scales-interacting dark sector.» In: *JCAP* 04 (2019), p. 042. DOI: `10.1088/1475-7516/2019/04/042`. arXiv: `1902.05532 [astro-ph.CO]`.

[97] Maria Archidiacono, Emanuele Castorina, Diego Redigolo, and Ennio Salvioni. «Unveiling dark fifth forces with linear cosmology.» In: (Apr. 2022). arXiv: `2204.08484 [astro-ph.CO]`.

[98] Jérôme Gleyzes, David Langlois, Michele Mancarella, and Filippo Vernizzi. «Effective Theory of Interacting Dark Energy.» In: *JCAP* 1508.08 (2015), p. 054. DOI: `10.1088/1475-7516/2015/08/054`. arXiv: `1504.05481 [astro-ph.CO]`.

[99] Jérôme Gleyzes, David Langlois, Michele Mancarella, and Filippo Vernizzi. «Effective Theory of Dark Energy at Redshift Survey Scales.» In: *JCAP* 1602.02 (2016), p. 056. DOI: `10.1088/1475-7516/2016/02/056`. arXiv: `1509.02191 [astro-ph.CO]`.

[100] Lam Hui, Alberto Nicolis, and Christopher Stubbs. «Equivalence Principle Implications of Modified Gravity Models.» In: *Phys. Rev. D* 80 (2009), p. 104002. DOI: `10.1103/PhysRevD.80.104002`. arXiv: `0905.2966 [astro-ph.CO]`.

[101] Shadab Alam et al. «Completed SDSS-IV extended Baryon Oscillation Spectroscopic Survey. Cosmological implications from two decades of spectroscopic surveys at the Apache Point Observatory.» In: *Phys. Rev. D* 103.8 (2021), p. 083533. DOI: `10.1103/PhysRevD.103.083533`. arXiv: `2007.08991 [astro-ph.CO]`.

[102] Yong-Seon Song, Gong-Bo Zhao, David Bacon, Kazuya Koyama, Robert C. Nichol, and Levon Pogosian. «Complementarity of Weak Lensing and Peculiar Velocity Measurements in Testing General Relativity.» In: *Phys. Rev. D* 84 (2011), p. 083523. DOI: `10.1103/PhysRevD.84.083523`. arXiv: `1011.2106 [astro-ph.CO]`.

[103] Sveva Castello, Nastassia Grimm, and Camille Bonvin. «Rescuing constraints on modified gravity using gravitational redshift in large-scale structure.» In: *Phys. Rev. D* 106.8 (2022), p. 083511. DOI: 10.1103/PhysRevD.106.083511. arXiv: 2204.11507 [astro-ph.CO].

[104] Camille Bonvin and Levon Pogosian. «Modified Einstein versus modified Euler for dark matter.» In: *Nature Astron.* 7.9 (2023), pp. 1127–1134. DOI: 10.1038/s41550-023-02003-y. arXiv: 2209.03614 [astro-ph.CO].

[105] Luca Amendola et al. «Cosmology and fundamental physics with the Euclid satellite.» In: *Living Rev. Rel.* 21.1 (2018), p. 2. DOI: 10.1007/s41114-017-0010-3. arXiv: 1606.00180 [astro-ph.CO].

[106] Yong-Seon Song, Lukas Hollenstein, Gabriela Caldera-Cabral, and Kazuya Koyama. «Theoretical Priors On Modified Growth Parametrisations.» In: *JCAP* 04 (2010), p. 018. DOI: 10.1088/1475-7516/2010/04/018. arXiv: 1001.0969 [astro-ph.CO].

[107] F. Köhlinger et al. «KiDS-450: The tomographic weak lensing power spectrum and constraints on cosmological parameters.» In: *Mon. Not. Roy. Astron. Soc.* 471.4 (2017), pp. 4412–4435. DOI: 10.1093/mnras/stx1820. arXiv: 1706.02892 [astro-ph.CO].

[108] B. P. Abbott et al. «GW170817: Observation of Gravitational Waves from a Binary Neutron Star Inspiral.» In: *Phys. Rev. Lett.* 119.16 (2017), p. 161101. DOI: 10.1103/PhysRevLett.119.161101. arXiv: 1710.05832 [gr-qc].

[109] Paolo Creminelli, Giovanni Tambalo, Filippo Vernizzi, and Vicharit Yingcharoenrat. «Dark-Energy Instabilities induced by Gravitational Waves.» In: *JCAP* 05 (2020), p. 002. DOI: 10.1088/1475-7516/2020/05/002. arXiv: 1910.14035 [gr-qc].

[110] Johannes Noller. «Cosmological constraints on dark energy in light of gravitational wave bounds.» In: *Phys. Rev. D* 101.6 (2020), p. 063524. DOI: 10.1103/PhysRevD.101.063524. arXiv: 2001.05469 [astro-ph.CO].

[111] Florian Beutler and Enea Di Dio. «Modeling relativistic contributions to the halo power spectrum dipole.» In: *JCAP* 07.07 (2020), p. 048. DOI: 10.1088/1475-7516/2020/07/048. arXiv: 2004.08014 [astro-ph.CO].

[112] Shohei Saga, Atsushi Taruya, Yann Rasera, and Michel-Andrès Breton. «Detectability of the gravitational redshift effect from the asymmetric galaxy clustering.» In: *Mon. Not. Roy. Astron. Soc.* 511.2 (2022), pp. 2732–2754. DOI: 10.1093/mnras/stac186. arXiv: 2109.06012 [astro-ph.CO].

[113] Albert Einstein. «The Foundation of the General Theory of Relativity.» In: *Annalen Phys.* 49.7 (1916). Ed. by Jong-Ping Hsu and D. Fine, pp. 769–822. DOI: 10.1002/andp.19163540702.

[114] R. V. Pound and J. L. Snider. «Effect of Gravity on Gamma Radiation.» In: *Phys. Rev.* 140 (3B Nov. 1965), B788–B803. DOI: 10.1103/PhysRev.140.B788. URL: https://link.aps.org/doi/10.1103/PhysRev.140.B788.

[115] R. F. C. Vessot et al. «Test of Relativistic Gravitation with a Space-Borne Hydrogen Maser.» In: *Phys. Rev. Lett.* 45 (26 Dec. 1980), pp. 2081–2084. DOI: 10.1103/PhysRevLett.45.2081. URL: https://link.aps.org/doi/10.1103/PhysRevLett.45.2081.

[116] W. S. Adams. «The relativity displacement of the spectral lines in the companion of Sirius.» In: *The Observatory* 48 (Nov. 1925), pp. 337–342.

[117] J. L. Greenstein and V. Trimble. «Gravitational redshifts of the white dwarfs.» In: *AJ* 72 (Apr. 1967), p. 301.

[118] Radoslaw Wojtak, Steen H. Hansen, and Jens Hjorth. «Gravitational redshift of galaxies in clusters as predicted by general relativity.» In: *Nature* 477 (2011), pp. 567–569. DOI: `10.1038/nature10445`. arXiv: `1109.6571 [astro-ph.CO]`.

[119] Iftach Sadeh, Low Lerh Feng, and Ofer Lahav. «Gravitational Redshift of Galaxies in Clusters from the Sloan Digital Sky Survey and the Baryon Oscillation Spectroscopic Survey.» In: *Phys. Rev. Lett.* 114.7 (2015), p. 071103. DOI: `10.1103/PhysRevLett.114.071103`. arXiv: `1410.5262 [astro-ph.CO]`.

[120] Shadab Alam et al. «Relativistic distortions in the large-scale clustering of SDSS-III BOSS CMASS galaxies.» In: *Mon. Not. Roy. Astron. Soc.* 470.3 (2017), pp. 2822–2833. DOI: `10.1093/mnras/stx1421`. arXiv: `1709.07855 [astro-ph.CO]`.

[121] Daniel Sobral-Blanco and Camille Bonvin. «Measuring anisotropic stress with relativistic effects.» In: *Phys. Rev. D* 104.6 (2021), p. 063516. DOI: `10.1103/PhysRevD.104.063516`. arXiv: `2102.05086 [astro-ph.CO]`.

[122] Daniel Sobral-Blanco and Camille Bonvin. «Measuring the distortion of time with relativistic effects in large-scale structure.» In: *MNRAS* 519.1 (2022), pp. L39–L44. DOI: `10.1093/mnrasl/slac124`. arXiv: `2205.02567 [astro-ph.CO]`.

[123] Isaac Tutusaus, Daniel Sobral-Blanco, and Camille Bonvin. «Combining gravitational lensing and gravitational redshift to measure the anisotropic stress with future galaxy surveys.» In: *Phys. Rev. D* 107.8 (2023), p. 083526. DOI: `10.1103/PhysRevD.107.083526`. arXiv: `2209.08987 [astro-ph.CO]`.

[124] Jeppe Trøst Nielsen and Ruth Durrer. «Higher order relativistic galaxy number counts: dominating terms.» In: *JCAP* 03 (2017), p. 010. DOI: `10.1088/1475-7516/2017/03/010`. arXiv: `1606.02113 [astro-ph.CO]`.

[125] HongSheng Zhao, John A. Peacock, and Baojiu Li. «Testing gravity theories via transverse Doppler and gravitational redshifts in galaxy clusters.» In: *Phys. Rev. D* 88.4 (2013), p. 043013. DOI: `10.1103/PhysRevD.88.043013`. arXiv: `1206.5032 [astro-ph.CO]`.

[126] Nick Kaiser. «Measuring Gravitational Redshifts in Galaxy Clusters.» In: *Mon. Not. Roy. Astron. Soc.* 435 (2013), p. 1278. DOI: `10.1093/mnras/stt1370`. arXiv: `1303.3663 [astro-ph.CO]`.

[127] Yan-Chuan Cai, Nick Kaiser, Shaun Cole, and Carlos Frenk. «Gravitational redshift and asymmetric redshift-space distortions for stacked clusters.» In: *Mon. Not. Roy. Astron. Soc.* 468.2 (2017), pp. 1981–1993. DOI: `10.1093/mnras/stx469`. arXiv: `1609.04864 [astro-ph.CO]`.

[128] Enea Di Dio, Francesco Montanari, Julien Lesgourgues, and Ruth Durrer. «The CLASSgal code for Relativistic Cosmological Large Scale Structure.» In: *JCAP* 11 (2013), p. 044. DOI: `10.1088/1475-7516/2013/11/044`. arXiv: `1307.1459 [astro-ph.CO]`.

[129] Basundhara Ghosh, Ruth Durrer, and Elena Sellentin. «General Relativistic corrections in density-shear correlations.» In: *JCAP* 06 (2018), p. 008. DOI: `10.1088/1475-7516/2018/06/008`. arXiv: `1801.02518 [astro-ph.CO]`.

[130] Yan-Chuan Cai and Gary Bernstein. «Combining weak-lensing tomography and spectroscopic redshift surveys.» In: *Monthly Notices of the Royal Astronomical Society* 422.2 (2012), 1045–1056. ISSN: 0035-8711. DOI: `10.1111/j.1365-2966.2012.20676.x`. URL: `http://dx.doi.org/10.1111/j.1365-2966.2012.20676.x`.

[131] Amir Aghamousa et al. «The DESI Experiment Part I: Science,Targeting, and Survey Design.» In: (2016). arXiv: `1611.00036 [astro-ph.IM]`.

[132] Arjun Dey et al. «Overview of the DESI Legacy Imaging Surveys.» In: *The Astronomical Journal* 157.5 (2019), p. 168. ISSN: 1538-3881. DOI: `10.3847/1538-3881/ab089d`. URL: `http://dx.doi.org/10.3847/1538-3881/ab089d`.

[133] P. J. E. Peebles. «From Precision Cosmology to Accurate Cosmology.» In: *37th Rencontres de Moriond on the Cosmological Model*. 2002. arXiv: `astro-ph/0208037`.

[134] Anthony R. Pullen, Shadab Alam, Siyu He, and Shirley Ho. «Constraining Gravity at the Largest Scales through CMB Lensing and Galaxy Velocities.» In: *Mon. Not. Roy. Astron. Soc.* 460.4 (2016), pp. 4098–4108. DOI: `10.1093/mnras/stw1249`. arXiv: `1511.04457 [astro-ph.CO]`.

[135] A. Pourtsidou, C. Skordis, and E. J. Copeland. «Models of dark matter coupled to dark energy.» In: *Phys. Rev. D* 88.8 (2013), p. 083505. DOI: `10.1103/PhysRevD.88.083505`. arXiv: `1307.0458 [astro-ph.CO]`.

[136] F. Lepori et al. «Euclid preparation. XIX. Impact of magnification on photometric galaxy clustering.» In: *Astron. Astrophys.* 662 (2022), A93. DOI: `10.1051/0004-6361/202142419`. arXiv: `2110.05435 [astro-ph.CO]`.

[137] Mike Shengbo Wang, Florian Beutler, and David Bacon. «Impact of Relativistic Effects on the Primordial Non-Gaussianity Signature in the Large-Scale Clustering of Quasars.» In: *Mon. Not. Roy. Astron. Soc.* 499.2 (2020), pp. 2598–2607. DOI: `10.1093/mnras/staa2998`. arXiv: `2007.01802 [astro-ph.CO]`.

[138] Camille Bonvin and Levon Pogosian. «Modified Einstein versus Modified Euler for Dark Matter.» In: *arXiv e-prints* (2022). arXiv: `2209.03614 [astro-ph.CO]`.

[139] Marco Raveri, Levon Pogosian, Kazuya Koyama, Matteo Martinelli, Alessandra Silvestri, Gong-Bo Zhao, Jian Li, Simone Peirone, and Alex Zucca. «A joint reconstruction of dark energy and modified growth evolution.» In: *arXiv e-prints* (July 2021). arXiv: `2107.12990 [astro-ph.CO]`.

[140] Tessa Baker, Pedro G. Ferreira, C. Danielle Leonard, and Mariele Motta. «New Gravitational Scales in Cosmological Surveys.» In: *Phys. Rev. D* 90.12 (2014), p. 124030. DOI: `10.1103/PhysRevD.90.124030`. arXiv: `1409.8284 [astro-ph.CO]`.

[141] Ryuichi Takahashi, Masanori Sato, Takahiro Nishimichi, Atsushi Taruya, and Masamune Oguri. «Revising the Halofit Model for the Nonlinear Matter Power Spectrum.» In: *Astrophys. J.* 761 (2012), p. 152. DOI: `10.1088/0004-637X/761/2/152`. arXiv: `1208.2701 [astro-ph.CO]`.

[142] T. M. C. Abbott et al. «Dark Energy Survey Year 1 Results: Constraints on Extended Cosmological Models from Galaxy Clustering and Weak Lensing.» In: *Phys. Rev. D* 99.12 (2019), p. 123505. DOI: 10.1103/PhysRevD.99.123505. arXiv: 1810.02499 [astro-ph.CO].

[143] Stefano Camera. «A novel method for unbiased measurements of growth with cosmic shear.» In: *arXiv e-prints* (June 2022). arXiv: 2206.03499 [astro-ph.CO].

[144] Francis Bernardeau, Takahiro Nishimichi, and Atsushi Taruya. «Cosmic shear full nulling: sorting out dynamics, geometry and systematics.» In: *MNRAS* 445.2 (Dec. 2014), pp. 1526–1537. DOI: 10.1093/mnras/stu1861. arXiv: 1312.0430 [astro-ph.CO].

[145] J. Muir et al. «DES Y1 results: Splitting growth and geometry to test ΛCDM.» In: *Phys. Rev. D* 103.2 (2021), p. 023528. DOI: 10.1103/PhysRevD.103.023528. arXiv: 2010.05924 [astro-ph.CO].

[146] Isaac Tutusaus, Camille Bonvin, and Nastassia Grimm. «First measurement of the Weyl potential evolution from the Year 3 Dark Energy Survey data: Localising the σ_8 tension.» In: (Dec. 2023). arXiv: 2312.06434 [astro-ph.CO].

[147] Philip Bull. «Extending cosmological tests of General Relativity with the Square Kilometre Array.» In: *Astrophys. J.* 817.1 (2016), p. 26. DOI: 10.3847/0004-637X/817/1/26. arXiv: 1509.07562 [astro-ph.CO].

[148] Shadab Alam et al. «Towards testing the theory of gravity with DESI: summary statistics, model predictions and future simulation requirements.» In: *JCAP* 11.11 (2021), p. 050. DOI: 10.1088/1475-7516/2021/11/050. arXiv: 2011.05771 [astro-ph.CO].

[149] Željko Ivezić et al. «LSST: from Science Drivers to Reference Design and Anticipated Data Products.» In: *Astrophys. J.* 873.2 (2019), p. 111. DOI: 10.3847/1538-4357/ab042c. arXiv: 0805.2366 [astro-ph].

[150] R. Laureijs et al. «Euclid Definition Study Report.» In: *arXiv e-prints* (2011). arXiv: 1110.3193 [astro-ph.CO].

[151] D. Spergel et al. «Wide-Field InfrarRed Survey Telescope-Astrophysics Focused Telescope Assets WFIRST-AFTA 2015 Report.» In: *arXiv e-prints* (2015). arXiv: 1503.03757 [astro-ph.IM].

[152] Joe Zuntz, Marc Paterno, Elise Jennings, Douglas Rudd, Alessandro Manzotti, Scott Dodelson, Sarah Bridle, Saba Sehrish, and James Kowalkowski. «CosmoSIS: modular cosmological parameter estimation.» In: *Astron. Comput.* 12 (2015), pp. 45–59. DOI: 10.1016/j.ascom.2015.05.005. arXiv: 1409.3409 [astro-ph.CO].

[153] Cullan Howlett, Antony Lewis, Alex Hall, and Anthony Challinor. «CMB power spectrum parameter degeneracies in the era of precision cosmology.» In: *JCAP* 1204 (2012), p. 027. DOI: 10.1088/1475-7516/2012/04/027. arXiv: 1201.3654 [astro-ph.CO].

[154] Antony Lewis, Anthony Challinor, and Anthony Lasenby. «Efficient computation of CMB anisotropies in closed FRW models.» In: *APJ* 538 (2000), pp. 473–476. DOI: 10.1086/309179. arXiv: astro-ph/9911177 [astro-ph].

[155] J. Prat et al. «Dark energy survey year 3 results: High-precision measurement and modeling of galaxy-galaxy lensing.» In: *Phys. Rev. D* 105.8, 083528 (Apr. 2022), p. 083528. DOI: `10.1103/PhysRevD.105.083528`. arXiv: `2105.13541 [astro-ph.CO]`.

[156] Levon Pogosian, Alessandra Silvestri, Kazuya Koyama, and Gong-Bo Zhao. «How to optimally parametrize deviations from General Relativity in the evolution of cosmological perturbations?» In: *Phys. Rev. D* 81 (2010), p. 104023. DOI: `10.1103/PhysRevD.81.104023`. arXiv: `1002.2382 [astro-ph.CO]`.

[157] Giulia Gubitosi, Federico Piazza, and Filippo Vernizzi. «The Effective Field Theory of Dark Energy.» In: *JCAP* 1302 (2013). [JCAP1302,032(2013)], p. 032. DOI: `10.1088/1475-7516/2013/02/032`. arXiv: `1210.0201 [hep-th]`.

[158] Jolyon K. Bloomfield, Éanna É. Flanagan, Minjoon Park, and Scott Watson. «Dark energy or modified gravity? An effective field theory approach.» In: *JCAP* 08 (2013), p. 010. DOI: `10.1088/1475-7516/2013/08/010`. arXiv: `1211.7054 [astro-ph.CO]`.

[159] Jerome Gleyzes, David Langlois, Federico Piazza, and Filippo Vernizzi. «Essential Building Blocks of Dark Energy.» In: *JCAP* 08 (2013), p. 025. DOI: `10.1088/1475-7516/2013/08/025`. arXiv: `1304.4840 [hep-th]`.

[160] Jolyon Bloomfield. «A Simplified Approach to General Scalar-Tensor Theories.» In: *JCAP* 12 (2013), p. 044. DOI: `10.1088/1475-7516/2013/12/044`. arXiv: `1304.6712 [astro-ph.CO]`.

[161] Federico Piazza, Heinrich Steigerwald, and Christian Marinoni. «Phenomenology of dark energy: exploring the space of theories with future redshift surveys.» In: *JCAP* 05 (2014), p. 043. DOI: `10.1088/1475-7516/2014/05/043`. arXiv: `1312.6111 [astro-ph.CO]`.

[162] Jérôme Gleyzes, David Langlois, and Filippo Vernizzi. «A unifying description of dark energy.» In: *Int. J. Mod. Phys.* D23.13 (2015), p. 1443010. DOI: `10.1142/S021827181443010X`. arXiv: `1411.3712 [hep-th]`.

[163] László Á. Gergely and Shinji Tsujikawa. «Effective field theory of modified gravity with two scalar fields: dark energy and dark matter.» In: *Phys. Rev. D* 89.6 (2014), p. 064059. DOI: `10.1103/PhysRevD.89.064059`. arXiv: `1402.0553 [hep-th]`.

[164] Emilio Bellini and Ignacy Sawicki. «Maximal freedom at minimum cost: linear large-scale structure in general modifications of gravity.» In: *JCAP* 07 (2014), p. 050. DOI: `10.1088/1475-7516/2014/07/050`. arXiv: `1404.3713 [astro-ph.CO]`.

[165] Macarena Lagos, Tessa Baker, Pedro G. Ferreira, and Johannes Noller. «A general theory of linear cosmological perturbations: scalar-tensor and vector-tensor theories.» In: *JCAP* 08 (2016), p. 007. DOI: `10.1088/1475-7516/2016/08/007`. arXiv: `1604.01396 [gr-qc]`.

[166] Tessa Baker, Pedro G. Ferreira, and Constantinos Skordis. «The Parameterized Post-Friedmann framework for theories of modified gravity: concepts, formalism and examples.» In: *Phys. Rev.* D87.2 (2013), p. 024015. DOI: `10.1103/PhysRevD.87.024015`. arXiv: `1209.2117 [astro-ph.CO]`.

[167] Pedro G. Ferreira, Tessa Baker, and Constantinos Skordis. «Testing general relativity with cosmology: a synopsis of the parametrized post-Friedmann approach.» In: *Gen. Rel. Grav.* 46 (2014), p. 1788. DOI: `10.1007/s10714-014-1788-x`.

[168] C. Skordis, A. Pourtsidou, and E. J. Copeland. «Parametrized post-Friedmannian framework for interacting dark energy theories.» In: *Phys. Rev. D* 91.8 (2015), p. 083537. DOI: `10.1103/PhysRevD.91.083537`. arXiv: `1502.07297 [astro-ph.CO]`.

[169] Sean M. Carroll, Vikram Duvvuri, Mark Trodden, and Michael S. Turner. «Is cosmic speed - up due to new gravitational physics?» In: *Phys. Rev. D* 70 (2004), p. 043528. DOI: `10.1103/PhysRevD.70.043528`. arXiv: `astro-ph/0306438`.

[170] Bharat Ratra and P. J. E. Peebles. «Cosmological Consequences of a Rolling Homogeneous Scalar Field.» In: *Phys. Rev. D* 37 (1988), p. 3406. DOI: `10.1103/PhysRevD.37.3406`.

[171] C. Wetterich. «Cosmology and the Fate of Dilatation Symmetry.» In: *Nucl. Phys. B* 302 (1988), pp. 668–696. DOI: `10.1016/0550-3213(88)90193-9`. arXiv: `1711.03844 [hep-th]`.

[172] C. Brans and R. H. Dicke. «Mach's principle and a relativistic theory of gravitation.» In: *Phys. Rev.* 124 (1961). Ed. by Jong-Ping Hsu and D. Fine, pp. 925–935. DOI: `10.1103/PhysRev.124.925`.

[173] Cedric Deffayet, Oriol Pujolas, Ignacy Sawicki, and Alexander Vikman. «Imperfect Dark Energy from Kinetic Gravity Braiding.» In: *JCAP* 10 (2010), p. 026. DOI: `10.1088/1475-7516/2010/10/026`. arXiv: `1008.0048 [hep-th]`.

[174] Alberto Nicolis, Riccardo Rattazzi, and Enrico Trincherini. «The Galileon as a local modification of gravity.» In: *Phys. Rev. D* 79 (2009), p. 064036. DOI: `10.1103/PhysRevD.79.064036`. arXiv: `0811.2197 [hep-th]`.

[175] C. Deffayet, Gilles Esposito-Farese, and A. Vikman. «Covariant Galileon.» In: *Phys. Rev.* D79 (2009), p. 084003. DOI: `10.1103/PhysRevD.79.084003`. arXiv: `0901.1314 [hep-th]`.

[176] C. Deffayet, Xian Gao, D. A. Steer, and G. Zahariade. «From k-essence to generalised Galileons.» In: *Phys. Rev. D* 84 (2011), p. 064039. DOI: `10.1103/PhysRevD.84.064039`. arXiv: `1103.3260 [hep-th]`.

[177] Jérôme Gleyzes, David Langlois, Federico Piazza, and Filippo Vernizzi. «Healthy theories beyond Horndeski.» In: *Phys. Rev. Lett.* 114.21 (2015), p. 211101. DOI: `10.1103/PhysRevLett.114.211101`. arXiv: `1404.6495 [hep-th]`.

[178] Jérôme Gleyzes, David Langlois, Federico Piazza, and Filippo Vernizzi. «Exploring gravitational theories beyond Horndeski.» In: *JCAP* 1502 (2015), p. 018. DOI: `10.1088/1475-7516/2015/02/018`. arXiv: `1408.1952 [astro-ph.CO]`.

[179] David Langlois and Karim Noui. «Degenerate higher derivative theories beyond Horndeski: evading the Ostrogradski instability.» In: *JCAP* 02 (2016), p. 034. DOI: `10.1088/1475-7516/2016/02/034`. arXiv: `1510.06930 [gr-qc]`.

[180] Marco Crisostomi, Kazuya Koyama, and Gianmassimo Tasinato. «Extended Scalar-Tensor Theories of Gravity.» In: *JCAP* 04 (2016), p. 044. DOI: `10.1088/1475-7516/2016/04/044`. arXiv: `1602.03119 [hep-th]`.

[181] David Langlois, Michele Mancarella, Karim Noui, and Filippo Vernizzi. «Effective Description of Higher-Order Scalar-Tensor Theories.» In: *JCAP* 05 (2017), p. 033. DOI: 10.1088/1475-7516/2017/05/033. arXiv: 1703.03797 [hep-th].

[182] T. Baker, E. Bellini, P. G. Ferreira, M. Lagos, J. Noller, and I. Sawicki. «Strong constraints on cosmological gravity from GW170817 and GRB 170817A.» In: (2017). arXiv: 1710.06394 [astro-ph.CO].

[183] Paolo Creminelli and Filippo Vernizzi. «Dark Energy after GW170817 and GRB170817A.» In: *Phys. Rev. Lett.* 119.25 (2017), p. 251302. DOI: 10.1103/PhysRevLett.119.251302. arXiv: 1710.05877 [astro-ph.CO].

[184] Jeremy Sakstein and Bhuvnesh Jain. «Implications of the Neutron Star Merger GW170817 for Cosmological Scalar-Tensor Theories.» In: *Phys. Rev. Lett.* 119.25 (2017), p. 251303. DOI: 10.1103/PhysRevLett.119.251303. arXiv: 1710.05893 [astro-ph.CO].

[185] Jose María Ezquiaga and Miguel Zumalacárregui. «Dark Energy After GW170817: Dead Ends and the Road Ahead.» In: *Phys. Rev. Lett.* 119.25 (2017), p. 251304. DOI: 10.1103/PhysRevLett.119.251304. arXiv: 1710.05901 [astro-ph.CO].

[186] C. D. Kreisch and E. Komatsu. «Cosmological Constraints on Horndeski Gravity in Light of GW170817.» In: *JCAP* 12 (2018), p. 030. DOI: 10.1088/1475-7516/2018/12/030. arXiv: 1712.02710 [astro-ph.CO].

[187] Johannes Noller and Andrina Nicola. «Cosmological parameter constraints for Horndeski scalar-tensor gravity.» In: *Phys. Rev. D* 99.10 (2019), p. 103502. DOI: 10.1103/PhysRevD.99.103502. arXiv: 1811.12928 [astro-ph.CO].

[188] Emilio Bellini, Antonio J. Cuesta, Raul Jimenez, and Licia Verde. «Constraints on deviations from ΛCDM within Horndeski gravity.» In: *JCAP* 1602.02 (2016). [Erratum: JCAP1606,no.06,E01(2016)], p. 053. DOI: 10.1088/1475-7516/2016/06/E01,10.1088/1475-7516/2016/02/053. arXiv: 1509.07816 [astro-ph.CO].

[189] Valentina Salvatelli, Federico Piazza, and Christian Marinoni. «Constraints on modified gravity from Planck 2015: when the health of your theory makes the difference.» In: *JCAP* 09 (2016), p. 027. DOI: 10.1088/1475-7516/2016/09/027. arXiv: 1602.08283 [astro-ph.CO].

[190] B. P. Abbott et al. «Gravitational Waves and Gamma-rays from a Binary Neutron Star Merger: GW170817 and GRB 170817A.» In: *Astrophys. J. Lett.* 848.2 (2017), p. L13. DOI: 10.3847/2041-8213/aa920c. arXiv: 1710.05834 [astro-ph.HE].

[191] David Alonso, Emilio Bellini, Pedro G. Ferreira, and Miguel Zumalacárregui. «Observational future of cosmological scalar-tensor theories.» In: *Phys. Rev.* D95.6 (2017), p. 063502. DOI: 10.1103/PhysRevD.95.063502. arXiv: 1610.09290 [astro-ph.CO].

[192] A. Spurio Mancini, R. Reischke, V. Pettorino, B. M. Schäfer, and M. Zumalacárregui. «Testing (modified) gravity with 3D and tomographic cosmic shear.» In: *Mon. Not. Roy. Astron. Soc.* 480.3 (2018), pp. 3725–3738. DOI: 10.1093/mnras/sty2092. arXiv: 1801.04251 [astro-ph.CO].

[193] Marco Crisostomi and Kazuya Koyama. «Self-accelerating universe in scalar-tensor theories after GW170817.» In: *Phys. Rev. D* 97.8 (2018), p. 084004. DOI: 10.1103/PhysRevD.97.084004. arXiv: 1712.06556 [astro-ph.CO].

[194] Alexandru Dima and Filippo Vernizzi. «Vainshtein Screening in Scalar-Tensor Theories before and after GW170817: Constraints on Theories beyond Horndeski.» In: *Phys. Rev. D* 97.10 (2018), p. 101302. DOI: 10.1103/PhysRevD.97.101302. arXiv: 1712.04731 [gr-qc].

[195] Ippocratis D. Saltas, Ignacy Sawicki, and Ilidio Lopes. «White dwarfs and revelations.» In: *JCAP* 05 (2018), p. 028. DOI: 10.1088/1475-7516/2018/05/028. arXiv: 1803.00541 [astro-ph.CO].

[196] Ippocratis D. Saltas and Jørgen Christensen-Dalsgaard. «Searching for dark energy with the Sun.» In: *Astron. Astrophys.* 667 (2022), A115. DOI: 10.1051/0004-6361/202244176. arXiv: 2205.14134 [astro-ph.SR].

[197] David Langlois, Ryo Saito, Daisuke Yamauchi, and Karim Noui. «Scalar-tensor theories and modified gravity in the wake of GW170817.» In: *Phys. Rev. D* 97.6 (2018), p. 061501. DOI: 10.1103/PhysRevD.97.061501. arXiv: 1711.07403 [gr-qc].

[198] T. A. Wagner, S. Schlamminger, J. H. Gundlach, and E. G. Adelberger. «Torsion-balance tests of the weak equivalence principle.» In: *Class. Quant. Grav.* 29 (2012), p. 184002. DOI: 10.1088/0264-9381/29/18/184002. arXiv: 1207.2442 [gr-qc].

[199] Carsten van de Bruck, Jack Morrice, and Susan Vu. «Constraints on Nonconformal Couplings from the Properties of the Cosmic Microwave Background Radiation.» In: *Phys. Rev. Lett.* 111 (2013), p. 161302. DOI: 10.1103/PhysRevLett.111.161302. arXiv: 1303.1773 [astro-ph.CO].

[200] Philippe Brax, Clare Burrage, Anne-Christine Davis, and Giulia Gubitosi. «Cosmological Tests of the Disformal Coupling to Radiation.» In: *JCAP* 11 (2013), p. 001. DOI: 10.1088/1475-7516/2013/11/001. arXiv: 1306.4168 [astro-ph.CO].

[201] Philippe Brax and Clare Burrage. «Constraining Disformally Coupled Scalar Fields.» In: *Phys. Rev. D* 90.10 (2014), p. 104009. DOI: 10.1103/PhysRevD.90.104009. arXiv: 1407.1861 [astro-ph.CO].

[202] Clifford M. Will. «The Confrontation between General Relativity and Experiment.» In: *Living Rev. Rel.* 17 (2014), p. 4. DOI: 10.12942/lrr-2014-4. arXiv: 1403.7377 [gr-qc].

[203] T. Damour, G. W. Gibbons, and C. Gundlach. «Dark matter, time-varying G, and a dilaton field.» In: *Phys. Rev. Lett.* 64 (2 Jan. 1990), pp. 123–126. DOI: 10.1103/PhysRevLett.64.123. URL: https://link.aps.org/doi/10.1103/PhysRevLett.64.123.

[204] Harry Desmond and Pedro G. Ferreira. «Galaxy morphology rules out astrophysically relevant Hu-Sawicki $f(R)$ gravity.» In: *Phys. Rev. D* 102.10 (2020), p. 104060. DOI: 10.1103/PhysRevD.102.104060. arXiv: 2009.08743 [astro-ph.CO].

[205] Kenneth Nordtvedt. «Equivalence Principle for Massive Bodies. I. Phenomenology.» In: *Phys. Rev.* 169 (5 1968), pp. 1014–1016. DOI: 10.1103/PhysRev.169.1014. URL: https://link.aps.org/doi/10.1103/PhysRev.169.1014.

[206] Sebastien Clesse and Juan García-Bellido. «Seven Hints for Primordial Black Hole Dark Matter.» In: *Phys. Dark Univ.* 22 (2018), pp. 137–146. DOI: 10.1016/j.dark.2018.08.004. arXiv: 1711.10458 [astro-ph.CO].

[207] David Wands, Josue De-Santiago, and Yuting Wang. «Inhomogeneous vacuum energy.» In: *Class. Quant. Grav.* 29 (2012), p. 145017. DOI: 10.1088/0264-9381/29/14/145017. arXiv: 1203.6776 [astro-ph.CO].

[208] Guido D'Amico, Zhiqi Huang, Michele Mancarella, and Filippo Vernizzi. «Weakening Gravity on Redshift-Survey Scales with Kinetic Matter Mixing.» In: *JCAP* 02 (2017), p. 014. DOI: 10.1088/1475-7516/2017/02/014. arXiv: 1609.01272 [astro-ph.CO].

[209] R. V. Pound and G. A. Rebka. «Gravitational Red-Shift in Nuclear Resonance.» In: *PRL.* 3.9 (Nov. 1959), pp. 439–441. DOI: 10.1103/PhysRevLett.3.439.

[210] James C. Lopresto, Charles Schrader, and A. K. Pierce. «Solar Gravitational Redshift from the Infrared Oxygen Triplet.» In: *APJ.* 376 (Aug. 1991), p. 757. DOI: 10.1086/170323.

[211] Young-Rae Kim and Rupert A. C. Croft. «Gravitational Redshifts in Simulated Galaxy Clusters.» In: *APJ.* 607.1 (May 2004), pp. 164–174. DOI: 10.1086/383218. arXiv: astro-ph/0402047 [astro-ph].

[212] Radoslaw Wojtak, Steen H. Hansen, and Jens Hjorth. «Gravitational redshift of galaxies in clusters as predicted by general relativity.» In: *Nat.* 477.7366 (Sept. 2011), pp. 567–569. DOI: 10.1038/nature10445. arXiv: 1109.6571 [astro-ph.CO].

[213] Nick Kaiser. «Measuring gravitational redshifts in galaxy clusters.» In: *MNRAS* 435.2 (Oct. 2013), pp. 1278–1286. DOI: 10.1093/mnras/stt1370. arXiv: 1303.3663 [astro-ph.CO].

[214] Pablo Jimeno, Tom Broadhurst, Jean Coupon, Keiichi Umetsu, and Ruth Lazkoz. «Comparing gravitational redshifts of SDSS galaxy clusters with the magnified redshift enhancement of background BOSS galaxies.» In: *MNRAS* 448.3 (Apr. 2015), pp. 1999–2012. DOI: 10.1093/mnras/stv117. arXiv: 1410.6050 [astro-ph.CO].

[215] Hongyu Zhu, Shadab Alam, Rupert A. C. Croft, Shirley Ho, and Elena Giusarma. «Effects of baryons on the gravitational redshift profile of ΛCDM halos.» In: (Jan. 2019). arXiv: 1901.05615 [astro-ph.CO].

[216] Shadab Alam, Rupert A. C. Croft, Shirley Ho, Hongyu Zhu, and Elena Giusarma. «Relativistic effects on galaxy redshift samples due to target selection.» In: *MNRAS* 471.2 (Oct. 2017), pp. 2077–2087. DOI: 10.1093/mnras/stx1684. arXiv: 1709.07856 [astro-ph.CO].

[217] Chris Blake et al. «The WiggleZ Dark Energy Survey: the growth rate of cosmic structure since redshift z=0.9.» In: *MNRAS* 415.3 (June 2011), pp. 2876–2891. DOI: 10.1111/j.1365-2966.2011.18903.x. eprint: 1104.2948. URL: https://doi.org/10.1111\%2Fj.1365-2966.2011.18903.x.

[218] Sveva Castello, Michele Mancarella, Nastassia Grimm, Daniel Sobral-Blanco, Isaac Tutusaus, and Camille Bonvin. «Gravitational redshift constraints on the effective theory of interacting dark energy.» In: *JCAP* 05 (2024), p. 003. DOI: 10.1088/1475-7516/2024/05/003. arXiv: 2311.14425 [astro-ph.CO].

[219] Richard L. Arnowitt, Stanley Deser, and Charles W. Misner. «The Dynamics of general relativity.» In: *Gen. Rel. Grav.* 40 (2008), pp. 1997–2027. DOI: 10.1007/s10714-008-0661-1. arXiv: gr-qc/0405109.

[220] Claudia de Rham and Scott Melville. «Gravitational Rainbows: LIGO and Dark Energy at its Cutoff.» In: *Phys. Rev. Lett.* 121.22 (2018), p. 221101. DOI: `10.1103/PhysRevLett.121.221101`. arXiv: `1806.09417 [hep-th]`.

[221] Tessa Baker, Enrico Barausse, Anson Chen, Claudia de Rham, Mauro Pieroni, and Gianmassimo Tasinato. «Testing gravitational wave propagation with multiband detections.» In: *JCAP* 03 (2023), p. 044. DOI: `10.1088/1475-7516/2023/03/044`. arXiv: `2209.14398 [gr-qc]`.

[222] Tessa Baker et al. «Measuring the propagation speed of gravitational waves with LISA.» In: *JCAP* 08.08 (2022), p. 031. DOI: `10.1088/1475-7516/2022/08/031`. arXiv: `2203.00566 [gr-qc]`.

[223] Ignacy Sawicki and Emilio Bellini. «Limits of quasistatic approximation in modified-gravity cosmologies.» In: *Phys. Rev. D* 92.8 (2015), p. 084061. DOI: `10.1103/PhysRevD.92.084061`. arXiv: `1503.06831 [astro-ph.CO]`.

[224] Luca Amendola, Martin Kunz, and Domenico Sapone. «Measuring the dark side (with weak lensing).» In: *JCAP* 0804 (2008), p. 013. DOI: `10.1088/1475-7516/2008/04/013`. arXiv: `0704.2421 [astro-ph]`.

[225] Edmund Bertschinger and Phillip Zukin. «Distinguishing Modified Gravity from Dark Energy.» In: *Phys. Rev. D* 78 (2008), p. 024015. DOI: `10.1103/PhysRevD.78.024015`. arXiv: `0801.2431 [astro-ph]`.

[226] Alessandra Silvestri, Levon Pogosian, and Roman V. Buniy. «Practical approach to cosmological perturbations in modified gravity.» In: *Phys. Rev. D* 87.10 (2013), p. 104015. DOI: `10.1103/PhysRevD.87.104015`. arXiv: `1302.1193 [astro-ph.CO]`.

[227] Levon Pogosian and Alessandra Silvestri. «What can cosmology tell us about gravity? Constraining Horndeski gravity with Σ and μ.» In: *Phys. Rev. D* 94.10 (2016), p. 104014. DOI: `10.1103/PhysRevD.94.104014`. arXiv: `1606.05339 [astro-ph.CO]`.

[228] Luca Amendola, Dario Bettoni, Ana Marta Pinho, and Santiago Casas. «Measuring gravity at cosmological scales.» In: *Universe* 6.2 (2020), p. 20. DOI: `10.3390/universe6020020`. arXiv: `1902.06978 [astro-ph.CO]`.

[229] Levon Pogosian, Marco Raveri, Kazuya Koyama, Matteo Martinelli, Alessandra Silvestri, Gong-Bo Zhao, Jian Li, Simone Peirone, and Alex Zucca. «Imprints of cosmological tensions in reconstructed gravity.» In: *Nature Astron.* 6.12 (2022), pp. 1484–1490. DOI: `10.1038/s41550-022-01808-7`. arXiv: `2107.12992 [astro-ph.CO]`.

[230] Cristhian Garcia-Quintero, Mustapha Ishak, and Orion Ning. «Current constraints on deviations from General Relativity using binning in redshift and scale.» In: *JCAP* 12 (2020), p. 018. DOI: `10.1088/1475-7516/2020/12/018`. arXiv: `2010.12519 [astro-ph.CO]`.

[231] Jaiyul Yoo and Matias Zaldarriaga. «Beyond the Linear-Order Relativistic Effect in Galaxy Clustering: Second-Order Gauge-Invariant Formalism.» In: *Phys. Rev. D* 90.2 (2014), p. 023513. DOI: `10.1103/PhysRevD.90.023513`. arXiv: `1406.4140 [astro-ph.CO]`.

[232] Enea Di Dio, Ruth Durrer, Giovanni Marozzi, and Francesco Montanari. «Galaxy number counts to second order and their bispectrum.» In: *JCAP* 12 (2014). [Erratum: JCAP 06, E01 (2015)], p. 017. DOI: 10.1088/1475-7516/2014/12/017. arXiv: 1407.0376 [astro-ph.CO].

[233] Daniele Bertacca, Roy Maartens, and Chris Clarkson. «Observed galaxy number counts on the lightcone up to second order: I. Main result.» In: *JCAP* 09 (2014), p. 037. DOI: 10.1088/1475-7516/2014/09/037. arXiv: 1405.4403 [astro-ph.CO].

[234] Enrique Paillas, Yan-Chuan Cai, Nelson Padilla, and Ariel G. Sánchez. «Redshift-space distortions with split densities.» In: *Mon. Not. Roy. Astron. Soc.* 505.4 (2021), pp. 5731–5752. DOI: 10.1093/mnras/stab1654. arXiv: 2101.09854 [astro-ph.CO].

[235] Zhiqi Huang. «Observational effects of a running Planck mass.» In: *Phys. Rev. D* 93.4 (2016), p. 043538. DOI: 10.1103/PhysRevD.93.043538. arXiv: 1511.02808 [astro-ph.CO].

[236] Luca Amendola, Valeria Pettorino, Claudia Quercellini, and Adrian Vollmer. «Testing coupled dark energy with next-generation large-scale observations.» In: *Phys. Rev. D* 85 (2012), p. 103008. DOI: 10.1103/PhysRevD.85.103008. arXiv: 1111.1404 [astro-ph.CO].

[237] P. A. R. Ade et al. «Planck 2015 results. XIV. Dark energy and modified gravity.» In: *Astron. Astrophys.* 594 (2016), A14. DOI: 10.1051/0004-6361/201525814. arXiv: 1502.01590 [astro-ph.CO].

[238] Adam G. Riess et al. «A Comprehensive Measurement of the Local Value of the Hubble Constant with 1 km s^{-1} Mpc^{-1} Uncertainty from the Hubble Space Telescope and the SH0ES Team.» In: *Astrophys. J. Lett.* 934.1 (2022), p. L7. DOI: 10.3847/2041-8213/ac5c5b. arXiv: 2112.04510 [astro-ph.CO].

[239] Minas Karamanis and Florian Beutler. «Ensemble slice sampling.» In: *Stat. Comput.* 31.5 (2021), p. 61. DOI: 10.1007/s11222-021-10038-2. arXiv: 2002.06212 [stat.ML].

[240] Minas Karamanis, Florian Beutler, and John A. Peacock. «zeus: a python implementation of ensemble slice sampling for efficient Bayesian parameter inference.» In: *Mon. Not. Roy. Astron. Soc.* 508.3 (2021), pp. 3589–3603. DOI: 10.1093/mnras/stab2867. arXiv: 2105.03468 [astro-ph.IM].

[241] Ignacy Sawicki, Ippocratis D. Saltas, Luca Amendola, and Martin Kunz. «Consistent perturbations in an imperfect fluid.» In: *JCAP* 01 (2013), p. 004. DOI: 10.1088/1475-7516/2013/01/004. arXiv: 1208.4855 [astro-ph.CO].

[242] Yong-Seon Song, Wayne Hu, and Ignacy Sawicki. «The Large Scale Structure of f(R) Gravity.» In: *Phys. Rev. D* 75 (2007), p. 044004. DOI: 10.1103/PhysRevD.75.044004. arXiv: astro-ph/0610532.

[243] Sean M. Carroll, Ignacy Sawicki, Alessandra Silvestri, and Mark Trodden. «Modified-Source Gravity and Cosmological Structure Formation.» In: *New J. Phys.* 8 (2006), p. 323. DOI: 10.1088/1367-2630/8/12/323. arXiv: astro-ph/0607458.

[244] Dan N. Vollick. «1/R Curvature corrections as the source of the cosmological acceleration.» In: *Phys. Rev. D* 68 (2003), p. 063510. DOI: 10.1103/PhysRevD.68.063510. arXiv: astro-ph/0306630.

[245] Christiane S. Lorenz, David Alonso, and Pedro G. Ferreira. «Impact of relativistic effects on cosmological parameter estimation.» In: *Phys. Rev.* D97.2 (2018), p. 023537. DOI: 10.1103/PhysRevD.97.023537. arXiv: 1710.02477 [astro-ph.CO].

[246] Roland de Putter, Jérôme Gleyzes, and Olivier Doré. «Next non-Gaussianity frontier: What can a measurement with $\sigma(f_{NL})\lesssim 1$ tell us about multifield inflation?» In: *Phys. Rev. D* 95.12 (2017), p. 123507. DOI: 10.1103/PhysRevD.95.123507. arXiv: 1612.05248 [astro-ph.CO].

[247] Ana Achúcarro et al. «Inflation: Theory and Observations.» In: (Mar. 2022). arXiv: 2203.08128 [astro-ph.CO].

[248] Marco Bruni, Robert Crittenden, Kazuya Koyama, Roy Maartens, Cyril Pitrou, and David Wands. «Disentangling non-Gaussianity, bias and GR effects in the galaxy distribution.» In: *Phys. Rev. D* 85 (2012), p. 041301. DOI: 10.1103/PhysRevD.85.041301. arXiv: 1106.3999 [astro-ph.CO].

[249] Toshiya Namikawa, Tomohiro Okamura, and Atsushi Taruya. «Magnification effect on the detection of primordial non-Gaussianity from photometric surveys.» In: *Phys. Rev. D* 83 (2011), p. 123514. DOI: 10.1103/PhysRevD.83.123514. arXiv: 1103.1118 [astro-ph.CO].

[250] Stefano Camera, Roy Maartens, and Mario G. Santos. «Einstein's legacy in galaxy surveys.» In: *Mon. Not. Roy. Astron. Soc.* 451.1 (2015), pp. L80–L84. DOI: 10.1093/mnrasl/slv069. arXiv: 1412.4781 [astro-ph.CO].

[251] David Alonso, Philip Bull, Pedro G. Ferreira, Roy Maartens, and M. Santos. «Ultra large-scale cosmology in next-generation experiments with single tracers.» In: *Astrophys. J.* 814.2 (2015), p. 145. DOI: 10.1088/0004-637X/814/2/145. arXiv: 1505.07596 [astro-ph.CO].

[252] Alvise Raccanelli, Francesco Montanari, Daniele Bertacca, Olivier Doré, and Ruth Durrer. «Cosmological Measurements with General Relativistic Galaxy Correlations.» In: *JCAP* 05 (2016), p. 009. DOI: 10.1088/1475-7516/2016/05/009. arXiv: 1505.06179 [astro-ph.CO].

[253] José Luis Bernal, Nicola Bellomo, Alvise Raccanelli, and Licia Verde. «Beware of commonly used approximations. Part II. Estimating systematic biases in the best-fit parameters.» In: *JCAP* 10 (2020), p. 017. DOI: 10.1088/1475-7516/2020/10/017. arXiv: 2005.09666 [astro-ph.CO].

[254] Matteo Martinelli, Roohi Dalal, Fereshteh Majidi, Yashar Akrami, Stefano Camera, and Elena Sellentin. «Ultralarge-scale approximations and galaxy clustering: Debiasing constraints on cosmological parameters.» In: *Mon. Not. Roy. Astron. Soc.* 510.2 (2022), pp. 1964–1977. DOI: 10.1093/mnras/stab3578. arXiv: 2106.15604 [astro-ph.CO].

[255] Jan-Albert Viljoen, José Fonseca, and Roy Maartens. «Multi-wavelength spectroscopic probes: prospects for primordial non-Gaussianity and relativistic effects.» In: *JCAP* 11 (2021), p. 010. DOI: 10.1088/1475-7516/2021/11/010. arXiv: 2107.14057 [astro-ph.CO].

[256] Jan-Albert Viljoen, José Fonseca, and Roy Maartens. «Multi-wavelength spectroscopic probes: biases from neglecting light-cone effects.» In: *JCAP* 12.12 (2021), p. 004. DOI: 10.1088/1475-7516/2021/12/004. arXiv: 2108.05746 [astro-ph.CO].

[257] Milad Noorikuhani and Roman Scoccimarro. «Wide-angle and relativistic effects in Fourier-space clustering statistics.» In: *Phys. Rev. D* 107.8 (2023), p. 083528. DOI: 10.1103/PhysRevD.107.083528. arXiv: 2207.12383 [astro-ph.CO].

[258] GFR Ellis and JE Baldwin. «On the expected anisotropy of radio source counts.» In: *Mon. Not. Roy. Astron. Soc.* 206 (1984), p. 377. DOI: 10.1093/mnras/206.2.377. URL: https://doi.org/10.1093/mnras/206.2.377.

[259] Nathan J. Secrest, Sebastian von Hausegger, Mohamed Rameez, Roya Mohayaee, Subir Sarkar, and Jacques Colin. «A Test of the Cosmological Principle with Quasars.» In: *Astrophys. J. Lett.* 908.2 (2021), p. L51. DOI: 10.3847/2041-8213/abdd40. arXiv: 2009.14826 [astro-ph.CO].

[260] Thilo M. Siewert, Matthias Schmidt-Rubart, and Dominik J. Schwarz. «Cosmic radio dipole: Estimators and frequency dependence.» In: *Astron. Astrophys.* 653 (2021), A9. DOI: 10.1051/0004-6361/202039840. arXiv: 2010.08366 [astro-ph.CO].

[261] Nathan J. Secrest, Sebastian von Hausegger, Mohamed Rameez, Roya Mohayaee, and Subir Sarkar. «A Challenge to the Standard Cosmological Model.» In: *Astrophys. J. Lett.* 937.2 (2022), p. L31. DOI: 10.3847/2041-8213/ac88c0. arXiv: 2206.05624 [astro-ph.CO].

[262] Charles Dalang and Camille Bonvin. «On the kinematic cosmic dipole tension.» In: *Mon. Not. Roy. Astron. Soc.* 512.3 (2022), pp. 3895–3905. DOI: 10.1093/mnras/stac726. arXiv: 2111.03616 [astro-ph.CO].

[263] Caroline Guandalin, Jade Piat, Chris Clarkson, and Roy Maartens. «Theoretical Systematics in Testing the Cosmological Principle with the Kinematic Quasar Dipole.» In: *Astrophys. J.* 953.2 (2023), p. 144. DOI: 10.3847/1538-4357/acdf46. arXiv: 2212.04925 [astro-ph.CO].

[264] Roy Maartens, Chris Clarkson, and Song Chen. «The kinematic dipole in galaxy redshift surveys.» In: *JCAP* 01 (2018), p. 013. DOI: 10.1088/1475-7516/2018/01/013. arXiv: 1709.04165 [astro-ph.CO].

[265] Tobias Nadolny, Ruth Durrer, Martin Kunz, and Hamsa Padmanabhan. «A new way to test the Cosmological Principle: measuring our peculiar velocity and the large-scale anisotropy independently.» In: *JCAP* 11 (2021), p. 009. DOI: 10.1088/1475-7516/2021/11/009. arXiv: 2106.05284 [astro-ph.CO].

[266] Anze Slosar, Christopher Hirata, Uros Seljak, Shirley Ho, and Nikhil Padmanabhan. «Constraints on local primordial non-Gaussianity from large scale structure.» In: *JCAP* 08 (2008), p. 031. DOI: 10.1088/1475-7516/2008/08/031. arXiv: 0805.3580 [astro-ph].

[267] Marco Celoria and Sabino Matarrese. «Primordial Non-Gaussianity.» In: *Proc. Int. Sch. Phys. Fermi* 200 (2020). Ed. by E. Coccia, J. Silk, and N. Vittorio, pp. 179–215. DOI: 10.3254/ENFI200009. arXiv: 1812.08197 [astro-ph.CO].

[268] Y. Akrami et al. «Planck 2018 results. IX. Constraints on primordial non-Gaussianity.» In: *Astron. Astrophys.* 641 (2020), A9. DOI: 10.1051/0004-6361/201935891. arXiv: 1905.05697 [astro-ph.CO].

[269] Emanuele Castorina et al. «Redshift-weighted constraints on primordial non-Gaussianity from the clustering of the eBOSS DR14 quasars in Fourier space.» In: *JCAP* 09 (2019), p. 010. DOI: `10.1088/1475-7516/2019/09/010`. arXiv: `1904.08859 [astro-ph.CO]`.

[270] Eva-Maria Mueller, Will J. Percival, and Rossana Ruggeri. «Optimizing primordial non-Gaussianity measurements from galaxy surveys.» In: *Mon. Not. Roy. Astron. Soc.* 485.3 (2019), pp. 4160–4166. DOI: `10.1093/mnras/sty3150`. arXiv: `1702.05088 [astro-ph.CO]`.

[271] G. Jelic-Cizmek et al. «Euclid Preparation. TBD. Impact of magnification on spectroscopic galaxy clustering.» In: (Nov. 2023). arXiv: `2311.03168 [astro-ph.CO]`.

[272] S. Yahya, P. Bull, M. G. Santos, M. Silva, R. Maartens, P. Okouma, and B. Bassett. «Cosmological performance of SKA HI galaxy surveys.» In: *Mon. Not. Roy. Astron. Soc.* 450.3 (2015), pp. 2251–2260. DOI: `10.1093/mnras/stv695`. arXiv: `1412.4700 [astro-ph.CO]`.

[273] A. J. S. Hamilton. «Uncorrelated modes of the non-linear power spectrum.» In: *Monthly Notices of the Royal Astronomical Society* 312.2 (Feb. 2000), pp. 257–284. ISSN: 0035-8711. DOI: `10.1046/j.1365-8711.2000.03071.x`. eprint: `https://academic.oup.com/mnras/article-pdf/312/2/257/2945062/312-2-257.pdf`. URL: `https://doi.org/10.1046/j.1365-8711.2000.03071.x`.

[274] Sveva Castello, Zhuangfei Wang, Lawrence Dam, Camille Bonvin, and Levon Pogosian. «Disentangling modified gravity from a dark force with gravitational redshift.» In: (Apr. 2024). arXiv: `2404.09379 [astro-ph.CO]`.

[275] George B. Arfken et al. *Mathematical Methods for Physicists. A Comprehensive Guide*. Academic Press, Elsevier Inc., Dec. 2012. ISBN: 978-0-12-384654-9. DOI: `10.1016/C2009-0-30629-7`.